Additives to Mitigate Against Slagging and Fouling in Biomass Combustion

Lee James Roberts

Submitted in accordance with the requirements for the degree of Doctor of Philosophy as part of the Integrated PhD with MSc in Bioenergy

December 2018

Centre for Doctoral Training in Bioenergy
School of Chemical and Process Engineering, Faculty of Engineering
University of Leeds

Declaration of Authorship

The candidate confirms that the work submitted is his own, except where work which has formed part of jointly-authored publications has been included. The contribution of the candidate and the other authors to this work has been explicitly indicated below. The candidate confirms that appropriate credit has been given within the thesis where reference has been made to the work of others.

The work contained in Chapter 4 is based on the following publication:

Roberts, L. J., Mason, P. E., Jones, J. M., Gale, W. F., Williams, A., & Ellul, C. (2018). Investigating the impact of an Al-Si additive on the resistivity of biomass ashes. *Fuel Processing Technology*, *178*, 13-23.

As lead author, the candidate conducted all experimental work, data analysis, statistical analysis and wrote the manuscript. The ash resistivity testing equipment was built by Dr. Mason, who also devised the methodology. The remaining authors provided supervision, guidance and corrections to the manuscript.

Part of the work contained in Chapters 6 and 7 is based on the following publication:

Roberts, L.J., Mason, P.E., Jones, J.M., Gale, W.F., Williams, A. (2018). The impact of aluminosilicate-based additives upon the sintering and melting behaviour of biomass ash. *European Biomass Conference and Exhibition Proceedings 2018 (26th EUBCE),* 453-457

As lead author, the candidate conducted all ash fusion testing and sinter strength experimental work and analysis, and wrote much of the publication. The remaining authors provided supervision, guidance and corrections to the manuscript.

Part of the work contained in Chapters 5, 6 and 7 has been submitted for review within the following publication:

Roberts, L.J., Mason, P.E., Jones, J.M., Gale, W.F., Williams, A., Hunt, A., Ashman, J. (2018). The impact of aluminosilicate-based additives upon the sintering and melting behaviour of biomass ash. Submitted to *Biomass and Bioenergy - Special Issue of the 26th European Biomass Conference and Exhibition held in Copenhagen, May 2018.*

As lead author, the candidate conducted all ash fusion testing and sinter strength experimental work, all data analysis and elucidation, and wrote much of the publication. Dr. Hunt conducted the high temperature viscosity experiments with the lead author present, and provided FactSage viscosity modelling and thermodynamic data. The remaining authors provided supervision, guidance and corrections to the manuscript.

Acknowledgements

I would like to start by thanking my supervisors, Professor Jenny Jones, Professor Bill Gale, Dr Patrick Mason and Professor Alan Williams. They have taught me so much, and their guidance, support and encouragement has been utterly invaluable. I am extremely thankful to have had the opportunity to work with them, both on this project and in general.

I would also like to mention the members of my research group: Ric Birley, Natalie Brown, Dr Yee-Sing Chin, Dr Ben Dooley, Dr Bijal Gudka, Dr Douglas Phillips, Andy Price, Dr Eddy Mitchell, and particularly Dr Paula McNamee and Dr Leilani Darvell. I am grateful for all the help and support you've given me over the years.

The University of Leeds staff have helped immensely with my research. In particular, I would like to thank James McKay, Emily Bryan-Kinns, Dr Adrian Cunliffe, Karine Alves Thorne, David Haynes, Ed Woodhouse, Dr Simon Lloyd, Diane Cochrane and Dr Bob Cochrane.

Many thanks go to the Engineering and Physical Sciences Research Council (EPSRC, EP/L014912/1) for my studentship; the Biomass and Fossil Fuels Research Alliance (BF2RA, Grant 22) for providing funding, materials and expertise to the project; the Materials Processing Institute, particularly Dr Adam Hunt, for allowing me to use their equipment and enabling me to undertake an important area of research; and Technische Universität Dortmund, particularly Christopher Schaak, for their hospitality during a fantastic research placement.

I consider myself extremely lucky to have been a part of the Bioenergy CDT, and even more so to have been a member of the 2014 cohort with Diarmaid Clery, Dr Luke Conibear, Andrew Dyer, Gillian Finnerty, Ollie Grasham, Hana Mandová, Tomi Oladipo, Kiran Parmar, Charlotte Stead and Rob White. Thank you all for making the last four years such a wonderful experience. It has been a pleasure to work with everyone in the CDT and in the Energy Building, but special mentions go to Dr Dave Allen, Fernando Barba, Dr Rob Bloom, Aaron Brown, Iram Razaq, Daisy Thomas, Charlotte Weaver, Flora Brocza, and plenty others, some of whom I've mentioned earlier. The most rewarding part of this PhD has been the friends I have made, and I hope that many will be friends for life.

I would also like to thank my friends outside of university, especially Lauren Anthony, Diana Marin and Michael Massey, for keeping me sane, providing encouragement, and for always being there for me. I can't stress how much I appreciate it.

Last, but certainly not least, I'd like to thank all of my family, but especially my Nana Lee (now Greville), Nana Roberts, my sister Gemma, who I have always looked up to (figuratively speaking), and my mum and dad, Kathy and Billy, who are my inspiration, my strength and my motivation. I am so proud to call you my parents, and I love you with all my heart.

Abstract

A crucial part of current and future energy strategy involves the replacement of coal with biomass. However, the composition of biomass creates operational issues in large scale combustion, potentially creating severe slagging and fouling deposition and in worst case scenarios boiler shutdown. Additives have shown promise in improving the deposition of biomass ashes, by altering the composition of the ash and subsequently improving the melting behaviour and deposit properties. However, the effect of additives upon the performance of large scale combustion boilers is not fully understood. This research focuses on the impact of two promising aluminosilicate-based (Al-Si) additives, coal pulverised fuel ash (PFA) and Kaolin powder (KAO), upon the ash properties of different biomass types (olive cake, white wood, bagasse and a power station fly ash).

The first area of research was to determine the effect of Al-Si additives upon the electrical resistivity of the ashes across a range of temperatures, which can have a significant impact upon electrostatic precipitator (ESP) performance. A bespoke resistivity test was designed and built for this purpose, based on existing standards. Results showed that biomass ash resistivity is typically lower than that of coal ash by an order of magnitude or more. In some cases, the resistivity may be low enough to cause operational problems and increased particle emissions. The use of additives resulted in increased resistivities, thereby reducing the risk of lower ESP collection efficiencies. Although ESP loads would be increased, this would not be expected to negatively impact emissions. Analysis of the ash compositions indicated that, contrary to previous experience with coal ashes, potassium concentration is an important factor in biomass ash resistivity, meaning that current predictive models are inadequate for biomass and biomass-additive compositions. Therefore, an existing model has been modified using the experimental data and taking into account potassium concentration; this produced reasonable predictions, and showed promise in predicting the resistivity of both biomass and coal ashes.

The second area of research was focused upon ash melting behaviour. High temperature viscosity was used to determine ash flow behaviour at temperatures

encountered in and around the combustion zone of large scale boilers. Results showed that KAO use with high potassium, high chlorine olive cake (OCA) would significantly improve the flow properties of the ash at combustion temperatures, resulting in ideal viscosities and significantly improved slagging deposition. Thermodynamic modelling data indicated that this was due to the decreased concentrations of magnesium and phosphorus and increased alumina concentrations within the ash, resulting in the formation of high melting temperature minerals and compounds. Ash fusion testing further indicated that KAO can significantly increase flow temperatures of biomass: however, PFA was observed to be less effective. In the case of high silica biomass, PFA was found to have a significant adverse effect upon flow temperature, which would lead to significantly worse slagging.

Sinter strength testing was investigated across a temperature range of 800-950°C. Both additives were found to improve the properties of OCA by binding potassium as silicates and aluminosilicates. This eliminates severe sintering caused by KCl sublimation and fluxing at 850°C by binding potassium as silicates and aluminosilicates. However, for the other biomass sinter strengths were increased with additive use. Although most results were below the strengths required for soot blower removal, high additive concentrations produced problematic sinter strengths. It was determined that kaolin has the greatest potential as an additive to reduce deposition issues from biomass combustion, due to its high kaolinite content. Coal PFA was determined to be less effective due to its high mullite and iron concentration. Finally, results indicated that Al-Si additive use is unsuitable for biomass containing high levels of SiO_2, and should be used only on biomass with either low SiO_2 or high KCl concentrations. However, lower additive rates need to be investigated in future.

Contents

Figures

Tables

Nomenclature

Symbols and Units

A	Amperes
bar	= 100,000 Pa
C	Coulombs (A s)
c	Speed of light in a vacuum (~3 x10^{8} m s^{-1})
E	Energy (J)
e	Euler's number (2.71828)
η	Viscosity (Pa s)
f	Frequency (s^{-1})
h	Planck Constant (6.636 x10^{-34} J s)
I	Electric current (A)
J	Joules (kg m^{2} s^{-2})
k	Boltzmann Constant (1.38 x10^{-23} J K^{-1})
λ	Wavelength (m)
ln	Natural logarithm
m	Metres
mol	Mole (unit)
Mtoe	Million Tonnes of Oil Equivalent
Pa	Pascal (kg m^{-1} s^{-2})
psi	Pounds per square inch (= 6.894757 kPa)
psig	Pounds per square inch gauge
Q	Charge (C)
Ω	Ohm (kg m^{2} s^{-3} A^{-2})
R	Electrical Resistance (Ω)

ρ	Resistivity (Ωm)
T	Temperature (K, or °C)
t	Time (s)
V	Volts (kg m^2 s^{-3} A^{-1})
W	Watts (kg $m^2 \cdot s^{-3}$)

Abbreviations

AFT	Ash Fusion Testing
Adtv.	Additive
ART	Ash Resistivity Testing
a.r.	As Received
B/A Ratio	Base-to-Acid Ratio
BA	Bagasse Ash
BECCS	Bioenergy with Carbon Capture and Storage
BFB	Bubbling Fluidised Bed
BS	British Standards
CFB	Circulating Fluidised Bed
COC	Condensable organic compounds
d.a.f.	Dry Ash Free
d.b	Dry Basis
EDX	Energy-Dispersive X-Ray Spectroscopy
Eqn.	Equation
ESP	Electrostatic Precipitator
FBC	Fluidised Bed Combustion
FA	Fly Ash
FT	Flow Temperature

GCV	Gross Calorific Value (MJ kg^{-1})
GHG	Greenhouse Gas
HT	Hemisphere Temperature
HHV	Higher Heating Value (MJ kg^{-1})
ICP-MS	Inductively Coupled Plasma Mass Spectroscopy
IDT	Initial Deformation Temperature
IEEE	Institute of Electrical and Electronics Engineers
KAO	Kaolin powder
LCPD	Large Combustion Plant Directive
LOI	Loss on Ignition
MS	Mass Spectroscopy
NBO	Non-bridging oxygen bonds
NBO/BO ratio	Ratio of non-bridging oxygen to bridging oxygen bonds
OCA	Olive Cake Ash
OECD	The Organization for Economic Cooperation and Development
PCA	Principal Component Analysis
PFA	Pulverised Fuel Ash (coal)
PF	Pulverised Fuel (combustion)
PIP	Peak impact pressure
ppm	Parts per million
PSD	Particle Size Distribution
SEM	Scanning Electron Microscope/Microscopy
SS	Sinter Strength

ST	Softening Temperature
STA	Simultaneous Thermal Analysis
T_{cv}	Temperature of critical viscosity
UNFCCC	United Nations Framework Convention on Climate Change
Wt. %	Percentage of weight (kg)
WWA	White Wood Ash
XRD	X-Ray Diffraction
XRF	X-Ray Flourescence

Thesis Outline

This thesis can be considered to be split into three main parts. The first part, Chapters 1-3, are intended as an overall introduction to thesis, justifying the project and providing in-depth background to the relevant topics. Chapter 4 focuses upon the impact of Al-Si additives upon ash resistivity. Chapters 5-8 focus upon the impact of Al-Si additives upon ash melting and deposition behaviour. Chapter 9 provides an overall summary of the thesis and overall conclusions. The details of each individual chapter are discussed below.

Chapter 1 is intended to introduce the reader to issues relevant to the research undertaken in this thesis, and to provide some justification for this research. The chapter begins with some background about the growth of the energy industry since the industrial revolution, and the basic mechanisms behind the greenhouse effect and global warming. Current and future climate change policy and energy trends are discussed, with a focus on the UK. The different types of large scale solid fuel combustion are described. Coal and biomass are introduced, with a brief description of and comparison between their compositions provided. The inorganic elements of the fuels, the ash, is briefly introduced, and the rationale behind additive use. Finally, the aims and objectives of the thesis are stated, with the chapters pertaining to each objective provided.

Chapter 2 gives an in-depth overview of topics relevant to the work conducted for this thesis, along with a review of the available literature. The chapter begins with a description of biomass ash composition and the inorganic species typically encountered within the ash. The inorganic transformations that occur during biomass combustion are then discussed in detail, with a focus upon silicate, oxide and chloride interactions, which are most relevant to this study. The mechanisms of ash deposition are outlined, and the sintering behaviour of deposited material is discussed. Slagging, fouling, corrosion and bed agglomeration are then described, with previous experience discussed and the available literature reviewed. Finally, the mechanisms by which additives work are presented, with a particular focus on Al-Si additives, which are the focal point of this study.

Chapter 3 introduces the samples used within this study, and outlines the processes and techniques involved in the initial characterisation of the samples. Ash preparation is described, and the compositions are presented along with some compositional analysis and further characterisation including particle size distribution.

Chapter 4 details experiments focusing on the electrical properties of the ashes, are of importance for effective ESP operation. The chapter opens with an overview of electrostatic precipitation, the principles and mechanisms behind ESP operation, the importance of ash resistivity, and a review of the available literature on the subject. The methodology used in resistivity experiments is then outlined in detail. Resistivity measurements were conducted over a temperature range of 80°C - 210°C, corresponding to the temperatures typically encountered by ESPs in large scale boilers. Results for each sample are analysed and discussed in the context of ESP performance. Regression analysis is used to determine the importance of the components within the ash. Finally, the results are used to modify a pre-existing model commonly used to predict the resistivity of coal ashes.

Chapter 5 focuses upon the flow behaviour of the ash at slagging temperatures. The chapter begins with a literature review of high temperature viscosity experiments. The network theory of silicate melts is introduced, and a number of empirical viscosity models that use this theory are described. The apparatus and methodology used in viscosity measurements are outlined, along with additional ash preparation required for these experiments. FactSage modelling was used to predict the viscosity of the ashes, and results are presented and analysed in the context of phase equilibrium predictions using MTData. Finally, viscosity results are compared to predictions from the empirical models.

Chapter 6 discusses ash fusion experiments. The chapter begins with a critical literature review of the ash fusion test, its limitations, and previous publications on the subject. Sample preparation is described, and deviations from the standard method are explained and justified. Pellet height profiles between 700 and 1600°C are presented, and the effect of additive concentration is discussed. Traditional ash fusion temperatures are also provided. Results are compared against literature, and any differences are discussed. Regression analysis is used

to determine important ash components for different ash fusion temperatures and is also applied to slagging indices from literature to determine their effectiveness.

Chapter 7 focuses on the sinter strength of ashes at different temperatures, and the effect of the additives upon sintering. The chapter begins with a review of sinter strength testing and issues related to deposition strength and soot blowing in boilers, including previous experimental experience in this field. The method used for sinter strength testing is described, with additional information provided with regards to the different behaviours observed. Samples were sintered between 800-950°C for a period of 3 hours, and their peak compressive strength recorded. Sinter strength measurements are provided and discussed, with SEM-EDX imaging and XRD spectra of the samples used to supplement the results and to give insight into the mechanisms involved. Finally, sinter strength results were compared to the ash composition of the samples through linear regression, in order to determine whether any particular ash components were having an effect upon sintering behaviour.

Chapter 8 brings together the research presented in Chapters 5-7, comparing the results of each experiment and providing an overview of the mechanisms that are postulated to be taking place. Recommendations for additive use to improve deposition behaviour are provided based upon the analysis of the preceding three chapters.

Chapter 9 provides a summary of the results of Chapters 4-8, and overall conclusions on the impact of Al-Si additives in biomass combustion. Potential areas of future research are outlined.

Chapter 1 - Introduction

1.1 - Background

The Industrial Revolution is considered one of the most important developments in human history, with a number of significant technological advancements leading to a sustained growth in global population, resource use and economic output on a scale never before experienced by humanity [1, 2]. Pre-Industrial Revolution, the predominant sources of energy were initially firewood (or woody phytomass) for small-scale heating, and charcoal in industrial uses such as iron smelting. This was followed by an uptake in the use of coal where it became the dominant source of energy in most British industries by the 1700s [3]. The invention of Watt's steam engine in 1769 precipitated a large expansion in coal production and consumption. This was followed by the internal combustion engine in 1875, which lead to the uptake of crude oil usage [4]. Finally, natural gas became a major source of energy due to advancements in pipeline construction methods in the 1930s [3], which allowed gas to be transported over greater distances.

The next significant event was World War II, which came at a great economic cost (not to mention human cost) for many of the countries involved. However, high investment in the years following the war lead to an economic boom in Western Europe, where real GDP rose almost twice as rapidly over the following 25 years when compared to any similar period before or since [5]. This coincided with a spike in population as birth rates increased dramatically. As a result of these factors, energy demand and, in turn, fossil fuel use grew exponentially, as shown in Figure 1.1. UK electricity consumption increased by 150% between 1948 and 1965 [6].

This period of growth has been most associated with a rapid loss of global sustainability, including the onset of exceptional CO_2 concentrations in the atmosphere. Although CO_2 concentrations had risen from 297 ppm in 1900 to 316 ppm in 1957, a concentration of 395 ppm was recorded in 2010 [7], indicating that the rate of CO_2 emissions had far outstripped that of the previous 50 years. This, alongside increases in the concentrations of other gases, has significant

implications for the planet in the form of global warming due to the greenhouse effect.

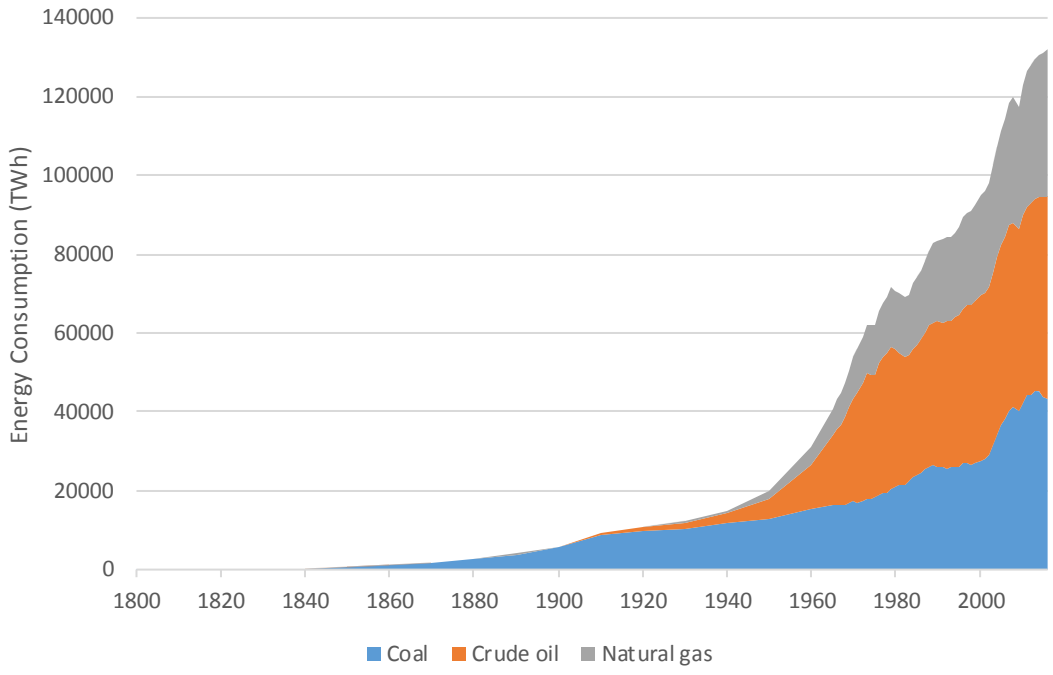

Figure 1.1 - Global fossil fuel consumption between 1800 and 2016 in terawatt-hours (TWh). Adapted from [3]

1.2 - The Greenhouse Effect

The greenhouse effect has been known for almost two centuries. In 1822, Joseph Fourier first determined that the temperature of the Earth was far greater than would be expected, based upon its size and distance from the Sun [8]. Since heated surfaces emit radiation in the form of thermal energy, Fourier calculated that the heat emitted by the Earth should result in far cooler temperatures: as a result the heat must be trapped, which he compared to how a greenhouse on a sunny day is much warmer when compared to outside. In this case, Fourier reasoned that the atmosphere is analogous to the glass of a greenhouse. John Tyndall's later experiments in 1859 showed that certain gases, such as methane, water vapour and CO_2 were effective in absorbing infrared radiation [9].

The mechanism by which the greenhouse effect occurs is as follows: the energy of a photon is inversely proportional to its wavelength, through the standard equation $E = \frac{hc}{\lambda}$, where E is energy, λ is wavelength, and h and c are the Planck

constant and the speed of light constant, respectively. Many of the photons emitted by the Sun are in the form of ultra-violet light (λ = 10nm - 400nm), visible light (400 - 700 nm) and infrared radiation (700 nm - 1 mm). Of the average total incoming solar radiation (approximately 340 W/m^2), 29% is reflected by the atmosphere, 23% is absorbed by the atmosphere, and 48% is absorbed at the Earth's surface. When this energy is absorbed by the Earth, its surface heats up, and emits lower energy infrared radiation to maintain thermal equilibrium.

When light radiation passes through a gas, there is a chance that the particles can absorb a photon and become excited. Different gases are more effective at absorbing certain wavelengths of radiation than others: this can be shown by their absorption spectra. The issue with greenhouse gases is that they are particularly effective at absorbing infrared radiation but do not absorb much in the way of UV or visible light, except for Ozone which protects against high energy UV radiation (Figure 1.2). This allows light from the Sun to pass through unhindered, but traps the infrared radiation emitted by the Earth.

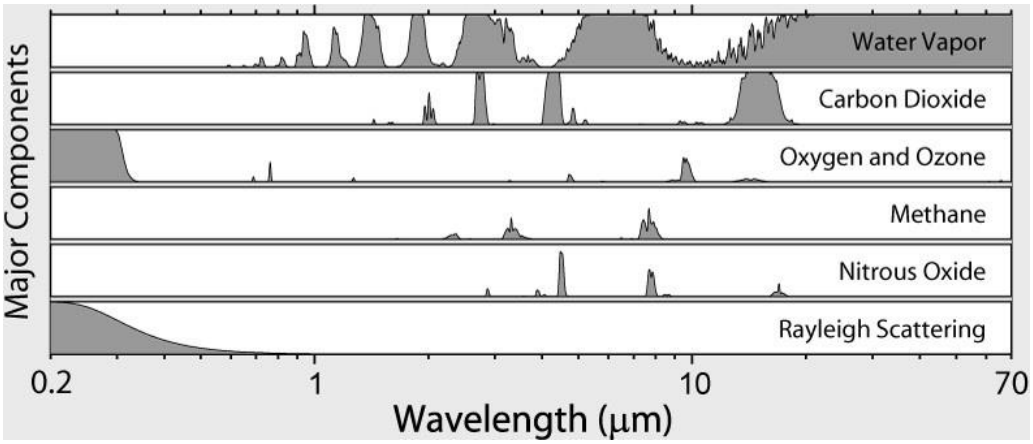

Figure 1.2 - Absorption spectra of various greenhouse gases. From [10]

As a result, an increase in greenhouse gas concentration increases the total heat absorbed from the infrared radiation emitted by the Earth's atmosphere, causing global temperatures to increase, leading to rising sea levels and more severe climates. The exponential increase in the use of fossil fuels, as shown in Figure 1.1, has resulted in a similar increase in CO_2 concentration within the atmosphere, as shown in Figure 1.3. This increase has an extremely strong correlation with increasing average global temperatures, also shown in Figure 1.3. The continued use of carbon-based fuels at current or increased rates has been estimated to increase global temperatures by 4°C by 2099, which would

have dramatic impacts on the planet including melting of the polar ice caps, ocean acidification and desertification [11].

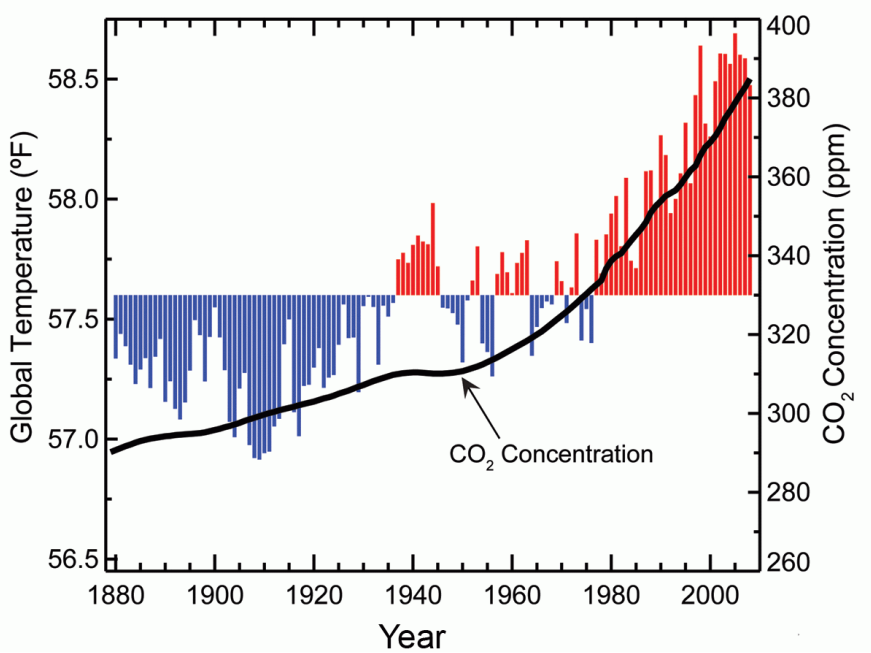

Figure 1.3 - Global average annual temperature compared with recorded atmospheric CO_2 concentration [12]

1.3 - Climate Change Policy

As a result of the findings of the scientific community, climate change has become an international political issue. The United Nations Framework Convention on Climate Change (UNFCCC) is an international environmental treaty created in 1992, with an aim to galvanise international co-operation in order to "stabilise greenhouse gas emissions at a level that would prevent dangerous anthropogenic interference with the climate system" [13]. The UNFCCC initially had 154 nations sign the treaty, growing to 197 parties, and although no binding targets were set it has led to several further significant treaties. The Kyoto Protocol, signed in 1997, extended this treaty further, and introduced legally binding commitments to reduce greenhouse gas emissions. In 2010, governments committed to "hold the increase in global average temperature below 2°C above pre-industrial levels", with a "Green Climate Fund" introduced to raise funds for developing countries [14]. Most recently, in 2016, 195 parties adopted the first legally binding targets in the form of the Paris Agreement, where each country is required to plan and regularly report on its Intended Nationally

Determined Contribution (INDC) in mitigating global warming to within 1.5°C of pre-industrial levels.

In Europe, a set of climate and energy targets to be met by 2020 were established in 2001, and later amended with Directive 2009/28/EC, known as the 20-20-20 targets: aiming for a reduction in EU greenhouse gas emissions of at least 20% when compared to 1990 levels, for 20% of total energy consumption to be provided by renewable sources, and a 20% reduction in primary energy use compared to projected levels, through increased energy efficiency [15]. In response to the Paris Agreement, the European Union submitted an INDC that aims for a minimum 40% reduction in greenhouse gas emissions compared to 1990 levels [16].

1.3.1 - UK Climate Change Policy

The flagship climate change policy in the UK is the Climate Change Act 2008 (CCA), which is regarded as the world's first attempt by a government to introduce legally binding climate change targets [17]. The aim of the CCA is to achieve reductions in greenhouse gas emissions of 80% compared to 1990 levels by 2050, through the use of carbon budgets. Each carbon budget is set 12 years in advance, every 5 years, with the intent of providing both confidence to investors in relevant markets and to constrain future governmental parties. However, the effectiveness of this has been disputed [18]. Further, as currently a part of the European Union, the UK is required to source at least 15% of its energy from renewable technologies by 2020 [15]. According to the Committee on Climate Change, no further adjustments are required in the wake of the targets agreed upon at the Paris Agreement [19], as UK policy was robust enough already.

However, there is much uncertainty regarding the future of UK energy policy in the wake of the United Kingdom European Union membership referendum in 2016, where a majority of 51.9% voted in favour of leaving the EU, from a turnout of 72.2%. Although this referendum was non-binding, the UK government began the process of leaving the EU, known as Brexit, in 2017. This has dominated British politics since the vote, and will continue to have substantial impacts on British policies in the short to mid-term future, including energy policy. It has been noted that the government is unlikely to meet the emission reductions set during the last two carbon budgets in the CCA due to key environmental policies being

scrapped in the name of austerity [17]. In addition, there are several EU directives that set emissions targets and actions that are not currently a part of British policies. Some of these are crucial for the UK to be able to meet its own energy targets [20] (see Figure 1.4), including the Renewable Energy Directive [15]. As a result, upon leaving the EU, Britain will have no legislated renewable energy targets beyond the overall emission reduction targets outlined by the CCA, and therefore it has no cohesive strategy [21]. Although this could be beneficial since it allows for more flexibility in policy choice [20], it does make the immediate future of UK energy policy unclear at this point. While the effect of Brexit upon EU budgets is likely to be significantly smaller than for Britain [22], there is a possibility that it will affect future EU energy budgets too.

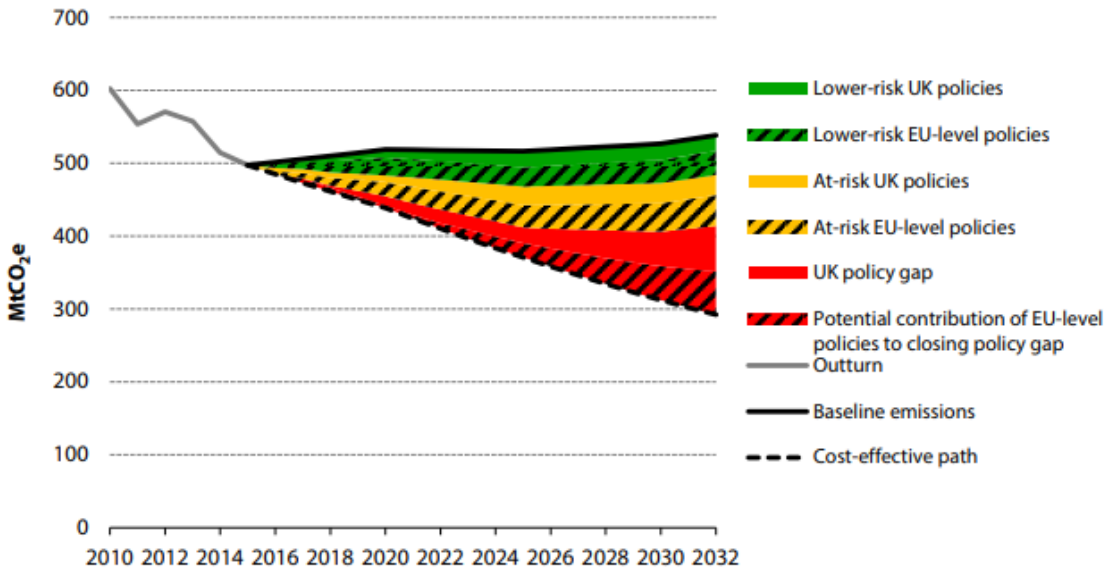

Figure 1.4 - Contribution of EU policies to UK capability of meeting carbon budgets and 2050 carbon emissions target. From [23]

1.4 - The Energy Industry

1.4.1 - Global Energy Trends

Demand for energy has largely increased in line with economic output and population growth, as outlined in Section 1.1, and has also exploded since the 1950s [7]. This has not slowed much since, with the world's total energy supply increasing from 346,408 petajoules (PJ) in 1990 to 551,688 PJ in 2015 [24], and shows no signs of slowing in the near future. Global energy demand increased

by 2.1% in 2017, compared with an average of 0.9% over the previous five years, reaching a total energy demand of 14,050 million tonnes of oil equivalent (Mtoe) [25], while the US Energy Information Administration (EIA) projects a further 28% increase in world energy use by 2040, with more than 60% of this projected growth coming from non-OECD countries such as China and India [26].

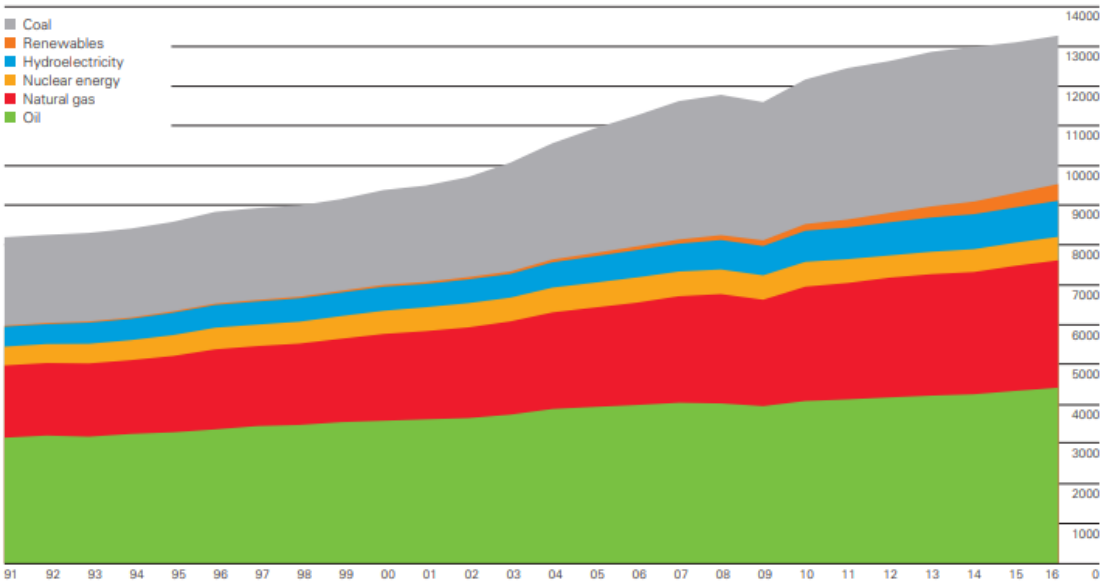

Figure 1.5 - Global fuel consumption, 1990-2016 [27]

Due to this rapidly increasing demand, fossil fuels remain a significant part of the global energy mix, accounting for the majority of energy consumed as shown in Figure 1.5. Coal, oil and natural gas accounted for approximately 86% of total energy production and consumption in 2014 [4], although these values vary significantly between regions. For instance, 64% of China's energy consumption came from coal, compared to just 5% in the UK [28].

1.4.2 - Emissions from Energy

As a result of the reliance upon fossil fuels, the energy industry is the largest contributor to global greenhouse emissions, and was estimated to account for 68% of global anthropogenic greenhouse gas (GHG) emissions in 2014 [29], as shown in Figure 1.6. Over 90% of emissions resulting from energy are in the form of CO_2 from fossil fuel combustion [30]. In particular, coal remains a significant player both in the role of energy production and in GHG emissions. It has historically fulfilled a major role in energy generation around the globe, particularly in developing countries due to its abundance, accessibility and ease of use.

Despite accounting for 28% of the world's total primary energy supply in 2015, coal was responsible for 45% of CO_2 emissions, comprising the single largest fuel share in terms of global carbon emissions [29]. In addition to CO_2 (and other GHGs such as methane), coal (and fossil fuel combustion in general) produces numerous other pollutants during combustion, such as sulphur oxides (SO_x), nitrogen oxides (NO_x), particulates and various other toxic substances such as hydrogen cyanide (HCN), which are known to have significant potential impacts on human health and the environment.

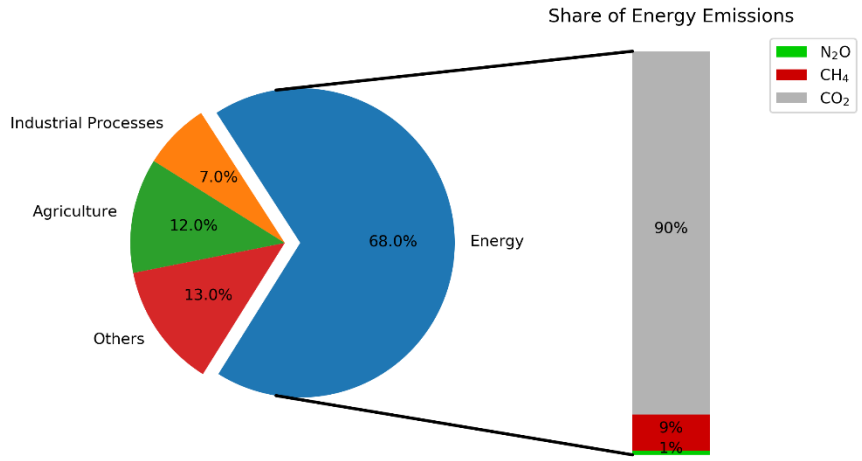

Figure 1.6 - Estimated shares of global anthropogenic greenhouse gas emissions as of 2014 [29]

1.4.3 - Energy in the UK

Total energy production in the UK has fallen significantly in recent decades, from 300 Mtoe to less than 130 Mtoe in 2017 [31]. Coal production, in particular, has sharply reduced by over 27% compared to 2016. In Q3 2017, coal comprised just 2.9% of electricity generation, a record low [32]. Significantly, energy from bioenergy and waste is now produced at six times the rate of coal, increasing 11.6% in 2017. This is in large part due to the government's plan to end unabated coal generation by 2025, a process that began in 2015 [33]. Immediately after this announcement, deep-mined coal production ceased entirely in 2016, with overall coal production and imports decreasing by approximately 80% within two years [31].

Many coal power stations were already under strict regulations due to the introduction of the Large Combustion Plant Directive (LCPD) in 2001, which

specifies emission limits for the aforementioned substances regarding power plants with a capacity of greater than 50 MW [34]. From 2007, combustion plants that predated 1987 were given the option to comply with emissions limits or to opt out; plants which opted out were then limited to 20,000 hours of further operation, and were required to close completely by the end of 2015. Within a year 11500 MW of energy had been opted out, with seven plants closed by August 2013 [35], initiating this transition from coal.

Although the government is yet to set out the routes it will take in reaching the complete abatement of coal by 2025, it has conducted consultations upon two main options [33]. The first option was carbon capture and storage (CCS), which the government ruled out due to a number of factors, including costs, the state and inefficiency of some current power stations and the unlikelihood that CCS will be ready for full scale implementation by 2025. The second option was to increase the CO_2 emissions limit to 450g/kWh, strictly for units burning any solid fossil fuel. One of the options recognised by the government as a solution to meeting these emissions limits was the co-firing of biomass at high levels, in order to prevent additional pressure on consumer electricity bills [33].

Some power stations are focused on converting to full biomass firing such as Drax, who are in the process of converting a fourth unit, having commenced upgrading the first unit in 2013 [36]. It is for these thermal solid fuel power stations that this thesis will be most applicable and, as such, will be the focus of the following sections.

1.5 - Power Generation from Solid Fuel Combustion

For large combustion plants (considered to have a thermal input of greater than 50MW), three combustion technologies are widely used: pulverised fuel (PF) combustion, fluidised bed combustion (FBC) and grate firing [37].

1.5.1 - Pulverised Fuel Combustion

Pulverised fuel combustion is the dominant method of generating energy through solid fuel combustion, and most large-scale applications are of this type. A PF boiler utilises fuel that is typically milled to particle sizes between 5 and 400 μm in diameter, with a maximum particle size of 10-20 mm [38]: as a result, most PF

boilers are fitted with a grinding mechanism positioned before the fuel is transported to the combustion zone. This means that the biomass often needs pre-treating, through a combination of drying, milling and compression, to ensure that effective grinding is possible before the fuel enters the furnace.

Start-up of the furnace is accomplished by using an auxiliary burner. The pulverised fuel is then mixed with some of the primary combustion air to carry the particles to the burner through a burner nozzle in the lower part of the boiler. This transport air is limited in temperature to approximately 100°C, to prevent ignition and explosions during transport [39]. The nozzle is designed to provide more strongly preheated secondary combustion air at the burner exit, in order to establish combustion conditions and to accurately control the air-fuel ratio during the combustion process [40]. Once temperatures are high enough, the auxiliary burner is turned off. Conventional PF boilers use air for combustion, where the high nitrogen content dilutes the CO_2 concentration in the flue gas. However, the potential capture of CO_2 from the flue gas, through amine stripping, can be relatively expensive. Therefore, the flue gas may be recycled as in oxy-fuel combustion, an emerging technology, where a combination of oxygen (typically greater than 95% purity) and recycled flue gas is used for the combustion of fuel, avoiding the need to strip CO_2 from the gas stream [41].

As the fuel particles are heated in the combustion zone of the boiler, the volatile components evaporate and combust once mixed with the primary air. The remainder of the particle, consisting of carbon and ash, then combusts at a slower rate. This occurs simultaneously within the combustion zone due to the small particle sizes, which allows for quick load changes that are not possible with other systems [38]. Residence times are on the order of seconds, and typical temperatures for pulverised coal combustion range from 1300-1500°C [40], and are lower for biomass (typically around 1200-1400°C [38]) due to its lower calorific value.

The heat produced by the combustion of the fuel is used to heat water passed through superheaters (Figure 1.7), creating steam at high pressure (typically 20-250 bar [38]). This steam is fed into a turbine, where it expands to a lower pressure, creating mechanical power which drives the turbine, in turn powering an electricity generator. A typical PF combustion plant will have a thermal

efficiency of 43-47% [37]. On average, approximately 20% of the total ash in PF combustion takes the form of bottom ash and slag [38].

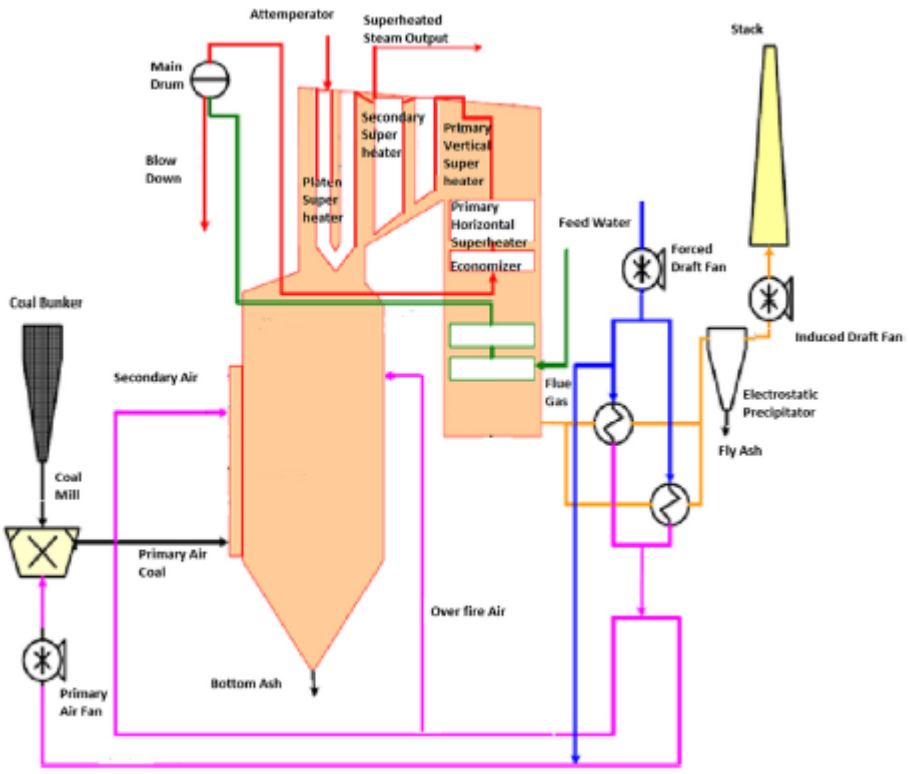

Figure 1.7 - Typical layout of a PF boiler [42]

1.5.2 - Fluidised Bed Combustion

When a sufficient gas flow is passed through a bed of solid particles, the particles can behave in such a way that they can be said to be fluidised, with the particles becoming suspended and behaving much like a liquid: for instance, spreading out to fill the space that they are contained within. Since the particles are suspended and agitated by this gas (known as a fluidisation medium), the contact area between the particles and the gas is significantly increased when compared to a fixed bed, allowing for high rates of heat transfer and mixing [38].

Fluidised bed (FB) combustion takes advantage of this phenomenon, and consists of a cylindrical boiler with a perforated bottom surface. Within the boiler is a bed material, typically silica or sand, which comprises over 90% of the total material in the boiler at any one time (including fuel) [38]. Limestone and dolomite have additionally been used in coal FB combustion, to control sulphur dioxide release [43]. Primary combustion air is used as the fluidisation medium, and pre-

burners are used to heat the bed material, which acts as a heat reservoir. The required start-up time is relatively long compared to other systems (8-15 hours) and is typically achieved with oil or gas burners [38]. The solid fuel is added to the fluidised bed, which both heats and mixes the particles and provides a homogeneous temperature distribution throughout the boiler [44]. The combination of heat and mixing with primary air initiates combustion of the fuel particles, with combustion temperatures much lower than in other systems. Fluidised bed combustion holds a number of advantages over conventional boilers, including high combustion efficiency, fuel flexibility, and low atmospheric emissions [45]. Also, fluidized bed conversion of solid fuels is of significant economic importance, especially in developing countries [44].

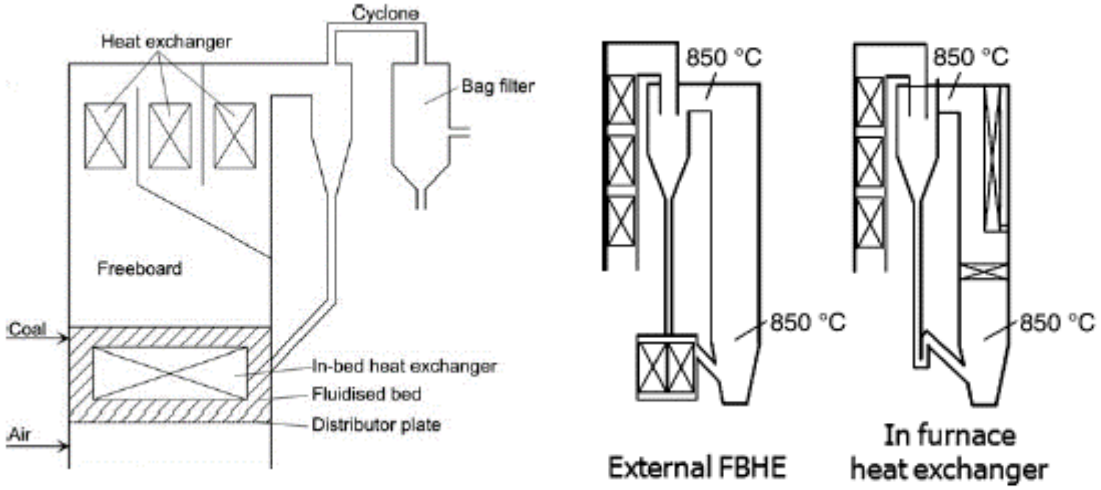

Figure 1.8 - Schematic of a BFB (L) and CFB (R) system [38]

There are two main types of fluidised bed biomass boilers (Figure 1.8), depending upon the fluidisation gas velocity. In bubbling fluidised bed (BFB) boilers, the gas velocity is enough to produce gas bubbles, but not to such an extent that large quantities of solids are transported from the combustion chamber. The particles within BFBs retain a close proximity to one another, and there is a well-defined upper surface [46]. Bed temperatures can be controlled in the range of 650-850°C [38], allowing for fuels with relatively low ash melting temperatures to be used.

In circulating fluidised bed (CFB) boilers, the fluidisation gas velocity is greater than that of a BFB boiler, and the particles are carried out of the combustion chamber within the flue gases. In this case, the solid particles are separated from the gas stream using a cyclone and recycled back to the bed. CFB boilers operate with smaller particle sizes than BFBs [46], and operating temperatures are slightly

higher at between 750°C - 900°C [38]. CFBs offer a number of advantages over BFBs, including a greater combustion efficiency, smaller bed area and a larger potential capacity [46], although this comes at the cost of a larger initial capital cost and greater size requirements [38].

Fluidisation is heavily influenced by temperature and air distribution [47], and careful control is needed to ensure that defluidisation does not occur. The ash composition of the fuel can have a significant effect upon the performance of FB boilers, with approximately 20-30% of the ash produced ending up as bottom ash [38]. With the use of some biomass, in particular those with high alkali concentrations, the risk of bed agglomeration and subsequent defluidisation is a serious risk in the operation of FB boilers. Bed agglomeration will be discussed in more detail in Chapter 3.

1.5.3 - Grate Firing

Grate-fired systems use either a moving or a stationary grate, over which the fuel particles are distributed. The combustion air is supplied through the grate itself from underneath. Although temperatures are lower than in PF boilers (approximately 1000-1200°C for biomass [38]), residence times are much longer (on the scale of minutes), which lends a number of advantages over PF and FB combustion. For instance, grate-fired systems can deal with biomass with a high moisture content and different particle sizes, meaning that the need for drying and milling is removed. For biomass with more difficult combustion behaviours and lower ash melting temperatures, rotating or vibrating grates can be used. However, the large number of moving parts paired with the area required for such a system means that grate-firing is rare for large scale applications and are usually used for incineration rather than as a primary energy source. In addition, grate furnaces suffer from a decreased efficiency due to high excess oxygen, and require a number of additional technologies in order to maintain low emissions levels [38].

Stationary grate (or fixed-bed) systems use a batch process and are reserved for small-scale applications. In a continuous moving system, the fuel is added to the grate which then transports it towards the furnace, drying in the process as temperatures increase. During combustion, the combustible volatile components of the dried fuel pile are released and, once mixed with secondary air, create a

flame above the bed. After this volatile release, the remaining char burns out, leaving a bed of coarse ash particles on the grate, which is collected. The primary air supply is divided into sections, depending on the region, and whether drying, pyrolysis and char combustion are to take place [38]. Although some of the ash is released in volatile form, much of it remains in the bed.

1.6 - Coal

As shown in Figure 1.5, coal is the most widely used solid fuel in the global energy mix, and remains the main source of energy across all fuels for developing economies such as China [24]. However, coal is also by far the most polluting fuel, on an emissions to energy basis [29]. Although coal use is declining due to strict legislation aimed at mitigating the effects of climate change, it will play a role in the global energy supply for the foreseeable future, due to both its significant contribution to the current energy supply and the vast investment and infrastructure that has been implemented over the last century.

Coal is a fossil fuel since it is formed predominantly from the remains of dead plants, which accumulate in wetland areas and degrade due to bacteria, fungi and enzymes, eventually forming peat. The peat layer thickens over time, and becomes buried under sedimentation, at which point the coalification process begins. Coalification is the physical transformation of peat into coal, first by biochemical processes, and then geological processes where the gradual burying of the peat by sediments results in increased temperatures and pressures [48]. Once buried, this peat is protected from oxidation and biodegradation, and over a timescale of up to millions of years is converted into coal.

1.6.1 - Coal Composition

The composition of coal is complex: it predominantly consists of aromatic hydrocarbon structures, with a small amount of inorganic impurities. The composition of the coal is dependent upon a number of factors, including the time, temperature and pressure under which it is formed, the composition of the original organic material, and the local geological conditions.

The extent of coalification affects the quality of the coal; this is known as coal rank. Coal rank is measured by a progressive decrease in moisture and volatile

content (caused by more intense coalification) and by extension an increasing in carbon content and calorific value [49]. Lignite has the lowest coal rank, followed by subbituminous coal, bituminous coal and finally anthracite; a comparison between carbon content and high heating value (HHV) of different coal ranks is shown in Figure 1.9. Examples of coal compositions are available in Section 1.7.3, Table 1.2.

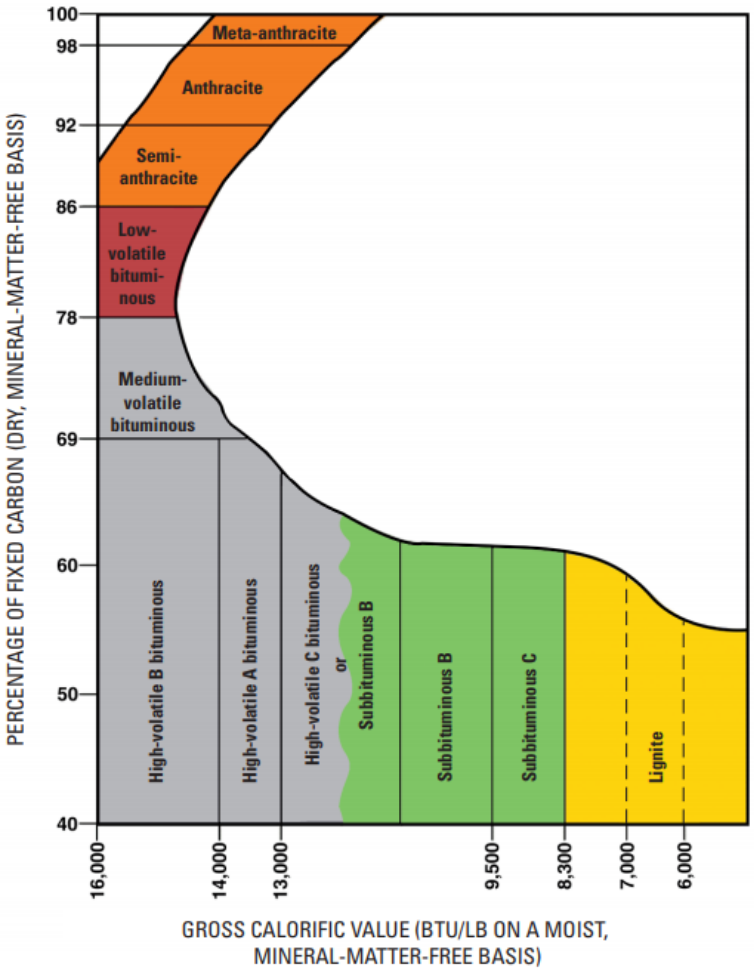

Figure 1.9 - The classification of coals by rank in the United States [50]

1.7 - Biomass

The conversion of coal power stations to biomass firing is an attractive proposition since it uses pre-existing infrastructure, thereby reducing the capital investment required, maintaining the power generation capacity and having the added benefit from the potential synthesis with CCS technologies [51]. Biomass has been used to reduce dependence on coal and to reduce emissions in a cost-effective way through co-firing for a number of years. The UK introduced a

number of schemes conducive to the uptake of biomass firing in the wake of the Large Combustion Plant Directive (LCPD), introducing the Energy Crop Scheme in 2001 to provide grants to farmers for establishing energy crops, and the Renewable Obligation in 2002 to provide credits to energy generators who used renewable resources in the production of energy.

Biomass, in the case of energy, is defined as biogenic material used as a fuel source, including plants and organic waste. Bioenergy has been the dominant source of energy for most of human history, until the last two centuries [3] as described in Section 1.1. As of 2017, biomass is the 3rd largest renewable electricity source in the world, and the leading renewable solution for both heating and transport [52].

1.7.1 - Composition

Biomass is a complex product containing both organic and inorganic components. It is comprised of natural constituents from plants (formed via photosynthesis), products from human and animal food digestion, and of products derived by processing these natural components [53]. These components take the form of both solid and liquid phase compounds and a range of minerals and phases. This complexity arises during the growth of the biomass source, where differences in composition are caused by an array of different factors. Some of these factors are summarised in Table 1.1.

Although biomass can be processed to create both liquid and gaseous fuels, the focus of this thesis will be on the use of biomass as a solid fuel. This can be classified into several groups and subgroups, as in Table 1.2.

The chemical compositions of biomass are highly variable due to the wide variety of different species involved [54]. Even with the same source plant, environmental and geographical factors can cause minor chemical variations [55]. However, woody, herbaceous and agricultural biomass accounts for most resources used in solid fuel combustion, particularly white wood and energy crops such as miscanthus. This biomass consists of the same basic components, being made of mostly lignocellulosic constituents (Figure 1.10), with some oils and ash making up the remainder. It is these lignocellulosic constituents that are the most important in terms of thermochemical conversion for energy. They are summarised briefly below.

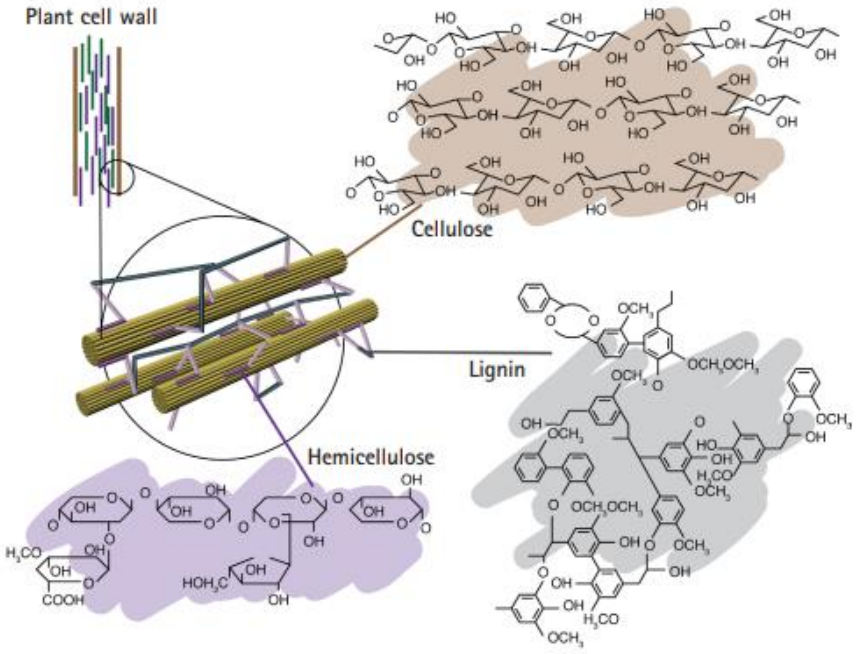

Figure 1.10- Structure of lignocellulose and its location within the plant cell. From [56]

Table 1.1 - Examples of factors affecting biomass and biomass ash composition. Adapted from [54]

Origin of Process	Type	Example Factors
Natural	Genetic	Type of biomass, plant species or part of plant
		Growth processes, such as ability of plant species to extract compounds from water, soil and air
	Environmental	Growing conditions, such as sunlight, geographic location, soil type and nutrients present
		Age of the plant at harvesting
Anthropogenic	Environmental	Use of fertiliser and pesticides, and doses used
		Distance from sources of pollution
	Collection/ processing	Harvesting time and method
		Storage and transport methods
		Inclusion of dust or soil during harvesting and transport

Table 1.2 - General classifications of biomass. Adapted from [53]

Biomass Groups	Biomass sub-groups, varieties and species
Wood and woody biomass	Coniferous or deciduous
	Angiospermous or gymnospermous
	Soft or hard
	Stems, branches, foliage, bark, pellets, briquettes, sawdust and others from various wood species
Herbaceous and agricultural biomass (including energy crops)	Grasses and flowers (such as switchgrass and miscanthus)
	Straws (such as barley, corn or rape)
	Other residues (including fruits, shells, husks, grains, seeds, stalks, cobs, kernels, bagasse, pulps, cakes, others)
Aquatic biomass	Marine or freshwater algae
	Macro or microalgae
	Seaweed, kelp, lake weed, water hyacinth, others
Animal and human biomass waste	Bones, meat-bone meal, chicken litter, various manures, others
Contaminated biomass/ industrial biomass waste	Municipal solid waste, sewage sludge, hospital waste, paper-pulp sludge, waste papers, paperboard waste, chipboard, fibreboard, plywood, wood pallets and boxes, others
Biomass mixtures	Blends of any of the above

1.7.1.1 - Cellulose

Cellulose $(C_6H_{10}O_5)_n$ is the major component of lignocellulosic biomass, and accounts for approximately half of the organic carbon in the biosphere [57]: as such, it is the most important component in terms of thermochemical conversion. It is a long chain polysaccharide consisting of linked glucose monomers, and provides the main structure and strength of both the primary and secondary cell walls. Cellulose mostly decomposes between 315-400°C [58].

1.7.1.2 - Hemicellulose

Hemicellulose is also a polysaccharide and exists in both primary and secondary cell walls. Hemicellulose composition varies, and consists of various saccharides in a random, amorphous structure [58], which links the cellulose fibres together forming a network [56]. It is structurally much weaker than cellulose, and requires

less energy to break, with decomposition mostly occurring between 220-315°C [58].

1.7.1.3 - Lignin

Lignin composition also varies between species. It is a complex polymer of cross-linked aromatic rings with various branches [58]. Lignin permeates the cell wall, between the cellulose-hemicellulose networks, providing additional strength and driving water conduction through the plant cell [56]. The decomposition of lignin occurs over a wide temperature range, between 100-900°C, due its complexity [58].

1.7.2 - The Carbon Cycle

Biomass is similar to coal in that it is effective as an energy source when combusted due to its carbon content, which reacts with oxygen and releases energy, which can then be harnessed. However, because of this, biomass combustion also produces CO_2 emissions, unlike other renewable energy sources.

Bioenergy is considered a renewable energy insofar as it is produced in a sustainable way [59], since any carbon released during combustion is sequestered through photosynthesis during the lifespan of the plant, offsetting emissions due to bioenergy growth and use, thus closing the natural carbon cycle [60]. The extent of this depends upon the total life cycle of the fuel, including the energy required for cultivation, harvesting, transport, storage and processing, which is a complex and crucial area of study [61-63].

In contrast, although coal is also a form of carbon sequestration, this occurs over a timescale of millions of years, compared to the time of growth for energy crops. This results in carbon being emitted into the atmosphere at a much greater rate than it is sequestered. This is the primary reason as to why biomass is being used as a direct replacement for coal in large-scale energy applications.

A significant potential advantage of bioenergy over other renewable energy sources is that the use of bioenergy with carbon capture and storage technology (BECCS) may further reduce the carbon footprint of biomass use, even to the point of producing negative emissions over the life cycle of the biomass. The use

of BECCS is considered critical in mitigating temperature increases, particularly for reaching the lower targets set out in the Paris agreements [64].

1.7.3 - Coal and Biomass as Fuel - a Comparison

Although biomass and coal are similar enough that they can be co-fired, they share different compositional and behavioural properties. Example comparisons between some biomass sources and coals can be found in Table 1.3. The most obvious difference between biomass and coal is the energy density, which is lower for biomass. This is because of the higher proportion of oxygen and hydrogen in the carbon-containing compounds within biomass; there is lower energy contained within carbon-oxygen and carbon-hydrogen bonds than in carbon-carbon bonds, which reduces the overall energy value of the fuel [65]. Generally, biomass also contains greater moisture and volatile matter than coal [54]. Moisture content in energy crops can be as high as 40% after harvesting, although this can be reduced to below 20% by field drying and choosing favourable harvesting times, while fresh wood can contain between 40-60% moisture [66]. This often means that biomass requires a drying stage before processing, otherwise moisture can dominate the combustion process [40].

In addition, biomass can sometimes require other pre-treatments to produce favourable behaviour before use as a fuel. Particle size can be important for combustion efficiency and NO_x emissions [67]. In large scale PF combustion, coal is pulverised in grinding mills before entering the primary gas stream, taking advantage of its brittle structure, which contains pre-existing flaws. Biomass has a very different, orthotropic structure, making grinding in such a manner impossible in its raw form [68]. The use of existing coal mills for biomass preparation has caused severe damage, including mill blockages and fires [67].

Some forms of pre-treatment are aimed at both improving the energy density and grindability of biomass. Torrefaction, for instance, uses low temperature pyrolysis (250-300°C) to remove moisture and volatile matter, while initiating the decomposition of hemicellulose and lignin, breaking down the cell wall structure and making grinding and milling easier [69]. Often, biomass is pelletised before being supplied to power stations: this process typically involves drying the biomass to 10% moisture, hammer milling to reduce particle size, and then densification in a pellet press [70].

Table 1.3 - Example proximate and ultimate analyses of various biomass fuels and coals

	Proximate Analysis (wt.% ar)				Ultimate Analysis (wt.%) and calorific values (HHV, MJ kg^{-1})				
Fuel	Moisture	Volatiles	Fixed Carbon	Ash	C	H	O	N	HHV
Beech wood [a]	7.4	74.0	24.6	0.4	49.4	6.2	41.2	0.4	19.2
Softwood [a]	8.8	70	28.1	1.7	52.1	6.1	41.0	0.2	20
Hardwood [a]	7.8	72.3	25.0	2.7	48.6	6.2	41.1	0.4	18.8
Wood bark [a]	8.8	66.6	31.6	1.6	53.1	6.1	40.6	0.2	20.5
Wheat straw [a]	8.5	63.0	23.5	13.5	45.5	5.1	34.1	1.8	17.0
Olive Husk [a]	9.2	70.3	26.1	3.6	50.0	6.2	42.2	1.6	19.0
Hazelnut Shell [a]	9.0	69.3	28.3	1.4	52.9	5.6	42.7	1.4	19.3
Brown coal, dried [b]	15.6	44.1	36.0	4.3	56.3	5.0	37.6	0.6	21.2 [c]
Bituminous coal [b]	5.5	30.1	56.6	7.8	82.3	5.1	10.3	1.4	33.3 [c]
Anthracite [b]	1.9	7.6	87.7	2.8	91.6	3.5	2.4	1.6	35.3 [c]

[a] A. Demirbaş, 1997 [71]

[b] De Jong et al, 2014 [72]

[c] HHVs calculated using Milne equation: $HHV_{Milne} = 0.341C + 1.322H - 0.12O - 0.12N + 0.0686S - 0.0153Ash$ [73]

Additionally, the combustion behaviours of biomass and coal are different. The high volatile matter in biomass results in a highly porous char fraction after the initial devolatilisation stage of combustion, which is highly reactive in comparison to coal [66]. In addition, the greater volatile, ash and load required to produce the same amount of energy from biomass compared to coal results in different combustion temperatures and gas compositions. This means that some combustion systems may require significant modification when switching from coal to biomass use: for instance, the addition of biomass and coal to BFB boilers must be treated differently: whereas coal is usually added onto the fluidised bed from above, biomass is required to be fed into the bed, due to the higher reactivity of biomass [38].

1.8 - Ash

All solid fuels contain non-gaseous inorganic elements and compounds that are, for the most part, non-combustible: it is these components that, when condensed, result in the production of ash during combustion. This hot ash remains in the system, either falling to the bottom of the boiler (bottom ash), sticking to boiler walls and tubes, or being carried by flue gases through to the cooler regions of the boiler and eventually out of the boiler completely (fly ash). Alongside GHG emissions, fly ash emissions are heavily regulated due to their negative health effects and potential toxicity. The fly ash within exhaust gases can be captured using electrostatic precipitators (ESPs). This will be covered in greater detail in Chapter 2.

1.8.1 - Additives

One method to potentially mitigate deposition problems when firing biomass is to use additives to modify the chemical composition of the resulting deposit. Such an additive can either be pre-mixed with the fuel, or added into the combustion chamber alongside the fuel. The components of the additive affect the aerosol chemistry within the combustion chamber of the boiler, converting troublesome species with low melting temperatures or high corrosive tendencies into compounds with more favourable characteristics. The choice of additive depends upon the composition of the fuel, the mechanisms by which the deposition is

forming, and the troublesome species present during the combustion process. The use of additives for deposition control is the main focus of this thesis and will be examined in greater detail in Chapter 2.

1.9 - Summary

It is clear that to meet current climate change targets and to effectively limit further temperature increases due to greenhouse emissions, the world's energy supply must transition away from the use of fossil fuels. Bioenergy has a significant role to play in the transition away from coal, the fossil fuel most responsible for CO_2 emissions. It is possible to use bioenergy within the existing infrastructure already in place for coal, providing an economical and practical solution with immediate results, if implemented in a sustainable way. The use of BECCS has the potential for negative carbon emissions, and both bioenergy and BECCS are considered crucial components of the future energy grid for reaching climate targets.

However, the compositional differences between biomass and coal mean that it is not as simple as directly replacing coal with biomass. In particular, the differences in ash composition pose significant problems for the power generation industry when switching from coal to biomass firing, and the mitigation of these ash-related problems is a significant challenge.

1.9.1 - Aims and Objectives of the Thesis

The motivation for the work contained in this thesis was to investigate the impact of two aluminosilicate additives, coal pulverised fuel ash (PFA) and kaolin (KAO), in the combustion of biomass, and in particular the effect of the additives upon the melting properties of the ash and its electrical properties, which are both important in minimising particulate emissions. The main objectives of this research are described below:

1. The characterisation of the biomass ashes and the additives used in this study.
2. Determining the behaviour of biomass ashes under heating, including the mechanisms involved, and how this translates to deposition behaviour in large-scale biomass boilers.

3. To assess the impact of the aluminosilicate additives in improving the melting characteristics of the biomass ash at high temperatures (>1200°C), and in turn the impact on slagging within biomass boilers.
4. To assess the impact of the aluminosilicate additives in improving the sintering characteristics of the ashes at lower (700-1000°C) temperatures, to determine the potential mitigation of fouling.
5. To assess the effect of the aluminosilicate additives upon the electrical behaviour, specifically the resistivity, of the resulting ash, and how this will affect ESP performance.
6. To determine whether the aluminosilicate additives in this study are effective across a range of ash compositions and, if not, to determine when and why their use is most effective, in order to inform best practice for minimising slagging and fouling in biomass combustion.

1.9.2 - Methodology

In order to achieve the objectives of this thesis, the methods used are outlined below:

Objective 1

A range of analytical methods were used to characterise the biomass ashes, including ICP ash analysis, standard tests including loss on ignition and CHNS, SEM-EDX and XRD analysis.

Objective 2

The behaviour of the biomass ashes under heating was determined through a series of standard tests that have been established in the literature, including ash fusion testing, high temperature viscometry and sinter strength testing. Further analysis including XRD and SEM-EDX were used to supplement these experiments.

Objective 3

The impact of the additives upon high temperature behaviour of a range of additive/biomass blend ashes was determined through ash fusion testing and high temperature viscometry. A comparison of the results with commonly used slagging and fouling indices was undertaken.

Objective 4

The assessment of the impact of the additives upon ash behaviour at lower temperatures was achieved through the development and use of sinter strength testing of various temperatures in conjunction with XRD and SEM-XRF.

Objective 5

The resistivity of various biomass and additive blends was investigated using bespoke ash resistivity testing equipment, based upon existing standard methods. Resistivity results were analysed and used to modify previously developed models based upon coal ash compositions, in order to predict the effects upon ESP performance.

Objective 6

The conclusions of Objective 6 are informed by the outcomes from Objectives 3, 4 and 5.

Chapter 2 - Overview of Ash Behaviour during Combustion

2.1 - Introduction

This chapter aims to give an overview of topics relevant to the work conducted for this thesis. The nature of biomass ash and its behaviour during combustion is discussed, along with examples of minerals, reactions and phase transformations that often occur in biomass ashes. Mechanisms of deposition are explained, along with the sintering mechanisms that occur within deposits. Studies on the nature of biomass ash deposits and methods of removal are discussed. Finally, the use of additives to improve deposition behaviour is examined, and previous studies on the topic reviewed.

2.2 - Ash Formation and Composition

Biomass contains a range of inorganic elements, both metals and non-metals, which are bound within different chemical phases. These inorganic elements play important roles in the growth and metabolism of plants. Potassium is, for instance, involved in turgor control, calcium is involved in enzyme activation, magnesium is an essential part of chlorophyll, and chlorine has importance in maintaining charge balance within the cells of the plant [74]. Further inorganics may arise from contamination of the plant or soil, or in transport and storage.

Si, Ca, Mg, K, Na, P, S, Cl, Al, Fe, Mn, N, Cu, Zn, Co, Mo, As, Ni, Cr, Pb, Cd, V, and Hg can all be present, with the most important ash-forming components being Si, Ca, Mg, K, Na, P, S, Cl, Al, Fe and Mn [75, 76]. Doshi et al. [77] determined that different species of inorganics in biomass can be placed into one of three categories: ionically bound salts; inorganics that are bound organically to carbonaceous material, such as carbonates; and minerals, both inherent in the fuel and in foreign material introduced later during transport and processing. Doshi et al list the species in Table 2.1 that are the most common in biomass.

The composition of the resulting ash is determined by the composition of inorganics in the plant, as well as the combustion conditions, where different species and phases may form depending upon the local temperature, temperature gradient, stoichiometry and compounds present. Biomass ashes are typically enriched in Mn, K, P, Cl, Ca, Mg and Na, and depleted in Al, Fe, Si and Ti when compared to coal ash compositions [78]. However, biomass and biomass ash can potentially contain the entire periodic table [79]. A comparison of coal and biomass ash compositions is available in Table 2.2. Although typical ash compositions are given using oxide analysis of elements in their highest oxidation states, other compounds such as silicates, carbonates, sulphates and phosphorus exist as part of various phases and minerals, which interact and undergo complex transformations under high temperatures.

Attempts to classify biomass ash compositions into different groups have been attempted in literature, although there is no universally accepted method of doing so. Vassilev et al [80] suggested that biomass ashes could be grouped into four different types, as shown in Figure 2.1. S type biomass is high in $SiO_2+Al_2O_3+Fe_2O_3+NaO_2+TiO_2$, K type is high in $K_2O+P_2O_5+SO_3+Cl_2O$, C type is high in CaO+MgO+MnO, and CK type is for compositions containing low acids (<40 wt%) that are intermediates of the C and K types. These 4 types can be divided into further subtypes, depending upon the acid concentrations, with low and medium acid C and K types available, as well as medium and high acid S type biomass.

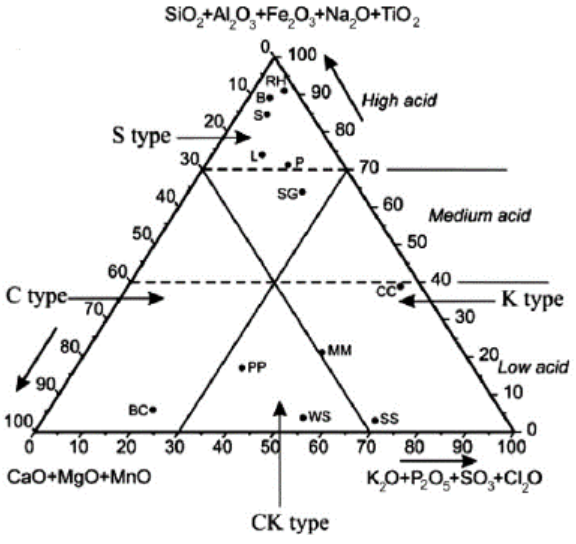

Figure 2.1 - Vassilev biomass classification using ash composition [78]

Table 2.1 - Speciation of biomass. From Doshi et al [77]

Element	Ionic Salts	Organically bound inorganics	Minerals
Na	$NaNO_3$, NaCl		
K	KNO_3, KCl		
Ca	$Ca(NO_3)_2$, $CaCl_2$, $Ca_3(PO_4)_2$	Calcium pectate	Calcium oxalate, calcite
Mg	$Mg(NO_3)_2$, $MgCl_2$, $Mg_3(PO_4)_2$	Chlorophyll, magnesium pectate	
Si	SiO_2 (amorphous)		Quartz, phytolite
S	SO_4 (2−)	Sulfolipids	
P	PO_4 (3-)		Phytates, phytic acid
Cl	Cl^-		
Al			Kaolinite
Mn		Protiens, carbohydrates	
Fe		Chelates, organic sulfates	Phytoferritin, iron oxide

Table 2.2 - Average ash oxide percentages for coal & biomass ash (range in brackets) [53]

Component (wt.%)	Coal		Biomass	
Ash Content (d.b)	19.80	(5.0 - 48.9)	4.90	(0.1 - 34.3)
SiO_2	54.06	(32.04 - 68.35)	29.14	(0.02 - 94.48)
Al_2O_3	23.18	(11.32 - 35.23)	4.49	(0.10 - 15.12)
Fe_2O_3	6.85	(0.79 - 16.44)	3.41	(0.22 - 36.27)
CaO	6.57	(0.43 - 27.78)	25.99	(0.97 - 83.46)
K_2O	1.60	(0.29 - 4.15)	19.40	(2.19 - 63.90)
Na_2O	0.82	(0.09 - 2.90)	2.54	(0.09 - 29.82)
MgO	1.83	(0.31 - 3.98)	5.60	(0.19 - 16.21)
TiO_2	1.05	(0.62 - 1.61)	0.24	(0.01 - 2.02)
P_2O_5	0.50	(0.10 - 1.70)	5.92	(0.54 - 40.94)
SO_3	3.54	(0.27 - 14.42)	3.27	(0.01 - 14.74)

2.3 - Inorganic Transformations

Inorganic minerals and phases can be pre-existing within the biomass (primary), may form during the combustion process (secondary) or can be added during fuel transport and storage (tertiary) [53]. During combustion, organically-bound inorganic species (K, Ca, P, Fe, S and Cl), are released as a vapour phase, while others remain in solid and liquid phases. Figure 2.2 summarises the general transformations of mineral matter in biomass.

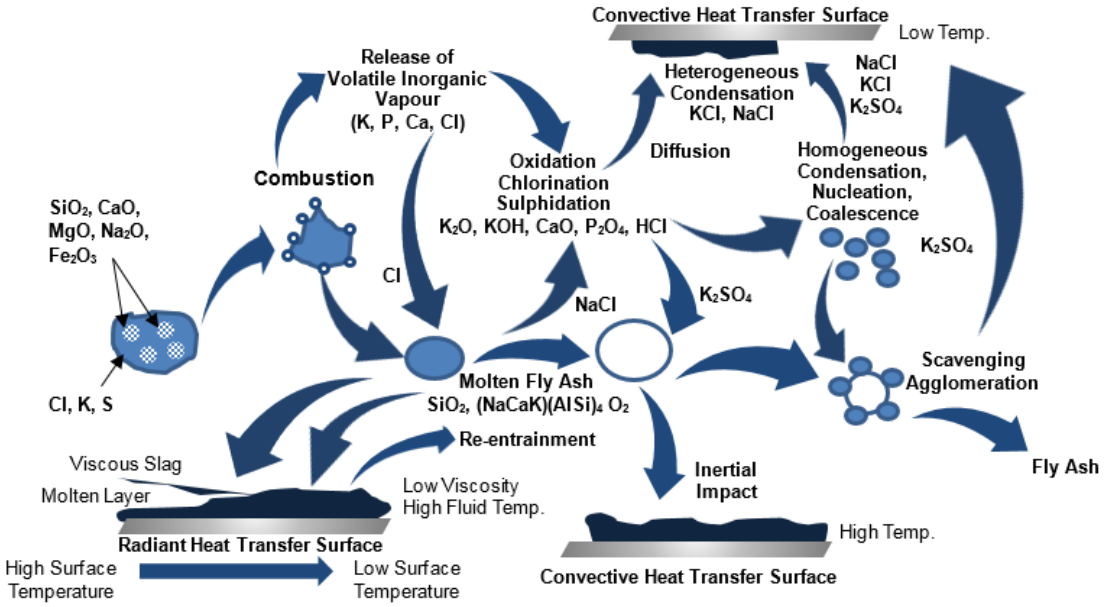

Figure 2.2 - Transformation of mineral matter in biomass. Adapted from [76]

All of these compounds can interact with each other within the combustion zone, forming secondary phases. During combustion, some of these compounds volatilise and are released into the gas phase, while refractory materials can undergo phase changes, creating small primary particles which ultimately result in ash formation [38].

The next sections will discuss some of the common phases and minerals encountered during biomass combustion, and their behaviour and formation, all of which will be relevant in this study. Other minerals and phases, such as sulphates, phosphates, nitrates [53, 54, 78, 80-82] and trace metals [83-87] have been reviewed and discussed in detail in the literature; however, these have not been the focus of this study.

2.3.1 - Silicates

Silica (SiO_2) can exist in various mineral phases with different properties due to variations in the crystal structure, known as polymorphs. Quartz and cristobalite are two examples of polymorphic silica often found in biomass ashes as both primary and secondary phases [54], transforming from naturally occurring opal at temperatures as low as 65°C [80]. SiO_2 may also be present in its amorphous state [78]. Silica also interacts with many other elements during combustion: over 80 silicate minerals are identified by Vassilev et al [78] as occurring in biomass ashes, of which the majority listed are variations of calcium, potassium, sodium and magnesium silicates and aluminosilicates, created from interactions of silica and oxyhydroxides of such elements. The majority of silicates are of secondary origin, due to reactions between pre-existing silicates and oxyhydroxides of Al, Ca, Fe, K, Mg, Mn and Na created from the decomposition of sulphides, sulphates, carbonates, chlorides, nitrates, phosphates, oxalates and organic matter [80] during combustion.

Although silica in all of its crystalline phases has a melting point of over 1700°C [76, 78], and the vapour pressure of silicon is low at combustion temperatures, this can change substantially in the presence of carbon and other minerals. Bryers gives the example of a heated mixture of aluminosilicate and graphite, which can result in the volatilisation of silicon monoxide at temperatures as low as 1150°C [76]. Some silicate compositions, such as potassium silicate (melting point 600-980°C) and potassium-sodium silicate (540-1170°C) eutectics can have initial melting temperatures far below typical combustion temperatures, resulting in volatilisation during combustion and later condensation in cooler regions of the boiler [78]. This is due to the high mobility of alkali metals, in particular potassium, which reacts with silica at relatively low temperatures and breaks the Si-O-Si bond [88]. In contrast, changing the concentration of Al_2O_3 in a potassium silicate eutectic can increase solidus temperatures from ~650°C to over 1500°C [89], while mullite (an aluminosilicate mineral that forms above 1100°C) has melting temperatures of above 1800°C.

While numerous silicates may be present in biomass ashes, their prevalence can differ significantly, and in contrast to coal ashes they do not play a major role in the ash of every biomass since silica content can be much lower (see Table 2.2)

[80]. Further information on the behaviour of silicate melts is provided in Section 2.4.2 and 2.4.3.

2.3.2 - Oxides

The occurrence of oxides in biomass ash is primarily due to secondary formation during biomass combustion, although oxides and hydroxides of silicon exist as primary forms within the biomass [38]. The primary precursors of secondary oxides are typically sulphides, sulphates, carbonates, chlorides, phosphates, oxalates and organic matter, which decompose and oxidise, and the dehydroxylation of certain minerals such as goethite, and portlandite [80]. The behaviour of oxides in biomass ash is similar to that in coal ashes, in that some oxides and oxide minerals may subsequently hydroxylate during cooling, and in subsequent storage and transportation, to re-form oxyhydroxides [90]. Due to this, secondary oxyhydroxides of Al, Ca, Fe, K, Mg and Mn tend to dominate in biomass ash [78].

In determining phase transformation behaviour during combustion, Fe and Mn are often ignored, since they often form individual oxides rather than interact with the other ash-forming elements in biomass ashes [75]. Instead, they tend to act as fluxes, reducing the melting temperature and viscosity of solid-liquid systems, and are particularly important in determining the behaviour of silicate melts and their viscosity [91, 92].

Boström et al [75] determined from thermodynamic data (Figure 2.3) that Ca and Mg oxides are highly stable, and under combustion conditions will remain solid at all times as long as no fluxing or reactions occur. As such, these particles will likely be liberated as small particles. Once liberated, CaO in the presence of high quantities of silica may result in much lower melting temperatures: Ohman and Nordin [89] show solidus temperatures of as low as 720°C in K_2O-CaO-SiO_2 ternary systems.

SiO_2 behaves similarly. However, in the char burning stage, some gaseous SiO may be released, which will quickly oxidise in the flue gas. Silica particles are initially formed as sub-micrometre sized particles [75], resulting in fast reactions and the behaviour noted in Section 2.3.1. Na and K, when not bound as silicates and aluminosilicates, will volatilise during combustion and enter the gas phase [93]. These form less stable oxides in comparison to the other ash-forming elements, and at high temperatures may reduce further to metal vapour, after which such species will react with water to form hydroxides [75].

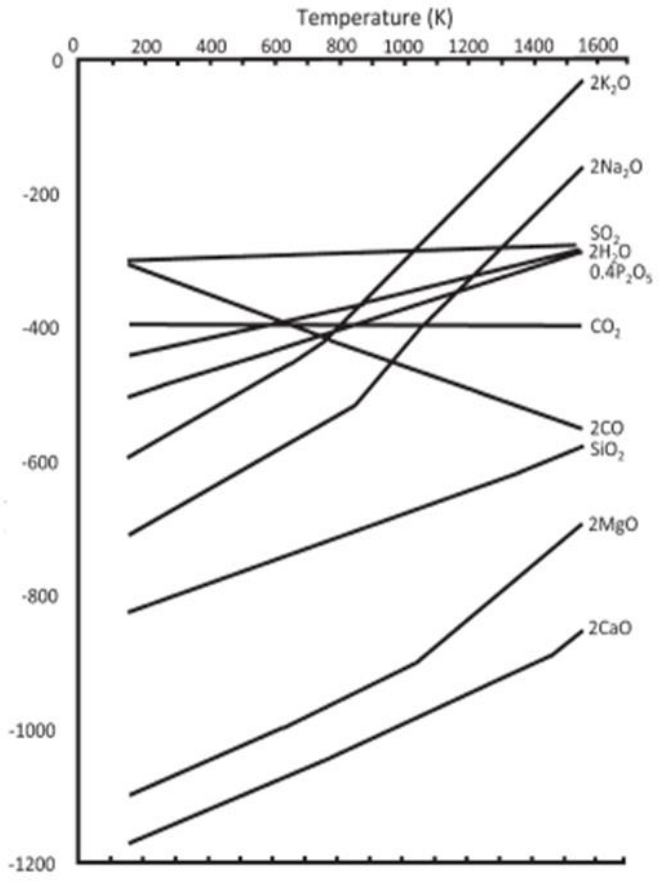

Figure 2.3 - The thermodynamic stability (ΔG^0) in kJ of major ash forming oxides [75]

Oxide composition has been used extensively as the primary indicator for fusibility of slagging deposits from coal ashes: Bryers [76] reported some 200 studies of the correlation between ash fusibility and base/acid ratio (see Chapter 5), which uses the eight most common oxides found in coal ash: SiO_2, Al_2O_3, TiO_2, Fe_2O_3, CaO, MgO, Na_2O and K_2O.

2.3.3 - Chlorides

Vassilev et al [80] identify most chlorides as being secondary products of combustion, and mostly found as "accessories" (defined by the authors as <0.1%) within the ash. However, both halite (NaCl) and sylvite (KCl) are identified as potentially forming (>10%) constituents of biomass ash, and both can be present from both primary and secondary sources. Cl is typically found in low

concentrations within woody biomass, while rapidly growing biomass such as grasses and, in particular, straws contain high levels of Cl [82]. Agroresidues additionally contain high levels of chlorine [88].

During combustion, alkali metals that have volatilised and entered the gas phase form unstable oxides as noted in Section 2.3.2 and Figure 2.3. These oxides may also be reduced into metal vapour, which in turn reacts with water vapour, forming more stable hydroxides. In the case of high ratios of potassium to S and Cl, potassium carbonates will form [94]. It is these hydroxides and carbonates that interact with HCl in the flue gas, forming metal chlorides such as KCl and NaCl through the reactions in Equations 2.1 and 2.2 which deposit on boiler surfaces through condensation [93].

$$MOH + HCl \leftrightarrow MCl + H_2O \qquad \text{(Eqn. 2.1)}$$

$$M_2CO_3 + 2HCl \leftrightarrow 2MCl + CO_2 + H_2O \qquad \text{(Eqn. 2.2)}$$

KCl and NaCl are among the most stable high temperature alkali metal species in the gas phase, with the only stable gaseous species for potassium above 1100°C being KCl and KOH [38]. The ratio of chlorine to alkali metals in the fuel can dictate the amount of volatile alkali metal species during combustion [88, 95], which in turn has an effect upon the nature of deposition in the boiler.

Chlorides are known for their fluxing behaviour during biomass combustion. NaCl and KCl have melting temperatures of 810 and 772°C respectively, while eutectic temperatures for KCl-$FeCl_2$ mixtures can be as low as 370°C [38]. In addition, Vassilev et al [81] give K–Na–Fe chlorides, K–Na sulphate–chloride, Na chloride–sulphate, Molysite ($FeCl_3$), Rokühnite ($FeCl_2$), Bischofite ($MgCl_2$), K halite and Ca chloride as fluxing minerals and phases during biomass combustion, all with melting temperatures below 800°C.

The most significant impact of chlorine in combustion is the corrosive tendencies of chlorine and its associated compounds. Further to the reactions of Equations 2.1 and 2.2, the deposited metal chlorides can react with SO_x in the gas (Equation 2.3), producing HCl local to the boiler surface and forming additional chlorides [93]. Although Niu et al [93] give the example of Equation 2.3, Aho and Silvennoinen [96] note specifically that SO_3 is required for fast sulphation to

occur, with iron oxide often acting as a catalyst for the conversion of SO_2 to SO_3. With the presence of further hydroxides and carbonates in the flue gas, this results in a regenerative process for gaseous chlorine and chloride deposits, which severely increases corrosion rates [38].

$$2MCl + SO_2 + \frac{1}{2}O_2 + H_2O \leftrightarrow M_2SO_4 + 2HCl \qquad \text{(Eqn. 2.3)}$$

Theis et al found that the Cl/S molar ratio is of importance as a result, with deposition rates from firing peat-bark and peat-straw mixtures increasing at a ratio of 0.15 and above [97]. Theis considers the high sulphur content to significantly decrease KCl concentrations in the flue gas through Equation 2.3; however, Riedl et al [94] state that this is not necessarily the case. Although chemical equilibrium equations suggest that all sulphur should be bound as solid K_2SO_4 below 900°C, kinetic considerations suggest that K_2SO_4 formation often will not reach equilibrium in the gas phase. As a result, only some of the potassium follows Equation 2.3, with mainly chlorides being formed during biomass combustion due to their higher reaction rates.

MCl conversion may also occur through an additional reaction in the presence of aluminosilicates. Due to the high melting temperature of aluminosilicates (Section 2.3.1), these reactions typically occur in and around the combustion zone, reducing the formation of fine particles and water-soluble alkali metal salts [98]. The prevention of alkali metal release early in combustion prevents the regenerative process for gaseous chlorine from occurring, since alkali chloride concentration is reduced within the flue gas.

$$Al_2O_3.2SiO_2 + 2MCl + H_2O \leftrightarrow M_2O.Al_2O_3.2SiO_2 + 2HCl \qquad \text{(Eqn. 2.4)}$$

Niu et al [93] give additional reaction routes for aluminosilicate reactions with alkali metal chlorides, while also noting that Equations 2.4-6 apply both for aluminosilicate compounds and systems containing individual SiO_2 and Al_2O_3 oxides (denoted by brackets):

$$(Al_2O_3 + 4SiO_2) + 2MCl + H_2O \leftrightarrow 2MAlSi_2O_6 + 2HCl \qquad \text{(Eqn. 2.5)}$$

$$(Al_2O_3 + 6SiO_2) + 2MCl + H_2O \leftrightarrow 2MAlSi_3O_8 + 2HCl \qquad \text{(Eqn. 2.6)}$$

2.4 - Ash Deposition

The nature of ash deposits within a boiler varies substantially. During pulverised fuel combustion in particular, the ash matter is strongly fractionated between bottom ash and fly ash, which form slagging and fouling deposits respectively, producing different behaviour to that seen in FB combustion [75].

2.4.1 - Deposition Mechanisms

Once the inorganic, non-combusted products are airborne, deposition can occur via a number of routes as shown in Figure 2.2. The most significant are discussed below. Fluid dynamic equations concerning some of the mechanisms can be found in work by Kaufmann et al [99].

2.4.1.1 - Inertial Impaction

Inertial impaction is the principal method of flue-gas borne ash deposition onto boiler tubes, and forms the main part of a deposit from biomass combustion [100]. Inertial impaction takes place when particles with a diameter of larger than 10 μm have a large inertial momentum. When the gas streamlines encounter a heat transfer surface, the particles cannot follow these around the tube, and instead impact the surface. The predisposition of the airborne ash particles to stick to a surface after impaction, known as the capture efficiency, depends upon the composition and viscosity of the particle, the characteristics of the surface including roughness and composition, the surface tension, and the thermal and chemical compatibility between the particle and the deposit/heat transfer surface [101]. This can be described using a sticking coefficient. Once a particle comes into contact with a clean tube, the melting point and momentum of the particle is of importance. A particle with too much kinetic energy will simply bounce back from the tube into the gas flow before sufficient heat transfer has taken place to condense the particle onto the surface, while a particle with a high melting point may solidify at the point of contact with the colder tube and will not retain its “sticky” nature. If the deposit has a low enough momentum, and is sufficiently thin, it will solidify on the surface. As the deposit thickness and surface temperature increase, the outer layer of the deposit remains sticky on the surface, causing an increase in capture efficiency of additional particles, and increasing the rate of deposition [102].

2.4.1.2 - Condensation

Condensation is particularly prevalent on surfaces such as heat transfer surfaces, where a high temperature gradient will exist [98].Condensation in the convective areas of the boiler results in the fly ash becoming a composite of silicates and salts, which readily deposit on surfaces, reducing heat transfer and promoting corrosion from chlorine [103].

2.4.1.3 - Thermophoresis

Thermophoresis is the induction motion of small particles (0.5-5 μm) by the presence of a temperature gradient, which transports the particles to cooled surfaces by the gas flow resulting from local temperature gradients [98]. If the particles are sticky when they impact, or if there is a rough surface or chemical reaction, they may form an evenly distributed, finely grained deposit, particularly around heat transfer tubes [101]. This is a dominant mechanism in the formation of corrosive deposits [94].

2.4.1.4 - Diffusion

Diffusion of small particles is the result of motion produced by a diffusion gradient in a liquid or gaseous flow, due to the Brownian motion of particles. The amount of material deposited in this process is less significant than that by vapour phase diffusion and condensation [101].

2.4.1.5 - Other Mechanisms

Other, less significant modes of deposition include electrophoresis, the thermoelectric effect, the Magnus effect and sedimentation. Deposits can result from a number of these different mechanisms at once, making prediction of composition and structure difficult. For instance, as shown in Figure 2.4, which illustrates condensation on a tube in a cross flow, the side in direct contact with the gas flow will predominantly experience deposition through impaction. However, this does not dominate on the opposing side. Instead, turbulent flow caused by the shape of the tube causes additional mixing of the flue gases, which may promote further chemical reactions, and the longer residence time in the area surrounding the tube increases the likelihood of condensation. This deposition through condensation dominates alkali chloride deposition [96].

2.4.2 - Particle Sintering

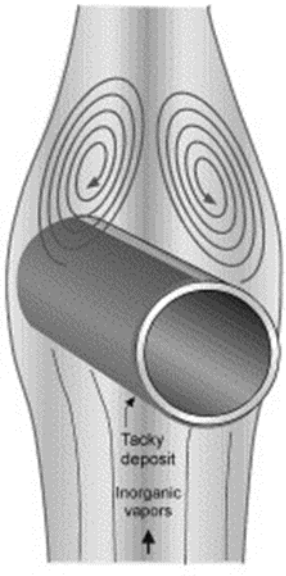

Figure 2.4 - Illustration of the different flow conditions around a superheater tube, affecting deposition. From [96]

Once the ash particles have deposited, further melting or chemical reactions often occur within the deposit. Low melting temperature K-Si systems (such as those discussed in Section 2.3.1) and ionic crystals or glasses, when heated to temperatures close to their inherent melting points, have a tendency to weld together when they come into close proximity to one another, through solid state diffusion and viscous necking [103]. This process is known as sintering. Sintering is the removal of pores between loose, fine particles through thermal processes, converting the particles into a solid, dense mass by heat and/or pressure, without fully melting the particles to the point of liquefaction. In order for sintering to occur, two requirements need to be met [104]. Firstly, a mechanism for material transport such as diffusion or viscous flow must be present. Secondly, a source of energy is required for material transport to begin and be sustained over a period of time.

During the initial stages of sintering, a rearrangement of particles typically occurs where particles slightly move or rotate, increasing the number of contact points between the particles. This is less relevant to ash deposition, as most sintering of ash occurs due to molten and semi-molten/sticky particles that contact through impactions and agglomerate, either on boiler walls, during transport in flue gases, or within the bed material in the case of fluidised bed boilers. Bonding between particles is initiated at points of contact, where material transport can take place and where surface energy is highest [104]. An example of this is shown in Figure 2.5.

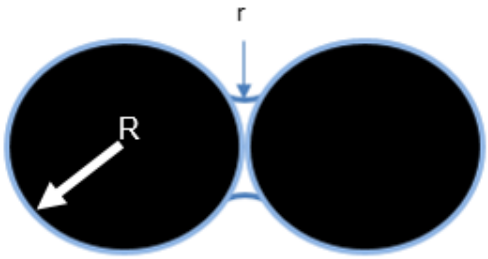

Figure 2.5 - Example of sintering: two partially melted ash particles in contact, with a liquid bridge connecting the two

Ash particles resulting from combustion are typically covered in a liquid phase layer, such as potassium silicates [75, 76] and potassium-calcium-silicate systems [89, 105]. A significant number of studies [43, 47, 105-107] have provided evidence that potassium is the key component for inducing bed agglomeration, since potassium silicate eutectics can have solidus temperatures of as low as 700°C [89]. As a result, ashes during combustion can potentially produce significant liquid fractions within the deposits.

Both Bryers [76] and Van Loo [38] give three general types of biomass ash, based upon their ash fusion temperatures and, in turn, their tendency towards furnace slag formation. Both high silica/high potassium/low calcium ashes (such as agricultural residues) and high potassium/high phosphorus ashes (wastes, including manure) have low ash fusion temperatures, and are more prone to slagging. Low silica/low potassium/high calcium ashes have high ash fusion temperatures. The different mechanisms of sintering are described in the following sections.

2.4.2.1 - Liquid-Phase Sintering

Liquid-phase sintering (also known as viscous flow or silicate melt sintering) is a significant densification mechanism in silicate systems, occurring typically at temperatures of greater than 1000°C [108]. The rate of sintering is dependent upon particle size, viscosity and surface tension [104]. Viscosity and surface tension are, in turn, highly dependent upon the composition of the ash and temperature. A small increase in temperature can result in a substantial increase in the presence of liquid phases. Silicate systems can form highly viscous liquid phases above the solidus temperature [109], creating capillary pressures of greater than 7 MPa [104]. Once the temperature falls below the solidus threshold the silicate liquid can vitrify due to its high viscosity, creating a glassy phase that sinters particles strongly together. As such, ashes under high temperatures are typically treated as glasslike silicate structures in empirical models, which will be discussed in more detail in Chapter 3.

Boström et al [75] outline a mechanism for the production of low melting temperature silica eutectics in the presence of potassium. Silica particles are initially formed as sub-micrometre sized particles, which increases particle surface area resulting in fast reactions. In the example below, potassium

hydroxide is used, although KCl has been described to behave in a similar way in other studies [38, 88, 93]: this is discussed in Section 2.3.3.

$$SiO_2 + 2KOH \leftrightarrow K_2SiO_3 + H_2O \quad \text{(Eqn. 2.7)}$$

This produces a low melting potassium silicate eutectic. KOH is highly available in the initial stages of combustion, only converting to KCl in the presence of HCl (see Section 2.3.3, Equation 2.1). This increases the chance of interactions with silica, increasing the density of molten K-silicate on the particle. As the fuel particle burns, it shrinks, bringing the molten silicate together and increasing the opportunity for contact: these particles will agglomerate, forming larger droplets that initiate deposit formation [75].

2.4.2.2 - Reactive Liquid Sintering

Reactive liquid sintering is commonly observed due to the melting of salts. The presence of ash with high concentrations of sodium, potassium, chlorine and sulphur will often result in low melting point eutectic systems: it is for this reason that an ash particle may partially melt at low temperatures of 500-700°C [108]. The amount of liquid phase present is responsible for the stickiness of the particle, and will induce particle agglomeration if great enough [109]. A capillary is created by the melted ash components, forming between the particles when in contact, which forms a negative radius (r in Figure 2.5) compared to that of the particles (R in Figure 2.5). This results in a negative pressure across the capillary relative to the solid particles, forcing the particles together. Significant compressive stresses are created across the capillary [110], resulting in greater solubility on the particle surface and diffusion of material between the ash particles. This diffusion leads to agglomeration: as such, reactive liquid sintering is frequently observed in fluid bed combustion [47, 89, 105, 108, 109, 111]. A significant number of studies [43, 47, 105-107] have provided evidence that potassium is the key component for inducing bed agglomeration.

2.4.2.3 - Vapour Phase Sintering

Material transfer can occur between solid particles due to differences in vapour pressure, resulting from the differences in surface curvature between the particles. Similarly to Figure 2.5, the surface of the particles has a positive radius

of curvature (R) and a high vapour pressure when compared with the negative radius of curvature (r) and lower vapour pressure of the contact region [104]: this difference in vapour pressure drives material transport. The rate of sintering through this mechanism is heavily dependent upon the size of the particles (with a smaller radius providing a greater surface curvature gradient) and the vapour pressure. Since vapour pressure increases exponentially with temperature, vapour phase sintering is strongly temperature dependent [110]. Vapour phase transfer is particularly important in the reactions of halides, such as NaCl and KCl [112].

Vapour phase sintering has been shown to be a significant mechanism in the fluid bed combustion of coal ashes containing significant quantities of CaO in the presence of CO_2 and SO_2: sintering temperatures were reduced from 900°C in dry air to 600°C with either 0.5% SO_2 or 20-40% CO_2 present, forming calcium sulphates and calcium carbonates, respectively [109]. Although vapour phase transport changes the shape of the pores between particles, inducing bonding and creating increased sinter strengths, it does not result in shrinkage or densification of the system [104].

2.4.2.4 - Solid State Sintering

Particles can also sinter by the diffusion of atoms or vacancies along the surface, through the bulk of the particle, or in the case of a crystalline material, along a grain boundary. Similarly to vapour phase sintering, diffusion is driven by the difference in chemical potential between the particle surfaces and the points of contact, taking place through the path of least resistance, and is particularly prevalent when vapour pressure is low [110]. Once again, particle size and temperature are important factors in determining the rate of sintering through this process.

2.4.3 - Slagging

Bottom ash is the term used for the ash fraction collected from the bottom of the furnace, and consists of heavier particles that remain within the high temperature regions of the boiler, near to the combustion zone (Figure 2.6). This ash often contains any minerals and impurities found within the biomass, typically silicon-rich minerals such as sand, stones and earth, or in the case of fluidised bed combustion, the bed material [38]. These impurities, along with other fluxing components such as alkali metals, can cause slag formation, where the impurities lower the melting point of the ash producing a viscous liquid which sticks to surfaces where high radiant heat transfer is present (see Section 2.3.1). Slagging may apply to fused ash deposits, to sintered deposits and to dry ash [76].

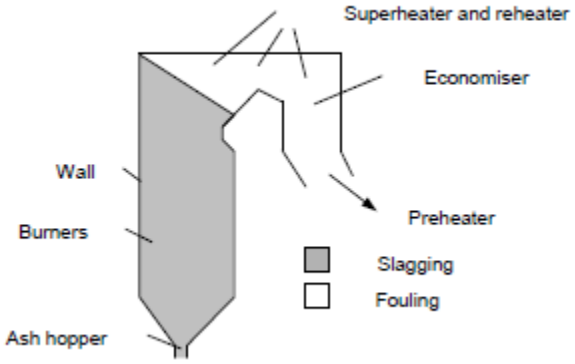

Figure 2.6 - Slagging and fouling regions within a boiler [101]

Slag deposits frequently consist of an inner layer with a powdery structure, covered by a liquid or semi-molten ash layer which insulates the inner layer somewhat. The nature and composition of the slags can vary throughout the furnace, depending upon the temperatures involved, absorption rates, gas flow, the composition and concentration of the ash, and even the oxygen level of the flue gas in contact with the heat-transfer surface [76]. Baxter et al [113] note that in the case of biomass fuels, slags can take the form of rock-like, ribbon-like, hair-like and other deposit structures.

Particles that are heated to above their solidus temperature will have an inherent viscosity and become sticky, where the rebound energy upon impaction with a surface is less than the energy of adhesion. This initial adhesion may occur through condensation, thermophoresis, impaction and van der Waals forces

[114]. Beyond this initial adhesion, dry particles may become embedded within the initial deposit if it remains sticky, increasing the density of the deposit and facilitating sintering reactions or fluxing, depending on the composition.

The main mechanism of slagging in coal and mid-high silica biomass combustion systems is silicate-melt induced slagging, which is dependent upon Si, Al and other refractory compounds with high melting points, and their interactions with fluxing material [93] producing a highly viscous glassy melt phase, which can form slag masses or running slags on refractory and water walls [113]. Released silica particles interact with chlorides and other fluxing compounds as outlined in Section 2.3.1, to form a sticky or partially liquid eutectic material. This gives the particles an inherent viscosity, which allows for agglomeration, particle growth and eventually inertial impaction on the boiler surface, upon which the particles may cool and solidify or remain sticky. In slagging regions of the boiler, the deposit builds with the addition of both sticky and dry particles, insulating the initial deposit which in turn solidifies once temperatures decrease sufficiently. As the deposit grows further from the cooler wall/superheater substrate, surface temperatures increase, inducing material transfer between points of particle contact through liquid phase sintering as outlined in Section 2.4.2. Further temperature increases, in turn, decrease the viscosity of the outer layer until a molten flowing slag occurs.

Severe slagging may also occur from the combustion of high alkali metal, low silica biomass. Vaporised alkali metals and alkali metal chlorides and sulphates will form through the reactions shown in Equations 2.1-2.3, before nucleating, agglomerating and condensing upon the cooler boiler surfaces. Wang et al [115] note that potassium from biomass ash can be released in four different forms at high temperatures. In low chlorine biomass, potassium is released in the form of K_2SO_4 for low K biomass and KOH for high K biomass. If high chlorine concentrations are present, KCl is the predominant form. Finally, KCN may be produced if the biomass contains both high K and N.

Niu et al [116] suggest that $K_2Ca(SO_4)_2$ and $K_3Na(SO_4)_2$ have a significant role in the onset and severity of slagging, while Aho and Silvennoinen [96] suggest that K_2SO_4 is the dominant substance, first nucleating in the flue gas and in turn acting as condensation nuclei for KCl at lower temperatures. Wang et al [117] found that

most of the alkali chlorides converted to alkali sulphate within the flue gas when firing straw and wood. In contrast, Niu et al [116] found that the major components of slag deposits from the combustion of cotton stalks varied between fuel composition. Despite “Fuel 1” in the Niu et al. study containing more SO_3 in ash analysis, the main components of the slag were KCl and NaCl, with only minor $K_2Ca_2(SO_4)_3$ and $CaSO_4$ present. “Fuel 2” contained a higher concentration of these sulphates, however high KCl was still present, indicating that the two reaction routes are not exclusive of one another. Saqib and Bäckström [87] studied the partitioning of chlorine from waste fuels fired at two grate-fired and four fluidised bed combustion facilities. Results showed that organically bound chlorine was released as HCl, while inorganically bound chlorine was recovered in the bottom ash as alkali metal chlorides. Studies by Öhman et al [118] have shown that high Si-K ratios produced less slagging, as did the addition of aluminosilicate additives, converting silicates to aluminosilicates and oxides. This will be discussed further in Section 2.5.

2.4.4 - Fouling

Of the total ash removed from large pulverised fuel boilers, approximately 80% is fly ash, collected either from the electrostatic precipitator (ESP), cyclones or air preheater hoppers [38]. The properties of fly ash differ slightly depending upon where it is collected. Ash collected from cyclones behind the combustion unit in the secondary combustion zone tend to consist of coarse particles, while particles collected by the ESP and fabric filters are usually sub-micron particles [38].

Fouling deposits occur in the lower temperature convective regions of the boiler, further away from the combustion zones, such as on superheaters and heat exchangers. In an ideal boiler, the flue gases leaving the combustion zone are cooled to a temperature below the initial melting temperature of the fly ash, followed by further water cooling [76]: if temperatures are too high, troublesome fouling may occur. High temperature fouling may occur through semi-fused, sintered ash deposits in the hotter flue gas regions (1300-900°C), while low temperature fouling can result from the formation of loose or slightly sintered deposits building up in the cooler regions of the boiler (900-300°C) [102]. The impaction of sticky particles, the condensation of previously volatilised species, and the reaction of volatile alkali metal mineral matter with fly ash in the gas

stream or at the tube surfaces are the main mechanisms of deposition given by Bryers [76], while Baxter et al [113] additionally propose thermophoresis and electrophoresis as important mechanisms. Riedl et al [94] suggest that little to no direct impaction occurs within hot water tube boilers, where flue gases pass inside the tubes. Instead, thermophoresis is considered to be the dominant mechanism.

The deposits often consist of alkali metal salts, particularly sulphates, chlorides and phosphates [38], which then promote adhesion of other non-sticky particles in the fly ash by impaction. Jenkins et al [119] give Si, K, Na, S, Cl, P, Ca, Mg and Fe as the most important elements in fouling. A study by Kaufmann et al [99] found that fouling deposits retained the same characteristics as the fly ash, indicating that any phase changes and reactions may be negligible at deposit temperatures of ~400°C.

Baxter et al [113] note that silica content is of high importance in determining fouling rates. Rice hull biomass with greater than 95% SiO_2 has been shown to produce little fouling, although other issues such as particulate emissions may occur. The presence of alkali and alkaline earth metals with silica however increases fouling tendencies due to the formation of low melting point compounds (as outlined in Section 2.2.1). In addition, fouling from wood biomass with low silica may occur due to contamination from soil and clay, since potassium is highly mobile in plants. Jenkins et al [119] found that the mineral composition of inorganic components is important to the mechanism of fouling, and that crystalline silicates and aluminium from clays, as well as potassium in the form of feldspar aluminosilicates, tend not to foul by inertial impaction due to their high melting point. Theis et al [97] [120] used peat as a “clean” low fouling fuel in their studies, with fairly low (36.9%) silica content in the ash, and low potassium (1.1%) and sodium (0.1%) concentrations. Mixing with bark (above 30%) and straw (above 70%) increased deposition rates, with fouling deposition increasing at Cl/S molar ratios of 0.15 and above. The authors found that both mixtures produced different deposition behaviours, with peat-bark mixture deposition being governed by sulphation interactions of alkali chlorides, and peat-straw mixtures being governed by aluminosilicate absorption of alkali metals by the

peat. Thus, fouling behaviour is complex, and heavily dependent upon the ash composition and phases present.

2.4.5 - Corrosion

Beyond the initial deposition, the presence of chlorine can be particularly harmful to the boiler, especially in conjunction with potassium hydroxides that often result from biomass combustion: this can result in the formation of KCl (Equation 2.1) of which small amounts can strongly accelerate the corrosion of the underlying surfaces [121]. Other compounds, such as NaCl and HCl, may also accelerate the oxidation of metal alloys, further increasing corrosion effects [122]. As chlorine is often found within straws and grasses alongside alkali metals, this makes them particularly difficult to utilise for combustion. In biomass boilers, high temperature corrosion of superheater areas is the main concern, due to the high metal and gas temperatures present around final stage superheaters [38].

High chlorine biomass ash can accelerate corrosion through a number of means. As discussed in Section 2.3.3, alkali metal chlorides have a low initial melting temperature, which can in turn flux any protective oxide layer on the boiler surface. This process is compounded, since chemical reactions are faster in liquid phase than solid deposits [123]. Erosion-corrosion may also occur, where any protective coating or oxide layer of a boiler surface may be eroded by abrasive dry fly ash particles, allowing corrosion of the exposed metal underneath. Degradation of boiler parts by biomass ash is affected by the flue gas velocity, the percentage of ash in the fuel, and the abrasiveness and corrosiveness of the components within the ash [124].

Riedl et al [94] name the chloride corrosion process “Active Oxidation”. Alkali metal chlorides condense upon boiler surfaces, creating a flux within already present deposits. In addition, the chlorides react with SO_2 and SO_3 in a similar reaction to that described in Equation 2.3, given by Niu et al [93], although this time chlorine gas is produced rather than HCl as shown in Equations 2.7 and 2.8.

$$2NaCl + SO_2 + O_2 \leftrightarrow Na_2SO_4 + Cl_2 \qquad \text{(Eqn. 2.8)}$$

$$2KCl + SO_2 \leftrightarrow K_2SO_4 + Cl_2 \qquad \text{(Eqn. 2.9)}$$

This chlorine is released within the deposit where, coupled with erosion of protective layers through abrasion and chemical means, it comes into contact and reacts with the exposed low alloy steel, forming $FeCl_2$ and damaging the metal structure. As $FeCl_2$ has a high vapour pressure, it diffuses through the deposit and, in turn, reacts with any excess oxygen in the flue gas, regenerating the chlorine in the gas as per Equations 2.10-12 and accelerating corrosion rates throughout the boiler.

$$3FeCl_2 + 2O_2 \leftrightarrow Fe_3O_4 + 3Cl_2 \quad \text{(Eqn. 2.10)}$$

$$2FeCl_2 + 1.5O_2 \leftrightarrow Fe_2O_3 + 2Cl_2 \quad \text{(Eqn. 2.11)}$$

$$FeCl_2 + O_2 + Fe_3O_4 \leftrightarrow 2Fe_2O_3 + Cl_2 \quad \text{(Eqn. 2.12)}$$

2.4.6 - Deposit Removal

Although some deposition is prone to shedding events, where the deposit crumbles under its own weight, most boilers employ soot blowers in order to remove the remaining ash deposits. This ensures proper heat transfer through heat transfer surfaces and prevents the progressive plugging of gas passes, which both affect pressures and flow rates, resulting in load limitation and tube erosion due to increased gas velocities [125]. Soot blowers work by directing a high velocity jet of steam, water or compressed air at a deposit, breaking the deposition structure by both thermal and mechanical means and forcing its removal from the boiler surface. In regions of the boiler where weak deposits are present, particularly in the cooler, convective regions of the boiler, sonic soot blowers can be deployed [126]. Sonic soot blowers operate by employing high energy, low frequency sound waves which dislodge non-sticky, weak deposits through vibrational forces. Although this method is ineffective for slagging or sintered deposits [125], they also avoid corrosive, erosion or mechanical damage to the boiler surfaces. Finally, under extreme circumstances with heavy, glassy slagging deposits, small explosive charges have been utilised [126]. Traditional soot blowers, mostly steam, are the main focus of fouling and boiler studies.

2.4.6.1 - Soot blowing

A soot blower is a lance or tube that is placed into the furnace through an opening in the boiler wall: this lance may have a two-directional nozzle at the end, to direct the steam jets across the heat transfer tubes, or it may have nozzles running throughout. These nozzles are approximately 12.5 mm in diameter [127]. Compressed air pressures can range between 6 and 30 bar, although typically a 13 bar gauge is used for operation [127]. Pohl and Juniper [114] note that steam blowers typically exert an air pressure of 0.7 - 2 MPa, and water blowers operate at approximately2 MPa. There are conflicting figures in the literature regarding the strength at which a deposit becomes difficult to remove: Pohl and Juniper [114] state that the Barnhart sinter strength compression test found that pellets with compression strengths of greater than 34.45 MPa are considered difficult to remove, which would suggest a pressure of over 10 times that which a soot blower can exert is needed. Gibb on the other hand suggests a figure of 5 MPa , which is much closer to the figures given by Pohl and Juniper for steam and water blowers. A study by Barnes et al [128] found that coal slagging deposits at zero porosity had compressive forces ranging from 96.5 MPa to over 2,740 MPa. As porosity increased to 25%, compressive strength reduced to 68.5 MPa.

Most research on the effect of soot blowing systems has been conducted upon coal-fired boilers, and focuses upon the removal of loose powdered deposits within convective regions of the boiler, and the effect it has upon heat transfer rate over a period of hours [129].

Senior et al [130] attempted to determine the maximum flue gas temperature in the convective regions of a coal-fired boiler in which ash deposition can be removed easily through soot blowing. The author states that deposition strength is strongly related to porosity, and that this deposition strength is fairly constant for porosity of greater than 25%. It is concluded that a 25% deposit porosity is a critical porosity for deposit removal through soot blowing.

Kalisz and Pronobis [131] attempted to optimise soot blower operation in coal pulverised fuel and circulated fluidised bed (CFB) boilers. The fouling rate was only measured in the convection pass of the boilers, where powdered deposits were observed. The required soot blowing frequency was then determined based upon this fouling rate. It was determined that fly ash particles with a diameter of

less than 30μm are the main influence upon the fouling rate of powdered sediments. The authors then developed a model, assuming that the maximum fouling time is a function of the following: relative tube spacing $\sigma_1=s_1/D$ and $\sigma_2=s_2/D$; relative tube diameter D/D_b; relative mean velocity of the flue gas in the tube bundle w/w_b; relative ash particle-size distribution $R_{0.03}/R_{0.03b}$ ($R_{0.03}$—percentage of particles bigger than 30 μm, %); relative mean temperature of the flue gas in the tube bundle T/T_b; and chemical constitution of the fly ash represented as B/A (base-to-acid ratio) c_m. This resulted in the following equation after futher statistical analysis:

$$\tau_{max}=9.01\sigma_2^{-1.723}\left(\frac{w}{w_b}\right)^{0.744}\left(\frac{R_{0.03}}{R_{0.03b}}\right)^{0.319}\left(\frac{T}{T_b}\right)^{0.249} \quad \text{(Eqn. 2.13)}$$

Where τ_{max} is the maximum fouling time corresponding to the most economical soot blowing frequency. Alongside these variables, the chemical composition of the fly ash and tube diameters were considered to be of importance in determining the fouling rate. In addition, a low longitudinal pitch was concluded to be the most practical arrangement for boiler tubes, in order to maximise sediment build up time. This study implies that lab-based experiments alone will not be sufficient in predicting the effectiveness of soot blowers and deposit removal, as the geometry of the boiler system plays a significant role in the rate and type of deposition.

Sandberg et al [129] conducted a long-term study on the effect of fouling and soot blowing upon the efficiency of superheaters in a fluidised bed biomass boiler, over a period of 3 years. The CFB boiler was capable of operating at 157MW, and deposition upon both superheaters and re-heaters were part of the experiments. Numerous types of biomass were used over the course of the study, while measurements of deposit thickness and heat transfer were taken. Deposit layer thickness was found to increase at a linear rate, despite the use of soot blowers, over the course of two and a half years. In this study, the rate of fouling was determined to be noticeably higher at the superheater positioned furthest away from the combustion zone. The use of soot blowers was found to drastically increase heat transfer rate in the superheaters in the hours after operation, with a 0.5-1MW increase in heat transfer reported by removing some of the deposition.

It was ultimately determined that there is no significant difference in the deposit layer growth rate and the heat transfer rate when varying the soot blowing cycle frequency from one to three times per day. This indicated that the growth of the hardest - and therefore most difficult to remove - part of the deposit is independent of the frequency of soot blowing.

2.4.7 - Bed Agglomeration

Bed agglomeration is an issue found only in fluidised bed combustion. The bed material in FB combustion is typically silica-based [38], which interacts with fluxing alkali metal compounds to sinter, particularly if high levels of alkali metals and/or chlorine are present. The bed particles increase in size and weight until the suspended particles no longer behave as a fluid. In severe cases, bed agglomeration can result in complete defluidisation, resulting in an unscheduled plant shut down, and is the subject of most research conducted with regards to the impact of using biofuels in fluidised bed boilers.

A study by Ergudenler and Ghaly [106] found that a 400 kW fluidised bed gasifier utilising silica sand and using wheat straw as a fuel will agglomerate at around 800°C, resulting in serious defluidisation. At higher temperatures of around 850°C, the straw ash fused and formed strong bonds with the sand, resulting in a hard, brittle mass, signifying that the agglomeration is temperature dependent. The ash of the wheat straw used in this study was found to have high K_2O (36.15%) and SiO_2 (27.26%) content. Furthermore, potassium was determined to be the major contributor to the onset of agglomeration, due to the lack of sodium in the ash: the potassium oxide melts would penetrate the voids of the silica, forming low temperature silicates which would sinter and bind the sand particles together [106].

A later study by Lin, et al. [47] attempted to determine the mechanisms responsible for the agglomeration induced by wheat straw, using a laboratory scale fluidised bed combustor with wheat straw containing 39% SiO_2 and 29% K_2O in the ash. The results showed that although defluidisation occurred at all temperatures tested - over a range between 725–930 °C - the time taken for defluidisation was found to be inversely proportional to the temperature of combustion. Significantly, the accumulation of potassium in the bed material was determined to increase with time during combustion. Agglomerates were

analysed through SEM/EDX analysis, and it was found that the major elements on the surfaces were silicon and potassium, with 20 wt.% present as K_2O. This provides clear evidence that the presence of potassium causes the formation of the sticky sand surfaces ready for agglomeration [47], supporting the assertions previously made by Ergudenler and Ghaly [106].

Öhman, et al. [105] studied the bed agglomeration characteristics of a number of biomass fuels, including wheat straw, wood, peat, and some waste materials, in a 5kW bench-scale reactor. SEM analysis revealed that a coating with a thickness of 10-50 µm was formed around all bed particles, with all coatings consisting of different ratios of silicates. These elements in the coatings were determined to be mainly fuel-related, and the melting of this coating material was identified to be the reason for the formation of a sticky layer on the bed particles, causing bed agglomeration. This melting behaviour was found to be very sensitive to the amounts of potassium in the sample, as determined in previous studies [47, 106]. However, the relative calcium content also appeared to have an impact. Fuels with high potassium and low calcium content in the ash, such as wheat straw (20.7% K, 6.9% Ca), were found to contain a very large amount of melt at temperatures below 900°C, while the opposite was true for samples with low potassium and high calcium, such as bark (6.36% K, 27.6% Ca) and wood residue (5.89% K, 21.7% Ca). It was suggested that silicate melts are responsible for the agglomeration [105].

Armesto, et al. [132] successfully conducted experiments on a 30 kW pilot scale bubbling fluidised bed boiler, using rice husks as fuel. The rice husk ash contained 87.7% SiO_2, 5.4% K_2O and 1.3% CaO. The potassium content, particularly in the form of potassium-calcium silicates, of the bed material was found to increase when the bed material was not changed between test runs, correlating with the findings of Lin, et al. [47]. The length of time used for each experimental run was not discussed in this paper, although the increasing potassium content within the bed material suggests that, with longer running times, the FB combustor would eventually suffer from defluidisation.

The effects of co-firing coal and biomass in FB combustion have also been studied on a number of occasions. Laursen and Grace [43] investigated the implications of co-firing a sub-bituminous coal with a relatively low ash content

(13.5%) and a sulphur content of 0.8%, with hog fuel (a blend of forest waste, including bark, twigs and low-quality wood) and sludge in a BFB boiler. The boiler was operated at a relatively low temperature of 750°C to specifically avoid agglomeration problems: as such, no agglomeration was reported. The hog fuel ash had a high Na_2O content (6%), and 2% K_2O: however, the ash also contained high CaO content (30.8%), supporting the results reported by Öhman et al. [105].

Fuel blending of biomass for FB combustion has also been considered. Salour, et al. [107] investigated whether bed agglomeration could be reduced or eliminated when burning rice straw in a FB combustor, by co-firing a rice straw – urban wood waste fuel blend in a pilot scale BFB reactor. The fuel ash analysis of the rice straw found a SiO_2 content of 76.7% and a K_2O content of 8.91%, in comparison to the waste wood which had 37.6% and 8.69%, respectively. Initial tests on the raw rice straw revealed large masses of agglomerates in the bed throughout all of the experiments attempted. Lower blending rates (75% rice straw, 25% wood) also resulted in agglomeration, however this blend also gave more stable reactor temperatures for longer periods of time than the raw fuel. This trend continued, with increasing blend rates resulting in longer stable temperature times, with “excellent stability” reported at a 10% rice straw concentration, although none of the experiments avoided agglomeration entirely. Similar to previous studies [47, 132], the concentration of K_2O in the spent bed materials was found to increase with time. Although the results suggest that fuel blending offers potential control for bed agglomeration, it did not avoid the problem entirely, and the extent to which tube fouling might be influenced was not assessed [107].

As noted throughout the previously discussed studies, alkali and alkaline earth metals are the most influential ash components when it comes to agglomeration and sintering, particularly with interactions between them and a silica sand bed material, which is often used. The release of alkali metal compounds from biomass combustion in the presence of silica, either from the bed material or the ash itself, will result in the formation of alkali metal-silicates (K_2O-SiO_2): these compounds have a eutectic point of approximately 770°C, while the eutectic point of K_2O-CaO-SiO_2 is even lower [133]. These low melting temperatures are often below the temperatures of combustion used in experiments. Lin, et al. [47] also observed that burning char particles led to temperatures significantly higher than

that of the bed. This, in turn, caused inorganic matter within the char particles to melt and flow to the surfaces, forming an agglomerate when the sand collided with it. In addition, the chars were suggested to behave as a liquid droplet at higher temperatures (>900°C), which may coat the sand grains, providing an important route for coating formation, with the existence of K-rich crystals on sand surfaces providing evidence for this. According to Öhman, et al. [105], the distribution of elements in the coatings differs significantly, preventing a comparison with standard ash analysis. Instead, for silicate melts, the viscosity of the melt must be taken into consideration to determine the fraction needed for 'stickiness' [105]. Melting behaviour was shown to be sensitive to the concentration of potassium and calcium in the silicate melt, while alkali metal sulphates and chlorides do not participate in the agglomeration process. It was determined that silicate melts are responsible for the agglomeration, which occurs through two distinct mechanisms: melt-induced and coating-induced [134].

These results suggest that silica bed materials should be avoided for combusting high alkali metal content biomass, such as straw. However, this is often not possible. Some alternatives, such as natural rock minerals, are often prone to attrition due to lower mechanical strength. synthetic bed materials could be used, but their high price, particularly on larger scales, becomes a major issue [133].

2.5 - Additives

To change the behaviour of the ash and help improve the rate and nature of deposition, additives are used to modify the chemical composition. This, in turn, achieves two things: the concentration of problematic species in the ash is decreased, and the melting temperature of the ash is increased [135]. The additive is either blended with the fuel before combustion or added into the combustion chamber. Most additives studied focus upon minimising and restricting the effects of potassium, the dominant alkali metal component in many biomass due to the fluxing effects of many of its compounds (see Section 2.3).

The choice of additive is a difficult one and numerous factors must be taken into consideration, including [134, 135]:

- Complex transformations and interactions during biomass combustion, which are affected by factors including ash composition, combustion temperatures and residence time.
- Potential property changes of additives as a result of the biomass combustion system and conditions.
- The difficulty in controlling the various complex interactions between the additive and biomass ash.

Because of this complexity, there are a wide range of potential candidates for use as additives in combustion, each with different effects. The additive may reduce deposition by directly altering the chemistry and interactions of the ash, by adsorbing the problematic species thereby preventing their release and interaction with deposits, by diluting the components of the ash, or by altering the structure of the deposits, making them more easily removable. A list of additives grouped into these four categories is displayed in Table 2.3.

Table 2.3 - List of additives and effects, as reported in the literature [135]

Effect	Additives	Main Components
Chemical Adsorption and interaction	Kaolin, halloysite	$Al_2Si_2O_5(OH)_4$, $Al_4(OH)_8/Si_4O10*10H_2O$
	Cat litter, emathlite, clay minerals, clay sludge	Mixture of aluminosilicates, silica and alumina
	Ilite	One explam $KAl_2Si_3AlO_{10}(OH)_2$
	Detergent zeolites	$Na_x[(AlO_2)_x(SiO_2)_y]*_zH_2O$
	Ammonia sulphate, aluminium sulphate, iron sulphate, ammonia phosphate, phosphoric acid	$(NH_4)_2SO_4$, $Al_2(SO_4)_3$, $Fe_2(SO_4)_3$, $(NH_4)_3PO_4$, H_3PO_4
	DCP	$Ca(H_2PO_4)_{2*}H_2O$
	Limestone, lime, marble sludge	$CaCO_3$, CaO
	Sewage sludge, paper sludge, peat ash, coal fly ash	ALxSiyOz
	Dolomite, bauxite, quartz, titanium oxide	$CaMg(CO_3)_2$, SiO_2, Al_2O_3, TiO_2
Physical adsorption	Kaolin, zeolite, halloysite	$Al_2O_{2*}(SiO_2)_{2*}(H_2O)_2$, $Al_2Si_2O_5(OH)_4$
	Clay minerals	Aluminium silicates with different Al/Si ratios
	Clay sludge, sewage sludge, paper sludge	Mixture of aluminium silicates, detergent zeolites
	Lime, limestone, dolomite, calcined dolomite	$CaCO_3$, CaO, $CaMg(CO_3)_2$, CaO*MgO
	Bauxite, gibbsite	Al_2O_3, $Al(OH)_3$
Dilution effect and inert elements enrichment	Bauxite, lime, limestone	Al_2O_3, $CaCO_3$, CaO
	Silicon oxide	SiO_2, $CaCO_3$
	Marble sludge	SiO_2, $CaCO_3$
Restraining and powdering effects	Lime, limestone	$CaCO_3$, CaO

2.5.1 - Aluminosilicate-based Additives

Al-Si type additives are a common first choice, due to a strong ability to convert vapour and liquid phase KCl and $KSiO_3$ to potassium aluminium silicates [98], according to the equations described in Section 2.3.1. Equations 2.4-6 are repeated below:

$$Al_2O_3.2SiO_2 + 2KCl + H_2O \leftrightarrow K_2O.Al_2O_3.2SiO_2 + 2HCl \quad \text{(Eqn. 2.4)}$$

$$(Al_2O_3 + 4SiO_2) + 2KCl + H_2O \leftrightarrow 2KAlSi_2O_6 + 2HCl \quad \text{(Eqn. 2.5)}$$

$$(Al_2O_3 + 6SiO_2) + 2KCl + H_2O \leftrightarrow 2KAlSi_3O_8 + 2HCl \quad \text{(Eqn. 2.6)}$$

Examples of Al-Si additives, such as Kaolinite, have displayed effectiveness in deposition control [136], alkali metal vapour removal [137, 138] and bed agglomeration control [89], while others such as bauxite and coal ash have been shown to decrease some of the gaseous alkali metal concentrations [139]. The main products between Al-based silicates and potassium chloride are described by the reaction in Equation 2.4 [98].

The ternary diagram in Figure 2.7 explains why this is desirable. The addition of Al-Si additives results in a shift in composition from the highlighted area, towards the Al areas of the diagram, as represented by the arrow. Al-Si additives act as a sorbent for the volatile alkali elements, essentially creating a K_2O-SiO_2-Al_2O_3 ternary system of particles [89]. As the composition of the system is shifted to the right of the diagram by the presence of Al_2O_3, the solidus phase temperatures as indicated on the diagram can be seen to increase, which would in turn inhibit sintering, vaporisation and flow of the ash.

In addition to the more favourable aluminosilicate formation, Al-Si additives also reduce the release of MOH and subsequent MCl deposition within the boiler, since the alkali metals are bound in aluminosilicate form rather than being released into the gas phase. Although the reactions shown in Equations 2.4-6 produce HCl, the potassium is bound in the bottom ash and solid fly ash rather than vaporised, preventing the formation of hydroxides, carbonates and later chlorides as outlined in Equations 2.1 and 2.2. In addition, aluminosilicate

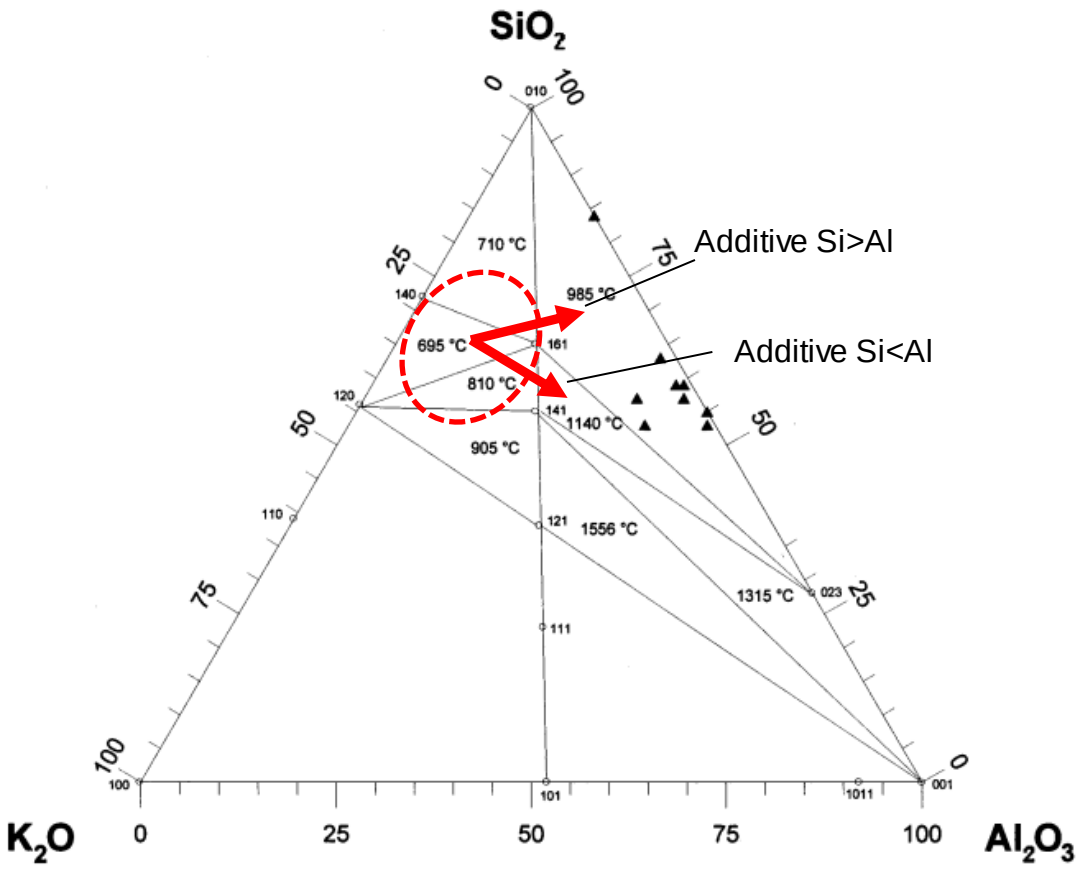

Figure 2.7 - K_2O – SiO_2 – Al_2O_3 ternary diagram, including solidus temperatures, and with the effects of using Al-Si based additives illustrated [89]

compounds have slow, diffusion-controlled reactions and small surface areas [135]. This prevents corrosion by active oxidation. Furthermore, the flue gas in boilers is often scrubbed to remove harmful compounds such as HCl, NO_2 and SO_2 before being emitted.

A number of studies investigating the effects of Si-Al-based additives upon biomass combustion deposition are available, some of which will be discussed further.

Steenari, et al. [140] studied the effect of adding kaolin, limestone powder and sodium bicarbonate to the combustion process for a number of agricultural residues, with a focus upon the binding of potassium and reduction of sintering. The experiments were conducted on a laboratory scale, using a lab oven up to 1000°C in open crucibles. Sodium bicarbonate was included to capture the SO_2 emissions resulting from the use of high sulphur biomass fuels. It was observed that the use of sodium bicarbonate had a detrimental effect upon the sintering

behaviour of the ash. The use of wheat waste with additives was found to increase sintering temperature from 700°C to above 1000°C, with the lime giving the best results. The amount of additive was varied, with a low and high dosage, which were observed to be just as effective as each other. The authors conclude that the best effect was achieved when both kaolin and limestone powder were used in amounts corresponding to 2-10% of the fuel weight [140]. The results indicated that the potassium salts reacted with the kaolin to form potassium aluminosilicate species with high melting points. However, phosphate species were found to interact with the silicate phases, and the authors recommend that these interactions need to be clarified to give a better understanding.

Aho and Silvennoinen [96] studied the effect of kaolin and pulp sludge on a range of biomass fuels within a bubbling fluidised bed reactor at 820 or 880°C. Pulp sludge was chosen as an alternative to the more expensive kaolin, due to its similar composition. In this case, kaolin was found to prevent Cl deposition at a certain dosage for a blend of agricultural waste and pine, while the pulp sludge was much less effective, suggesting that potassium aluminium silicate formation dominates over sulphation in inhibiting Cl deposition. The agglomerated bed material was observed to contain potassium, calcium and phosphorus, indicating that a significant part of the alkali metals remain in the bed. According to the authors, agglomerates that soon would have led to defluidisation were found after just two-hour stable running periods.

Ohman and Nordin [89] studied the combustion of wheat straw and bark in a 5kW bench scale reactor using a regular sand bed, with kaolin powder added to the bed material. A small amount of kaolin was found to increase the critical temperature for initial bed agglomeration by over 100°C. However, the corresponding increase with bark as fuel was only about 10°C. The formation of potassium aluminium silicate compositions was determined to be the reason, with a decreased potassium content as a result of kaolin being transformed to meta-kaolinite particles, which then adsorbed potassium species.

Of particular interest are two studies examining the effects of coal PFA as an additive. Barišić et al. [134] used both a bench scale (100kW) defluidisation reactor, and a pilot-scale (1MW) CFB reactor to examine wood, straw and olive

waste combustion. It was determined that fuels with a high alkali metal content (those that suffer mostly from the coating-induced mechanism of agglomeration) benefitted most from the addition of the coal PFA. As a result, olive waste deposition was lessened with pfa use more than straw, which reacts with a prevalent melt induced mechanism. In a worst-case scenario, the use of coal ash improved the resistance to agglomeration by a factor of two, when compared to a regular sand bed material. The larger surface area of the coal PFA provides more surfaces upon which particles can adhere to without causing larger agglomerates, and the capture of potassium species, were determined to be the key reasons for these results. It was noted, however, that improper management of the coal ash may lead to increased fouling if uncontrolled.

Wu, et al. [141] studied the ash transformation and deposition of pulverised wood combustion, both with and without coal fly ash, in a full-scale 800 MW suspension-firing boiler. Without the additive, the pulverised wood was found to create deposits containing a large amount of K_2SO_4, KCl and KOH/K_2CO_3, as a result of condensation. Also, deposit build-up was found to take place slowly, without any shedding events observed. The addition of the coal ash, at a rate of four times the mass of the wood ash content, was found to greatly reduce the presence of KCl, K_2SO_4 and KOH in the flue gas, while deposits built up quickly, and there was frequent shedding of large layers of deposit. Deposition behaviour was found to remain unchanged in low temperature regions (800°C), however KCl content was greatly reduced. The unburned carbon within the fly ash was also found to play an important role in deposition, acting as activated carbon and improving adsorption capacity. The study strongly implies that the addition of coal pfa, at least in pulverised wood combustion, can reduce ash deposition problems, even on a large scale.

Although studies into Al-Si additives, including coal pfa, appear to demonstrate an improvement to the deposition process, it is clear that some gaps in the knowledge exist. The positive effect upon specific biomass compositions is apparent. However, the benefits are less clear for other biomass fuels, and to gain a fuller understanding of the effects and benefits, additional studies are needed. In addition, some reaction mechanisms such as the phosphate-silicate reactions observed by Steenari, et al. [140], are not fully understood. However,

the general consensus is that Al-Si additives reduce deposition related issues, through the dilution and/or adsorption of alkali metal species, in particular potassium, which are found in larger quantities within biomass compared to other fuels. As such, additives with high Al-Si contents are desirable, to promote aluminium silicates production and chlorine removal in the deposits [96].

2.5.2 - Calcium-based Additives

Ca-based additives are likely effective through dilution of the ash or adsorption of alkali metal salts: this is because of the porous surface of the particles, in combination with the calcination of the problematic species [98]. Similar to the effect of Al-Si based additives, the ternary K-Ca-Si system that results from the use of Ca additives results in an increased first melting temperature, in comparison to binary K-Si and high Si systems usually found in deposits [89].

2.5.3 - Sulphur-based Additives

The main effect of S-based additives is to convert KCl into K_2SO_4, which has a higher melting temperature of approximately 840°C, which lowers deposition rates [135]. In addition, the sulphation of KCl results in the release of chlorine into the flue gas, reducing the amount found in deposits and hence reducing corrosive effects [96]. S-based additives are typically added as part of a solution, to avoid additional decomposition of sulphates [135].

2.5.4 - Phosphorus rich Additives

Potassium may react with phosphorus to form potassium phosphates, which then further react with CaO: this, in turn, reduces the potassium available to form low melting silicates [135].

2.5.5 - Effectiveness of Additives

Literature shows that the hardest deposits result from strongly sintered components within the ash, and ashes containing significant amounts of alkali metal salts (particularly potassium compounds), with low initial melting temperatures, that remain sticky throughout a larger region of the boiler, are the main cause [98, 113, 133, 135, 142]. This, in turn, suggests that deposition resulting from biomass containing significant amounts of potassium, such as the olive cake being studied within this project, may be particularly problematic in

terms of removal via soot blowing. The addition of aluminosilicate-based additives, such as coal pfa and kaolin, has been observed to have a significant effect upon the sintering behaviour of biomass ash [89, 115, 134, 135, 140], by promoting the formation of potassium aluminium silicates over lower melting potassium silicate compounds and fluxing potassium chlorides. This is therefore the basis of this study.

2.6 - Conclusions

The composition of biomass and its resulting ash is complex, and a wide range of elements can be present: theoretically, the entire periodic table may be present. The behaviour and interactions between these elements is crucial in the performance of biomass as a fuel, including the behaviour of its ash and the deposits that form. These deposits form through several mechanisms: semi-molten ash particles may impact on boiler tubes to initiate deposition, while volatile species may condense upon boiler surfaces. This leads to decreased boiler efficiency and potential damage to boiler surfaces, and in worst cases complete shutdown.

Studies have shown that alkali metal concentrations in particular are crucial in determining ash behaviour. Although silica is the dominant element in biomass slagging deposits (except for some cases involving low silica biomass), and it has melting temperatures of up to 1700°C, the presence of alkali metals can reduce silicate melting temperatures to as low as 700°C, while alkali metal chloride formations can produce eutectics of temperatures as low as 400°C. In addition, alkali metal chloride formation in the flue gas can result in severe deposition and corrosion, through the process of active oxidation and the regeneration of chlorine. The sintering of deposits may occur, increasing the strength and density and inducing chemical reactions that further damage the boiler surfaces. Deposit removal methods such as soot blowing are dependent upon deposition strength: severe sintering can significantly increase the compressive strength of the deposit to above the peak impact pressure of the soot blower.

Additives have shown promise in reducing the rate and strength of deposition and corrosive tendencies of high potassium biomass ash, due to their strong ability to convert alkali chlorides and silicates into aluminosilicates with higher melting

temperatures. This additionally prevents the formation of alkali metal hydroxides and carbonates, which are precursors to troublesome alkali metal chlorides. The work in this thesis aims to examine the effect of two such aluminosilicate additives on the melting behaviour of biomass ashes, and the potential effects that additive addition will have on the boiler system.

Chapter 3 - Ash Characterisation

3.1 - Introduction

This chapter outlines the processes and techniques involved in the initial characterisation of the biomass and biomass-additive ash samples. Ash preparation and composition is discussed, with rationale given for the samples chosen for study. The compositions are analysed in the context of biomass classifications suggested in literature, and correlations between ash components are considered. Finally, the methods used for producing homogenous samples are outlined, and particle size distributions are provided. Any further preparation that was required for specific experiments will be outlined in future chapters, in the relevant experimental methodology sections.

3.2 - Ash Compositions

Three biomass samples of interest to large scale biomass generators were selected for use in this study, with fly ash taken directly from a large-scale biomass-fired plant used as a comparison. Olive cake (OCA) and bagasse (BA) were provided as biomass by UK power stations, while white wood pellet (WWA) and the power station fly ash (FA) were supplied as ashes: WWA was ashed at standard biomass laboratory conditions of 550°C, while the FA was taken directly from the cyclones of a large-scale biomass power station.

Two aluminosilicate additives were additionally used, both of which have been shown in the literature to have promise in reducing ash deposition issues from biomass combustion. Coal pulverised fuel ash (PFA) was provided by a UK power station, and kaolin powder (KAO) was supplied by Sibelco. Moisture [143], carbon-in-ash [144] and ash content [145] were determined using British Standard methods. Oxide analysis of the ashes was carried out using ICP ash analysis conducted by an external laboratory, apart from the kaolin figures which were provided by Sibelco. The compositions of these ashes are shown in Table 3.1.

Ash compositions for all samples and sample-additive blends, in wt.%, mol. % and atomic concentration %, can be found in Appendix A.

Table 3.1 - Oxide composition of samples used in this study

Ash Component (wt.%)	Coal pfa (%)	Kaolin (%)	Olive Cake (%)	Fly Ash (%)	White Wood (%)	Bagasse (%)
Ash Content (d.b)	-	-	9.87	-	1.20	4.70
Moisture in ash	0.48	12.3	0.52	0.38	0.26	0.45
Carbon in ash (d.b)	2.79	11.6	1.54	1.35	1.43	1.67
SiO_2	58.2	48.3	11.2	48.8	27.1	49.7
Al_2O_3	20.8	36.4	1.2	19.1	4.6	6.8
Fe_2O_3	9.3	0.9	0.9	5.9	2.3	3.0
TiO_2	0.9	0.06	0.1	0.8	0.3	0.4
CaO	2.9	0.04	10.3	10.9	24.8	2.9
MgO	1.4	0.4	3.0	2.7	4.7	1.5
Na_2O	2.3	0.06	0.6	1	1.5	0.2
K_2O	1.7	2.6	32.3	6.4	9.2	3.7
Mn_3O_4	0.1	-	0.1	0.4	1.5	0.1
P_2O_5	0.2	-	5.0	0.9	2.0	1.4
SO_3	0.9	-	2.4	0.6	1.6	0.8
Preparation	As Received	As Received	Lab @550°C	As Received	Lab @550°C	Lab @550°C

3.2.1 - Ash-Additives Blends

Alongside the unblended ash samples, three different blend rates of the additive with biomass ash samples were studied, at rates equivalent to 5%, 15% and 25% additive to raw biomass, in accordance with the recommendations of the industrial partners involved with the project. As some of the samples were provided in ash form, it was determined that in order to maintain consistency, the samples would all be ashed before mixing. The ashes were blended at the ratios shown in Table 3.2, placed into containers and shaken vigorously to produce a homogenous sample. The calculation used to determine the ash content ratio required to simulate a biomass-additive blend is as follows:

$$\frac{\%\ \text{dry fuel} * \text{dry fuel ash content}}{(\%\ \text{dry fuel} * \text{dry fuel ash content}) + \%\text{additive}}$$

Afterwards, the mixtures were heated to 650°C, to produce an ash that was representative of expected biomass-additive compositions.

Table 3.2 - Ratio of sample ash to additive concentration at each blend rate

Blend rate	5%	15%	25%
OCA	0.65	0.36	0.23
Adtv.	0.35	0.64	0.77
WWA	0.19	0.10	0.06
Adtv.	0.81	0.90	0.94
BA	0.47	0.30	0.21
Adtv.	0.53	0.70	0.79
FA	0.14	0.05	0.02
Adtv.	0.86	0.95	0.98

3.2.2 - Composition Analysis

The ash compositions used in this study were plotted onto the Vassilev ternary classification system that was discussed in Chapter 2.2. The three biomass samples exist within three different groups, with OCA composition corresponding

to K-type, WWA composition a C-type biomass ash, and BA an S-type. The use of the additives results in all but OCA5% samples having a high acid S-type composition, as shown in Figure 3.1.

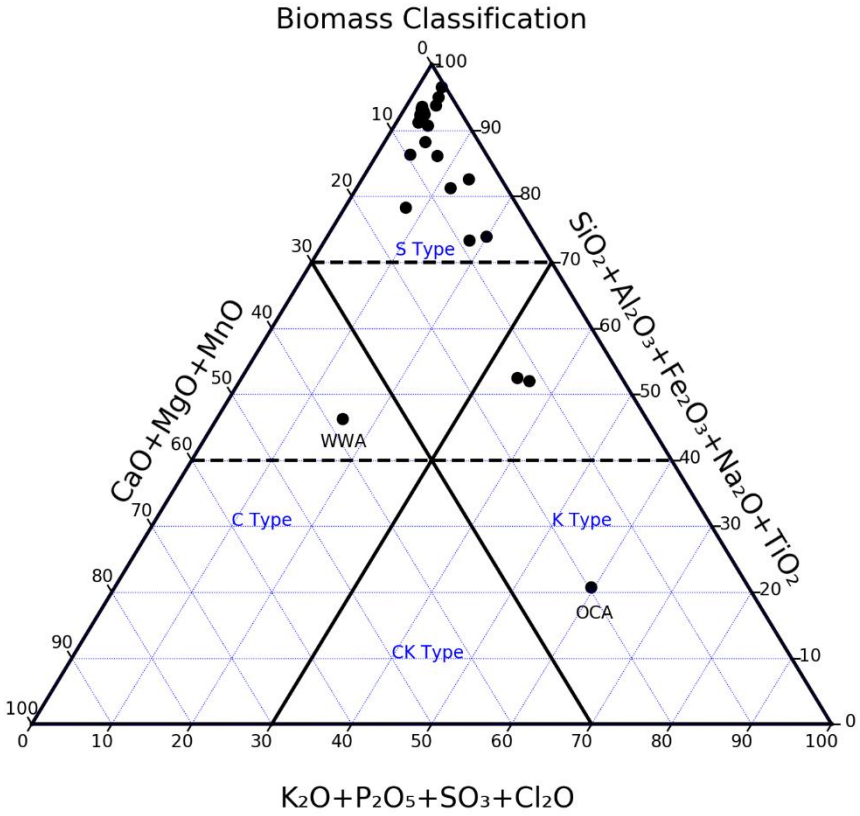

Figure 3.1 - Sample ash compositions within the context of the Vassilev ternary classification [80]

Principal component analysis (PCA) was conducted upon the composition of the ashes and blends to determine any correlations between elemental content, as shown in Figure 3.2. There is a clear positive correlation between Si and Al content (as expected when increasing alumina-silicate additive concentration). Fe and Ti concentration increase with increasing Si and Al, and a second strong correlation between K and P content exists in the samples and blends studied. Na and K content are shown to be negatively correlated, however the spread of results makes the correlation weak (as indicated by the short length of the Na vector). Na concentration also correlates with Si, Al, Ti and Fe, corresponding to the predictions of the Vassilev ternary diagram in Figure 3.1.

3.2.3 - Sample Preparation

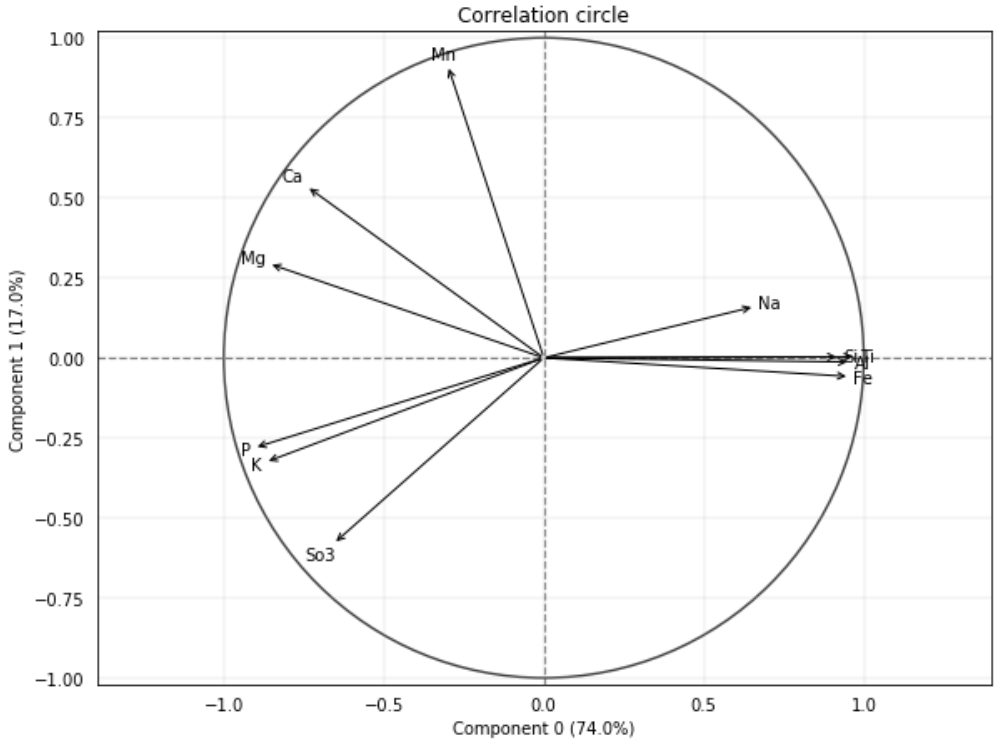

Figure 3.2 - Correlation circle for ash compositions studied (created with Prince [146])

Once mixed and re-ashed, the samples needed to be prepared in order to maintain consistency and homogeneity during experiments. A Retsch RS 200 vibrating disc mill was used to reduce the particle size of the ashes. The samples are placed into a grinding jar along with a grinding set consisting of a thick grinding plate surrounded by a larger grinding ring. The grinding jar is placed into the disc mill and secured, which is then subjected to circular horizontal vibrations that subject the ash to extreme impaction and frictional forces. Once ground for a period of 30 seconds, the grinding jar is removed from the mill, and the grinding set is removed from the jar. The ashes were then placed into a 215μm sieve and container, which was then secured onto a sieve shaker, and the sub-215 μm ash collected for use in experiments. The entirety of the sample in each case was milled to below 215- μm, with no larger particles removed. Any samples were dried at 100°C for 2 hours before testing, in order to remove any additional moisture that may have been re-absorbed during storage.

3.2.4 - Particle Size Distribution

The ground ashes were subjected to particle size distribution analysis, using a Malvern Panalytical Mastersizer 2000E laser diffraction particle size analyser capable of analysing particles between 20nm and 2000µm. A small amount of sample was added to distilled water, which is used to transport the particles through the system for multiple runs. An average distribution is taken, and the spread of the distributions is checked to ensure consistency. These results are summarised in Figure 3.3.

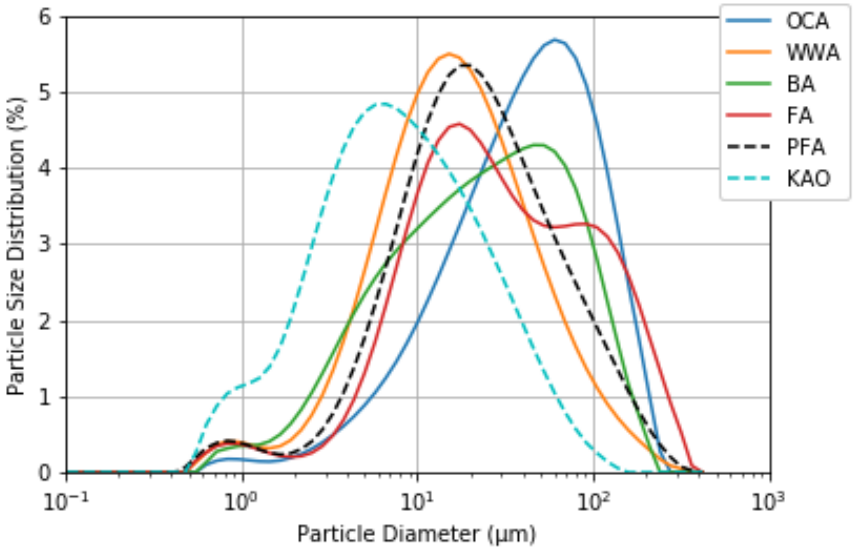

Figure 3.3 - Particle size distribution of unblended samples

Chapter 4 - Impact of Additives upon the Resistivity of Biomass Ash

4.1 - Introduction

Particle resistivity is an important factor in determining the efficiency of electrostatic precipitators, and hence particulate emissions. This chapter will detail experiments undertaken to determine the resistivity of the biomass and additive mixtures encountered within this study. The chapter begins with an overview of electrostatic precipitation (ESP), including the principles and mechanisms behind ESPs, the importance of ash resistivity, and a review of available literature on the subject. The equipment and methodology for the experiments is then outlined in detail, along with justifications for the methods used. It should be noted that the use of atomic percentage for ash composition analysis is exclusive to this chapter, due to the models being developed with atomic percent data. Finally, resistivity results are presented and analysed, with context provided for what the results mean with regards to ESP efficiency and potential particulate emissions.

4.2 - Ash Resistivity

4.2.1 - Electrostatic Precipitators

Electrostatic precipitators (ESPs) have been in use within the power generation industry since 1923 [147], as an effective filter of fly ash particles from the flue gas stream at the back end of a boiler system. Typical modern ESPs are often required to operate at collection efficiencies of greater than 99.8% in order to meet the strict emissions regulations noted in Section 1.4.3.

Figure 4.1 shows an illustration of the design principle of electrostatic precipitation. A high voltage is passed across exposed discharge electrodes and collection plates positioned parallel to the gas stream, creating an electric field across the system and ionising the gas around the discharge electrodes, producing a corona. Positive ions are immediately captured by the negatively

charged electrodes, while negative ions are influenced by the electric field and drift into the space between the electrodes. As the flue gas passes through the device, the suspended fly ash particles are charged either by collision with the ions, or through induction charging for the smallest particles [148], and migrate to the earthed collection plate under the influence of the Coulomb force. These particles are then retained on the collection plates through a combination of electrical and van der Waals' forces, and are generally removed through frequent mechanical rapping, although wet ESPs may use water to clear the plates. The frequency and intensity of rapping is crucial, so as to prevent efficiency losses through the build-up of an insulating layer of dust on the electrode surface, and to prevent particle re-entrainment as a result of too much force, respectively.

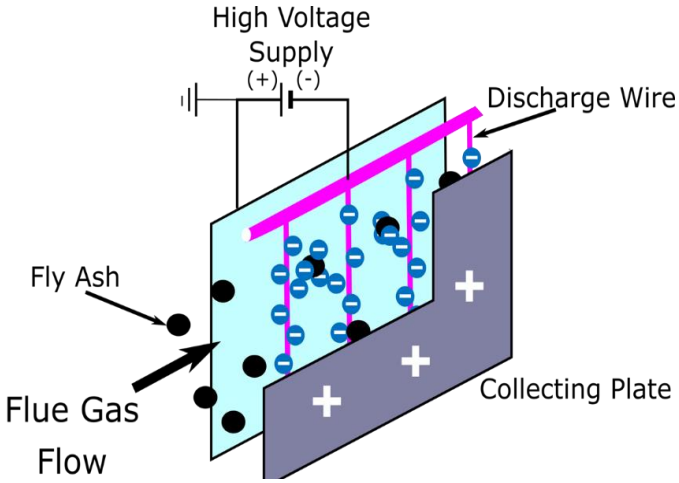

Figure 4.1 - Diagram of the principle of electrostatic precipitation, showing a plate-and-wire ESP configuration

ESP design varies depending on its purpose: for instance, ESPs used for air cleaning will use a significantly lower voltage (6-12 kV) than ESPs used in industrial applications (>100 kV). Wet precipitators may be used in certain applications, where gases need to be cooled, harmful gases such as SO_x and HCl removal is desirable, or in instances where the precipitated material is either sticky or in liquid form, when intermittent water washing may be used to remove the resulting layer [148].

Typically, large power plants will utilise dry ESPs. While other electrode types exist, such as those found in flat plate and tubular ESPs [149], the most common ESP type in large scale industrial operations is a plate-and wire-configuration, as

shown in Figure 4.1. The flue gas flows parallel to plates of sheet metal and high voltage electrodes which are in the form of weighted suspended wires. This allows multiple flow lanes to operate in parallel; each lane covers large areas and is able to deal with large volumes of gas, suiting larger scale applications.

A number of factors serve to influence fly ash collection efficiency in ESPs, including inlet dust loading, gas velocity, particle size, shape and surface properties [148], the choice of discharge electrode depending upon fly ash properties [150], and plate spacing [151]. However, the major effect of particle composition upon ESP performance is related to the electrical resistivity of the deposited material.

4.2.2 - Ash Resistivity

Resistivity determines how strongly a material opposes the flow of electric current, and is typically a strong function of temperature. The resistivity of a material is heavily dependent upon the nature of its structure (for instance, the dimensions of the particle and the nature of the crystalline and amorphous structures present). Fly ash compositions emitted into the atmosphere by coal-fired power plants mostly consist of Al_2O_3, SiO_2 and Fe_2O_3, which can constitute up to 90% of the total mass [152]. The use of biomass, either to replace coal or to co-fire, introduces increased quantities of additional compounds containing calcium, potassium and phosphorus. Maximum fly ash resistivity typically occurs at 140-160 °C, with a decrease above these temperatures resulting from a volume property of the ash [153]. The value of resistivity of a fly ash particle can affect the required exposure time within the electric field of an ESP by up to a factor of four or more [148].

4.2.2.1 - Conduction Mechanisms

Particle resistivity is determined through two main conduction mechanisms: volume conductivity and surface conductivity. Volume, or bulk conduction, decreases with increasing temperature according to an Arrhenius equation of the form:

$$\rho = Ae^{\frac{-E}{kT}} \qquad \text{(Eqn. 4.1)}$$

Where ρ is the resistivity, A is a complex material parameter considered to be a constant, E is the electron activation energy, k is Boltzmann's constant and T is temperature. Volume conductivity flows through the particle itself (Figure 4.2), and is therefore heavily influenced by particle composition.

Figure 4.2 - Ash particle covered in a thin film, with volume conduction (white) and surface conduction (red) paths displayed

Surface conduction is the main conduction mechanism for temperatures below approximately 150°C in boilers, where species from the flue gas composition (such as water vapour, SO_x and ammonia) are adsorbed on the particle surface, producing more highly conductive chemical films. Surface resistivity is also sensitive to the ash composition, as alkali metals serve as charge carriers [154]; therefore, it would be expected that surface resistivity effects are more likely to be present in high base-to-acid (B/A) ratio biomass ashes.

4.2.2.2 - Problems Associated with Ash Resistivity

Various figures have been quoted in studies with regards to the optimal resistivities for fly ash collection, likely due to differences in ESP geometry and specifications. Recommended safe ESP working limits of 10^6 - 10^{10} Ωm [148], 10^6 - 10^9 Ωm [155], 10^2 - $5x10^8$ Ωm [156] and 10^2 - 10^9 Ωm [157] are all quoted in the literature. Outside of these limits, collection efficiencies sharply decrease, resulting in potentially significant re-entrainment of particles. Figure 4.3 shows the effect of changing resistivity upon collection efficiency.

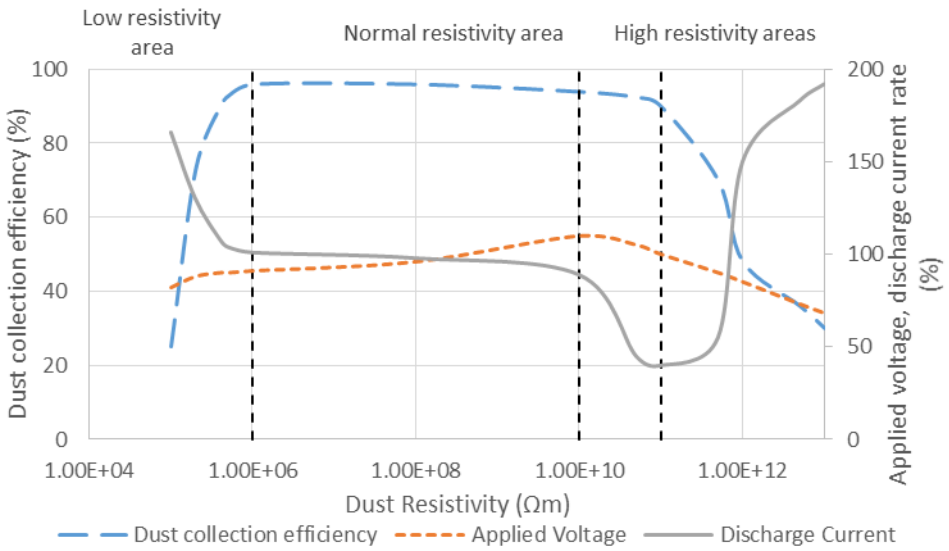

Figure 4.3 - Collection efficiency vs dust resistivity for electrostatic precipitators (adapted from Mizuno [156], Parker [148]). Dashed vertical lines represent boundaries between low resistivity, normal resistivity and high resistivity regions

4.2.2.2.1 - High Resistivity Ash

As resistivities increase, particles more effectively retain their charge. A consequence of this is that, at resistivities of close to 10^{10} Ωm [148], particles deposited on the collection surface lose their charge so slowly that a voltage build up occurs through the dust layer, creating an electric field. Once this field becomes strong enough, electric breakdown occurs, creating sparking [156]. At higher resistivities, the voltage increase reaches a point that results in the emission of positive ions in a phenomenon known as back corona or reverse ionisation, which in turn neutralises the negative charge present upon migrating particles. In addition, this will affect the electric field within the ESP, further reducing collection efficiency. Emissions may increase by a factor of 10 as a result [148].

Fly ash can be conditioned within the flue gas, in order to mitigate reverse ionisation by reducing the resistivity of fly ash before the particles enter the ESP. Small amounts of gaseous SO_3 can be injected into the flue gas stream ahead of the ESP (at a rate of approx. 15 p.p.m. [148]), which reacts with any moisture present to create a sulphuric acid mist. This mist condenses on the fly ash particles, creating a thin film of acid that induces surface conductivity effects.

While other reagents are available [152, 158, 159], sulphur conditioning is the most widely used [152].

4.2.2.2.2 - Low Resistivity Ash

The re-entry of previously collected dust from collection plates into the gas flow is known as re-entrainment, and is a particular issue for dust particles with resistivities of below 10^6 Ωm [148]. In this instance, although the particles are charged by the corona produced by the discharge electrode, the charge is lost before they can reach the collection plates. As a result, the uncharged particles are then charged by the plates, and are repelled back into the flue gas stream, where they are again charged by the corona discharge. This can occur multiple times throughout the ESP and may ultimately result in the particle escaping.

Re-entrainment is also an issue for fine dust particles. Typically, dust particles coagulate when they impact upon the deposited layer, producing large particles that are more easily collected. Fine particles are more likely to be re-entrained during the rapping process, or even as a result of being picked up by increased gas velocities around the collecting plate/electrode.

4.2.2.3 - Effect of Composition upon Resistivity

Fly ash compositions emitted into the atmosphere by coal-fired power plants mostly consist of Al_2O_3, SiO_2 and Fe_2O_3, which can constitute up to 90% of the total mass [152]. In contrast, biomass ashes typically contain relatively high concentrations of other compounds, such as CaO, K_2O, Na_2O, P_2O_5 and MgO, as well as alkali carbonates and sulphates. The structure and phases present within the ash also have a major influence on resistivity. All fly ashes contain both amorphous and crystalline silicon dioxide, and aluminium oxide, which have well understood conductivity/resistivity characteristics due to use as ceramics and semiconductors. Ceramics such as these often have extremely high resistivities, at ambient temperatures, acting as insulators due to the wide electron band gap present [160]. At higher temperatures however, these materials act as ionic conductors: alumina (Al_2O_3) for instance has a minimum resistivity of 10^{12} Ωm at 20°C, decreasing to 10^{10} Ωm at 200°C, and further to 10^6 Ωm at 600°C.

4.2.2.3.1 - Influence of Alkali Metals on Conductivity

Bickelhaupt conducted a number of studies on the components of ash resistivity in coal ashes [154, 161-163], resulting in a predictive model that remains in use for predicting coal ash resistivity when designing ESPs [148]: this model is discussed in detail in Section 4.2.2.4. Volume resistivity experiments [161] were conducted on dry fly ash samples mixed with 3% of polyvinyl alcohol, which were dried, filtered and then pressed into discs using a 2270kg load. Resistivity was then measured using a gold alloy paste to create electrodes on opposite sides of each disc.

The ionic migration of alkali metals was determined to be the primary mechanism for volume conduction, in particular influenced by the sodium content of the sample. Although both lithium and potassium migration were identified during experiments, the lithium content was typically too low in the samples tested (a range of 0.01-0.06 wt. % Li_2O) to make a large contribution to conductivity, while potassium migration was observed to be extremely small in comparison to the concentration within the ashes (a range of 0.2-3.88 wt. % K_2O). Bickelhaupt postulates that iron content may have an influence, through the known effect of iron upon the glassy phase present within ash particles, which in turn alters the structure in such a way that it further promotes the migration of alkali metal ions, increasing conductivity.

Surface resistivity experiments [154] were conducted upon a group of coal ashes for temperatures between 60°C and 250°C, in an atmosphere of air with approximately 9% moisture. A varied selection of coal ashes were studied, with a wide range of MgO, Fe_2O_3, Al_2O_3 and SiO_2 contents present. The author again observed that alkali metal ions migrated through the fly ash toward the negative electrode under voltage, suggesting that these ions act as charge carriers, and therefore have a significant effect on the resistivity. While a negative correlation was observed for resistivity plotted against lithium and sodium content, potassium content showed no correlation. However, combined potassium plus iron content showed a negative correlation with resistivity.

The role of potassium was determined to be dependent upon iron content: the presence of iron is suggested to influence the reactivity between the ash and the environment, resulting in the release of potassium within the sample. It was

subsequently proven that the release of alkali ions in the presence of moisture is enhanced in ashes with high iron content. It was postulated that surface conduction is the result of the ash reacting with an agent (e.g. water) which is capable of releasing the alkali ions on the surface, in turn enabling them to act as charge carriers, similar to the behaviour of a silicate glass (to which the ash approximates, with additional impurities). This is dependent upon a number of factors, and sodium was deemed more readily released than potassium.

4.2.2.3.2 - Studies of Biomass Ash Resistivity

Studies investigating biomass resistivity are scarce: typically, ESP performance [164-166] and factors such as particle size distribution [150, 167] and elemental composition of fly ash [168-170] are the focus. However, some studies containing resistivity data exist.

Lillieblad et al [171] reviewed the properties of particles formed in biomass combustion from a number of different Scandinavian biomass fired boilers, focusing particularly upon the effects of increasing boiler load on particle size distribution. Greater loading was determined to result in coarser particles and an increased particle concentration within the flue gas. Volatile components were determined to enrich in the fine particle mode (0.1-0.5 μm), where ESP efficiency is reduced, indicating that biomass fly ash may cause operational issues. However, ESP use with forest residues was found to be effective in reducing emissions, with ESP collection efficiency greatly increased with a greater collection area. Loss on ignition (LOI) testing of collected fly ashes showed that residual carbon content can be high for wood fired grate boilers, with LOIs of 28% at low load up to 72% at high boiler load, as a result of increasing entrainment of material from the flue bed. Although this unburned carbon can both reduce dust resistivity and pose a potential fire risk, the use of cyclones was found to decrease LOI in ESP collected ash to 3%. The authors advise that, in order to reduce unburned material and to prevent hollow, low resistivity particles from forming, a low gas velocity should be used.

Beyond this, resistivity is discussed only briefly. The measured resistivity for dust collected from the “last fifth ESP field” of a pulverised coal boiler firing South African coal is compared to fly ash collected in a single field ESP installed downstream from a multi-cyclone after a forest residue fired grate boiler. The

resistivity of the forest residue was found to be several orders of magnitude lower than that of the coal, with resistivities as low as $1x10^6$ Ωm recorded at temperatures of 150°C. Unusually, the peak resistivity (approximately $5x10^8$ Ωm) for the dust was determined to be approximately 200°C. The lower resistivity was determined to be due to a higher moisture content, different fly ash composition and higher quantities of unburned particles, although the actual figures and reasoning for this are not discussed further.

Nussbaumer [155] characterised particles from biomass combustion using a lab-scale tube-type ESP connected to a pellet boiler. The same standard as in this study, IEEE Std 548-1984, was used as the basis for determining electrical conductivity. The resistivity was reported for three distinct particle types arising from wood combustion: soot, salts and condensable organic compounds (COC), rather than as a bulk sample. These three particle types exhibit very different electrical properties due to the differences in chemical composition. Soot was found to produce resistivities of as low as 10^3 Ωm, below lower operating ESP limits where high re-entrainment would be expected, while COC resistivity peaked at approximately $5x10^{12}$ Ωm, beyond upper recommended limits where back corona may occur. The resistivity of the salt was found to be within ideal ESP operating limits.

The authors concluded that ESP operation would be acceptable under ideal conditions during wood combustion, where mainly inorganic particles would be present in the flue gas. However, during start-up phases, low combustion temperatures and throttled air conditions, ESP operation may reach critical levels.

Jaworek et al [157] studied the differences between fly ash from two different boilers: a pulverised fuel boiler utilising coal, and a fluidised bed boiler where wood was combusted. Fly ash was collected from different stages of the ESP, where particle size decreases with each stage. Bio-ash particles were noted to be highly irregular, due to high unburned lignin content. The density of wood particles was noted to be lower than the mineral components, and therefore more difficult to remove by the ESP. The bulk density of the wood ash was higher in the first stage of the ESP than that of the coal fly ash, and was significantly lower in the following stages. The authors note that this raises issues with rapping of the collection electrodes in the ESP. The biomass ash was noted to have a

significantly greater proportion of low diameter ash particles when compared to the coal ash: this is likely due to the increased volatile content of biomass.

Resistivity measurements showed that the resistivity of coal ash was greater than the resistivity of the biomass ash, as expected. A correlation was found between decreasing carbon content and reduced resistivity in subsequent ESP stages. It should be noted, however, that volatile components within the ash (such as potassium) have a tendency to condense into finer particles (as noted by Lilliebald et al [171]), while coarser particles are more effectively collected in the first stage of the ESP. This means that the lower resistivities in subsequent ESP stages may be the result of increased potassium content within the samples, rather than carbon content, although the authors do not consider this. Peak biomass fly ash resistivity (10^{10} Ωm) was recorded at a temperature of approximately 80°C, lower than typically seen in other studies. Peak coal ash resistivity was measured at approximately 10^{12} Ωm, at 50°C or below.

A significant flaw in the Jaworek study is the lack of information regarding flue gas composition. It is noted that sulphur atomic concentration increases with each ESP stage: however, no explanation is given as to why the 2nd stage had significantly lower resistivities than the third stage, despite increasing sulphur concentration. The authors only suggest that both volume and surface conduction mechanisms were operating simultaneously (which would be expected regardless, in any flue gas containing any moisture), without giving any explicit reason as to why this may be the case. The authors suggest that the decreasing temperature in each stage of the ESP causes increased water vapour condensation, but this is in conflict with the experimental results, for which results from each ESP stage were taken over the same temperature ranges. In addition, although elemental analysis is provided, no analysis was conducted upon the compounds or minerals that were present in the ash. Nussbaumer [155] showed that salts produce lower resistivities than condensable organic compounds; however, the Nussbaumer study found that only soot would produce resistivities on the order of magnitude seen by Jaworek et al.

At the time of writing, no literature is available on the effect of additive use upon ash resistivity.

4.2.2.4 - Predictive Models

As a consequence of the scarcity of ash resistivity studies for biomass, no attempts have been made to develop an empirical model for the prediction of biomass ash resistivity. While several empirical models exist for determining the resistivity of ash particles, the models are derived from resistivities of coal ashes and their compositions. The Bickelhaupt model [163] for instance is often used as a predictive tool for new industrial applications, where an approximation of ash resistivity is necessary in determining ESP size for a specific efficiency [148]. However, while coal ash compositions cover a range of oxide concentrations, as shown in Table 4.1, they will not account for the increased alkali metal content found within biomass, particularly in the case of potassium.

As a result, it is highly unlikely that these models will be suitable for predicting biomass ash resistivity. However, the application of these models to biomass compositions is useful in demonstrating the limitations of the existing models, and the predictions will help to indicate the key components involved in biomass resistivity that may be missing from such models.

Table 4.1 - Typical range of chemical composition for coal fly ashes [172]

Component	Bituminous	Subbituminous	Lignite
SiO_2	20-60	40-60	15-45
Al_2O_3	5-35	20-30	10-25
Fe_2O_3	10-40	4-10	4-15
CaO	1-12	5-30	15-40
MgO	0-5	1-6	3-10
SO_3	0-4	0-2	0-10
Na_2O	0-4	0-2	0-6
K_2O	0-3	0-4	0-4

4.2.2.4.1 - Bickelhaupt Model

Bickelhaupt [163] built upon his earlier work on surface resistivity (as described in Section 4.2.2.3.1) by attempting to develop an empirical model to describe the resistivity of coal ashes in relation to their composition. The methodology used to measure resistivity is similar to that utilised within this project, but with the added benefit of controlling the atmospheric environment: initial resistivity testing was conducted in a dry nitrogen environment, before being changed to a baseline environment of dry nitrogen, with 5% oxygen, 13% carbon dioxide, 9% water and 500ppm sulphur dioxide in order to more accurately simulate a flue gas environment. Measurements were then taken as the furnace cooled naturally from 460°C, down to 85°C. The addition of moisture and sulphur dioxide promotes the onset of surface resistivity phenomena as described in Section 4.2.2.1, allowing for a complete measurement of resistivity. Measurements were taken for 43 different coal ash compositions, with 16 from this set then investigated further to determine the effects of sulphur and water concentration.

Each resistivity measurement produced the characteristic “inverted-V” shape curve which became linear at higher temperatures, as described by the Arrhenius equation for volume resistivity (Equation 4.1). From this part of the curve, the activation energy can be calculated. From the resistivity results at each temperature measured, the values of resistivity for each coal ash were plotted against Li+Na, Fe, and Mg+Ca concentration, all converted to atomic percent (rather than wt.% of oxides, for instance). The plots under linear regression analysis produced a correlation corresponding to a logarithmic trend of the form:

$$\ln \rho = a + b \ln x \qquad \text{(Eqn. 4.2)}$$

Where x corresponds to the atomic concentration for each plot.

The Li+Na relationship was determined to be the dominant component in determining resistivity through surface resistivity: however, at higher temperatures the gradient of the resistivity-concentration relationship was observed to degrade, indicating that other ash components were influencing volume resistivity. In response, the author undertook a number of normalisation

steps, in an attempt to determine the true effect upon resistivity of each of the aforementioned ash components.

The first step involved normalising resistivity to values that would be expected for a Li+Na concentration corresponding to 0.4%, which corresponds to the median of the data within the work. A slope of -2.0 was used, corresponding to the gradient of the resistivity-temperature relationship for Li+Na at low temperatures ('b' in Equation. 4.2), where surface resistivity effects dominate. The authors do not give the exact methods used for normalisation, or values for each new relationship. However, the following normalisation equations, when applied to the dataset, produce results to within reasonable values, likely due to rounding errors. Equation. 4.3 is a modification of Equation. 4.2:

$$\ln \rho = -2 \ln A_{ls} + \beta \qquad \text{(Eqn. 4.3)}$$

Where ρ is the original experimental value, A_{ls} is the combined atomic concentration of lithium and sodium corresponding to, and β is related to the properties of the ash. Rearranging this equation allows β to be determined:

$$\beta = \ln \rho + 2 \ln A_{ls} \qquad \text{(Eqn. 4.4)}$$

Therefore, in order to normalise resistivity to values that would be expected if all ashes contained 0.4 atomic percent combined lithium and sodium, the following equation was used:

$$\rho_N = -2 \ln(0.4) + \ln \rho + 2 \ln A_{ls} \qquad \text{(Eqn. 4.5)}$$

Where ρ_N is the normalised resistivity.

Once this equation was applied to all experimental values, these values were then plotted as a function of atomic percent iron for ashes containing a limited range of magnesium + calcium concentration: ashes containing between 1.9% and 2.7% were used in order to restrict the effects of magnesium and calcium on resistivity as much as possible, although the authors fail to justify why these specific values were chosen. Once plotted, a new relationship between normalised resistivity and iron was determined, taking the form of Equation. 4.2.

The gradient from this equation was then used to normalise these values to 1.0% iron concentration in the same manner as before.

This process was then repeated for the remaining ashes, with the second iteration of normalised resistivity values plotted against combined magnesium and calcium concentration, and a new relationship established according to Equation 4.2. The correlations established between resistivity and iron concentration, and resistivity and combined magnesium and calcium concentration, were then used to produce a secondary correlation for resistivity and combined lithium plus sodium concentration, with ashes normalised to 1.0% iron and 2.5% combined magnesium plus calcium. This resulted in three relationships, with each trendline corresponding to the true relationship between resistivity and each individual ash component: resistivity normalised to 1.0% iron and 2.5% combined magnesium plus calcium vs combined lithium plus sodium atomic concentration; resistivity normalised to 0.4% lithium plus sodium and 2.5% combined magnesium plus calcium vs iron atomic concentration; and resistivity normalised to 0.4% lithium plus sodium and 1.0% combined iron vs combined magnesium plus calcium atomic concentration.

These three trendlines were then "summed": the resistivity is determined by reading from the Li+Na trendline, superimposing the Fe trendline and extrapolating, and then repeating for the Mg + Ca trendline. This allows a series of corrected values to be calculated, giving the following set of equations to estimate total resistivity ρ_{vsa} using volume resistivity ρ_v, which is primarily influenced by ash composition, surface resistivity ρ_s, which is influenced by both ash composition and water concentration, and acid resistivity ρ_a, which considers the concentration of sulfuric acid in the ash. In the absence of sulfuric acid, the total resistivity is comprised of the ρ_v and ρ_s components as below.

$$\log_{10}\rho_v = -1.8916\log_{10}A_{ls} - 0.9696\log_{10}A_{ls} - 1.237\log_{10}A_{mc} - 0.03E + \frac{4334.515}{T} + 1.57595 \quad \text{(Eqn. 4.6)}$$

$$\log_{10}\rho_s = -2.33348\log_{10}A_{ls} - 0.000764C_w - 0.03E - 0.000321C_w e^{\left(\frac{2303.3}{T}\right)} + 11.98555 \quad \text{(Eqn. 4.7)}$$

$$\log_{10} \rho_a = 25.65278 - 0.371201 C_{SO3} - \frac{4334.515}{T} - 0.03E \quad \text{(Eqn. 4.8)}$$

$$\frac{1}{\rho_{vs}} = \frac{1}{\rho_v} + \frac{1}{\rho_s} \quad \text{(Eqn. 4.9)}$$

$$\frac{1}{\rho_{vsa}} = \frac{1}{\rho_{vs}} + \frac{1}{\rho_a} \quad \text{(Eqn. 4.10)}$$

Where A_{ls} is the atomic concentration of lithium and sodium, A_I is the atomic concentration of iron, and A_{mc} is the atomic concentration of magnesium and calcium. E is electric field intensity in units of kV/cm, T is temperature in K, C_w is water concentration in %, and C_{SO3} is SO_3 concentration in ppm. The Al and Si content, while typically high in coal ashes, was presumably ignored simply because a low content of the minor elements could be assumed to correspond to a high Al and Si content, and vice-versa: therefore, minor element content alone is sufficient to produce a prediction.

The coefficients used in equations 4.6-4.10 are the result of the normalisation calculations discussed earlier in equations 4.2-4.5: the term "-1.8916 logA_{ls}" in Equation 4.6 for instance is the gradient found when plotting resistivity values (normalised to 1.0% iron and 2.5% combined magnesium and calcium concentrations) against combined lithium plus sodium concentration within the ash. 35 coal fly ashes were subjected to resistivity experiments. A wide range of CaO was present in the samples (0.3% - 32.2%), as well as MgO (0.8% - 8.9%): a wide enough range to cover the biomass samples used in this study, although only a few coal ashes contained more CaO than the WWA sample. K_2O (0.2% - 4.4%) and P_2O_5 (0.1% - 1.2%) concentrations within the Bickelhaupt study are far from sufficient for the biomass within this study, in particular OCA (32.3% and 5.0%, respectively).

4.2.2.4.2 - Chandra Model

Chandra [173] produced a modified version of the Bickelhaupt model for use with Indian coals. In this case, the coefficients from equations 4.5 and 4.6 are altered, and the correction for the effects of SO_3 (equations 4.7 and 4.10) ignored due to low SO_3 content in the coals analysed.

$$\log_{10}\rho_v = -3.6695\log_{10}A_{ls} - 2.1861\log_{10}A_i + 2.5514\log_{10}A_{mc} - 0.05885E + \frac{3394.117}{T} + 1.4613 \quad \text{(Eqn. 4.8)}$$

$$\log_{10}\rho_s = -2.6756\log_{10}A_{ls} - 0.02493C_w - 0.08438E - 0.002169C_w e^{\left(\frac{1870.1284}{T}\right)} + 11.7254 \quad \text{(Eqn. 4.9)}$$

$$\frac{1}{\rho_{vs}} = \frac{1}{\rho_v} + \frac{1}{\rho_s} \quad \text{(Eqn. 4.10)}$$

The Chandra model was specifically developed for Indian coals, which according to the authors do not contain enough sulphur to induce surface conductivity. In addition, the Chandra study appears to have only used 20 fly ash samples from Indian coal power stations in the development of the model, significantly less than the Bickelhaupt model. The full range of compositions used within the study are also not given, and so the applicability of the model is unknown. Of the typical coal compositions presented, the variation in oxide concentration is significantly less than those within the Bickelhaupt study. CaO content of typical samples was less than 3%, with a K_2O content of less than 1.5% and P_2O_5 typically below 0.2%, indicating that the model has extremely limited use. Such little variation suggests that the study was conducted exclusively on a subset of coals, possibly bituminous, however this is not stated within the paper.

4.2.2.4.3 - Li Maximum Resistivity Model

A third model for predicting the resistivity of coal ashes was devised by Li et al [174]. The equations are derived empirically from a database of 120 Chinese coal fly ashes, with two main steps: a sensitivity analysis on the ash composition, followed by normalisation based on the maximum value and ash compositions.

Based upon the relationship between ash content and maximum resistivity, a negative linear dependence was found for lithium plus sodium, with a slight positive correlation for aluminium content. The remaining components were found to have no correlation with maximum resistivity. As a result, the authors isolated the relationship for resistivity with lithium and sodium content, resulting in the following approximation equation:

$$\log_{10} \rho_{max} = -1.210 \log_{10} A_{ls} + \beta \qquad \text{(Eqn. 4.11)}$$

Where A_{ls} is the atomic percentage of lithium plus sodium, ρ_{max} is the maximum resistivity and β is a factor dependent upon ash properties.

As the lithium and sodium were considered to affect the resistivity significantly in comparison to the remaining components, the average value of lithium plus sodium atomic content is used to normalise the remaining compounds, to assess their effect. Thus, using the following equation to find normalised resistivity (ρ_N):

$$\log_{10} \rho_N = -1.210 \log_{10} (0.4) + \beta \qquad \text{(Eqn. 4.12)}$$

And substituting equation 1 for β, results in an equation of the following form:

$$\log_{10} \rho_N = \log_{10} \rho_{max} + 1.210 \log_{10} A_{ls} + 0.48151 \qquad \text{(Eqn. 4.13)}$$

Using this equation, the authors found that the normalised resistivity showed no relationship with resistivity for aluminium, potassium, magnesium plus calcium and sulphur concentration. A relationship was found with iron content however, resulting in the following equation for β:

$$\beta = -0.782 \log_{10} A_i + \gamma \qquad \text{(Eqn. 4.14)}$$

Where γ is a coefficient related to water content. This gives the final form of the equation for predicting maximum ash resistivity:

$$\log_{10} \rho_{max} = -1.210 \log_{10} A_{ls} - 0.782 \log_{10} A_i + \gamma \qquad \text{(Eqn. 4.15)}$$

For the purposes of this work, the water concentration term has been ignored since peak resistivity for the samples in Chapter X.3 all occur at temperatures of 100°C or more. For reference, γ was derived as:

$$\gamma = 12.1 - 0.122 C_w \qquad \text{(Eqn. 4.16)}$$

Where C_w is water concentration in percent.

4.3 - Experimental Methodology

4.3.1 - Samples

Resistivity experiments focused solely on the biomass-coal PFA blends in Table 4.2, with ashes prepared according to the methods outlined in Chapter 3.

Table 4.2 - Test matrix of samples used in resistivity experiments

Wt% Adtv to dry fuel	0%	5% (PFA)	15% (PFA)	25% (PFA)	5% (Kao)	15% (Kao)	25% (Kao)
OCA	X	X	X	X			
WWA	X	X	X	X			
BA	X	X	X	X			
FA	X	X	X	X			
PFA	X						
Kaolin							

4.3.2 - Methodology

The ash resistivity testing equipment was based upon the guidelines set out under IEEE standard STD 548-1984 “Standard Criteria and Guidelines for the Laboratory Measurement and Reporting of Fly Ash Resistivity” [175]. Before testing, the prepared ashes were passed through a 177µm sieve, to remove foreign objects and debris. The test cell consists of a weighted upper electrode, and a flat dish with a 5mm depth that doubles as the lower electrode, as displayed in Figure 4.4. The sample was poured into the test cell until overflowing, at which point a straight-edge was used to strike the ash level with the upper edge of the dish, in such a way that the ash was not significantly compacted. The dish was then agitated to determine whether any further settling occured: if so, additional ash was added, and the process repeated.

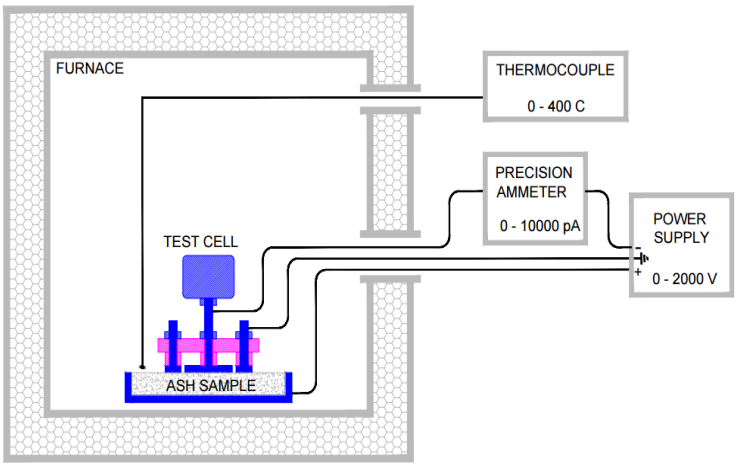

Figure 4.4 - Schematic of the ash resistivity testing equipment used in this study

Once the dish was filled and settled, the dish was placed inside a furnace and connected to a variable 2kV power supply, to allow for the measurement of ash resistivity over a range of temperatures. The weighted upper electrode, which is in turn connected to a Keithley high-precision picoammeter (Model no. 6485), was carefully placed on the sample, so as to not compact the sample too much, and the furnace door shut.

The resistivity of each ash sample was measured under two sets of conditions. First, measurements were taken using an increasing temperature profile. The sample was heated to 80°C for a minimum of 90 minutes. An initial 200V voltage was applied to the sample, and the current through the sample recorded by the picoammeter. The voltage was then increased in increments of 200V, up to a maximum of 2kV, with the current recorded at each step. The temperature was increased to 100°C, and left for a minimum of 30 minutes. This was repeated at 120°C, 140°C, 150°C, 160°C, 180° and 210°C. The standard recommends larger temperature intervals of 30°C, from 95°C to 215°C: however, more precise temperature intervals were chosen, with smaller intervals near to ESP working temperatures of approximately 150°C [153]. The resistivity can be determined for each temperature using Ohm's law and the following equation for resistivity, ρ:

$$\rho = \frac{R * A}{d} \qquad \text{(Eqn. 4.17)}$$

Where R is resistance (calculated from the average readings for current at each voltage increment), d is the depth of the bottom electrode/dish, and A is the surface area covered by the top electrode.

The initial residence time of 90 minutes, and subsequent residence times of 30 minutes for increasing temperature measurements, were determined to be the minimum time for the internal temperature of an ash sample to reach within 1°C of the temperature within the furnace. In order to determine this, ash samples were prepared in a similar fashion, and subjected to the same heating rates, with a thermocouple inserted into the sample, the results of which are shown in Figure 4.5.

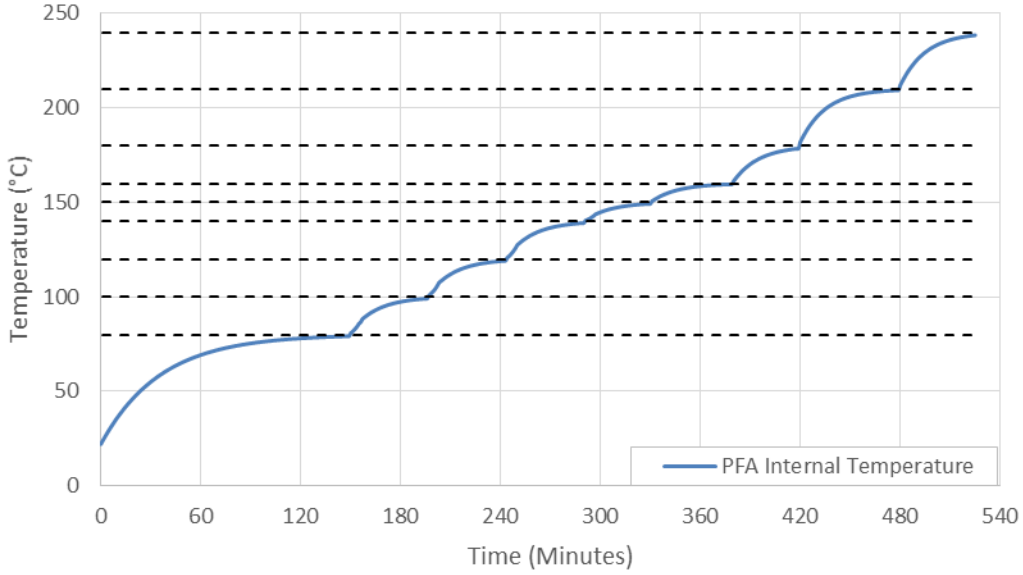

Figure 4.5 - Internal temperature measurements over time for coal PFA with increasing furnace set temperature. Temperatures used for experiments are indicated by dotted horizontal lines

Once a full set of measurements was taken, the furnace temperature was increased to 480°C and left overnight. The following morning, the furnace was turned off and allowed to cool. At the same temperature intervals as previously conducted, a voltage was applied to the sample in the same method as previously described. Initial temperature tests using the thermocouple while cooling indicated that sample insulation has a negligible effect on the internal cooling rate when compared to the furnace and, at temperatures of 240°C and below, the difference between furnace temperature and internal sample temperature was negligible. An example of this is shown in Figure 4.6.

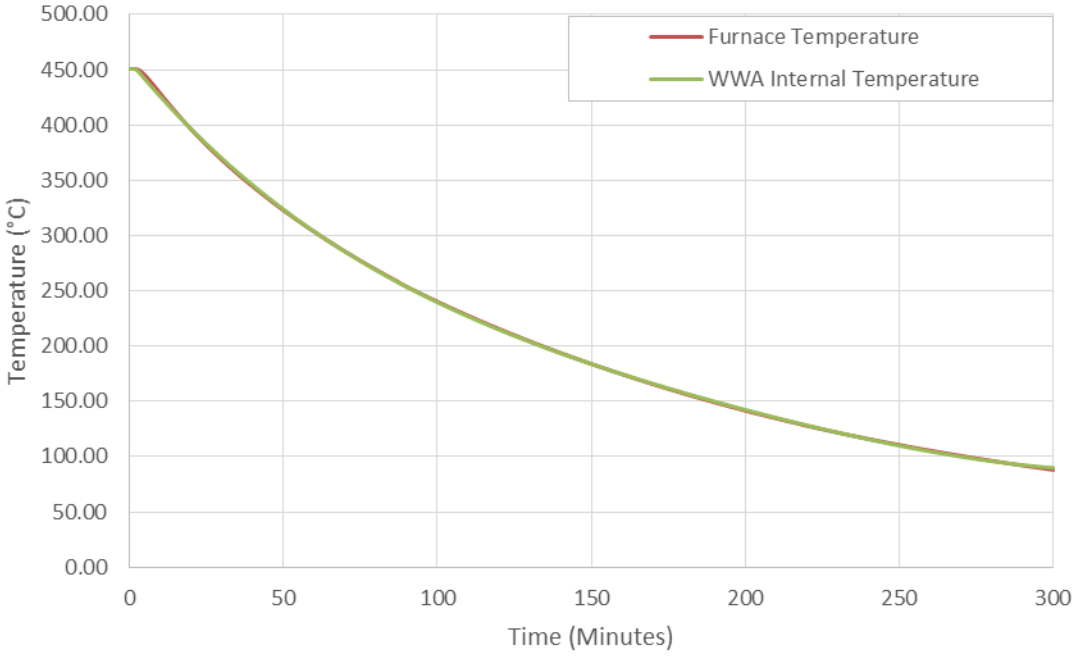

Figure 4.6 - Comparison of furnace temperature and internal sample temperature for WWA during cooling

In accordance with the recommendations of the standard, the results reported in the following sections are the highest resistivity values [157].

4.4 - Resistivity Results

Resistivity - temperature relationships are presented in Figure 4.7 for all samples tested. In contrast to previous coal ash studies, where peak resistivities are asserted to occur between 140-160°C [174], higher potassium biomass such as OCA (Figure 4.7a) and WWA (Figure 4.7b) showed peak resistivities at closer to 100°C. Results for OCA and PFA ash blends (Figure 4.7a) indicated that, at typical cool-end ESP working temperatures of approximately 150°C, increased concentration of PFA results in higher resistivities. The resistivity of OCA produced the lowest resistivity at 150°C of all samples measured within the experiment, and significantly lower than coal PFA. Despite the OCA samples containing the highest SO_3 concentration within the ash (2.4%) the OCA results showed few surface resistivity effects at temperatures approaching 100°C.

With the addition of coal PFA, decreasing resistivity values are observed as temperatures fall below 120°C, indicating that surface conductivity effects are present. While potassium has been postulated to act as a charge carrier, multiple

studies have found no correlation between potassium and resistivity [154, 163, 173, 174]. The results of Figure 5.7a seem to verify this: 100% OCA contains the greatest potassium content of any sample, yet displays little surface conductivity; i.e. a peak resistivity occurring at low temperatures, indicating that potassium may not inherently induce surface conductivity.

Therefore, the decreasing resistivity at lower temperature observed with PFA addition may be due to the influence of iron concentration, which is present within the PFA (9.3%) at higher quantities compared to OCA (0.9%). Iron in the presence of alkali compounds has been shown to promote conductivity by influencing the release of alkali ions. An increase in iron content results in increased ion release from alkali metals in water during transference experiments [162]. OCA contains significant concentrations of potassium (32.3%), which is generally found to agglomerate upon the surface of ash particles. It is this combination of increased iron content in the presence of potassium which is postulated to result in the decreased resistivities displayed by the OCA-PFA blends at lower temperatures. As PFA concentration increases, the relative concentration of potassium within the sample decreases, in turn reducing the number of ions available and leading to an increase in resistivity at higher concentrations, as shown by the resistivity profile for the 25% PFA/75% OCA sample. However, surface conductivity effects remain visible within the sample, despite increased resistivities.

Additionally, both WWA (Figure 4.7b) and particularly BA (Figure 4.7c) show signs of surface conductivity at lower temperatures: both samples contain relatively high concentrations of potassium (9.2% and 3.7% respectively), and greater iron content (2.3% and 3.0% respectively) than the OCA. In contrast, for the PFA, FA, FA/PFA blends, and WWA/PFA blends (which contain a minimum of 80% coal PFA concentration), no decrease in resistivity with decreasing temperature is observed. This again implies negligible surface conductivity effects. This suggests that the relationship between iron and potassium content is a key factor in affecting resistivity in biomass ash samples.

WWA (Figure 4.7b) produced a peak resistivity of approximately twice that of OCA (1.23×10^9 Ωm vs 6.53×10^8 Ωm, respectively), and both peaks occur at similar temperatures of approximately 100°C. In contrast to OCA, WWA

displayed a sharp peak resistivity at approximately 120°C, with a significant decline at lower temperatures. This indicates that surface conductivity is occurring, likely due to the increased concentration of sodium (1.5%) and iron (2.3%) in comparison to OCA. Although OCA contains a much greater concentration of potassium (32.3% compared to 9.2% in WWA), sodium ions have been shown to be significantly more mobile than those of potassium [154], while the effects of iron concentration with potassium have been discussed previously. As with OCA, WWA has much lower resistivities at ESP working temperatures than coal PFA.

The addition of coal PFA increased resistivities as expected, due to the increase in silica and alumina content. Due to the low ash content of white wood (1.2%), the addition of 5% PFA to white wood pellets results in an ash that contains over 80% coal PFA, resulting in a similar resistivity profile for all WWA/PFA blends when compared with pure coal PFA.

In contrast to the other biomass ashes, the BA sample (Figure 4.7c) showed a peak resistivity at a much higher temperature (~160°C) when compared to the OCA and WWA samples (~100°C). In addition, the BA sample has a peak resistivity of greater than both of the aforementioned samples, and appears to retain a relatively high resistivity over a wide temperature range: for instance, BA resistivity decreases by only $2x10^7$ Ωm between 150 and 180°C, compared to a decrease of $1.15x10^8$ Ωm and $1.46\ x10^8$ Ωm over the same temperature range, for the OCA and WWA samples respectively. The BA samples contain high SiO_2 concentration at approximately 50%, second only to the PFA, and also contain the lowest Na_2O concentration of all samples, at 0.2%.

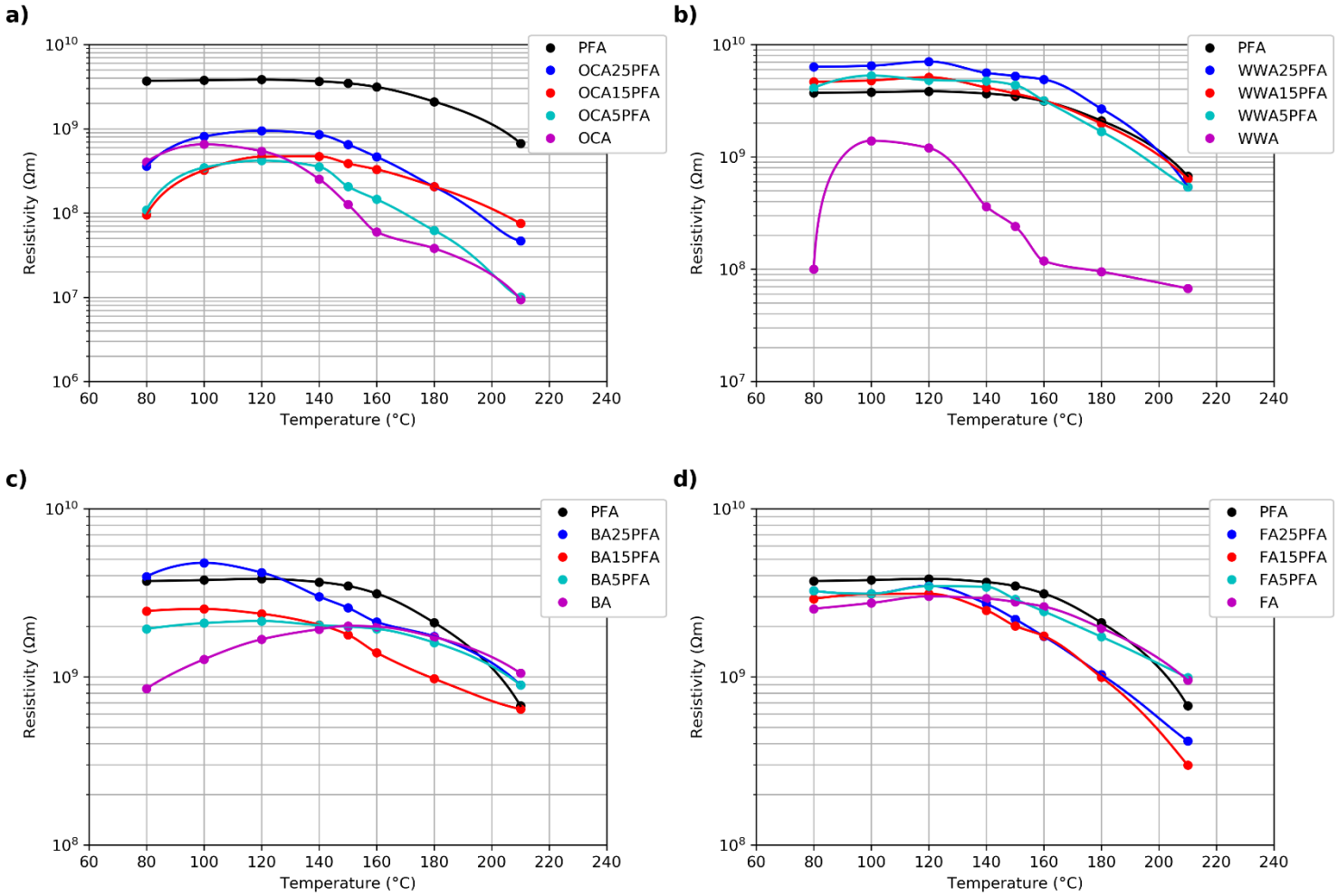

Figure 4.7 - Resistivity of (a) olive cake ash (OCA), (b) white wood pellet ash (WWA), (c) bagasse ash (BA), and (d) power station fly ash (FA) blended with a coal PFA additive at different percentages, on a logarithmic scale

Ash characterisation showed that the power station fly ash (FA) contained silica and alumina concentrations of 48.8% and 19.1% respectively, and as a result high resistivities were recorded. The greater concentration of alkali compounds within FA compared to coal PFA can explain the lower resistivities (Figure 4.7d) at lower temperatures, although the results between the two samples were within the recommended experimental error for a single sample, at less than a factor of 2.7. Therefore, the addition of PFA to FA resulted in relatively little difference when compared to the resistivity of pure FA. The results of PFA blending at various temperatures of interest are summarised in Figure 4.8.

The resistivity results for each sample and blend tested are compared at normal ESP operating temperatures of 150°C (Fig. 4.8b), as defined by Bäck [153]. OCA and WWA, which contain low silica and high alkali metal concentration compared to the other samples, are more significantly affected by the addition of coal PFA during combustion. This effect is increased at higher temperatures (Figure 4.8c). BA, which contains a high silica content, experiences a minimal increase with increasing coal PFA concentration at the temperatures examined in Figures 4.8 a and b, while in Figure 4.8c no increase is observed. At lower temperatures (~80°C), a greater influence from PFA addition is visible, although this is likely to be outside the operating conditions for most power station ESPs. The FA blends experience little to no change with increasing additive concentration, due to the already high silica and alumina content within the ash.

Although Li et al. and Bickelhaupt report that resistivity is expected to peak at approximately 140-160°C [163, 174], the results for both OCA and WWA in Figure 4.8a show an increase in resistivity at 120°C when compared to Figure 4.8b. A significant observation is noted regarding the OCA results at this temperature: in this case, an increase in concentration of coal PFA appears to result in a slight decrease in resistivities, up to a 65% coal PFA concentration. This is possibly due to surface resistivity effects resulting from the presence of sufficient quantities of iron and potassium.

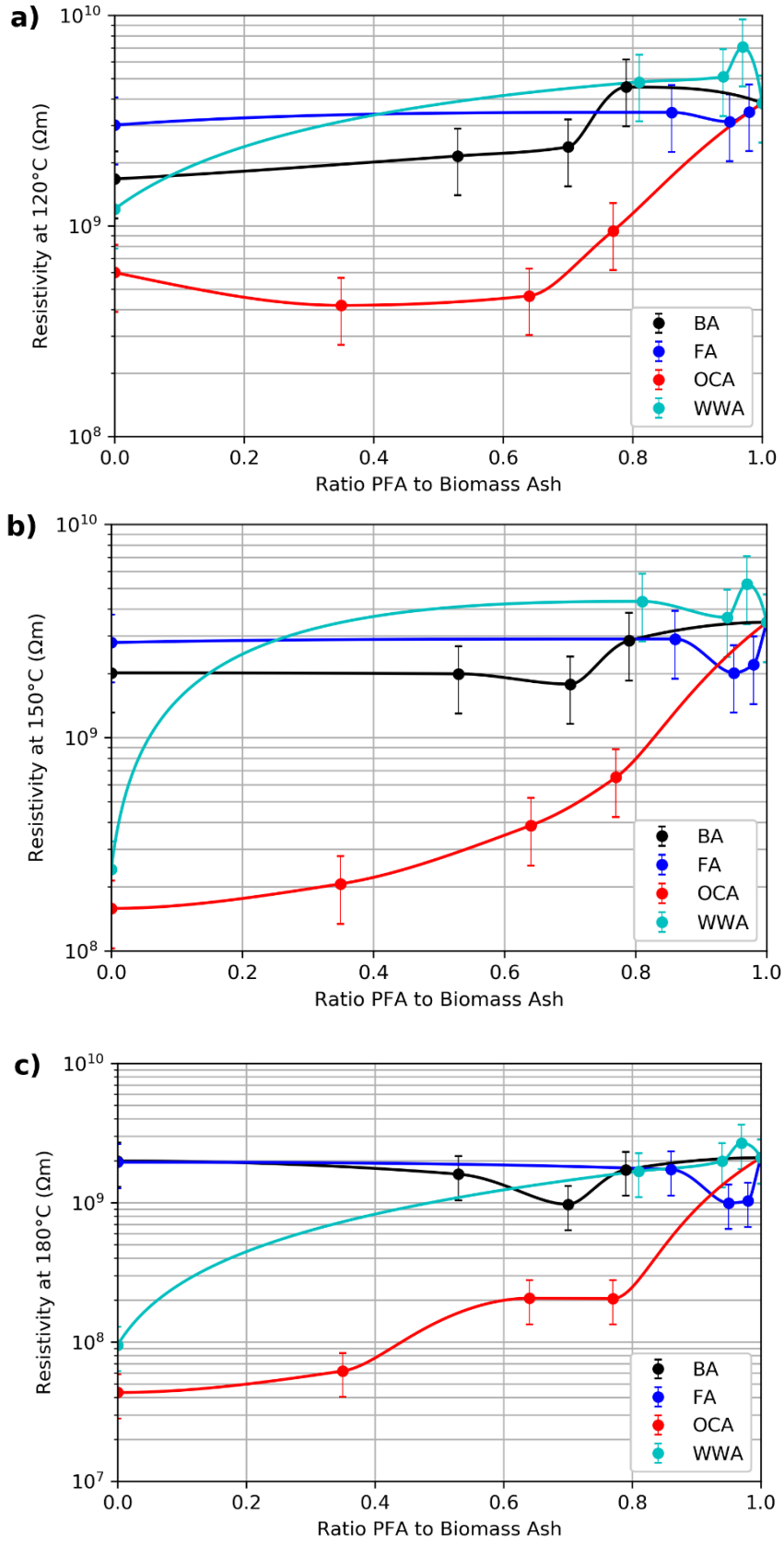

Figure 4.8 - Comparison of resistivity results (log scale) at (a) 120°C, (b) 150°C and (c) 180°C with increasing additive concentration

4.4.1 - Discussion

There are a number of considerations for ESP collection efficiency, namely particle composition and resistivity, gaseous environment, carbon-in-ash, particle density and particles size. Results indicate that some biomass fuels may be troublesome for ESP collection efficiency, and hence emissions. The resistivity of OCA and WWA is low enough that, with the addition of moisture and gaseous SO_3 from combustion, resistivities may be reduced to levels comparable or below the minimum recommendation for ESPs, given in literature as being as high as $1x10^6$ Ωm [148]. The effects of moisture and sulphur on resistivity are shown in Figures 4.9a and b, respectively.

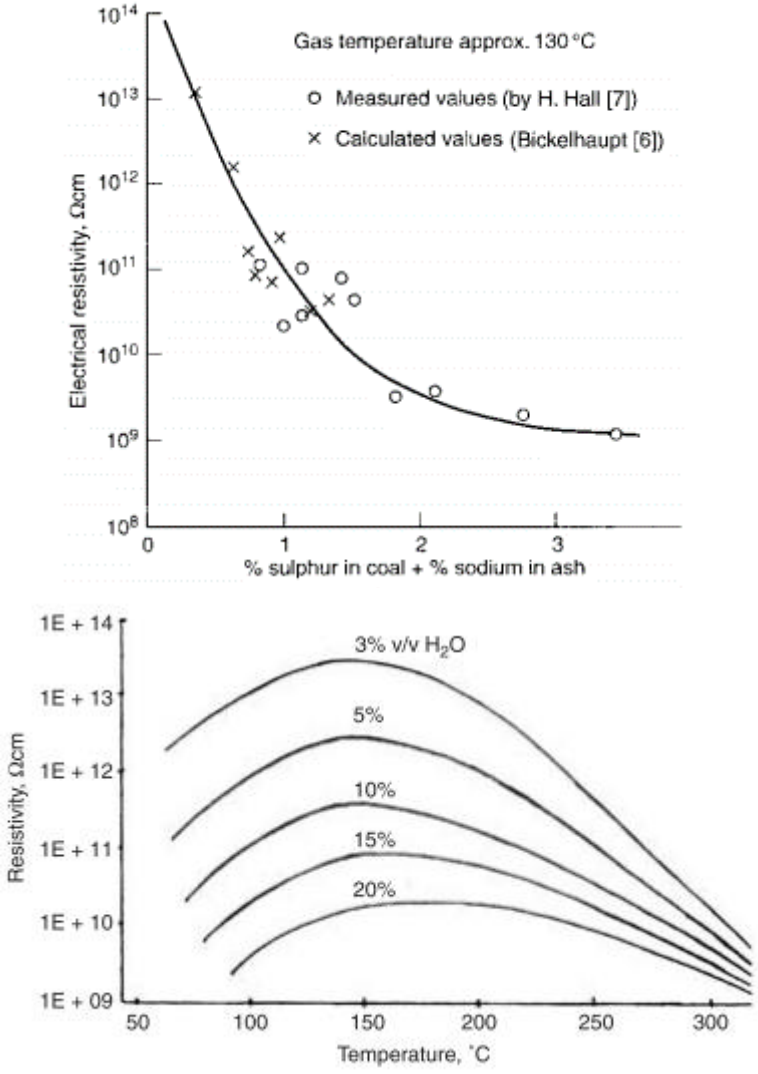

Figure 4.9 - The relationship between resistivity and a) sulphur content in coal, and b) moisture content [148]

Another issue arises from the combustion characteristics of the biomass fuel, which may further reduce resistivity: LOI of white wood collected from grate combustion has been shown to be as high as 72% under high loading

conditions [171]. This translates to a high carbon content, posing fire risks and increasing conductivity and the potential for sparkover [148]. Olive cake would be expected to have a higher LOI, due to the high ash and lower carbon content of the fuel which will likely impact combustion properties. The BA sample in particular was found to be of a low density (191 kg/m^3, compared to 791 kg/m^3 for coal PFA), which may raise issues with mechanical rapping of the ESP collection electrodes. Finally, the high potassium content of such biofuels may result in the production of a greater number of fine particles, since the potassium has been shown to be present in volatile form [171], which are inherently more difficult to collect through ESP use.

The use of an additive will increase the resistivity of the ash and as such will reduce the risk of operational issues. In addition, the additive will bind potassium in the form of high melting temperature potassium aluminium silicates [98], reducing the production of fine particles due to the volatilisation and condensation of alkali species. This would be expected to improve collection efficiency through the ESP.

Conversely, the use of an additive may increase LOI during combustion, increasing the quantity of low resistivity unburned particles, while the quantity of incombustible material within the boiler will be increased, leading to a greater load on the boiler, which may be exacerbated if a high fuel feed rate is required to offset any reduction in combustion temperature or LOI.

As a result, the effect of additive use on potential emissions is dependent upon the specifications and capabilities of the boiler and ESP system. A suitably large ESP, designed to effectively collect dust from high ash coal firing, would likely be capable of coping with a biomass-additive blend and will operate at effective collection efficiencies, while a lower flue gas velocity may be used to reduce LOI. Therefore, the use of additives to mitigate slagging and fouling in large scale biomass combustion should not negatively impact emissions, although some minor operational changes may be required to maintain high ESP collection efficiencies.

4.4.2 - Resistivity and Ash Composition Regression Analysis

To determine the effect of specific components within the ash on reistivity, correlations of resistivity at three different recorded temperatures of 120°C, 150°C and 180°C were computed for a number of key ash components, which are shown in Table 4.3. Typically, elemental atomic concentration is used for such correlations as recommended by Bickelhaupt [163], rather than oxide concentration. This is because lithium and sodium ions have been shown to act as principal charge carriers, functioning as mobile ions rather than oxide molecules [163]: the number of mobile ions is proportional to the atomic concentration of the element within the sample. Correlations for Mg+Ca and K+Fe were also calculated due to the recommendations of Bickelhaupt, who recommended that resistivity models should take Mg + Ca into account [163] , while K+Fe was reported to play a minor role in surface conductivity [154] through the promotion of ion release from alkali metals. K+Na+Fe was also correlated for this reason. The correlations were calculated using the Pearson correlation coefficient (r).

A negative correlation is observed between combined Mg+Ca concentration and resistivity, with a fairly strong correlation developing between 140°C and 180°C. Previous experiments, most notably by Bickelhaupt in the development of the Bickelhaupt resistivity model [163], found a positive correlation between Mg+Ca concentration and resistivity in coal ashes. This indicates that other components are more dominant in determining resistivity for the wider sample compositions (particularly increased potassium and lower silica/alumina content) found within this study. K+Fe results in a strong negative correlation with resistivity, similar to yet stronger than that observed by Bickelhaupt, although notably K concentration alone produces a stronger correlation than when combined with Fe concentration.

Table 4.3 - Correlations between resistivity and atomic concentration of various ash components, at different temperatures

Ash Component	Temperature °C							
	80	100	120	140	150	160	180	210
Si	0.598	0.546	0.641	0.789	0.826	0.860	0.846	0.816
Al	0.583	0.533	0.620	0.756	0.771	0.797	0.744	0.665
Fe	0.599	0.535	0.614	0.742	0.748	0.769	0.706	0.609
Ca	-0.668	-0.484	-0.554	-0.700	-0.711	-0.743	-0.721	-0.650
Ti	0.621	0.573	0.657	0.786	0.800	0.823	0.775	0.700
Mg	-0.745	-0.597	-0.669	-0.804	-0.811	-0.835	-0.802	-0.720
Na	0.240	0.322	0.300	0.227	0.184	0.151	0.080	-0.003
K	-0.847	-0.866	-0.902	-0.909	-0.910	-0.899	-0.900	-0.879
Mn	-0.307	0.003	-0.050	-0.243	-0.240	-0.291	-0.259	-0.167
P	-0.844	-0.846	-0.882	-0.881	-0.865	-0.849	-0.825	-0.766
S	0.036	-0.315	-0.282	-0.085	-0.104	-0.063	-0.122	-0.264
K+Na	-0.784	-0.809	-0.859	-0.893	-0.914	-0.914	-0.932	-0.944
Mg+Ca	-0.688	-0.508	-0.579	-0.726	-0.735	-0.766	-0.740	-0.663
K+Fe	-0.786	-0.833	-0.877	-0.893	-0.909	-0.903	-0.917	-0.925
K+Na+Fe	-0.718	-0.765	-0.818	-0.853	-0.884	-0.886	-0.914	-0.945

Li et al [174] determined that, after normalising for Li+Na, only Fe showed an inverse relationship with normalised resistivity for coal ashes: Al, K, Ca+Mg, and S were determined to have no correlation. However, these results are not as useful, as the study is extremely limited in that it only considers the maximum resistivity regardless of temperature, whereas in reality significant temperature differences may be observed. While it may be possible to simplify maximum resistivity predictions to only two components of the ash, this gives no further information, and is likely the result of correlations between ash components, rather than those two components having a more significant effect.

Although phosphorus shows an extremely strong negative correlation with resistivity across the three temperatures, and titanium has a positive correlation initial ash composition correlations (Chapter 3, Figure 3.2) show that P and K concentration within the samples are strongly correlated, as is titanium concentration with Si, Al and Fe. As a result, any increase in resistivity with an increase in titanium is most likely due to the corresponding increase in Si, Al and Fe, rather than any significant effect from Ti. This also explains the positive sodium correlations seen in this study, in contrast with the strong negative correlations seen in most other studies: potassium and sodium concentration in the samples studied share an inverse relationship, while sodium is positively correlated with Si, Al and Fe content. Therefore, these correlations do not indicate that sodium increases resistivity, only that Na concentration increases with other components that serve to increase resistivity.

Correlations for sodium, iron, combined magnesium and calcium, and combined potassium and iron, at 120°C, 150°C and 180°C, are shown in Figures 4.10-4.13. These figures correspond to the elemental correlations used in the Bickelhaupt and Chandra models.

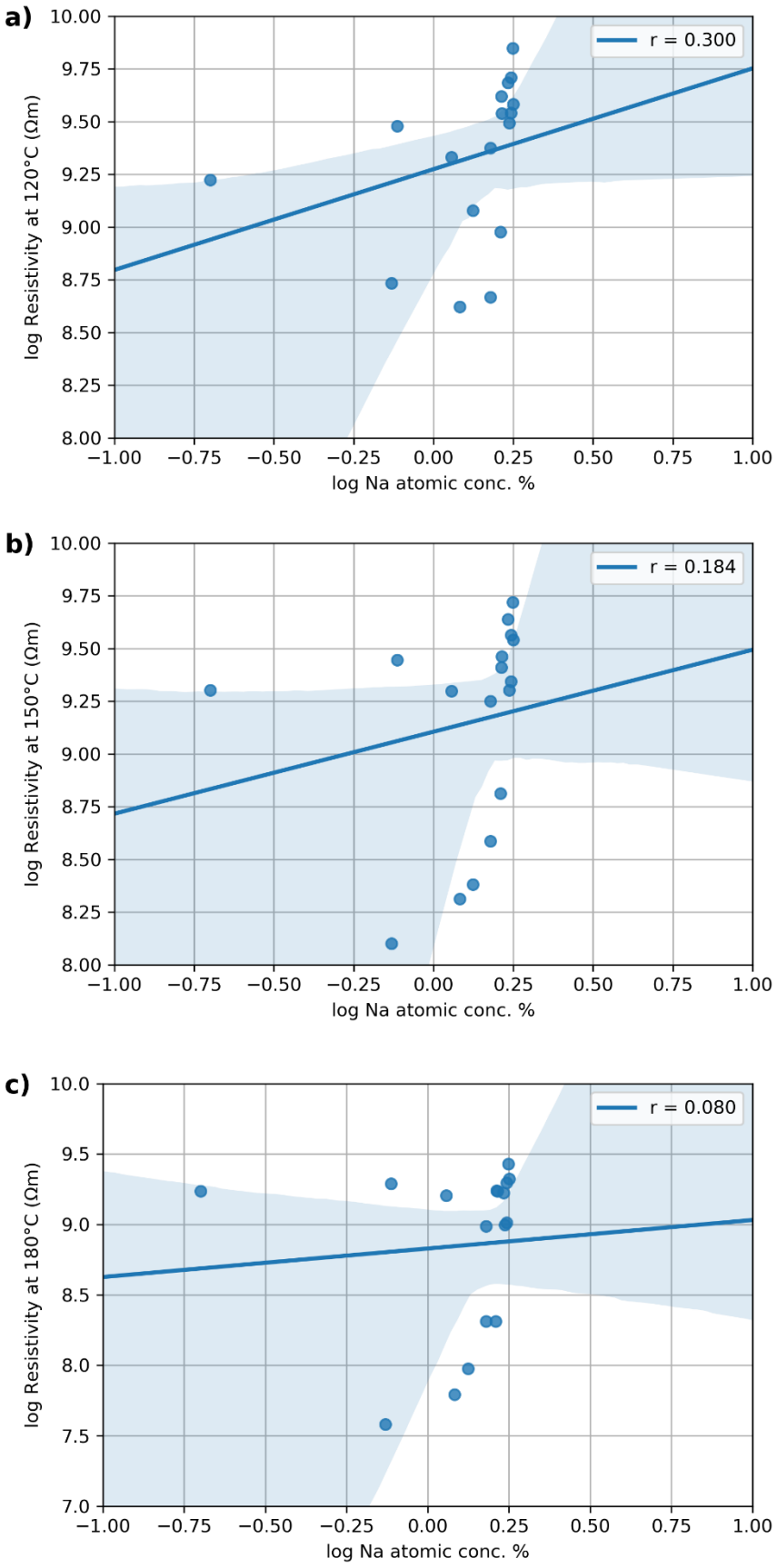

Figure 4.10 - Resistivity vs atomic concentration for sodium at a) 120°C, b) 150°C and c) 180°C

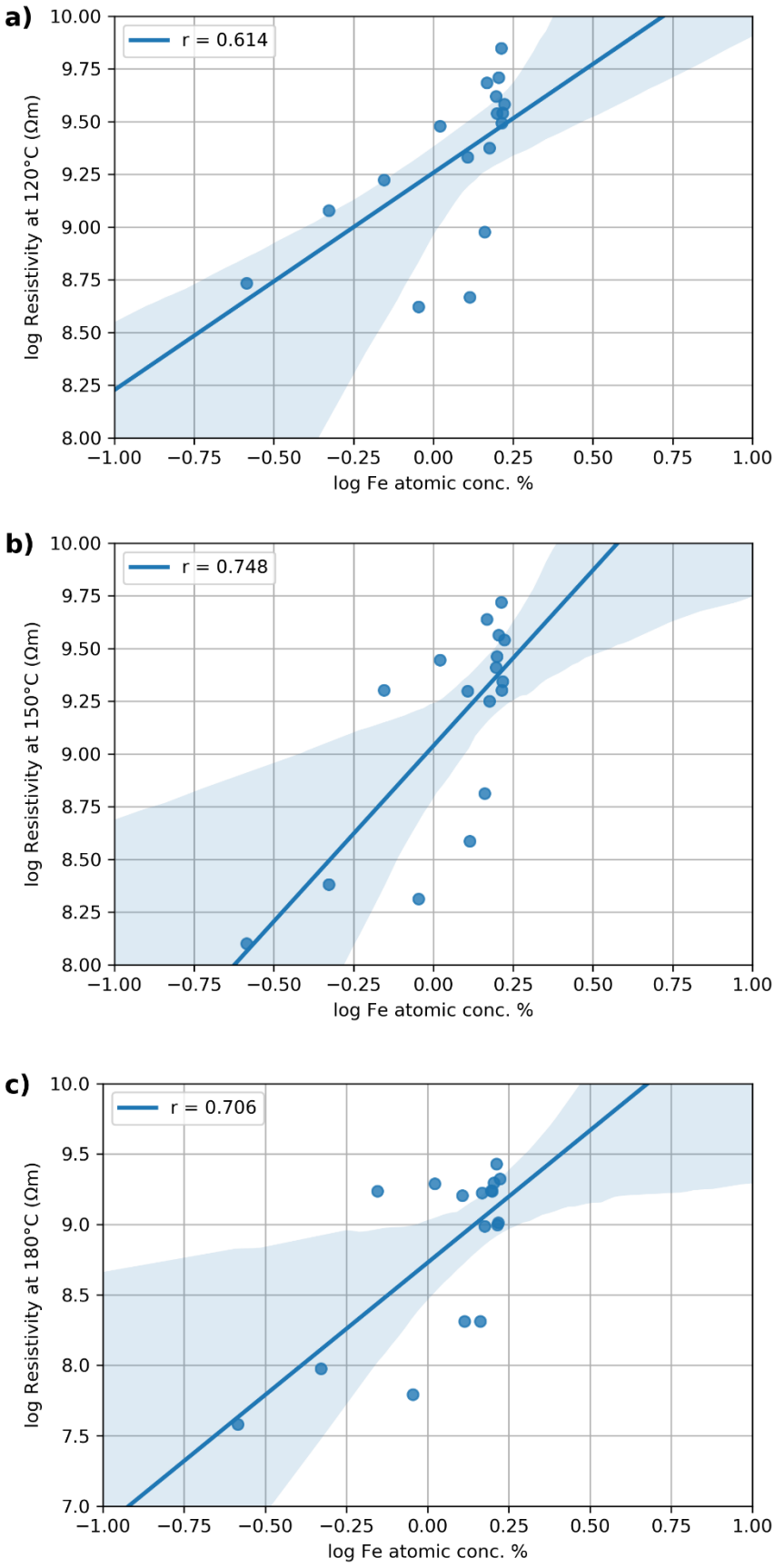

Figure 4.11 - Effect of Potassium Concentration upon Resistivity vs atomic concentration for iron at a) 120°C, b) 150°C and c) 180°C

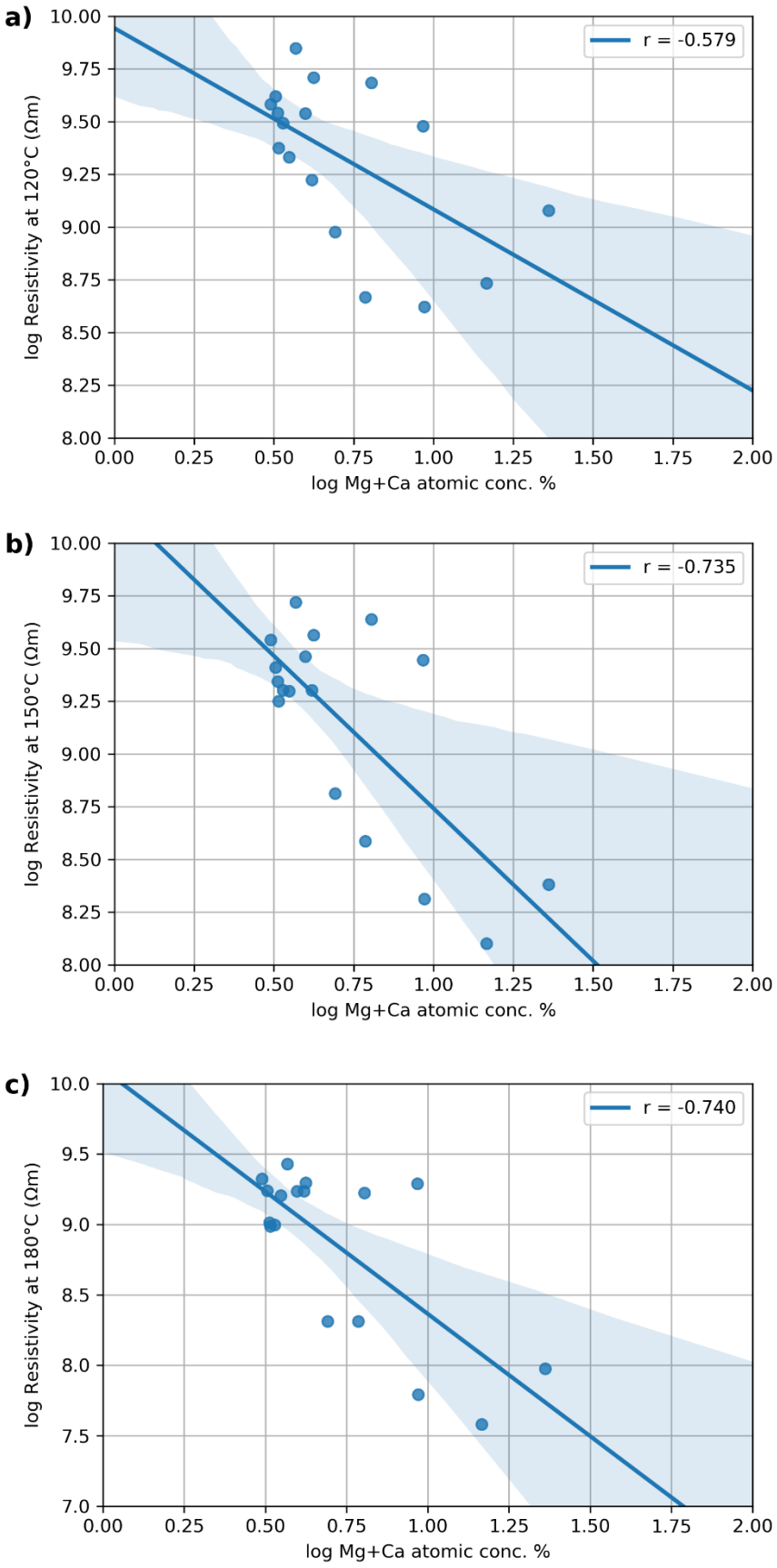

Figure 4.12 - Resistivity vs atomic concentration for combined magnesium and calcium concentration at a) 120°C, b) 150°C and c) 180°C

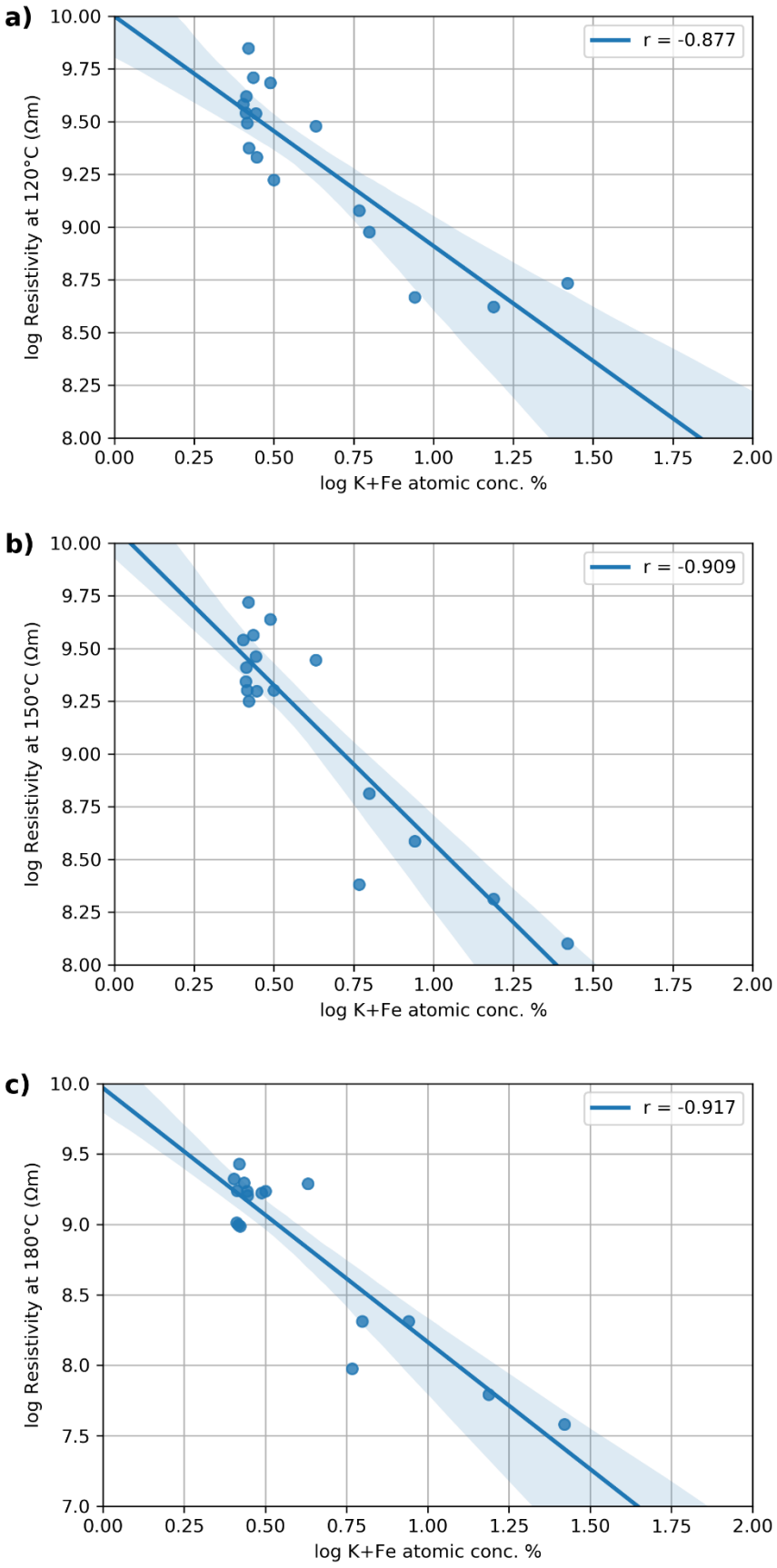

Figure 4.13 - Resistivity vs atomic concentration for combined potassium and iron concentration at a) 120°C, b) 150°C and c) 180°C

4.4.3 - Effect of Potassium Concentration upon Resistivity

The effect of potassium concentration upon resistivity is particularly pertinent to this study, as the K contents of the biomass used in the experiments are greater than those encountered in previous studies on resistivity, particularly those focused on coal ash compositions. Table 4.3 shows a significant negative correlation between potassium concentration and resistivity across a range of temperatures, in contrast to the studies of Bickelhaupt, Chandra and Li et al, where no correlation was found. These correlations are displayed in Figure 4.14.

The reason for these differences in results is related to the range of potassium concentrations used within the studies, and the fact that biomass typically contains much greater potassium concentrations that those found in coal ash compositions. This is most easily highlighted by least squares fitting of the whole dataset, and then splitting the data into two parts and repeating linear regression analysis: the first was conducted upon samples with less than 3% atomic concentration of potassium (the boundary for most of the coal ash compositions in previous studies), with the second for the remaining samples. The atomic concentration and resistivity show a non-linear Arrhenius relationship of the form:

$$\rho = e^{a}\, x^{b} \qquad \text{(Eqn. 4.18a)}$$

Where x is the atomic concentration of the element in the ash, and ‘a’ and ‘b’ are determined by least squares fitting. To conduct a linear regression, Equation 4.18 is used in logarithmic form:

$$\ln \rho = a + b \ln x \qquad \text{(Eqn. 4.18b)}$$

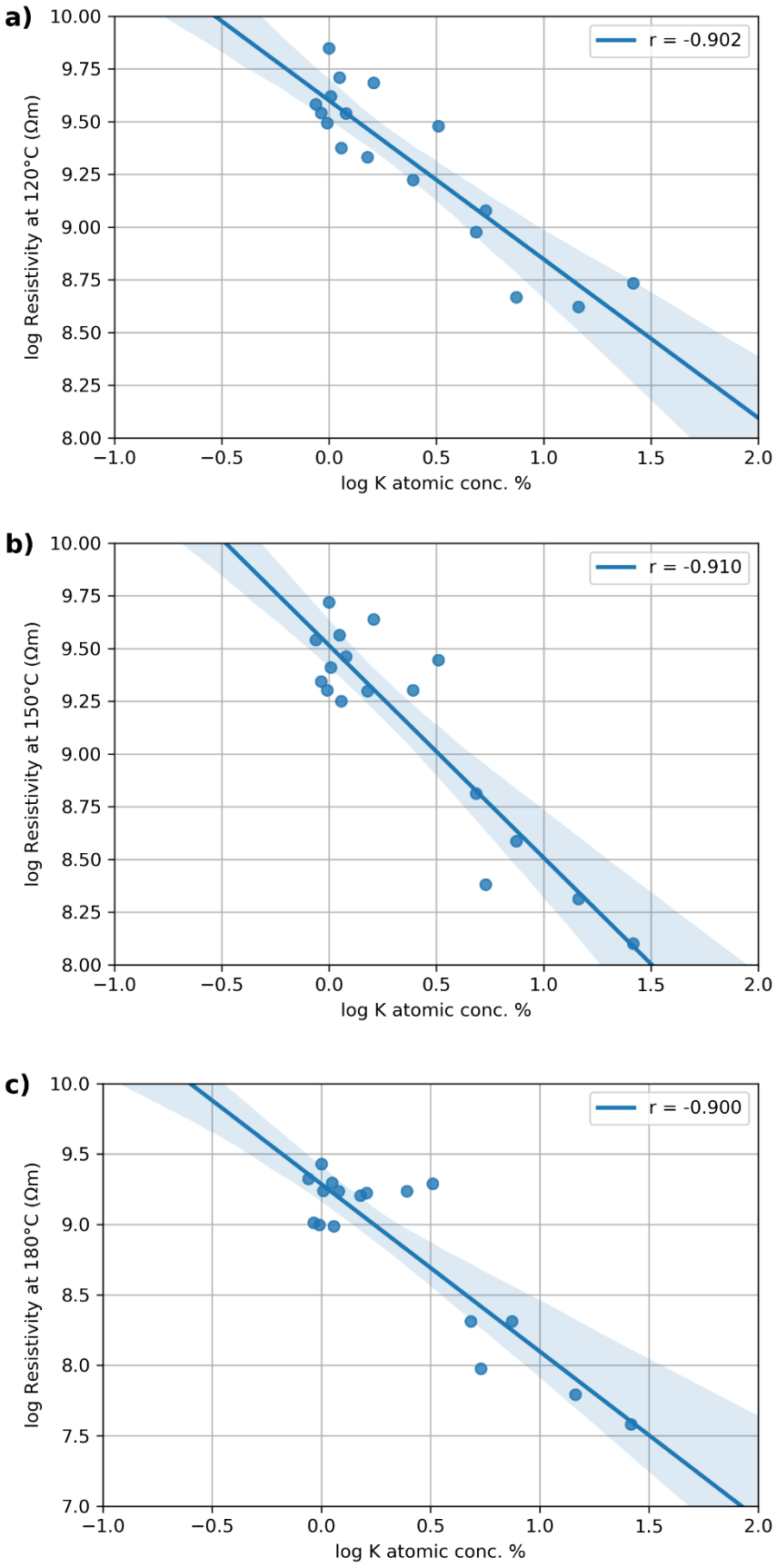

Figure 4.14 - Resistivity vs atomic concentration for potassium concentration at a) 120°C, b) 150°C and c) 180°C

4.4.3.1 - Linear Regression Comparison

The linear regression methodology described above was implemented for temperatures of 120°C, 150°C and 180°C, in order to see the influence of temperature upon correlations around typical ESP working temperatures. The results of these regressions are displayed in Figure 4.15. At temperatures of 120°C (Figure 4.15a), the gradients of the resulting linear regressions vary only slightly, with only a minor change when looking at low and high potassium samples, although the fit is much better when considering high potassium samples.

At higher temperatures, however, a clear difference begins to emerge between the low and high potassium concentration regressions: at 150°C, only a very minor inverse relationship occurs for low potassium concentrations, one that is likely to disappear with an increased sample size based upon larger studies such as those conducted by Bickelhaupt [163] and Li [174], while at 180°C (Figure 5.15c) the regression for low potassium concentration samples shows no correlation between potassium concentration and resistivity, replicating the findings of Bickelhaupt and Li et al. A clear inverse relationship is shown for high potassium samples at both temperatures.

Repeating this process for other ash components continues to show a clear difference in behaviour for samples containing less than and greater than 3% concentration of potassium, indicating that above 3% concentration, potassium becomes the dominant component affecting resistivity. This effect is highlighted for combined magnesium and calcium concentrations in Figure 4.16. Once again, in both cases the resulting Pearson correlation values show greater similarities to the findings of Bickelhaupt [163]. This indicates that the potassium concentration has a significant effect upon resistivity at the concentrations found in this study, any future resistivity model for biomass and biomass-additive ash mixtures must take into account potassium concentration.

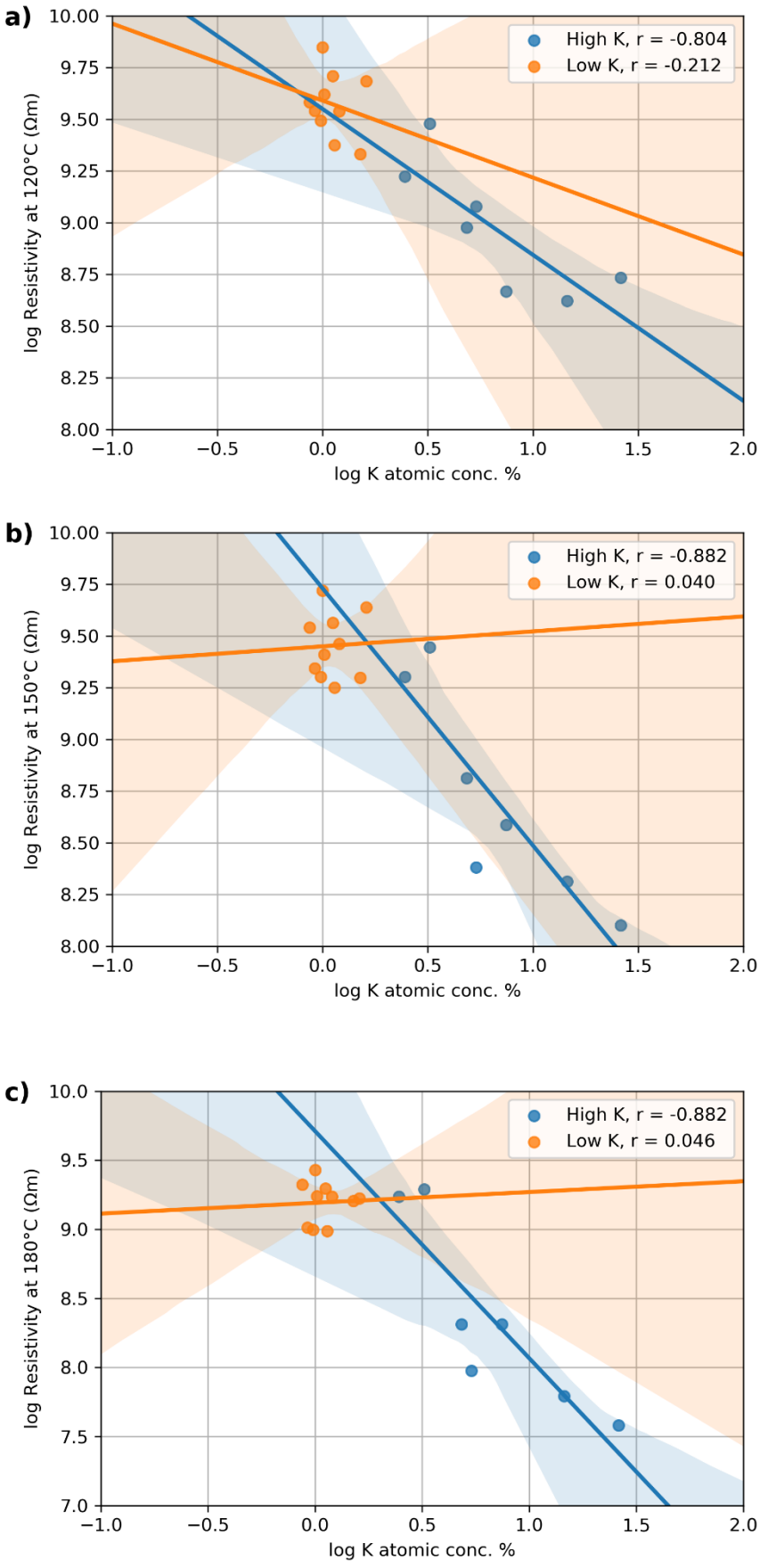

Figure 4.15 - Linear regression analysis for resistivity vs potassium concentration for low and high potassium concentrations at (a) 120°C, (b) 150°C and (c) 180°C

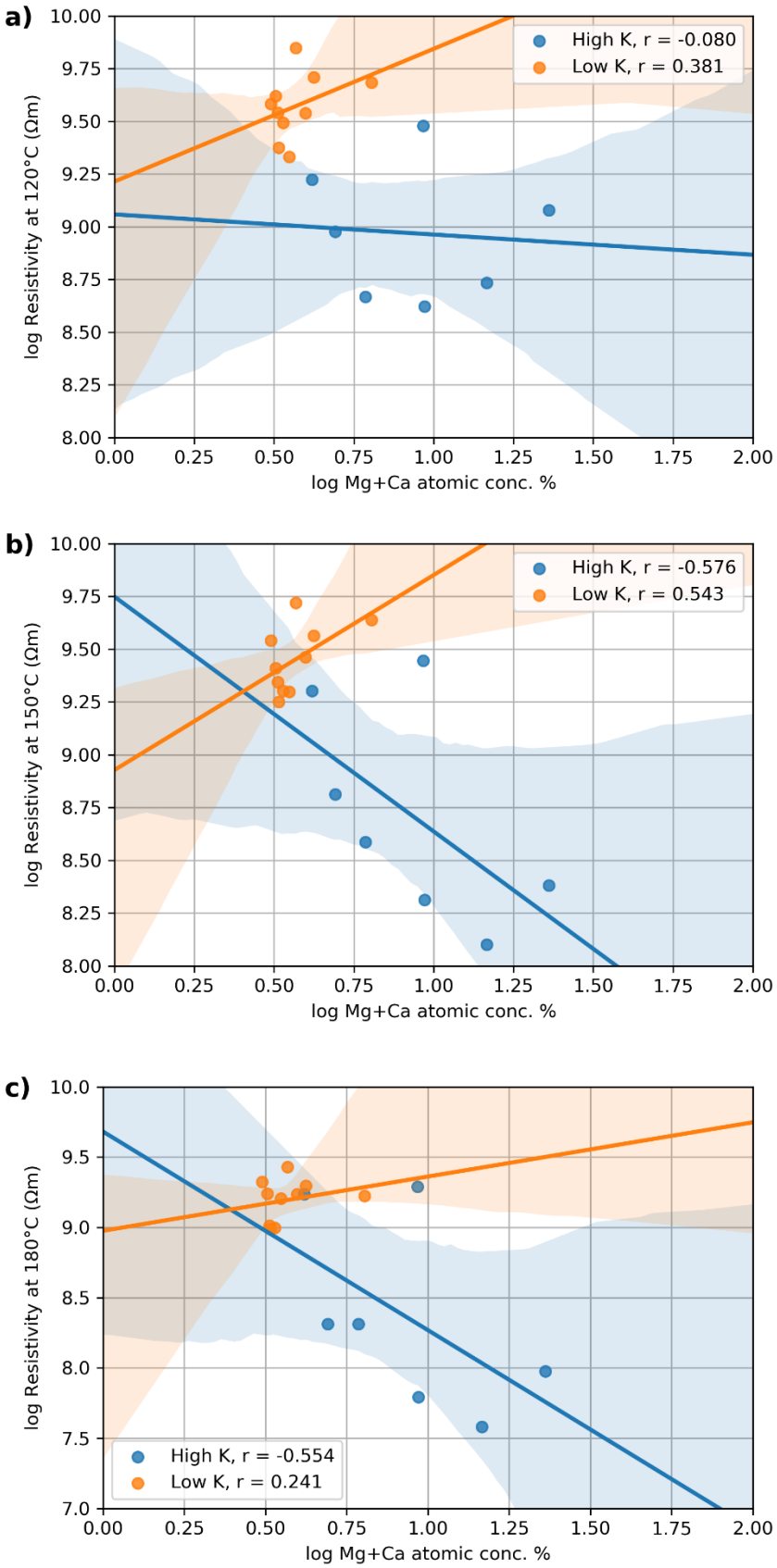

Figure 4.16 - Linear regression analysis for resistivity vs combined magnesium and calcium concentration for low and high potassium concentrations at (a) 120°C, (b) 150°C and (c) 180°C

4.4.4 - Comparison of Resistivity Measurements with Model Predictions

4.4.4.1 - Bickelhaupt/Chandra Models

Figure 4.17 shows the models outlined in Section 4.2.2.4 with experimental results for the four ash samples used in this study. The existing models fail to predict the resistivity-temperature relationship for the biomass ashes tested (Figures 4.17 a-c). Both models predict to within an acceptable error the resistivity of the FA sample (Figure 4.17d). According to IEEE standard STD 548-1984, section 7.4.2, a ratio of 2.7 (higher/lower) is the maximum acceptable variation in resistivity measurements carried out between different laboratories, and as such the models would, at a minimum, be expected to perform within this range.

As noted in Section 4.2.2.4, both of these models were developed through empirical means using coal ash compositions, which contained a maximum of 4.4% K, with a significant proportion of the compositions containing 3% K or less. Between Figure 4.17 and the results of Section 4.4.2, this indicates that current models are only valid for ash compositions containing less than 3% potassium, where ash resistivity behaviour replicates that found within such studies. As a result, for many biomass samples and some biomass-additive blends, current models will require modification to account for the different behaviour encountered with high potassium concentrations.

4.4.4.2 - Li Maximum Resistivity Model

A resistivity profile comparison was not possible for the Li et al. [174] model, as it only produced numerical predictions for maximum resistivity regardless of temperature. The peak resistivity measurement for each sample and blend tested was instead compared with the model predictions, as shown in Table 4.4. The model provided accurate predictions for the maximum resistivity of some biomass ash compositions, in particular OCA. This was despite the fact that this model was developed empirically from coal ash compositions. In addition, all of the predicted resistivities are within the maximum 2.7 ratio recommended in IEEE standard STD 548-1984, implying that the maximum resistivity of any sample can be determined without the need to take into account alkali metal content. This is

likely due to the fact that increased alkali content leads to increased mobile ion concentrations, which generally induce surface conductivity.

However, as previously stated, the model suffers from significant drawbacks. Li et al developed the model with the assumption that maximum resistivity occurs between 140-160°C, while the maximum resistivity of samples within this study range from 100-160°C (a greater range is found in literature, as low as 50-80°C [155] and as high as 200°C [171]), outside the operating range of some ESPs. The application of the model will, in turn, result in significant overestimates at ESP operating temperatures for some samples. As a result, such a model will more likely be based upon those developed by Bickelhaupt, rather than one that replicates this method, despite the apparent effectiveness of the Li et al model.

Table 4.4 - Comparison of Li model predictions against maximum recorded resistivities

Sample	Peak Resistivity	Model Prediction	Residual	% difference
Adtv.	3.83E+09	2.6E+09	1.23E+09	32.10
OCA	7.04E+08	6.84E+08	1.99E+07	2.83
OCA 5%	4.19E+08	4.86E+08	6.70E+07	15.97
OCA15%	4.71E+08	7.24E+08	2.50E+08	53.67
OCA25%	9.48E+08	9.9E+08	4.20E+07	4.40
WWA	1.39E+09	2.26E+09	8.70E+08	62.59
WWA5%	5.29E+09	2.18E+09	3.11E+09	58.75
WWA15%	5.11E+09	2.43E+09	2.68E+09	52.44
WWA25%	7.06E+09	2.5E+09	4.56E+09	64.54
FA	3.01E+09	2.26E+09	7.47E+08	24.83
FA5%	3.46E+09	2.49E+09	9.67E+08	27.95
FA15%	3.12E+09	2.56E+09	5.58E+08	17.88
FA25%	3.48E+09	2.58E+09	9.01E+08	25.88
BA	2.01E+09	5.07E+09	3.10E+09	152.29
BA5%	2.15E+09	3.2E+09	1.00E+09	48.76
BA15%	2.53E+09	2.82E+09	2.90E+08	11.27
BA25%	4.76E+09	2.72E+09	2.05E+09	42.93

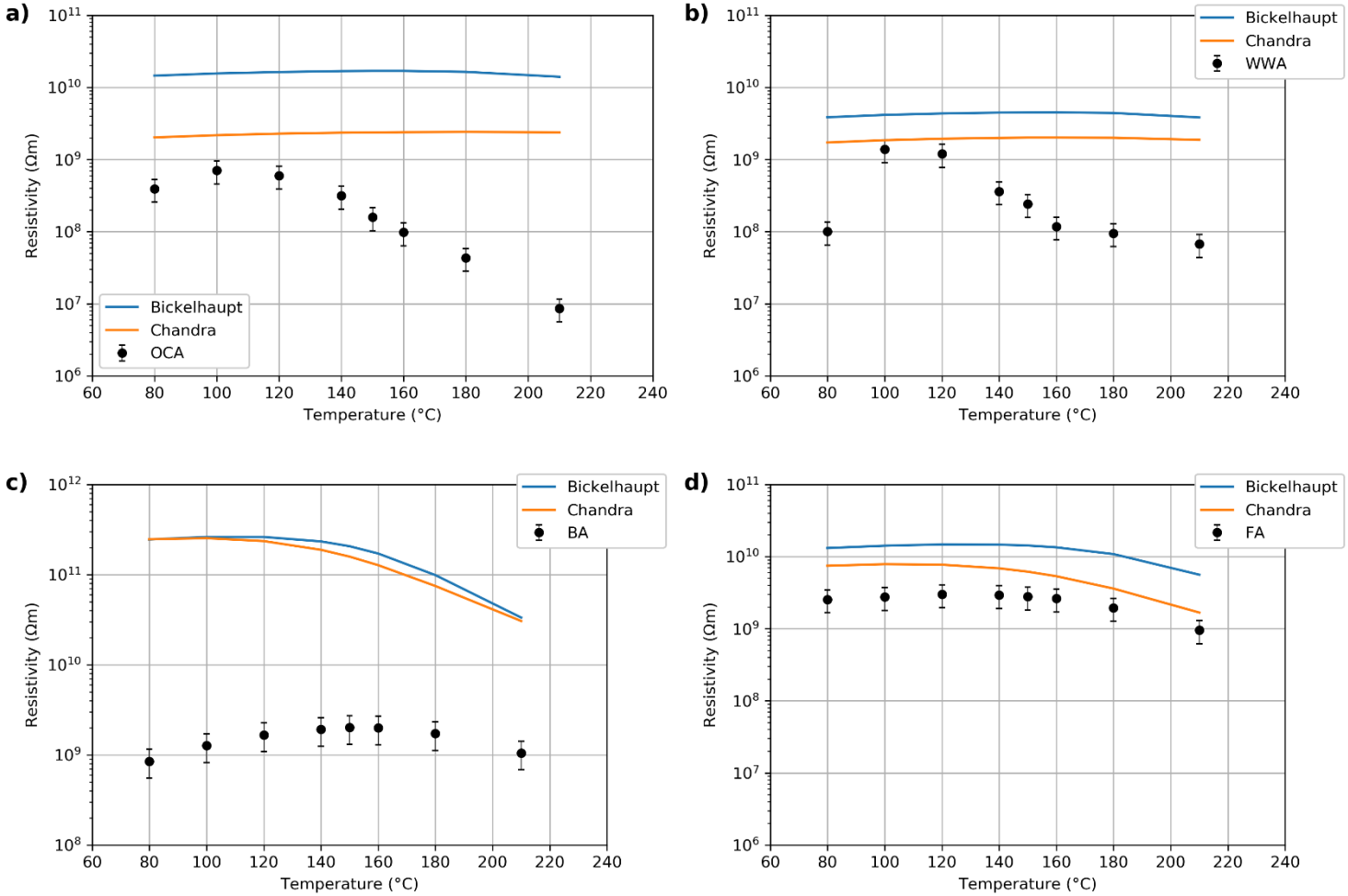

Figure 4.17 - Comparison of a) OCA, b) WWA, c) BA and d) FA experimental resistivities with model predictions.

4.4.5 - Bickelhaupt Potassium Modification

4.4.5.1 - Volume Resistivity

Using the experimental data in Section 4.4.3.1, a modification to the Bickelhaupt model was attempted. The same method was followed as described in the original work [163], with correlations between resistivity and temperature used to determine key components and normalise data. Table 4.3 shows a strong correlation between alkali content (K+Na) and resistivity, and as such was used for the initial normalisation procedure. This results in the following modification to Equation 4.5:

$$\rho_N = -1.33\ \ln(2.85) + \ln\rho\ + 1.33\ln A_{Alkali} \qquad \text{(Eqn. 4.19)}$$

Where -1.33 corresponds to the regression slope found for Na + K content with resistivity at 80°C, 2.85 corresponds to the median value of Na + K concentration, ρ is the experimental resistivity value to be normalised, and A_{alkali} is the atomic concentration of K + Na for the corresponding value. The regression values for 80°C are used for all data, according to the method applied by Bickelhaupt [163]: regression data was observed to degrade at higher temperatures, indicating that other variables other than composition were affecting volume resistivity results. This equation is applied to each experimental value, to normalise resistivity values for a fixed alkali content.

These normalised resistivity values were then plotted against other components of ash at a high temperature, to determine the true effect of other components upon volume resistivity. For this, resistivity values at 210°C were selected. Figure 4.18 shows the normalised regressions for Fe and Mg + Ca content: despite previous studies showing that both affect volume resistivity, no significant correlation is observed here, indicating that at greater alkali concentration the alkali content becomes the dominant factor in determining resistivity of a sample.

As a result, the Bickelhaupt volume resistivity equation (Equation 4.6) was simplified to include only the term for alkali concentration in predicting volume resistivity, ρV:

$$\log_{10}\ \rho_E = \frac{23.3046 - (1.607\ \ln(A_{Alkali}))}{2.303} \qquad \text{(Eqn. 4.20)}$$

$$\log_{10} \rho V_0 = \frac{\log_{10} \rho_E - \left(\frac{\theta}{k} * \log_{10}(e)\right)}{T} \quad \text{(Eqn. 4.21)}$$

$$\log_{10} \rho V = \log_{10} \rho V_0 + \frac{\left(\frac{\theta}{k} * \log_{10}(e)\right)}{T} \quad \text{(Eqn. 4.22)}$$

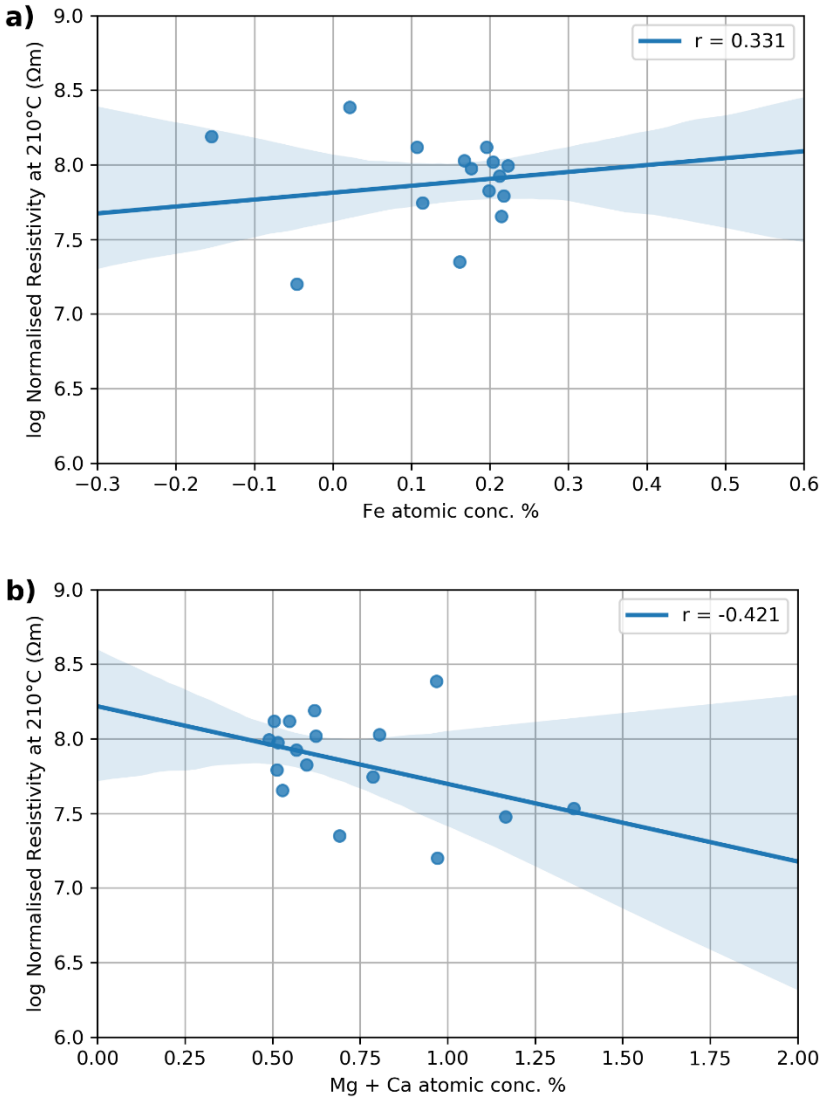

Figure 4.18 - Regression coefficients for resistivity values normalised to 2.85 atomic concentration of alkali metals, against a) Fe atomic concentration and b) Mg+Ca atomic concentration

4.4.5.2 - Surface Resistivity

Surface resistivity was calculated in the same method as that proposed by Bickelhaupt, once again substituting Na + Li atomic concentration for Na + K concentration. Regression values were used for results at T=80°C, producing Equation 4.23:

$$\log_{10} \rho_S = \frac{23.3046 + (-1.607 * \ln(2.71))}{2.303} \qquad \text{(Eqn. 4.23)}$$

No adjustment is required for electric field strength, as the field strength used for experiments was 2kV/cm. This value of ρ_S was then used to determine the maximum surface resistivity in Equation 5.24, using the constants determined by Bickelhaupt during water and sulphur concentration experiments [163]:

$$\log_{10} \rho_S = \log_{10} \rho_{S0} - \left(\log_{10}(e) * K_0 * e^{\left(\frac{K_1}{T}\right)} \right) * W \qquad \text{(Eqn. 4.24)}$$

Where ρ_{SO} is the maximum surface resistivity as the effect of water vapour approaches zero at high temperatures, W is water vapour concentration in volume percent, T is absolute temperature in K, and K_0 and K_1 are the respective intercept and gradient terms as determined by Bickelhaupt for the relationship between resistivity and water concentration. Once ρ_{SO} was determined, ρ_S was able to be estimated across a range of temperatures by changing the T value in Equation 4.24.

4.4.5.3 - Predictions

Total resistivity, ρ_{VS}, was determined by combining ρ_S and ρ_V for each temperature in the same manner as the original Bickelhaupt method, using Equation 4.9:

$$\frac{1}{\rho_{vs}} = \frac{1}{\rho_v} + \frac{1}{\rho_s} \qquad \text{(Eqn. 4.9)}$$

The model predictions were compared to experimental data from a repeated OCA experiment, to ensure that the predictions give reasonable accuracy, which is shown in Figure 4.19 along with confidence intervals of 95%. The comparison shows that the model accurately reflects experimental results, with volume resistivity predictions having greater accuracy than surface resistivity, which is slightly underestimated. This is likely due to the use of values derived by Bickelhaupt: the experimental apparatus used in this study was incapable of controlling environmental gases and moisture, and as such a proper determination of the effects of water and moisture upon high potassium ashes was not possible.

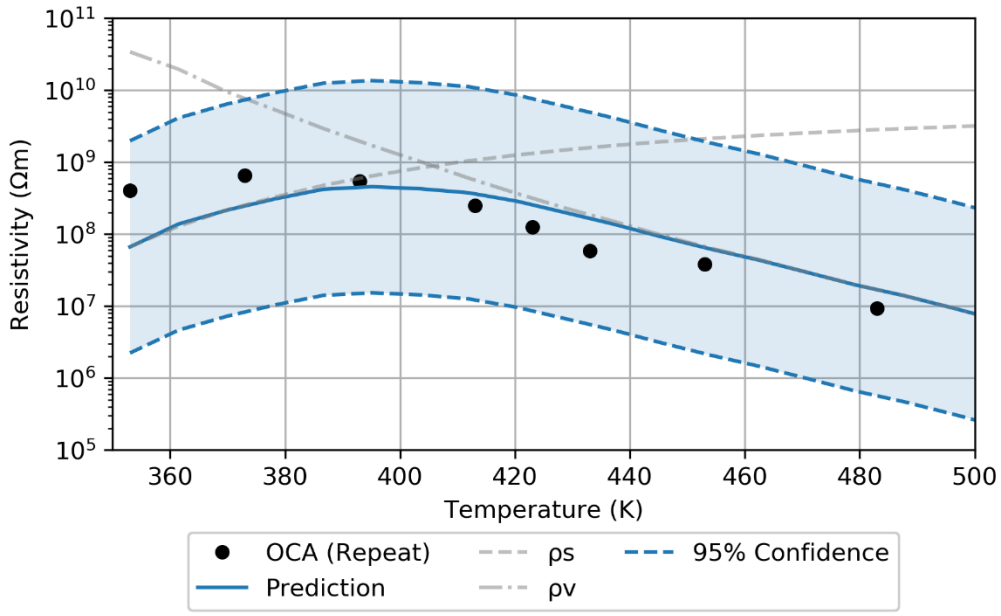

Figure 4.19 - Comparison of potassium modification model prediction with OCA experimental results

The model was then compared to two coal ashes from the Bickelhaupt study [163], and wood ash from the first and third stage of an ESP placed after a fluidised boiler [157]. These studies were chosen since both contain all of the pre-requisite information required for the calculations, including ash composition and electric field strength. All four samples contain greater than 3 wt. % K_2O. Flue gas water content is not given in the Jaworek study: only that the biomass contains 15-25% moisture initially. The water content alone was found to have minimal effect on surface resistivity moisture (with a <1% difference in resistivity values with water content between 0.1-25%), and so 15% was selected in this case. The model predictions for each ash are shown in Figure 4.20, with key ash components outlined in Table 4.5.

Table 4.5 - Selected components of ashes in literature tested against the modified high potassium model [157, 163], in atomic concentration percentage

Sample	Li+Na	K	Mg+Ca	Fe
Bickelhaupt (Coal101)	0.37	2.34	2.3	2.5
Bickelhaupt (Coal104)	0.35	2.04	2.5	2.1
Jaworek (Wood Stage1)	0.28	4.15	10.26	0.29
Jaworek (Wood Stage3)	0.75	14.19	9.26	0.3

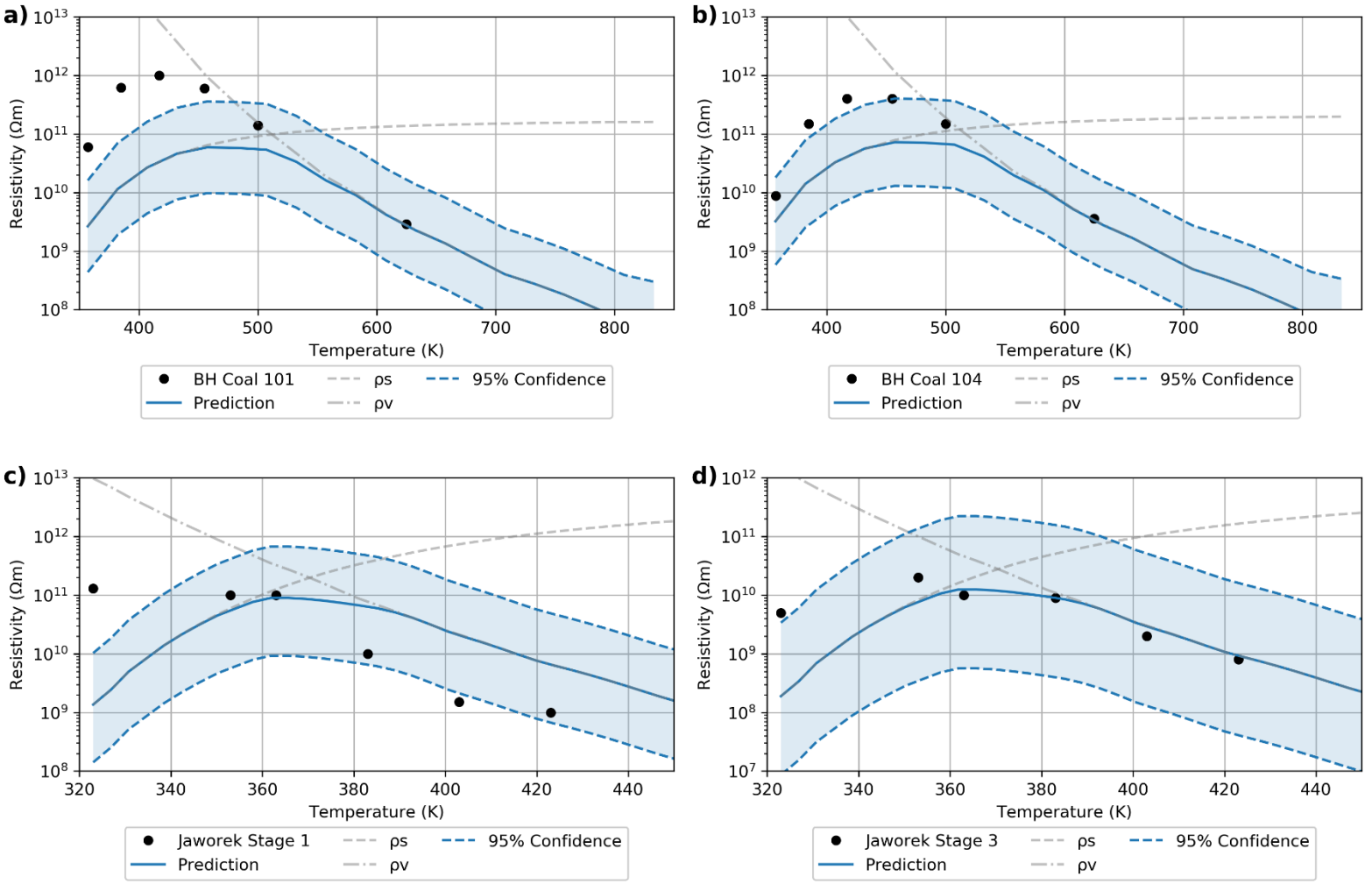

Figure 4.20 -Comparison of potassium modification model predictions with experimental results for a) Bickelhaupt coal ash 101, b) Bickelhaupt coal ash 104, c) Jaworek wood ash 1st Stage and d) Jaworek wood ash 3rd Stage

Figure 4.20 shows that, despite the limited data used to develop the model, a good agreement is possible in the limited samples that it has so far been applied to. Volume resistivity, particularly for the Bickelhaupt coal ashes, appears to give extremely accurate predictions, indicating that surface resistivity predictions require greater accuracy. This is most likely due to the fact that experiments within this study were unable to determine the effects of water and sulphur upon high potassium/alkali samples: it is possible that increased concentrations will produce different behaviour compared to the ashes studied by Bickelhaupt, whose values were used for surface resistivity predictions.

Despite the promise of the results in Figure 4.20, any such model will require further experimental data in order to reduce uncertainty: for instance, the Bickelhaupt model utilises 43 separate compositions, compared to the 17 used in this study. This is even more important for biomass ashes due to the wide range of compositional differences, particularly in terms of potassium and calcium concentration. In addition, for an accurate determination of surface resistivity effects in such samples, a controlled environment containing water vapour and sulphur would be required. Therefore, significant further work is required in order to produce a verifiable model, based upon the Bickelhaupt method, and this work will form the basis of such a model.

4.5 - Conclusions

The resistivity of olive cake (OCA), white wood (WWA) and bagasse (BA) ashes, as well as that of a power station fly ash (FA), have been investigated across a range of temperatures using a bespoke test assembly, and compared against a coal pulverised fuel ash (PFA) from a large-scale power station. Results show that biomass ash resistivity is typically lower than that of coal ash by an order of magnitude or more. In particular, OCA and WWA showed resistivities close to the lower effective operating limits of ESPs recommended in the literature. The measured resistivities indicate that, when accounting for additional moisture and SO_3 content, high alkali biomass may pose operational issues in ESPs, resulting in particle re-entrainment.

In addition, an Al-Si additive, namely coal PFA, was blended with the biomass samples at rates of 5%, 15% and 25% additive to fuel, and the resulting effect upon resistivity investigated. Increasing PFA concentration during combustion leads to increased resistivities. At ESP working temperatures, the addition of PFA to WWA increased resistivity by a factor of 26 at the lowest blends tested, due to the low ash content of white wood. BA blends showed a small increase with increasing PFA concentration, while the FA blends experienced no significant change in resistivity with increasing PFA concentration. OCA blends displayed increased resistivity compared to OCA, although this effect was negligible at lower blend rates. The use of the additive will lead to greater ESP loading due to increased amounts of non-combustible material within the boiler, as well as through decreased deposition in slagging and fouling regions leading to greater particle concentrations in the flue gas, although at low additive rates this would result in ash percentages comparable with some coal compositions. Reduced fine particle content and increased resistivities are expected when blended with high alkali biomass. Therefore, the use of additives to mitigate slagging and fouling in large scale biomass combustion should not negatively impact emissions, although some minor operational changes may be required to maintain high ESP collection efficiencies.

Composition analysis showed that potassium has an important influence on ash resistivity, contrary to previous studies. However, samples containing potassium at less than 3% atomic concentration showed little to no correlation with resistivity. Producing separate correlations for samples with less than and greater than 3% potassium concentration produced a greater fit for the sample set as a whole, indicating a change in behaviour above these concentrations. As a result, existing empirical models failed to accurately predict biomass ash and biomass-additive blend resistivities, as existing models were developed using ranges of 4% or less K_2O concentration. It was concluded that current models will require modification in order to take into account the conductive effects of high potassium content, and that the Bickelhaupt model will provide the most appropriate basis for such a model. Initial modelling work has been attempted and shows some promise: however, additional data is required before any new model can be validated.

Chapter 5 - Ash Viscosity

5.1 - Introduction

The formation of a liquid phase is key for deposit strength development because of viscous flow sintering. Therefore, understanding the flow behaviour of a slagging deposit, and its relationship with temperature, is crucial. Two main methods are used to estimate the flow characteristics of a slag or ash [176]:

a) Determination of the ash-fusion characteristics, particularly the hemisphere and flow points, during ash fusion testing.
b) Determination of the viscosity-temperature characteristics of the slag. Ideally these should be obtained by direct measurement in a viscometer, however this is time-consuming, and the characteristics are usually predicted from the chemical composition of the ash or slag, sometimes in conjunction with the ash-fusion characteristics.

This chapter will discuss viscosity temperature relationships, including empirical models that have been developed for predicting coal ash viscosity. Ash fusion characteristics and slagging indices will be discussed in Chapter 6. Although presented first, chronologically viscosity results were the last to be obtained: viscosity testing was only conducted upon OCA samples based upon the results of other tests (see Chapters 6 and 7). Sample preparation and experimental results for the viscosity-temperature relationship for OCA and OCA with 5% KAO compositions are presented, along with an analysis of the differences in behaviour and the possible benefits of using kaolin as an additive for OCA combustion.

5.2 - Literature Review

5.2.1 - Viscosity - Temperature Characteristics

The viscosity of the ash is described as its resistance to flow: once deposition has occurred, a deposit with a greater viscosity, and hence a greater resistance to flow, will have a greater inherent strength and be more difficult to remove. This can allow for a determination of the potential for sintering or agglomeration; this potential is expected to increase with a decreasing viscosity of the liquid phase.

The viscous behaviour of fly ashes strongly affects the tendency towards deposit formation and deposit sintering [92].

This does, however, depend upon several additional factors. The thermal properties of ash deposits depend more upon the structure of the deposit, rather than the composition: the particle size, porosity, sintering time and temperature all have an effect upon the nature of the deposit [101].

It is generally accepted that for satisfactory tapping of slag, the temperature in the furnace should be sufficient to maintain the slag below 25 Pa s [176]. This is desirable for wet-bottom plants, which are designed for this to happen [103]; however, for all other types of boilers this is extremely undesirable. This is partly because of the large surface area of the boiler walls that can be covered by these deposits, in turn influencing heat transfer, and due to the aggressive nature of the compounds that may be present in the running slag, which can result in corrosion.

5.2.2 - Network Theory of Silicate Melts

As discussed in Chapter 2, the release of volatile matter during combustion creates a bottom ash that is rich in refractory material such as silica, alumina, iron and other heavier minerals. Due to the prevalence of viscous flow sintering in slagging regions (Chapter 2.4.2.1), ashes under high temperatures can be considered to behave as a silicate glass melt and are often treated using the network theory of glasses as a result.

Several glass and melt properties show a relationship with silica content, particularly the ratio M/Si where M is metal cations. For properties governed by bond strength, it has been observed that the activation energy of viscous flow is often a systematic function of silica content [177]. The type of silicon-oxygen bonds within a silicate system has a significant effect upon the melting and flow behaviour of the system, with either bridging oxygen (Si-O-Si) or non-bridging (Si-O) bonds present [144].

Bridging oxygen formers, more commonly known as network formers, are typically acidic oxides such as SiO_2 and TiO_2. The high ionic potential of these components within the ash results in favourable interactions with oxygen, creating the underlying structure of the glass melt. Non-bridging oxygen modifiers, or network modifiers, produce conversions of bridging oxygen bonds

to non-bridging oxygen bonds, which are weaker than bridging bonds. High concentrations of non-bridging oxygen bonds disrupt the melt network, reducing the activation energy required for viscous flow (Figure 5.1) and lowering the melting temperature. Ash constituents typically regarded as network modifiers include alkali metals such as Na_2O, K_2O, CaO and MgO.

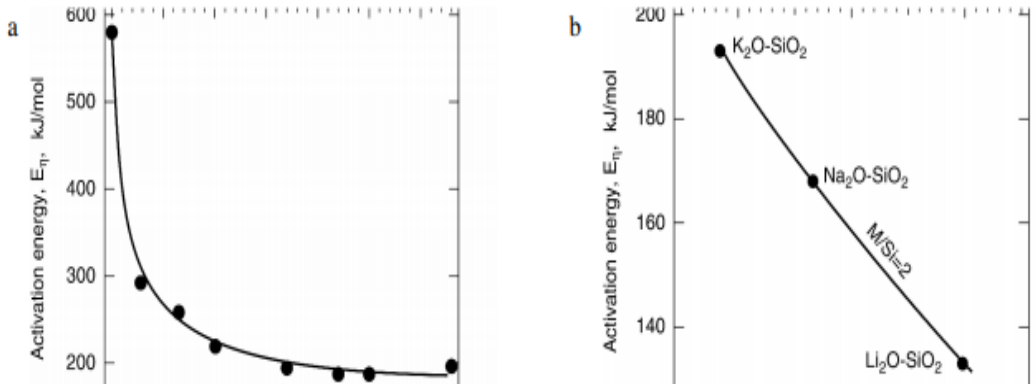

Figure 5.1 - Activation energy of viscous flow for a) SiO_2-Na_2O systems and b) as a function of ionisation potential Z/r^2, showing the effect of different alkali metal oxides in silicate systems [177]

5.2.2.1 - Amphoterics

Some common components within the ash can behave as both a network former and a network modifier, including some iron compounds (Fe_2O_3, Fe_3O_4 [76]) and Al_2O_3. These components, known as amphoterics, balance their charge in the presence of network modifiers and behave as network formers, reducing the presence of melt phases [178]. However, when insufficient modifiers are present amphoterics will behave as modifiers, acting as fluxing agents and increase the presence of melt phases.

Park et al [179] concluded that Al_2O_3 behaves as an amphoteric oxide depending upon the composition of a slag: at 10 mass % or less, the alumina behaves as a network former, creating strong chemical bonds with oxygen atoms. Above this concentration, alumina behaves as a network modifier, which are typically present as ions within the slag. In contrast, Herath Banda and Glasser's [180] study on the burning of CaO-Al_2O_3-Fe_2O_3-SiO_2 cement systems found that adding Al_2O_3 to a 5.0% Al_2O_3, 3.2% Fe_2O_3 clinker composition did not act as a flux, in that it did not increase the maximum percentage of liquid at a temperature of 1338°C.

Iron on the other hand is particularly complex. Fe^{3+} oxide shows amphoteric properties, and ferrous oxides can co-exist in a number of different forms and structures, which has a significant impact on the resulting melt behaviour [91]. In glass compositions with high silica concentration iron typically behaves as a network modifier, altering the structure of the glass network, and is typically in the form of ions. Fe^{2+} is found to be more prevalent in these compositions, since it binds oxygen less effectively than more highly charged Fe^{3+} ions [181]. However, studies are conflicting on the role of iron with regards to viscosity and melting temperatures.

The valence state of the iron is important, as ferric iron is predominant under oxidative and inert atmospheres, while ferrous and metallic iron is more predominant under reductive conditions [182]. Bool and Helble [183] showed that increasing the iron content within an aluminosilicate melt has been shown to drastically affect the melting temperature and viscosity of the melt, as Fe (II) acts as a weak base, reducing the ash particle and slag viscosity even at relatively low temperatures. Results showed that the temperature and iron oxidation state have a significant effect upon the deposit collection efficiency of the ash, with an increasing temperature producing an increased collection efficiency due to increased particle stickiness. Crucially, an increased deposition rate was shown in the glass containing only Fe (II): the oxidation of Fe (II) to Fe (III) decreased the collection efficiency by a factor of between 2 and 4. The authors postulate that this is due to an increased particle viscosity resulting from the conversion of Fe (II) to Fe (III), which in turn decreases ash stickiness. It was also noted that concentration of Fe (III) at the particle surface would likely be higher.

Liu et al [182] corroborated these results, finding an increased transition of Fe (III) to Fe (II) during heating of coal ashes, as the initial Fe_2O_3 content within the ash increased. Decreased melting temperatures were deduced to be the result of an increase in FeO content. Fe (II) reduced these temperatures by forming chemical bonds with O_2, and by forming eutectic compounds with other oxides at high temperatures. In addition, the melt formation was found to be different with increased iron content, with the formation of microparticles present on the surface of the ashes present as in Figure 5.2.

Experimental data from Seki and Oeters [184] on liquid slags in a CaO-FeO-Fe_2O_3-SiO_2 system showed a clear trend that overall iron content decreases the viscosity of such a system significantly. The impact of this change in viscosity was found to be more prevalent in acidic slags (slags with higher SiO_2 content) than basic slags (high CaO). The ratio of Fe_2O_3 to FeO was not considered to be significant to the observed changes in viscosity, however. Slag density was found to change drastically at Fe_2O_3 / (FeO+CaO) =0.5 due to a change in the atomic structure of the glass.

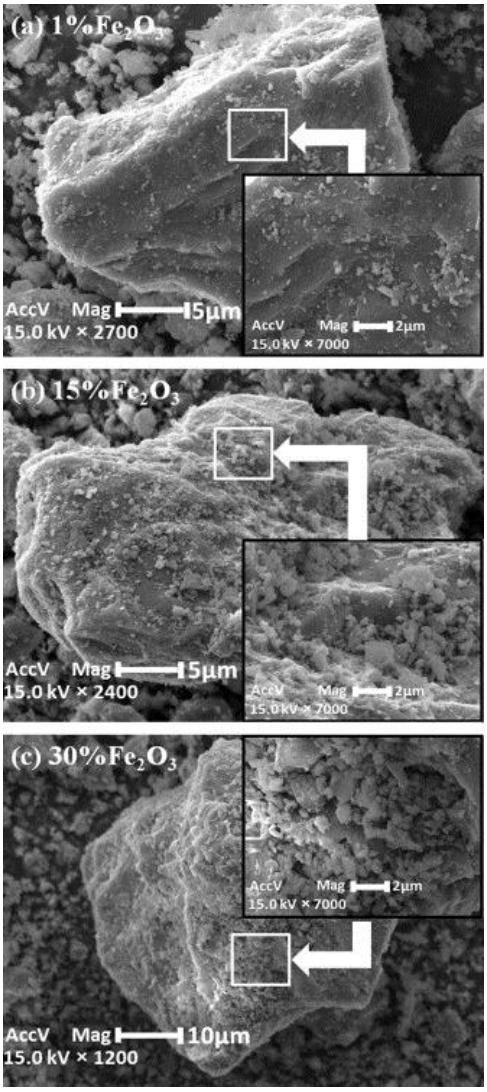

Figure 5.2 - SEM images of synthetic ashes with increased Fe2O3 at concentrations of a) 1% b)15% and c) 30%, Liu et al. [182]

Herath Banda and Glasser [180] found that the addition of Fe_2O_3 up to 3.26% resulted in a significant increase in liquid proportion up to a maximum of 22%. A further increase in Fe_2O_3 content reduced liquid presence, with a concentration of 4.35% Fe_2O_3 reducing liquid content to its original value of 19.2%. A ratio of 1.38 for Al_2O_3 to Fe_2O_3 content was considered to be the most effective combined flux, providing the most liquid content at the lowest temperature. Herath Banda and Glasser found that the presence of K_2O and FeO in low amounts would not reduce the melting point by much, but a clinker estimated to contain 22% liquid but containing 0.5% Na_2O, 1% K_2O and 2% MgO is stated to develop 25.5% liquid, decreasing the viscosity of the system.

These reports suggest that the iron content has the potential to reduce the viscosity and eutectic point of a silicate-based system, which will in turn increase the rate of sintering under heating through viscous flow sintering. However, the extent of this appears to be heavily dependent upon the type and structure of iron

that is present within the sample, how that potentially changes during heating, the other components present and the conditions under which heating takes place.

5.2.3 - Modelling

The viscosity-temperature relationship of an ash composition provides crucial information in determining the behaviour of the resulting slag. Although programs utilising thermodynamic databases (such as FactSage) have seen widespread use in recent decades, the development of an empirical model that accurately predicts the viscosity-temperature relationship for a given composition is highly desirable. Several such models have been developed in an attempt to accurately replicate experimental results. These models have all been developed using coal ash compositions; however, they have in recent years been applied to biomass and coal/biomass blends, to study the potential fouling effects that may result from their combustion [103, 185]. A number of these models are explained briefly below: although their use is only applicable to the range of ash compositions used in their development, the equations give important insight into the ash components that are most crucial in determining viscosity.

5.2.3.1 - S-Squared

The S^2 model was developed by the British Coal Utilization Research Association [186], and is based upon the Arrhenius form of the viscosity equation, given as [187]:

$$\eta = A\, e^{\left(\frac{E}{RT}\right)} \qquad \text{(Eqn. 5.1)}$$

The S^2 model is based upon the analysis of a number of bituminous coal ash slag compositions: as a result, minor components such as alkali oxides are not considered in the model [92]. The model utilises the following equation to recalculate the equivalent Fe_2O_3 content within the ash, from the total iron content by weight basis, assuming that all iron is bound as Fe_2O_3:

$$\text{Equiv. } Fe_2O_3 = Fe_2O_3 + 1.11FeO + 1.43Fe \qquad \text{(Eqn. 5.2)}$$

The composition of the ash is then recalculated from the original analysis using the following equation:

$$SiO_2 + Al_2O_3 + Equiv.Fe_2O_3 + CaO+MgO = 100 \text{ (wt. \%)} \qquad \text{(Eqn. 5.3)}$$

Using this recalculated composition, the silica ratio is calculated:

$$S = \frac{100 * SiO_2}{SiO_2 + Equiv.Fe_2O_3 + CaO + MgO} \qquad \text{(Eqn. 5.4)}$$

Finally, the viscosity is determined with the following equation, where all constants have been fitted from experimental data:

$$\log \eta = 4.468 \left(\frac{S}{100}\right)^2 + 1.1265 * \frac{10^4}{T} - 8.44 \qquad \text{(Eqn. 5.5)}$$

The S^2 model is an early example of an ash analysis model, and has since been surpassed by others: according to Vargas, et al. [92], the model frequently tends to underestimate viscosity, with an average temperature sift of 66K when comparing the temperature at which viscosity was measured to be 25 Pa s. In addition, the omission of minor elements within the calculation process means that the model also may fail when examining low-rank coals [187]. It is still, however, of interest to study whether these coal models may be applicable when used for biomass viscosity predictions, and the simplicity of the model may help in determining the most important factors for viscosity prediction.

5.2.3.2 - Watt-Fereday

This model was also developed at the British Coal Utilisation Research Association [186], and so uses the same recalculation as the S^2 model above, and hence also ignores the minor elements within the ash. The model uses a slope and intercept principle based upon the recalculated composition, to determine two parameters, m and c.

$$\text{Slope: } m = 0.00835*SiO_2 + 0.00601 * Al_2O_3 - 0.109$$

$$\text{Intercept: } c = 0.0415 * SiO_2 + 0.0192 * Al_2O_3 + 0.0276 * Fe_2O_3 + 0.0160 * CaO - 4.92$$

The viscosity is then determined as a function of temperature using these constants:

$$\log \eta = \frac{m*10^7}{(T-423)^2} + c \qquad \text{(Eqn. 5.6)}$$

Streeter, et al. [187] observed that the value of viscosity given by this model was often underestimated in the experiments undertaken. However, conversely, a number of studies have observed that the model overestimates the viscosity of multi-component slags [92].

5.2.3.3 - Bottinga-Weill

Bottinga and Weill [188] initially developed this model in order to study the viscosity of geological magma flows: however, the model is designed to determine the viscosity of silicate liquids, and takes into account a wide range of compounds, making is practical to use for ash slagging analysis.

This method utilises a comprehensive table system, found in Appendix B, using a number of constants for each component found within the ash, depending upon the temperature being studied and for different levels of SiO_2 content. For each major component within the ash, the molar fraction of each individual species is multiplied by the corresponding constant according to temperature, for a range of 1473-2073 K at 50 K intervals. This is repeated for all major components present (where molar fraction is greater than 5%), and summed, giving rise to the following equation:

$$\log \eta = \sum_i x_i * d_i - 1 \qquad \text{(Eqn. 5.7)}$$

Where x_i is the molar fraction of each individual species, and di is the appropriate constant.

Bottinga and Weill [188] made the assumption that Al_2O_3 combines with a number of other oxides to form compounds such as $KAlO_2$ and $NaAlO_2$, until all aluminium is exhausted, based upon the observations of other studies. In addition, the study was based upon data containing very few iron-containing silicate liquids. It has been found that the model is not suitable for the study of melts with high contents of aluminium [92], while some of the assumptions made may not be strictly valid [189].

5.2.3.4 - Shaw

The Bottinga-Weill model was studied by Shaw [190]: Shaw determined that it was possible to estimate the viscosity using a quicker method, using four partial molar coefficients of SiO_2, thereby avoiding the extensive use of tables required previously. This is based upon the assumption that for any chemical system, a log η vs $10^4/T$ curve (arising from the Arrhenius equation) will intercept with the curve for pure SiO_2 at an invariant point with set x and y values (c_t and c_η) [92]. These constants were found through an extensive study of data, giving values of $c_t = 1.50$ and $c_\eta = -3.78$. The method developed uses the following constants in Table 5.1, which are in turn used to determine the constant a, below.

Table 5.1 - Constants used for the calculation of a in the Shaw model [190]

Metal Oxide	a_i^0
K_2O, Na_2O, Li_2O	1.2
MgO, FeO	1.5
CaO, TiO_2	2
AlO_2	2.9

The constant a is then determined by:

$$a = \frac{x\,SiO_2 * \sum (x_i * a_i^0)}{1 - xSiO_2}$$

Finally, the viscosity is determined using a rearranged Arrhenius form of the viscosity equation:

$$\log \eta = a * \frac{10^4}{T} - c_T * a + c_\eta \qquad \text{(Eqn. 5.8)}$$

Shaw, after testing the performance of the model on wider set of data, concluded that the model should not be used for values greater than 10^7 Pa s, since this may produce underestimates, and that the viscosity determined does not take into account the effect of thermal or compositional gradients [190]. Although, according to Urbain, et al. [189], the model has some advantages, due to its

simplicity and the fact that dissolved water can be included, it appears that this is generally not a valid expression for liquid silicate viscosities.

5.2.3.5 - Urbain

The Urbain model [189] was developed by studying a large number of ternary mixtures, and takes into account a greater number of species than previous models. The species in the liquid are first grouped into glass formers, x_g, glass modifiers, x_m, and amphoterics (molecules that can act both as an acid and a base), x_a, as follows [92].

$$x_g = SiO_2 + P_2O_5$$

$$x_m = FeO + CaO + MgO + NaO_2 + K_2O + MnO + NiO + 2(TiO_2 + ZrO_2) + 3CaF_2$$

$$x_a = Al_2O_3 + Fe_2O_3 + B_2O_3$$

These values are then used to calculate x_a:

$$x_a = \frac{x_m}{x_m + x_a} \qquad \text{(Eqn. 5.9)}$$

A parameter, b, is then calculated using four parabolic equations using x_a, considering the molar ratio of the collective glass forming species, to determine b using a power series equation:

$$b_0 = 13.8 + 39.9355\, x_a - 44.049a^2$$

$$b_1 = 30.481 - 117.1505\, x_a + 129.9978a^2$$

$$b_2 = -40.9429 + 234.0486x_a - 300.04a^2$$

$$b_3 = 60.7619 - 153.9276x_a + 211.1616a^2$$

$$b = b_0 + b_1 * x_g + b_2 * x_g^2 + b_3 * x_g^3$$

A second parameter, a, is then calculated from b, using the equation:

$$-\ln a = 0.2693 * b + 13.9751 \qquad \text{(Eqn. 5.10)}$$

Finally, the viscosity can be determined as a function of temperature, using the Weyman equation:

$$\eta = a * T * e^{(b*10^3)/(T)} \qquad \text{(Eqn. 5.11)}$$

According to Vargas, et al. [92], the model is capable of predicting viscosities within a magnitude of the results, and can describe viscosity at high temperatures (i.e. low viscosities). However, this model struggled for high rank coal ashes.

5.2.3.6 - Kalmanovitch

Kalmanovitch and Frank [92] modified the Urbain model, using compositions of SiO_2-Al_2O_3-CaO-MgO glass compositions. This produced the following changes to the relationship between a and b:

$$-\ln a = 0.2812 * b + 15.1305 \qquad \text{(Eqn. 5.12)}$$

5.2.3.7 - Riboud

The Urbain model was modified after an experimental study of a quaternary system by Riboud, et al. [191], producing the following equations for determining the parameters a and b:

$$\ln a = -35.76\,Al_2O_3 + 1.73(FeO+CaO+MgO+MnO) + 7.02(Na_2O+K_2O) - 5.82\,CaF_2 - 19.81$$

$$b = 68.833Al_2O_3 - 23.896(FeO + CaO + MgO + MnO) - 39.159(NaO_2 + K_2O)$$

$$- 46.356CaF_2 + 31.140$$

Where each compound is molar fraction. In the original paper, the equation for b is printed in two different forms: the third term is altered slightly, either as $39.519(Na_2O + K_2O)$ or $39.159(Na_2O + K_2O)$ [191]. Vargas, et al. [92] suggest the former, and so this is the equation used for the remainder of the study.

5.2.3.8 - Lakatos

The Lakatos model utilises the Vogel-Fulcher-Tamann equation, in the following form:

$$\log \eta = a + \frac{b}{T-c} \qquad \text{(Eqn. 5.13)}$$

Where a, b and c are compositional-specific constants, as determined from the study of 30 laboratory-prepared compositions [92], and as calculated below:

$$a = 1.5183Al_2O_3 - 1.6030CaO - 5.4936MgO + 1.4788NaO_2 - 0.8350K_2O - 2.4550$$

$$b = 2253.4Al_2O_3 - 3919.3CaO + 6285.3MgO - 6039.7Na_2O - 1439.6K_2O + 5736.4$$

$$c = 294.4Al_2O_3 + 544.3CaO - 384.0MgO - 25.07Na_2O - 321.0K_2O + 471.3$$

Where the value used for each compound is the molar ratio of each species per mole of SiO_2: for instance Al_2O_3 = moles of Al_2O_3/moles of SiO_2.

According to Vargas, et al. [92], the equation used produces an “S-shape”, independent of the conditions used, immediately indicating that the model cannot be wholly descriptive of the true relationship, and appears to significantly deviate at higher temperatures for some compositions: however, the model has general acceptance due to its simplicity, and can be useful for certain compositions.

5.2.3.9 - Model Constraints

All of these models are the result of empirical fitting of data and assume Newtonian behaviour: the predictions apply only to completely molten systems. As a result, the models are inherently constrained to the range of conditions examined in each study for which they were created, and care must be taken when applying these models to compositions that lie outside of the ranges used within the original studies. These constraints are summarised in Appendix C, where possible. Although the Urbain, et al. study [189] states the use of 60 experiments as part of the study, the conditions and compositions used are not elaborated upon, and therefore the constraints cannot be known for certain. In this case, the model has been applied to every composition analysed.

There have been examples in literature of all of the aforementioned models being applied to biomass ash compositions, most notably in studies by Arvelakis et al [185] and Vargas [103], both of which show that the model predictions differ over a significant range of viscosity at a set temperature. As an example, a factor of over 10000 difference was observed between the Shaw model and Watt-Fereday model predictions when applied to leached superheater ash from MSW firing at 1150°C in the Arvelakis study [185].

Both the Arvelakis and Vargas studies apply the models to ash compositions outside of the model ranges presented in Appendix C. For instance, the Al_2O_3 concentrations of the samples in these studies fall outside the lower limit of the compositions used to develop the S2 and Watt-Fereday studies, and both models perform poorly when compared to experimental values from both studies as a result.

Despite this, some models were shown to produce fairly good predictions of viscosity. Although the wheat straw studied by Vargas [103] had CaO and Na_2O - K_2O concentrations that fell significantly below the ranges used within the Urbain study, the Urbain model produced an excellent reproduction of the experimental viscosity data. The study by Arvelakis et al [185] found that the Shaw model gave good predictions for leached 2nd and 3rd pass MSW deposition at high temperatures despite significantly lower SiO_2 concentrations than used in the Shaw study, although the model failed at temperatures of 1200°C and below.

An additional consideration is that each of the models are designed for completely molten silicate systems: this may not be representative due to the formation of crystals or the presence of solids within the composition at higher temperatures, and therefore the models may particularly struggle to replicate experimental results that display a temperature of critical viscosity, T_{cv}, outlined in Figure 5.3. Examples of this are present in the study by Arvelakis et al [185], where all experimental results display significant changes in viscosity which the models fail to replicate. This temperature represents an abrupt change in the viscosity-temperature relationship and can be assumed to mark the division between viscosities that have been influenced by the presence of crystals (non-Newtonian) and viscosities that have not, which can therefore be considered Newtonian in nature. Viscosities above T_{cv} are of interest to boiler operation, as T_{cv} represents the temperature at which the slag properties alter during cooling, behaving as a Bingham plastic rather than a molten slag [192].

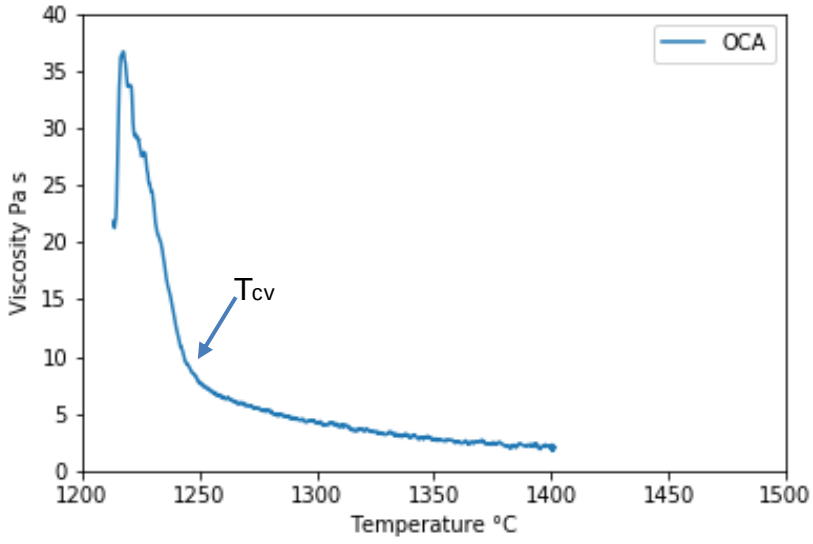

Figure 5.3 - An example of the temperature of critical viscosity, labelled T_{cv}

5.3 - Experimental Methodology

5.3.1 - Samples

For this study, experiments were solely conducted for OCA and OCA5%KAO. OCA 5% PFA was initially intended for these experiments, alongside WWA and WWA5%PFA; however, the iron content of the PFA is unsuitable for use in a rotational viscometer due to a tendency of such mixtures to bubble over. Time constraints prevented WWA experiments from taking place. Initial ash preparation was conducted according to the methods outlined in Chapter 3.

Table 5.2 - Test matrix of samples used in viscosity experiments

% Adtv. to dry fuel	0%	5% (PFA)	15% (PFA)	25% (PFA)	5% (Kao)	15% (Kao)	25% (Kao)
OCA	X				X		
WWA							
BA							
FA							
PFA							
Kaolin							

5.3.2 - Sample Preparation

In order to conduct viscosity experiments upon biomass ash samples, washing was required. This was due to the typically high content of alkali metals, chlorine and sulphur that are found in biomass, which will often form salts such as $CaSO_4$ or KCl during combustion. In a full-scale boiler, the only location where significant viscosities are encountered is typically in and around the combustor, where temperatures are high enough for silicate melting to occur. Therefore, viscosity measurements are only useful if the conditions experienced by particles in the hot regions of the boiler are replicated, and alkali salt layers that form in the ash will affect results [103]. In addition, platinum crucibles were used in this experiment, meaning that certain conditions should be avoided. This includes reducing atmospheres, metals such as Fe, K, Na, Si, HCl with an oxidising agent,

halogens, KCl, NaCl, $MgCl_2$, alkali carbonates and alkali sulphates, all of which may cause damage to the crucible and sensor materials [92, 103, 193].

OCA contains high levels of KCl and potassium which is not removed at typical biomass ashing temperatures of 550°C. To remove these troublesome compounds from the ash, the sample was subjected to repeated washes. A ratio of 30g of ash to 300ml of de-ionised water was used, placed into a beaker and onto a hot-plate stirrer at 125°C for one hour with a stirrer bar set to 600 rpm. The sample is then removed and allowed to cool, and the insoluble sediment allowed to settle before filtering using qualitative filter paper with an 11µm pore size. Part of the wash water was then filtered again using a syringe filter with pore size 0.45µm, to conduct ion chromatography for the determination of removed potassium and chlorine. This was repeated five times for both samples. Ion chromatography was conducted upon the wash water for each sample, to ensure that mobile potassium and chlorides were being removed during washing; these results are available in Table 5.3. Calcium concentration within the wash water was observed to increase with successive washes: significantly so for OCA5%KAO. The reason for this is unknown. Finally, any residual carbon within the ash was removed by decarburising the ash at 700°C for 16 hours.

Table 5.3 - Ion chromatography of wash waters

	OCA			OCA5%KAO		
Component	Wash 1	Wash 4	Wash 5	Wash 1	Wash 4	Wash 5
Na	0.4	0.152	0.093	0.243	0.413	0.143
K	19.82	1.413	0.46	6.061	3.415	1.254
Ca	0.11	0.468	0.391	0.454	0.576	4.525
Mg	0.06	0.139	0.114	0.092	0.099	0.167
Cl	2.11	0.179	0.14	1.041	0.362	0.142
SO_4	1.92	0.341	-	1.623	1.714	0.372

Since the purpose of the additive is to bind potassium from potassium salts (as discussed in Chapter 2.5), washing of samples ashed at typical biomass ashing temperatures of 550°C will remove many of the salts before any chemical reactions with the kaolin can take place. To produce a representative composition for the OCA5%KAO sample, the ash was re-heated at 800°C for 3 hours before washing. This temperature was chosen as KCl precipitation was observed in OCA

samples at as low as 700°C, and kaolin has been shown to effectively bind potassium from chloride salts.

24g of sample was required for viscosity measurements. The low density of the ash made pre-fusing necessary. The samples were pre-fused at up to 1450°C in a platinum-gold crucible, to increase the density of the samples. Pre-fusing OCA at 1300°C produced a glassy melt that did not produce a flow. The sample flowed sufficiently at 1400°C to pour from the crucible. In contrast, the OCA5%KAO sample failed to produce a flowing melt at 1450°C, making measurements in the viscometer impossible for the sample.

A concern was that the re-heating temperature used for the OCA5%KAO sample was too low, resulting in most of the potassium being removed during washing. Samples were prepared for XRF analysis by combining 0.6g of fused sample with 6g of lithium borates. XRF results (Table 5.4) showed that the washed OCA5%KAO sample contained significantly greater concentrations of potassium when compared to washed OCA. These results indicated that much of the potassium in the OCA was in the form of potassium salts which had been subsequently removed during the washing process, while a much higher quantity of the potassium was bound as immobile compounds in OCA5%KAO, indicating that the additive was effectively converting KCl to KAlSi at temperatures of 800°C.

Table 5.4 - XRF Analysis of ashes after five washes

	OCA5%KAO	OCA
SiO_2	34.80	30.53
Al_2O_3	20.95	4.18
Fe_2O_3	3.34	3.02
CaO	10.22	30.80
MgO	5.29	14.19
K_2O	18.04	2.86
Na_2O	0.49	0.69
TiO_2	0.40	0.22
P_2O_5	5.30	14.19
Cr_2O_3	0.044	0.060

These results further indicate that potassium concentration within OCA is not responsible for lower flow temperatures, since much of the potassium is

devolatilised at lower temperatures. Instead, the SiO_2-CaO ratio was postulated to be responsible, paired with the greater Al_2O_3 concentration within the ash producing higher melting temperature aluminosilicates.

5.3.3 - Viscosity Measurements

A VIS 403 high temperature rotational viscometer was utilised for viscosity measurements. The fused sample was placed into the cup, inside a furnace capable of temperatures up to 1500°C. The sample was gradually heated up to a target temperature at which the sample became molten, at which point the temperature is held for 10 minutes to allow the sample to heat fully and reach equilibrium. The viscosity was measured by recording the shear stress and shear rate of a rotating bob which was immersed in the molten ash, and the temperature was cooled at a controlled rate of 10°C/min.

Viscosity testing of washed OCA was initially attempted at a rotational speed of 200 RPM, using a starting temperature of 1400°C. This test showed signs of slag crystallisation, with a break temperature observed at 1275°C leading to unreliable readings. The break temperature is due to the occurrence of glass transition/crystallisation within the melt, producing a two-phase system which interferes with the viscosity measurements. The test was repeated at a speed of 300RPM, which prevented the onset of early crystallisation. Critical viscosity was observed at approximately 1245°C, as indicated by the rapid change in viscosity gradient in Figure 5.4. The test was stopped at the onset of crystallisation, which occurs at approximately 1225°C and is indicated by the increased noise of the readings.

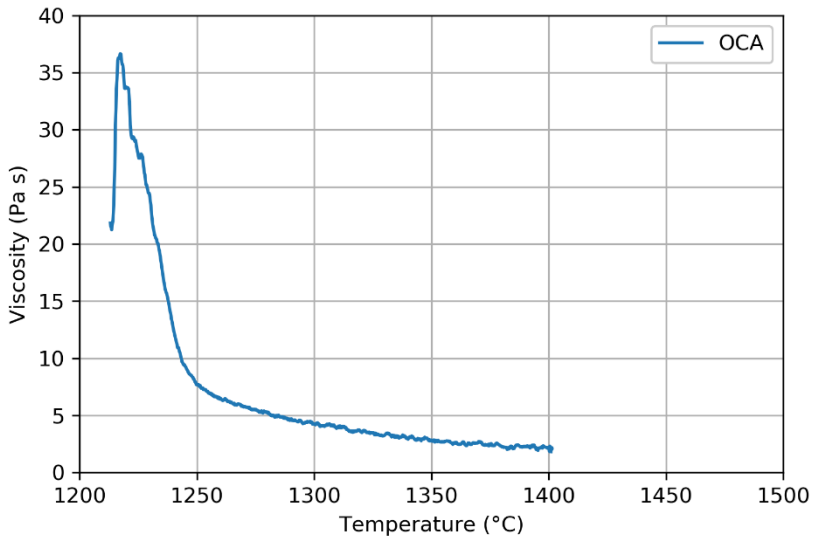

Figure 5.4 - Viscosity measurements for washed OCA

For context, water has a viscosity at room temperature of approximately 0.1 Pa s, with honey having a viscosity of 2-10 Pa s. The low viscosity of the OCA indicates that the sample will produce a flowing slag at temperatures of 1250°C and above, resulting in the creation of dense deposits that may be difficult to remove. The uncontrolled build-up of such a deposit would require boiler shutdown in order to remove the sample, which could cause damage to refractory materials and boiler components if shedding were to occur. This is one of many reasons why OCA is currently rarely used in pulverised fuel combustion.

5.3.4 - Viscosity Predictions

As noted in Section 5.3.2, the OCA5%KAO sample failed to produce a flow at temperatures of up to 1450°C, making viscosity measurements impossible. Instead, the XRF data from the washed ashes was input into FactSage thermochemical software to produce a prediction of viscosity. Predictions were first compared to the OCA data, to determine the ability of the software to produce an accurate prediction. The results in Figure 5.5 show that the FactSage prediction for OCA gives a comparable result to the actual viscosity of the sample.

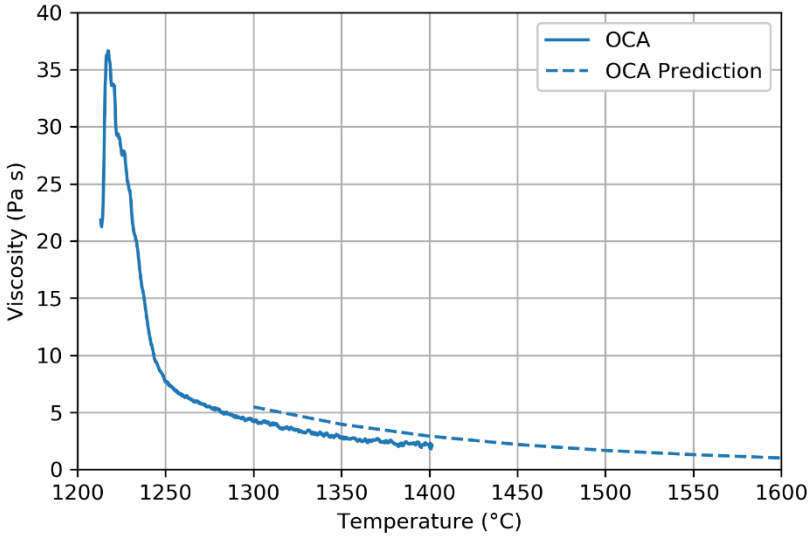

Figure 5.5 - Comparison of FactSage viscosity prediction with OCA data

The sample composition was also analysed with MTData, using the MTOX database. The equilibrium diagram in Figure 5.6 showed that OCA is expected to create a fully liquid phase at approximately 1300°C, below which the presence of olivine ($(Mg^{2+}, Fe^{2+})_2SiO_4$) and $\alpha CaSiO_2$ would be expected. The onset of critical viscosity corresponds to an MTData prediction of approximately 80% liquid phase with 10% olivine and 10% $\alpha CaSiO_2$.

Next, the XRF results of OCA5%KAO were input to the software. Viscosity predictions (Figure 5.7) indicate that, despite the much greater concentration of potassium within the washed OCA5%KAO sample, the viscosity was estimated to increase by a factor of 50 at 1350°C. It should be noted that FactSage assumes a single-phase liquid system, meaning that viscosity predictions in this case are likely underestimated. The presence of crystalline/glassy phase will increase the viscosity of the system. This is in line with the observations of OCA5%KAO during fusing where, although clear melting and deformation was visible, no flow was

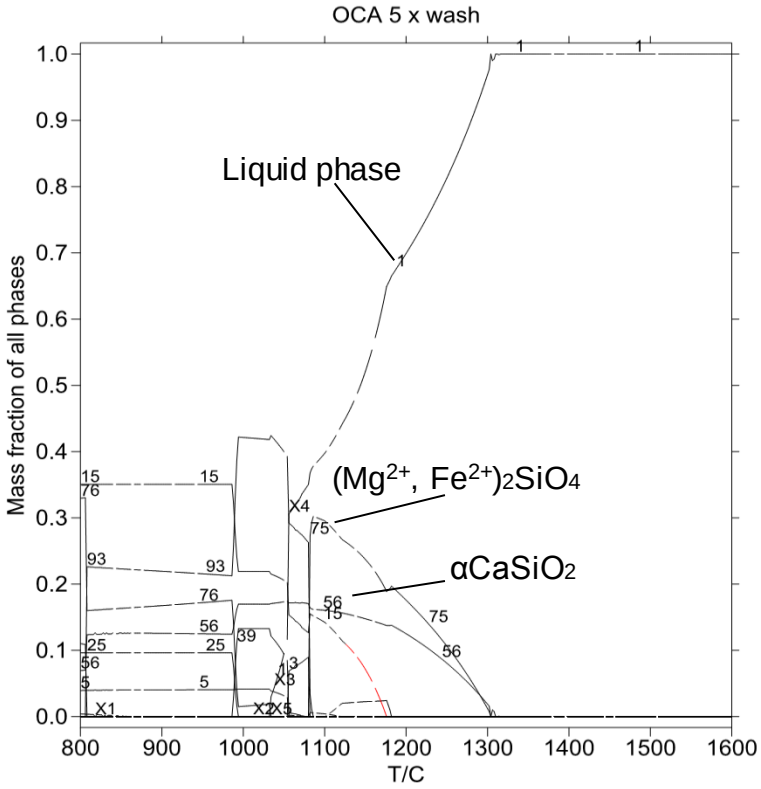

Figure 5.6 - MTData phase equilibrium predictions for washed OCA

observed upon removal of the sample from the furnace at 1450°C. Such a sample will form deposits that are substantially less dense than OCA, indicating that the addition of 5% KAO will significantly improve the deposition characteristics of OCA around the combustion zone, potentially making removal via soot blowing possible and shedding events less hazardous to boiler components.

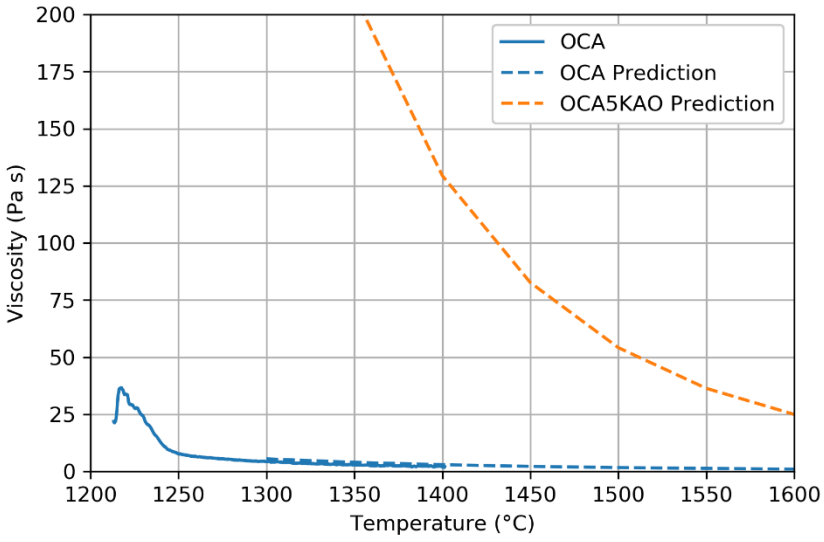

Figure 5.7 - Comparison of FactSage predictions for OCA and OCA5%KAO with OCA viscosity measurements

MTData results indicated that a fully liquid phase would be expected at temperatures of 1450°C and above. Below this temperature, solid phase nepheline ($Na_3K(Al_4Si_4O_{16})$) is expected to form rapidly with cooling, with approximately 20% solid phase expected at 1400°C along with a small mass fraction of spinel formation (likely aluminium spinel in the form of $MgAl_2O_4$). Phase predictions are shown in Figure 5.8. This would explain the absence of flow despite deformation and liquid phase being present during fusing, as the sample temperature would drop to below 1400°C within seconds of removal from the furnace. 20% solid mineral phase corresponds to the onset of critical viscosity recorded during OCA viscosity experiments, so it can be inferred that a similar critical viscosity is reached for OCA5%KAO at 1400°C. This is in line with experiences presented in Sections 2.3.1 and 2.5, that increased aluminium content is typically crucial for higher melting temperatures, with both high temperature-forming mineral phases in OCA5%KAO containing aluminium.

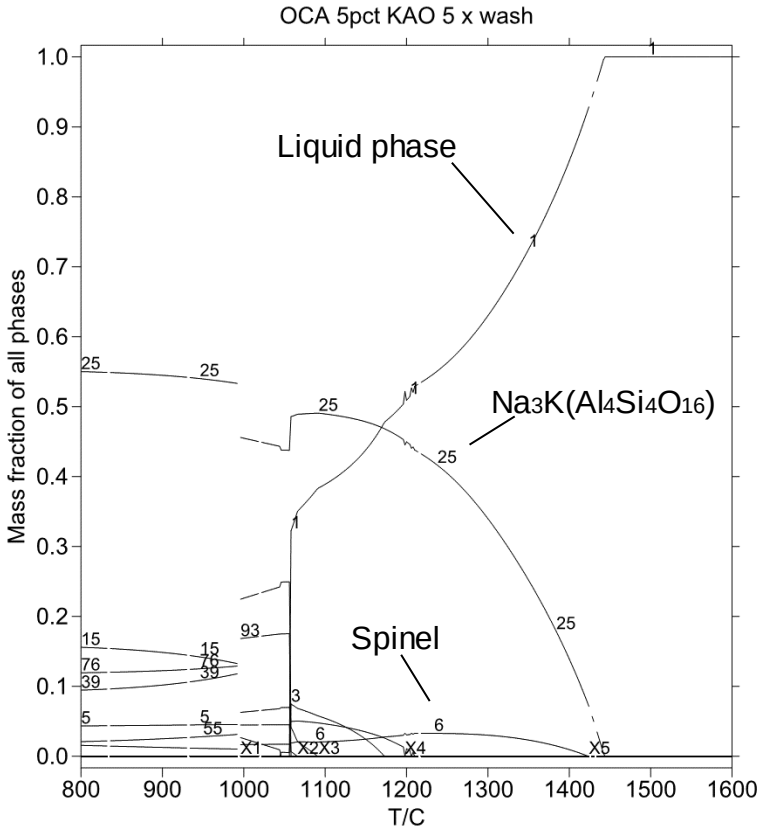

Figure 5.8 - MTData phase equilibrium predictions for washed OCA5%KAO

5.3.4.1 - Comparison with Empirical Models

The viscosity models introduced in Section 5.2.3 have been applied to the compositions of Table 5.4 and compared to the experimental viscosity results and FactSage predictions. Figure 5.9 shows that many of the models produce a significant underestimate of the viscosity of OCA, most likely due to the high P_2O_5 content which is a component that is not considered within the models. Despite this, and although the model predictions give an unusual viscosity trend, the Bottinga-Weill model produces excellent predictions of viscosity across the range of temperatures measured, up to T_{cv} where the model is expected to fail. If a trendline is taken of the Bottinga-Weill predictions (as denoted by the dotted line), an extremely close match with the FactSage viscosity prediction is found. The Bottinga-Weill model was shown in a study by Vargas [103] to produce similarly good predictions for washed wheat straw.

As noted in Section 5.3.4, FactSage predicted that viscosities would increase significantly with the addition of kaolin to OCA. Although all of the model predictions increase for the OCA5%KAO composition when compared to the predictions for OCA, the viscosities are significantly different to those predicted by FactSage, as shown in Figure 5.10. In particular the Bottinga-Weill model performs much worse, predicting viscosities of a factor of 10 lower than the FactSage predictions. Despite many of the models predicting a similar trend, only the Lakatos model in this case produces a viscosity prediction of within a factor of three of that predicted by FactSage. As referenced in Appendix C, many of the models were ill-equipped to deal with high Na_2O and K_2O concentrations, and this appeared to be the case for the OCA5%KAO composition.

This work, along with studies by Arvelakis et al [185] and Vargas [103], implies that a new model is required for the empirical prediction of biomass ash and biomass-additive ash viscosities. In all three studies, the Urbain methodology produced trends that accurately replicate the gradient of the measured viscosity (if not the actual viscosity predictions themselves), indicating that a future model may be possible by applying the Urbain methodology to a comprehensive range of biomass ash compositions to determine new constants.

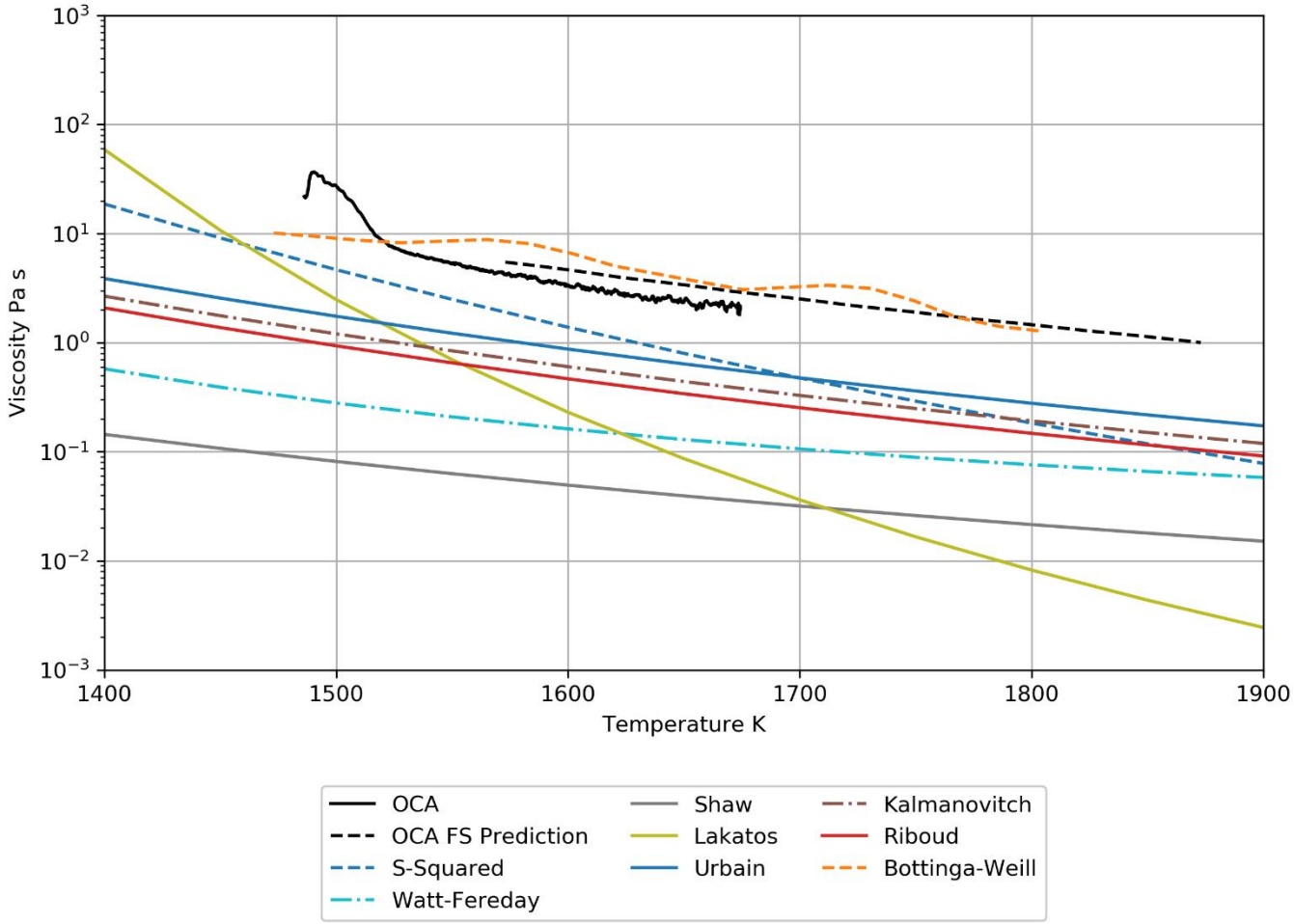

Figure 5.9 - A comparison of empirical model performance with experimental data (OCA) and FactSage predictions (OCA FS Prediction) for washed OCA

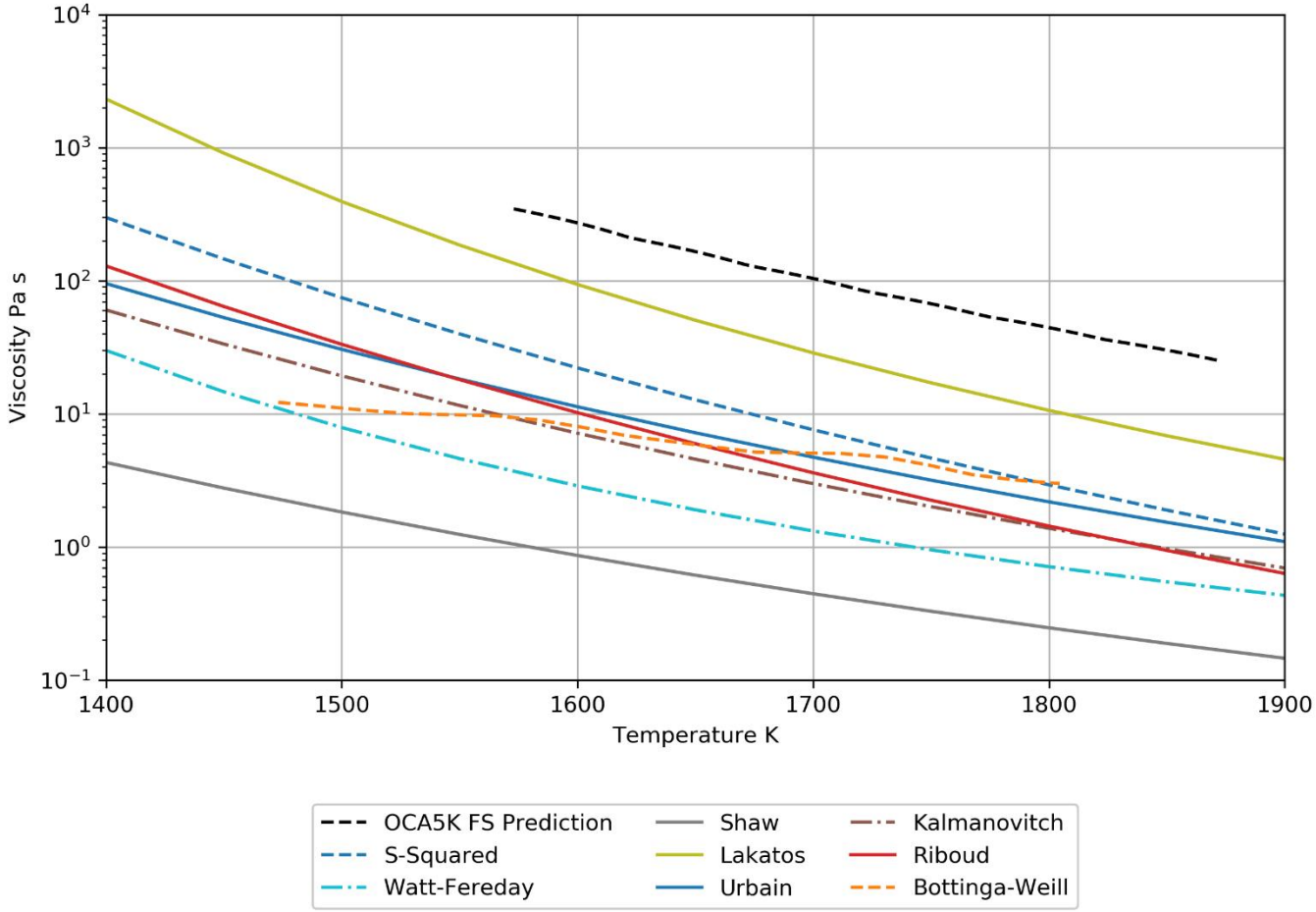

Figure 5.10 - A comparison of empirical model predictions with Fact Sage predictions for washed OCA5%KAO (OCA5K FS Prediction)

5.4 - Summary

The importance of liquid phase and viscosity upon the slagging potential of biomass ashes has been discussed. The frequent presence of silica in the ash means that biomass and coal ash compositions are often treated as silicate glass melts. The viscosity of silicate glasses at high temperatures is highly dependent upon the concentration of alkali metals and amphoteric components within the ash, which has implications for the behaviour of slagging deposits in boilers.

The viscosity of OCA and OCA5%KAO has been investigated using high temperature viscometry and thermodynamic predictive modelling. Sample preparation clearly showed that the use of kaolin resulted in significantly increased potassium concentration within the ash after washing, indicating that kaolinite adsorbs and reacts with potassium to form potassium aluminosilicates at temperatures of 700°C. Viscosity testing showed that, despite the increased potassium concentration within the ash, viscosities are significantly increased with the use of kaolin due to decreased concentrations of magnesium and phosphorus, and increased alumina concentrations within the ash resulting in the formation of high melting temperature aluminosilicates. The use of 5% kaolin with OCA is expected to result in significantly improved flow behaviour at combustion temperatures, reducing troublesome slagging in biomass boilers.

Chapter 6 - Ash Fusion Testing

6.1 - Introduction

This chapter will discuss ash fusion testing in detail. As noted in Chapter 5, a second method of determining ash flow characteristics is the ash fusion test (AFT), which is a well-established standard test that has been used for coal ash analysis for decades. The chapter begins with a critical review of ash fusion testing, its limitations and attempts to improve the method. Previous experiments that utilise ash fusion testing for biomass are discussed and critiqued. The method of sample preparation and test conditions are outlined, along with the samples used. Test results are provided both for traditional ash fusion temperatures, which allows both for comparisons between previous studies and linear regression against slagging indices, and for pellet height profiles with increasing temperature.

6.2 - Ash Fusion

Furnaces are typically designed to remove ash deposition as a powdery residue, utilising soot blowers. As a result, the fusibility of ash is an important factor to consider in boilers, and is a property that has been studied extensively within the coal industry. The standard test for determining this is the ash fusion test (AFT), which has been used for decades to give indications of the melting behaviour of coal ashes in boilers [76, 144, 185, 194].

AFT is designed to determine the significant temperatures at which a sample of ash will suffer from significant melting, where deposit strength drastically increases. Typically a cylinder or cone of ash is placed into a furnace and viewed as temperature is increased at a designated rate. The temperatures at which the sample shows certain characteristics (first signs of deformation, rounding of edges, hemispherical shape, and flow temperature) are then recorded. A diagram of these characteristic temperatures is shown in Figure 6.1.

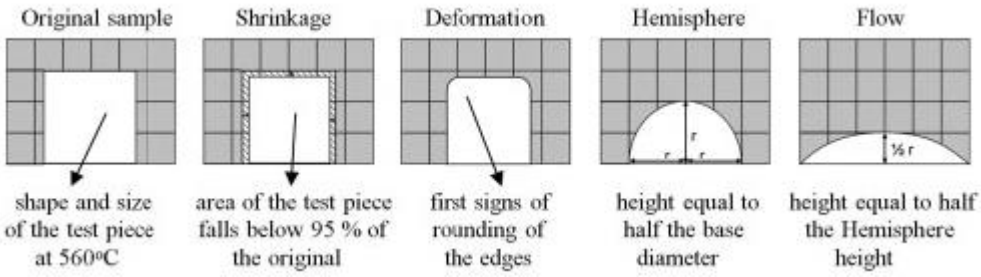

Figure 6.1 - Diagram showing the typical characteristic temperatures as measured during ash fusion testing

6.2.1 - AFT - Issues and Improvements

This method has a number of limitations: as an entirely empirical method, interpretation of the values obtained is subjective and prone to margins of error. As a result, there are inherent reproducibility issues, even without taking into account the different behaviours of samples conducted at the same time, from minor differences in composition, porosity and heating. It has been reported that ash fusion testing with the same operator, procedure and equipment will yield reproducibility to within 30-40°C, but potentially as high as 50-70 °C [195]. In addition, it has been suggested in the literature [81, 119, 195, 196] that the specific melting temperatures currently in use may not be sufficient to describe biomass ash behaviour under heating. It can be difficult to ascertain temperatures at which shrinkage takes place [196], while the softening temperature used in some AFT methods may not be appropriate in some cases [81], as the rounded shape produced can be the result of melting and other phase transformations. A standard ash fusion test can produce results where two ash samples have the same ash fusion temperatures, yet have very different melting temperatures: although the height of a sample may not change, the pore size and porosity can change significantly [195].

In an attempt to circumvent this issue, a few methods have been used. Baxter et al [196] chose to not report ash shrinkage temperatures as a result of uncertainties, instead opting to report deformation, hemisphere and flow temperatures along with basic notes on the test piece behaviour during heating. This is despite deformation temperature being a subjective measurement. This was paired with STA analysis, to determine the evolution of gases during heating. It was determined that K_2O content within the ash provides a non-linear correlation with melting temperature, while high phosphorous biomass was found

to lower melting temperatures. The peak endotherm temperature of STA analysis was suggested as a good estimate of the hemisphere temperature in ash fusion testing during this study. Further work on this subject conducted by Xing et al [197] determined that this method is less reliable, with hemisphere temperatures found to be consistently higher than recorded endotherm temperatures.

Pang et al [195] used an alternative method, by reporting the height of the test piece throughout heating, and comparing the ash fusion results with sinter strength testing conducted on the samples. Four distinct regions were reported in this case: a region where the sample is unaffected by heat treatment, a sintering region where initial shrinkage takes place and the test piece densifies through sintering and melting, an expansion phase which was determined to be the result of thermal expansion, trapped air and the evolution of gases during heating being trapped by a liquid/semi liquid film, and an excessive melting/degassing phase. Ash samples that experienced a significant expansion phase were found to have a substantially weaker structure during sinter strength testing, due to the presence of voids within the sample resulting in increased porosity. Conducting ash fusion testing by recording the sample height and sinter strength testing was additionally found to improve reproducibility significantly. The authors [195] concluded that this method, named the 'Advanced Ash Fusion Test', enables the prediction of slagging/fouling propensity when paired with the boiler temperature profile.

Weiland et al [198] attempted to produce "sticking probabilities" based upon ash fusion testing data. The first assumes a linear dependence between initial deformation temperatures and flow temperatures, giving an incredibly simple method. The second method uses the height of the pellets during testing, where the sticking probability is normalised between the maximum recorded height of the pellet [Max(h)] and the minimum sample height [Min(h)], for which flow temperature is used, giving the following equation:

$$P_{stick}(T) = \frac{Max(h) - h(T)}{Max(h) - Min(h)} \qquad \text{(Eqn. 6.1)}$$

Where h(T) is the height of the pellet at T temperature.

However, these models assume that no liquid phase is present before pellet deformation, which has been shown to be incorrect in other studies [195], as

porous samples can experience initial melting phases without showing external signs of deformation. Additionally, the authors [198] use the assumption that sample height increases solely due to thermal expansion and phase transitions to justify using sticking probabilities only beyond the maximum expansion of the pellet: this is despite the fact that the presence of phase transitions often indicates that liquid phases will be present within the sample during expansion. The authors [198] attempt to differentiate between height increase and decrease-phases by stating that sintering and fusion processes only dominate thermal expansion during periods of decreasing pellet height, yet the rate of sintering is directly related to a change in porosity as a function of time, as outlined in a well-known model of sintering developed by Mackenzie and Shuttleworth [199]:

$$\frac{\epsilon}{\epsilon_0} = e^{-\frac{3t\sigma}{2r_p\mu}} \qquad \text{(Eqn. 6.2)}$$

Where ϵ_0 and ϵ are the initial porosity and porosity after a time period t, respectively; r_p is the pore radius, σ is the surface tension and μ is the ash viscosity. This model suggests that ash viscosity is of critical importance for determining sinter rate, and therefore the presence of even a small quantity of liquid phase will result in sintering and stickiness due to viscous necking enabling the transport of material between particles, contradicting the assumptions of the authors. Therefore, such models that rely solely on IDT/flow temperatures or external pellet deformation will potentially grossly overestimate the temperature at which stickiness will occur, and as such are unreliable.

Ideally, the AFT test should be made as objective as possible, such as the methods reported by Pang et al [195] to accurately record pellet dimensions, and reported in conjunction with other experimental data such as sinter strength and mass spectrometry, in order to determine the presence of liquid phase and volatile species respectively. Doing so will significantly increase both the accuracy and the usefulness of the ash fusion test. The use of empirical models based upon characteristic temperatures is unreliable, since characteristic temperatures rely solely upon visual cues and give no information about the pellet behaviour.

6.2.2 - AFT with Biomass

Although the effect of coal ash composition upon ash fusion testing behaviour is fairly well understood [76], the wide range of composition between different biomass ashes means that determining such correlations can prove difficult. The different compositions and behaviour of biomass ashes means that experience with coal ashes does not translate well. Numerous studies of biomass ash behaviour during ash fusion testing have been published, of which some are discussed below.

Bryers [76] provides a comparison of biomass ash softening temperatures from various studies with previously known coal ash correlations of different types, plotted against the basic percentage (Fe_2O_3+CaO+MgO+K_2O+Na_2O in wt.%) of the ash. Bryers concluded that three types of biomass systems exist, each of which behave differently under ash fusion testing: high Si/K, low Ca ash such as from grasses, low Si, high K/Ca ash such as wood and shells/pits, and high Ca/P ash from waste. Ash softening temperatures of high Si/K biomass were found to decrease significantly with increasing basic concentration, while softening temperatures were found to increase with increasing basic concentration for low SiO_2 biomass ash. Wood bark biomass ashes were found to have high softening temperatures and high basic concentration, but little correlation was observed between the samples.

Vassilev et al [81] extended the concept of different biomass types further, classifying biomass ash into four distinct types. S type biomass is high in SiO_2+Al_2O_3+Fe_2O_3+NaO_2+TiO_2, K type is high in K_2O+P_2O_5+SO_3+Cl_2O, C type is high in CaO+MgO+MnO, and CK type is for compositions containing low acids (<40 wt.%) that are intermediates of the C and K types. These 4 types can be divided into further subtypes, depending upon the acid concentrations, with low and medium acid C and K types available, as well as medium and high acid S type biomass. These classifications are shown in Figure 6.2. Low acid K and CK type biomass ashes are noted by the authors as some of the most problematic, both technologically and environmentally.

Low deformation temperatures (<1100°C) and hemisphere temperatures (<1200°C) were found by Vassilev et al. [81] to be limited to K type and medium acid S type biomass ashes, with high DTs (>1300°C) and HTs (>1400°C) found

exclusively in low acid C type and very high acid S type biomass ashes. Ash acidity was noted to be heavily dependent upon SiO_2 content within biomass ash, and as such silica was determined to play a primary role in biomass ash fusion.

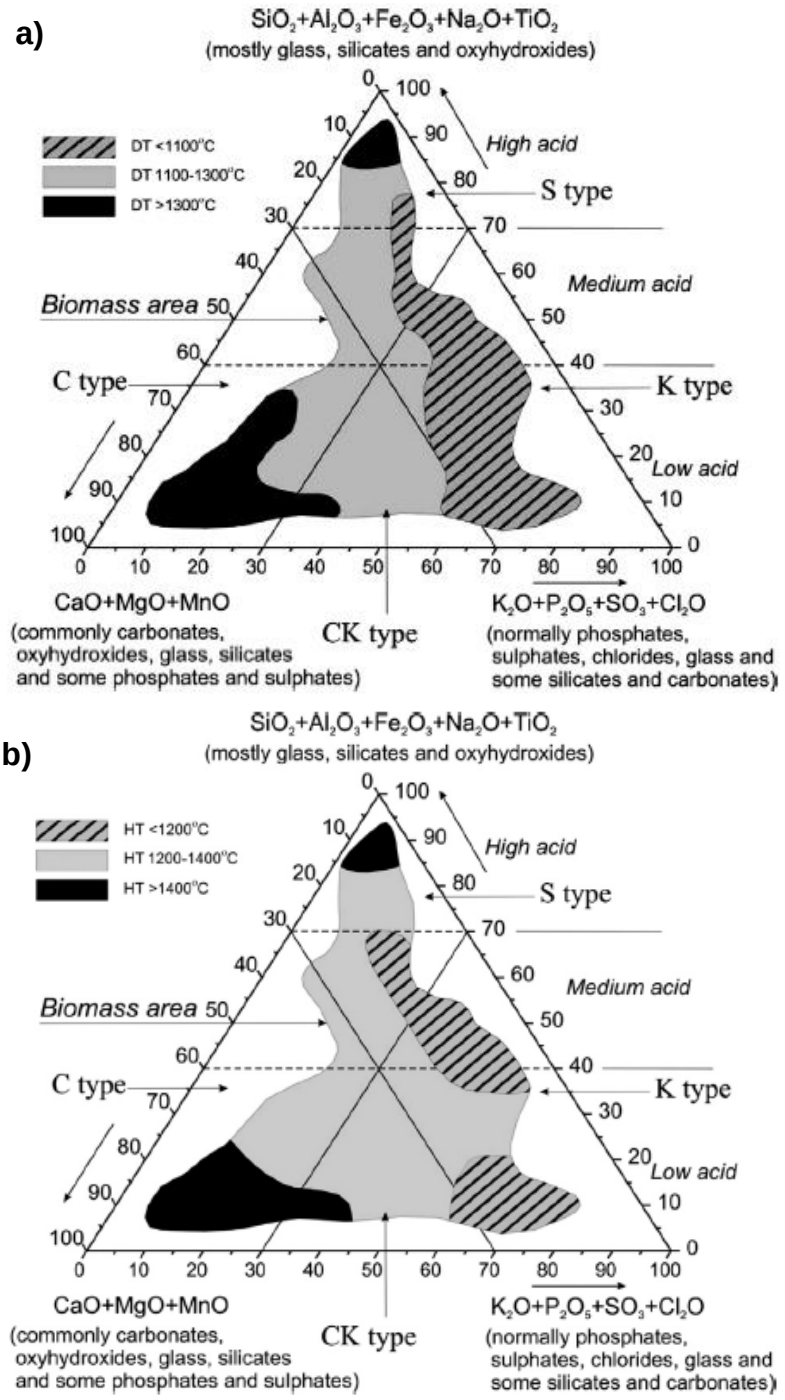

Figure 6.2 – Biomass ash classification based upon ash composition, compared with measurements of a) softening temperature, and b) hemisphere temperature. From [81]

Baxter et al [196] conducted ash fusion tests upon Miscanthus crops and separated leaves and stems. Samples were prepared at 550°C using the

standard biomass ashing techniques outlined in BS EN 14775:2009. Standard AFT measurements were taken, with IDT, HT and FT recorded for each sample. The authors chose to ignore shrinking temperatures due to uncertainties produced by the size of the test pieces and the low resolution of the images. IDT error was found to range between 3-35°C, while HT and FT variation was much better at 5-10°C. Although errors between duplicate samples were low, high variation was observed between similar samples harvested at different times. Samples with lower deformation temperatures were noted to produce swelling at the IDT, with some bubbling present due to the release of volatile gases. Shrinking was visible in some samples at as low as 560°C. Non-linear parabolic correlations were observed for IDT, HT and FT when compared to the base percentage (Fe_2O_3+CaO+MgO+K_2O+Na_2O in wt. %), with minimum temperatures at 40-45% basic components within the ash. Unfortunately, the residual errors on these correlations were not provided by Baxter et al. [196], and the goodness of fit cannot easily be determined. With the presence of numerous significant outliers from the correlations provided, some with over 200°C difference between some data points and the correlation line given, these correlations do not seem entirely reliable.

Although these correlations matched fairly well with those provided by Bryers [76], the Bryers data appeared to intentionally avoid using a parabolic correlation, instead opting for separate non-linear correlations for three different systems of biomass: high Si/K, low Ca ash such as from grasses, low Si, high K/Ca ash such as wood and shells/pits, and high Ca/P ash from waste. Baxter et al [196] provided a separate correlation solely for leaves which provides an excellent fit with no outliers. The leaves were high in Ca and low in Cl and compared to the other parts of the crop, indicating that they belong to a separate biomass system that behaves differently to the leaves and whole crop. The stems, which contained lower Ca and higher K than the other samples, correlated well with the high K_2O samples used in the Bryers study, indicating that a single correlation for different systems of biomass (even different parts of the same plant) may not be the correct approach.

Furthermore, although Vassilev et al [81] did not compare AFTs to base concentration, areas of low deformation temperature (<1100°C) and hemisphere temperature (<1200°C) were found to be limited to K type and medium acid S

type biomass ashes, with high DTs (>1300°C) and HTs (>1400°C) found exclusively in low acid C type and very high acid S type biomass ashes. This lends further weight to the notion that a single correlation for all biomass types is inadequate for the prediction of biomass AFT behavior, since very different systems can show similar behaviour, while similar compositions can show a range of characteristic temperatures.

Pang et al [195] did not report characteristic temperatures, instead opting to record pellet height through the use of edge detection software. The authors do not give ash compositions, making it impossible to determine what types of biomass where used in the context of Vassilev et al [81]. The only composition information is a comparison between shrinking temperature and “Group 1/Group 2”, which are vaguely defined as “predominantly… potassium and sodium” and “essentially calcium and magnesium” respectively. A strong correlation is found between shrinking temperature and Group1/Group 2, despite the data points including a coal ash and multiple different types of biomass. This also is in contrast to the findings of Vassilev et al [81], who state that silica concentration is of significant importance to ash fusion temperatures. It is possible that Pang et al [195] were looking at low acid biomass and coal, and as a result were focused upon C, K, and CK type compositions; however, without knowing the actual compositions, it is impossible to tell, and this is a major drawback of this study.

Li et al [192] studied the effect of kaolinite and dolomite upon the ash fusion behaviour of straw. Kaolinite was observed to increase deformation temperatures significantly in all biomasses, while resulting in a decrease in flow temperature up to a 10% mass ratio of additive to corn stalk. Flow temperatures greatly increased at ratios of 15% and above. Dolomite was observed to increase all characteristic temperatures for all samples. AFTs were considered to be dependent upon the ratio of non-bridging oxygen components to bridging-oxygen components within the ash, behaving as silicate melts. Increases in bridging oxygen concentration typically resulted in increased AFTs, although it did not account for rice stalk having higher concentrations than wheat straw, or for variation in behaviour with the addition of dolomite. Li et al [192] speculated that this may be due to the higher ionic potential of Ca^{2+} and Mg^{2+} in comparison to K^{+}, resulting in higher melting temperatures. This would also explain the behaviour described by Vassilev et al [81], with high HTs found for biomass high in Ca and Mg.

6.2.3 - Slagging Indices

To supplement experimental data, empirical indices derived from the data are often used to predict the severity of the deposition resulting from a composition of ash. Many of these indices were originally developed using coal ash compositions and are often limited to the composition range of the coal ashes within the study. Despite this, these indices are often applied to biomass ash compositions within literature.

Indices are typically based upon oxide components within the ash. Although many indices exist, only those that have been used in multiple studies for biomass are discussed below. The most common index is the base to acid (B/A) ratio, which has been used in numerous biomass AFT studies [119, 196, 197, 200] however, Niu et al [93] note that this may not be entirely reliable, being an index derived from coal ash compositions. Instead, the authors recommend the Biomass Slagging Evaluation Index, although they also state that the absence of key components such as Si, Al, K and Cl is a drawback of such indices. Li et al [192] considered AFT results in the context of the network theory of silicate melts (discussed in Section 5.2.2), comparing AFT temperatures against the ratio of non-bridging oxygen bonds (NBO, Si-O) to bridging oxygen bonds (BO, Si-O-Si), also called the NBO/BO ratio. Other commonly used indices are reported by Seggiani [201] as effective for biomass when used as part of a suite of correlations for ash fusion temperatures, namely the Silica value, Dolomite Ratio, R250 and Basic Percentage, which is additionally used by both Bryers [200] and Baxter [196]. The equations for each of these indices are provided in Table 6.1.

6.3 - Experimental Methodology

6.3.1 - Samples

For this study, experiments were conducted for all biomass ashes and additives, at three different blend rates as outlined in Table 6.2, with ashes prepared according to the methods outlined in Chapter 3.

Table 6.1 - Examples of slagging indices commonly applied to biomass ash compositions in literature

Slagging Index	Equation
Base to Acid Ratio	$\frac{Fe_2O_3+CaO+MgO+K_2O+Na_2O}{SiO_2+Al_2O_3+TiO_2}$
Biomass Slagging Index	$\frac{Fe_2O_3+MgO+Al_2O_3}{CaO+P_2O_5}$
Silica Value	$\frac{SiO_2}{SiO_2+Fe_2O_3+MgO+CaO}$
Dolomite Ratio	$\frac{CaO+MgO}{Fe_2O_3+CaO+MgO+K_2O+Na_2O}$
R250	$\frac{SiO_2+Al_2O_3}{SiO_2+Al_2O_3+Fe_2O_3+CaO}$
Basic Percentage	$Fe_2O_3+CaO+MgO+K_2O+Na_2O$
NBO/BO	$\frac{CaO+MgO+K_2O+FeO-(Al_2O_3+Fe_2O_3)}{SiO_2+2(Al_2O_3+Fe_2O_3)}$

Table 6.2 - Test matrix of samples used in heating experiments

% Adtv. to dry fuel	0%	5% (PFA)	15% (PFA)	25% (PFA)	5% (Kao)	15% (Kao)	25% (Kao)
OCA	X	X	X	X	X	X	X
WWA	X	X	X	X	X	X	X
BA	X	X	X	X	X		
FA	X	X	X	X	X		
PFA	X						
Kaolin	X						

6.3.2 - Sample Preparation

Ash fusion tests were conducted following the procedures described in ASTM D1857, using ashes prepared according to the methods outlined in Chapter 3. Samples were prepared using a solution of deionised water with 10% dextrin as

a binder, in a cylindrical mould. The solution was added to the ash in drops using a pipette to minimise leaching and to ensure that a structurally sound pellet is produced. Once the mixture was of the correct consistency, it was inserted into the mould and dried in ambient air for approximately 20-30 minutes. The pellets were then placed onto ceramic tiles in duplicate and left overnight.

6.3.3 - Procedure

Up to four tiles were then placed onto a stand, which was inserted into a Carbolite CAF tube furnace, equipped with a greyscale camera for the capture of images. The samples were then heated up to 550°C, at which point the temperature was set to increase at a rate of 5°C/min under oxidising conductions, up to a maximum temperature of 1585°C according to the limits of the furnace. The camera was set to take images at 5°C intervals.

Standard ash fusion testing records the temperatures at which four characteristic features are observed for each sample by analysing the images post-test through observation, rather than direct measurement:

Shrinking Temperature (ST): the temperature at which the first signs of rounding of the test piece occurs, due to melting (typically taken at 95% of the original height).

Deformation Temperature (DT): the temperature at which the edges of the test piece start to round.

Hemisphere Temperature (HT): the temperature at which the test piece approaches the shape of a hemisphere, where the height becomes equal to half of the base diameter.

Flow Temperature (FT): the temperature at which the ash melt is spread out of the supporting tile in a layer, the height of which is equal to one third of the height of the test piece at the hemisphere temperature.

An issue with this method is the inherent subjectivity of the analysis, even before taking into account the different behaviour of some samples (particularly when comparing coal and biomass sample behaviour): some samples experience significant swelling, making softening and hemisphere temperature determination impossible. In addition, duplicate samples may behave differently due to minor

changes in composition (should the sample be inhomogeneous) or structure as a result of different packing density within the mould or faults introduced when removing the sample from the mould. It has been reported that ash fusion testing with the same operator, procedure and equipment will generally yield reproducibility to within 30-40 °C, but potentially as high as 50-70 °C [195].

As a result, in addition to the standard procedure, edge detection of the pellets was attempted. However, the images were of low resolution, and the background of the furnace was too noisy and of poor contrast in comparison to the pellets, meaning that detection of individual pellets was not possible. Image sharpening followed by increasing contrast did not help, and so pellet height was recorded instead.

The height of the pellet in pixels was measured within the first image, corresponding to the 5mm height of the sample mould, and measured for each subsequent image to produce a profile of pellet height with increasing temperature. This allows for more precise determination of shrinking and flow temperatures, and easier comparison between the heating behaviour of different pellets. In order to avoid subjectivity, the use of deformation temperature has been avoided: ST, HT and FT can all be determined solely through the height of the pellet.

6.4 - Ash Fusion Testing Results

6.4.1 - Height Profiles

The height profiles of the samples without additives are provided in Figures 6.3a-d. OCA was observed to experience shrinking at much lower temperatures than the other samples, with shrinking occurring at ~900°C, indicating that slagging and fouling onset will occur at much lower temperatures than for the other biomass. In contrast, FA showed no shrinking below 1200°C., close to the onset of significant melting and HT. WWA similarly showed little deformation before the onset of large liquid phases and critical viscosity. BA showed signs of deformation at below 1000°C; however, the pellet retained some structure up to 1400°C, the highest onset of melting seen in the non-additive samples. Bubbling within the BA sample is clearly visible from the height profiles.

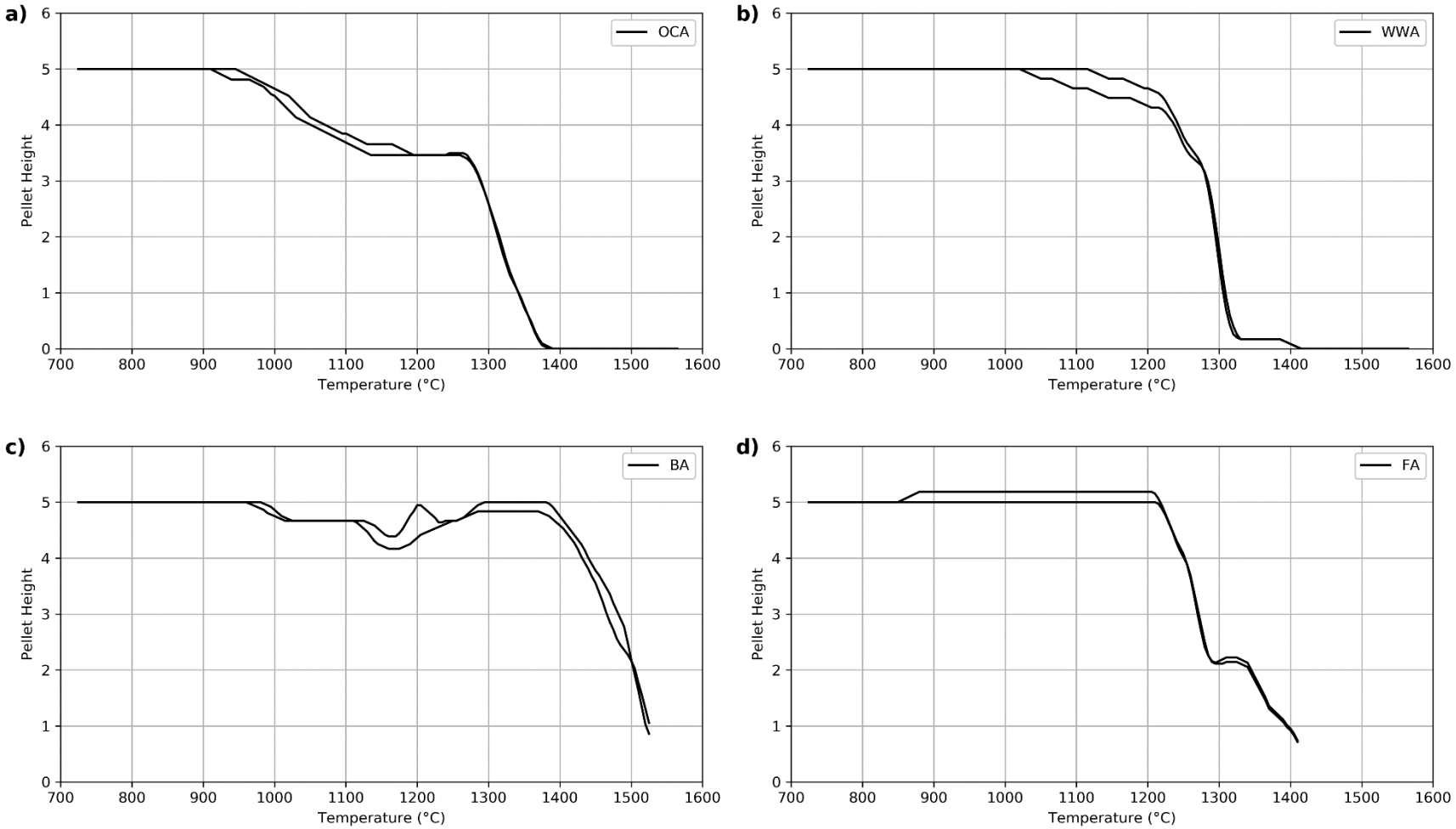

Figure 6.3 – AFT height profiles for a) OCA; b) WWA; c) BA; and d) FA

The addition of PFA to the samples resulted in the height profiles found in Figures 6.4 a-d. PFA was observed to increase initial STs for all BA and WWA samples, indicating that PFA addition may reduce the temperature range of deposition within a boiler. OCA5%PFA also increased STs by ~100°C: however, further PFA addition resulted in earlier shrinking. This indicates that deposition will be present in lower temperature regions of the boiler, and as such high concentrations of PFA addition should be avoided with olive cake biomass. Initial shrinking temperatures were significantly decreased for PFA addition to the FA sample.

PFA addition showed significantly increased flow temperatures for all additive rates for OCA, WWA and FA, with successive increases in PFA concentration resulting in a further increase in flow temperature in all cases. Of these three samples, 5% PFA addition had the least effect upon OCA flow temperatures, with a ~25°C increase observed compared to greater than 50°C for the same rate with WWA and FA. In contrast, BA flow temperatures were significantly decreased with PFA use, decreasing by ~200°C. This indicates that critical viscosities are reached at temperatures well below typical combustion temperatures, and that a severe flowing slag will be present when using PFA as an additive with bagasse. As such, PFA use with bagasse should be avoided.

As OCA and WWA were the main two candidates for additive use during combustion, the experiment was repeated using KAO: these results are shown in Figure 6.5. KAO had a significant effect upon flow temperatures, with 5% KAO resulting in a 100°C increase for OCA (Figure 6.5a) compared to the 25°C increase observed with PFA use (Figure 6.4a). Further, the addition of KAO caused initial deformation temperatures to increase, indicating that both slagging and fouling are potentially improved. Once again, the greatest increase was observed for a 5% addition, similar to the OCA/PFA blends tested.

The use of KAO with WWA (Figure 6.5b) increased flow temperatures to above the limit of the AFT furnace (1585°C), and as a result flow temperature was not reached. Such compositions would not result in a flowing slag, instead building rapidly on the walls and surfaces of the boiler. This would result in potentially dangerous shedding events occurring frequently, which could damage the boiler tubes and refractory materials. Due to this, KAO addition at the rates measured is not advised for use with WWA.

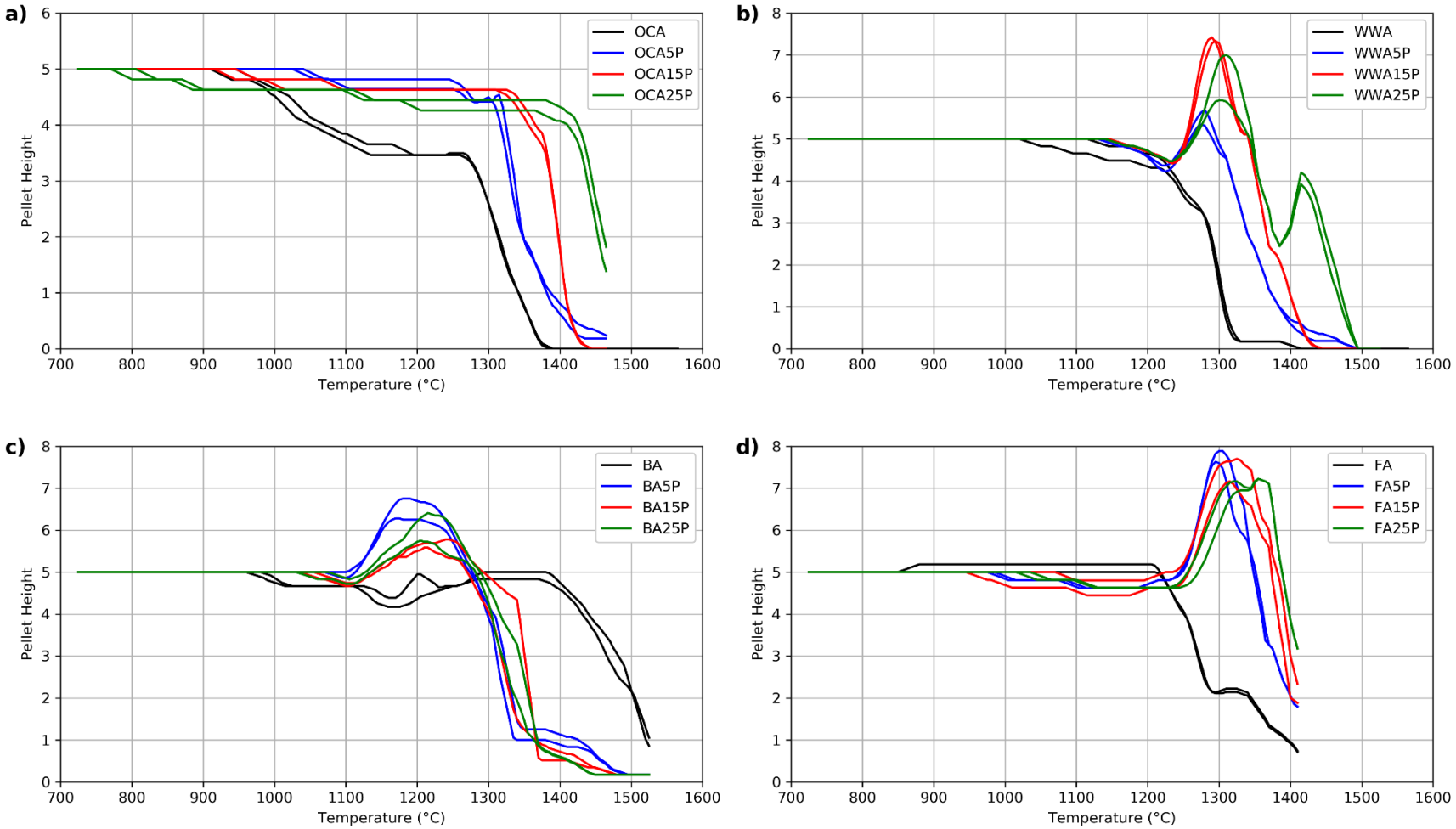

Figure 6.4 - AFT height profiles for PFA blends compared to a) OCA; b) WWA; c) BA; and d) FA

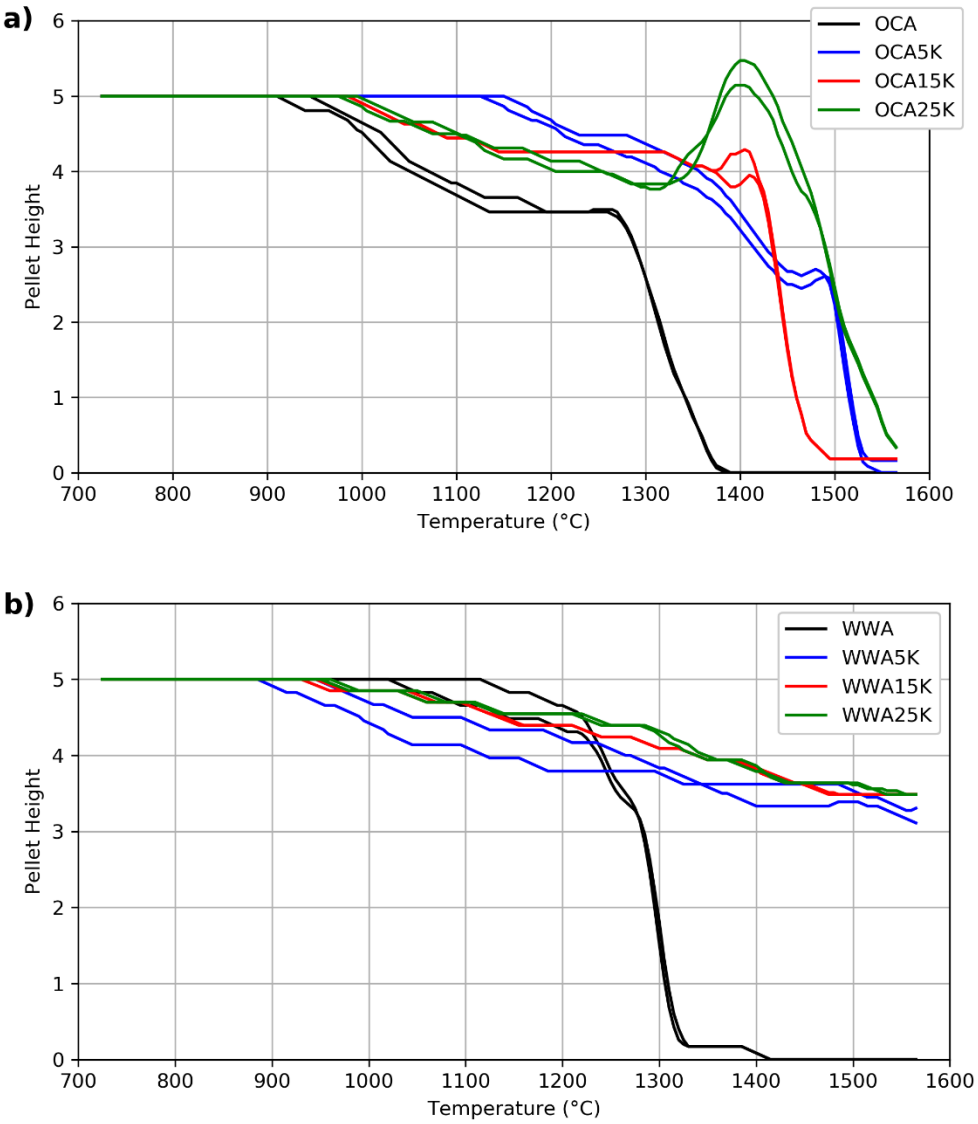

Figure 6.5 - Comparison of AFT height profiles for KAO blends with a) OCA; and b) WWA

6.4.2 - Ash Fusion Temperatures

Table 6.2 summarises the ash fusion testing results, using the criteria established in Section 6.3.3. The PFA results allow for a useful baseline comparison to coal, due to being combusted within a large-scale power station. OCA and BA showed shrinkage at similar temperatures of 935°C, approximately 100°C lower than for coal. In contrast, WWA shrinkage did not occur until 1075°C, with FA displaying the highest ST in the study at 1205°C. A 5% rate of additive initially increased ST for OCA, WWA and BA while significantly reducing ST for FA samples. However, a further increase resulted in a large reduction in ST for OCA (with both PFA and KAO addition) and BA samples: OCA 25% KAO showed the earliest STs, with an

average of 790°C. Conversely, STs increased with greater additive use for both WWA and FA. KAO use with white wood markedly decreased STs.

Table 6.3 - Average ash fusion temperatures for biomass ash samples and biomass-additive mixes

	ST		HT		FT	
OCA	935	±10	1290	±5	1325	±5
OCA5%PFA	1027.5	±5	1325	±5	1360	±5
OCA15%PFA	937.5	±15	1380	±5	1390	±5
OCA25%PFA	790	±15	1437.5	±10	1460	±5
OCA5%KAO	1135	±10	1445	±5	1500	±5
OCA15%KAO	995	±5	1430	±5	1440	±5
OCA25%KAO	985	±10	1475	±5	1520	±5
WWA	1075	±40	1275	±5	1290	±5
WWA5%PFA	1130	±5	1320	±5	1375	±5
WWA15%PFA	1150	±5	1345	±5	1390	±5
WWA25%PFA	1140	±5	1350	±5	1452.5	±10
WWA5%KAO	927.5	±25	-		-	
WWA15%KAO	932.5	±5	-		-	
WWA25%KAO	962.5	±5	-		-	
FA	1205	±5	1260	±5	1370	±5
FA5%PFA	982.5	±5	1347.5	±10	1410	±5
FA15%PFA	1012.5	±25	1380	±5	1430	±5
FA25%PFA	1030	±10	1380	±5	1460	±5
BA	980	±10	1470	±5	1500	±5
BA5%PFA	1090	±5	1320	±5	1325	±5
BA15%PFA	1055	±5	1330	±5	1340	±5
BA25%PFA	1055	±10	1325	±5	1340	±5
PFA	1018	±5	1308	±5	1320	±5
KAO	1170	±10	-		-	

The range between ST and HT varies significantly. In contrast to ST results, FA samples showed the lowest recorded HT from the experiment at 1260°C. All ash samples showed HTs within 50°C of PFA, which recorded the highest HT of 1308°C. FTs of PFA, OCA and BA were similar at approximately 1320°C, with WWA recording the lowest FT of the experiment at 1290°C. The use of additives

was shown to consistently increase both HT and FT across all samples. The use of 5% PFA was most effective when mixed with bagasse, increasing HT by over 150°C and FT by 175°C. HT and FT temperatures increased with increased PFA concentration, with the exception of BA 15% PFA.

KAO significantly increased HT and FT compared to PFA. OCA 5% KAO resulted in higher FT and HT than the highest concentration of PFA tested and increased both by over 150°C when compared to an equivalent concentration. The use of KAO with WWA at all rates tested increased HT and FT to beyond the temperature limit of the furnace (1580°C). This indicates that flow temperature will not be reached within the combustion zone of the boiler, creating thicker slagging deposits with a tendency to experience shedding events. Shedding events in this area of the boiler are highly undesirable due to the potential to damage firing nozzles and refractory material, particularly since deposits are usually dense due to the heavier components of the ash concentrating within the slags. As such, the use of KAO with WWA at blend rates of 5% and above is not recommended. The use of KAO with OCA however results in FTs that are comparable with combustion temperatures. This will prevent shedding events and produce a flowing slag that is desirable in large scale PF combustion.

For comparison the ST and HT results have been plotted in the context of the Vassilev biomass classification [81]. As discussed in Chapter 3, the ash compositions are predominantly within the HS type classification. As a result, it would be expected that many of the HT and ST temperatures should lie within the high melting temperature regions outlined within the Vassilev study [81]. A comparison of softening temperature recorded in this study against Vassilev deformation temperatures (Figure 6.6) shows that all of the experimental values within the high DT region are smaller than the 1300°C lower boundary, with many experiencing deformation at temperatures below the low DT region limit of 1100°C.

The main reason for this discrepancy is likely due to differences between the typical composition of biomass, upon which the classification is based, and the composition of the additives. The additives contain significantly greater alumina and (in the case of PFA) iron than would be found in biomass ash compositions.

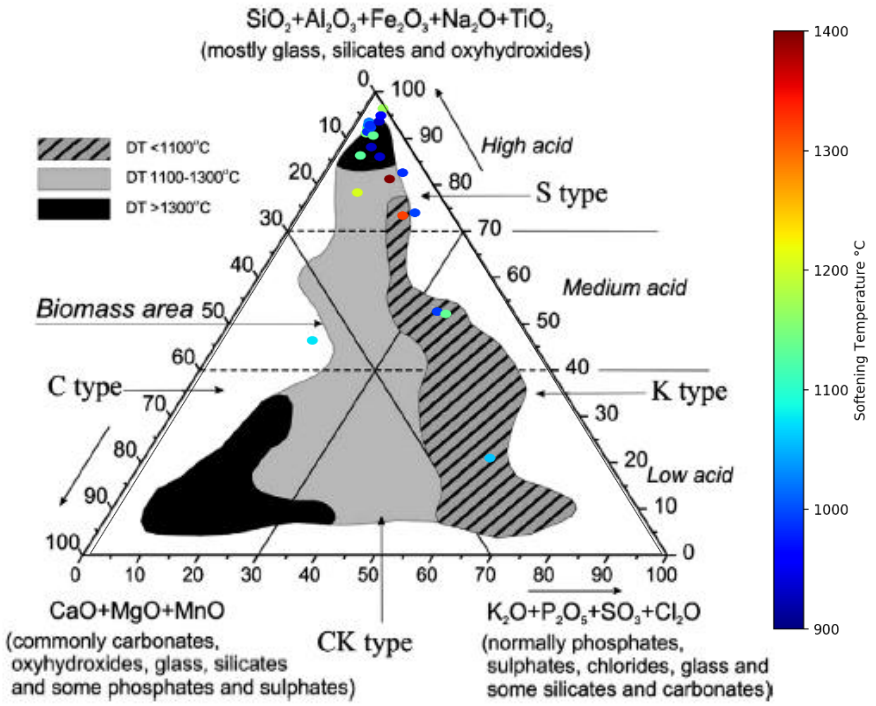

Figure 6.6 - Comparison of softening temperatures against Vassilev et al [81] classification and results

As established in Chapter 5.2.2, both iron and alumina can behave as bases when few network modifiers are present. The addition of the additive at the rates tested in this study increases Al_2O_3 content to over 10 wt.% for all samples, with the exception of OCA5%PFA. Above 10% Al_2O_3, it has been shown that Al_2O_3 begins to exhibit network modifying properties [179], which would increase the presence of melt phases. Further, iron has been shown to have a significant effect upon viscosity [91], and transitions between valence states has been observed in coal ashes during heating that decrease melting temperatures [182].

Comparison of hemisphere temperatures with the regions provided by Vassilev et al (Figure 6.7) shows a better match, with high temperature results (>1500°C) found exclusively in the HS type classification. However, several low temperature results (<1350°C) also fall within this region, and within regions where HT is expected to be greater than 1400°C, indicating that biomass classification systems may not be sufficient in predicting the behaviour of biomass and Al-Si additive blends. Additionally, blends of 5% additive with OCA show compositions

within the MK type classification, where HT is expected to be <1200°C: instead, recorded HTs are above 1300°C.

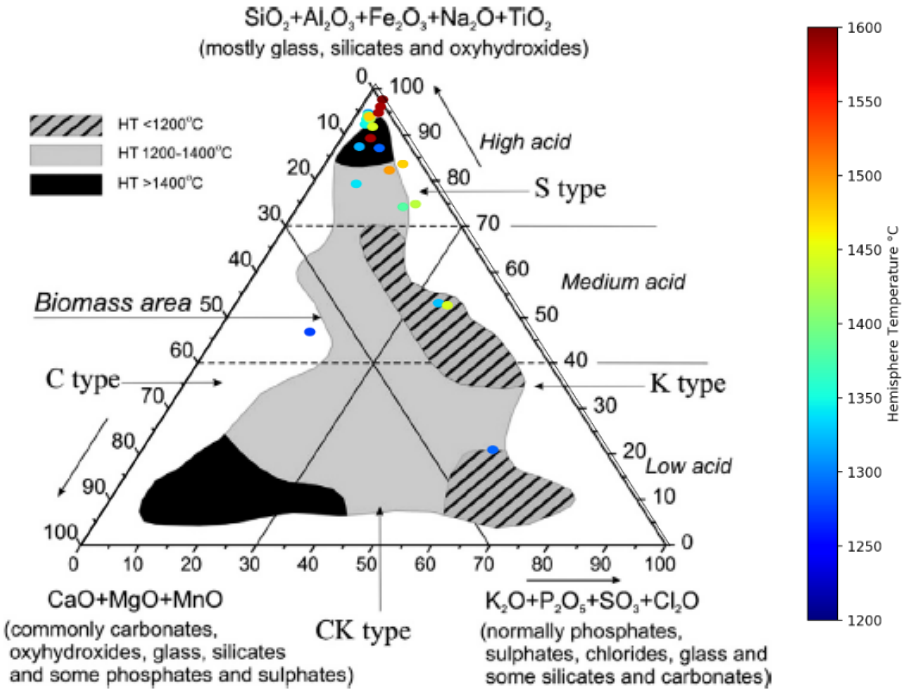

Figure 6.7 - Comparison of hemisphere temperatures against Vassilev et al [81] classification and results

HTs within this study appear to be lower in many cases than those observed by Vassilev et al [81], while STs are much lower. As discussed in Section 7.2.1, discrepancies exist between traditional ash fusion tests, particularly between different labs. This makes it difficult to determine whether these differences are due to the use of additives rather than biomass compositions, or whether differences and the imprecise nature of the ash fusion test is causing these differences. In any case, clearly different trends exist between the results of this study and those previously reported.

6.4.3 - AFT Correlations

ST, HT and FT were compared against various slagging and fouling indices, as well as oxide concentrations within the sample, to determine possible correlations between AFT indicators and traditional indices. Initial correlations between characteristic temperatures showed that HT and FT have an extremely strong correlation, as expected and in line with findings of literature. This is shown in Figure 6.8. 'r' is the Pearson correlation coefficient, where 1 is a perfect positive

correlation, -1 indicates a perfect negative correlation, and 0 indicates no correlation. 95% confidence intervals are also provided.

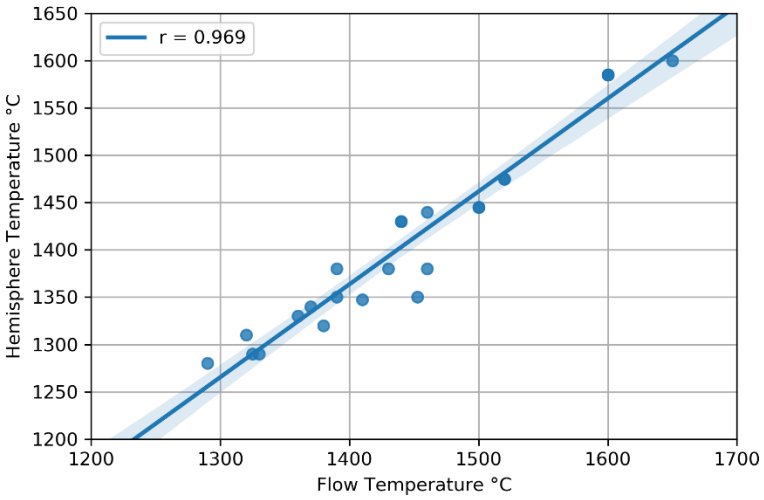

Figure 6.8 – Linear regression of hemisphere and flow temperatures

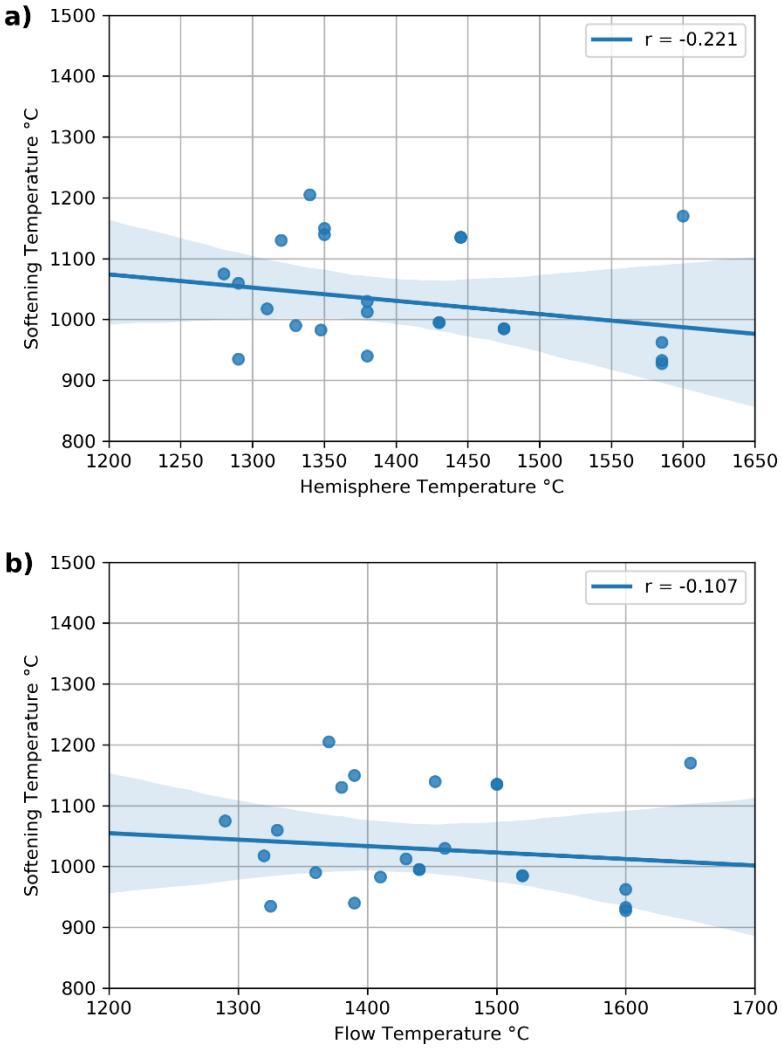

Figure 6.9 – Linear regression of softening temperature with a) hemisphere temperature; and b) flow temperature

However, ST does not correlate with HT or FT, as shown in Figures 6.9a and b respectively. This is likely because HT and FT are determined by the same melting mechanisms (predominantly due to silicate melting), while ST can be determined by any combination of silicate melting, volatilisation and phase transformations depending upon the sample composition. In addition, the primary use of Al-Si additives is to capture potassium that would otherwise be emitted in the form of KCl, meaning that the rate of volatilisation is different between samples with and without additives. This has the potential to change the mechanisms by which shrinking is occurring in samples, making a comparison of STs between different samples unreliable without additional information, such as knowledge of volatilised elements.

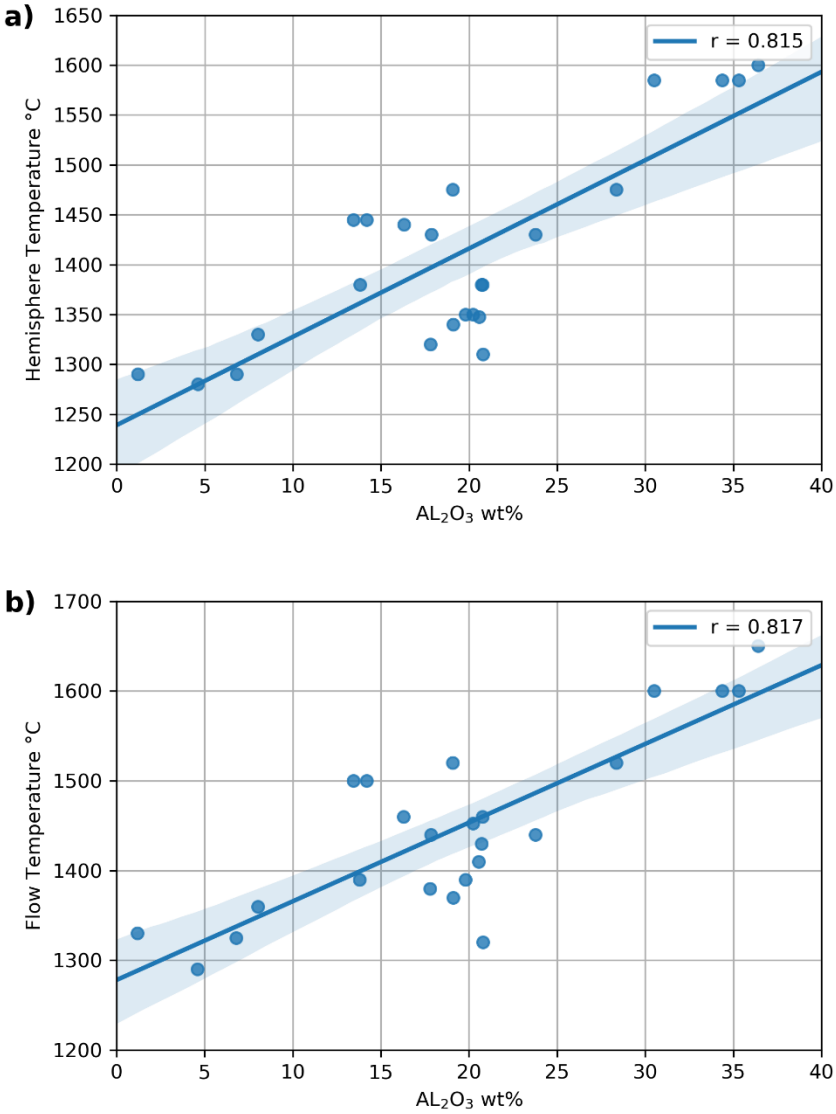

Figure 6.10 – Correlation of Al_2O_3 concentration within sample with a) hemisphere temperature and b) flow temperature

Of the ash components, none showed any correlation at all with ST, and only two oxides showed any signs of a reasonable correlation with FT and HT. Al_2O_3 concentration had a strong positive correlation with both HT (Figure 6.10a) and FT (Figure 6.10b), indicating that the use of additives was increasing melting temperatures and inhibiting the onset of melting phases within the pellets. This is in line with expectations from literature, with the conversion of silicates to higher melting temperature aluminosilicates observed in previous studies.

Despite the strong correlations between Al_2O_3, SiO2 and Fe_2O_3 concentrations within samples as reported from principal component analysis in Chapter 3 (Figure 3.2), no correlation was found between silica (Figures 6.11a and b) or iron (Figures 6.11c and d) content with both HT and FT. The only other ash component to show any reasonable linear correlation with HT and FT was MgO concentration (Figures 6.12a and b, respectively). Although CaO concentration (Figures 6.12c and d) shows a similar trend and shows a positive correlation with MgO concentration in Figure 3.2, the correlation coefficient is reduced and cannot be considered a good fit.

It should be noted that MgO and Al_2O_3 concentration are negatively correlated in Figure 3.2, with the opposite correlation arrows reflecting this. As Al_2O_3 has a better fit, it also has a better coefficient of determination (r^2), which indicates the proportion of variance in the dependent variable (in this case HT and FT) that is predictable from the independent variables (ash composition). Therefore, it can be reasoned that Al_2O_3 concentration is the main factor in determining ash flow temperatures from these results.

Slagging indices were also compared to AFT results. Although none of the indices showed a strong linear correlation, basic percentage and base-to-acid ratio both showed a reasonable non-linear logarithmic correlation against HT and FT results (Figure 6.13), with a stronger correlation present for hemisphere temperature. This indicates that the basic concentration is a key indicator in determining ash fusion temperature, and hence ash melting and flow behaviour. Indices which solely utilise acidic components failed to give any meaningful correlations.

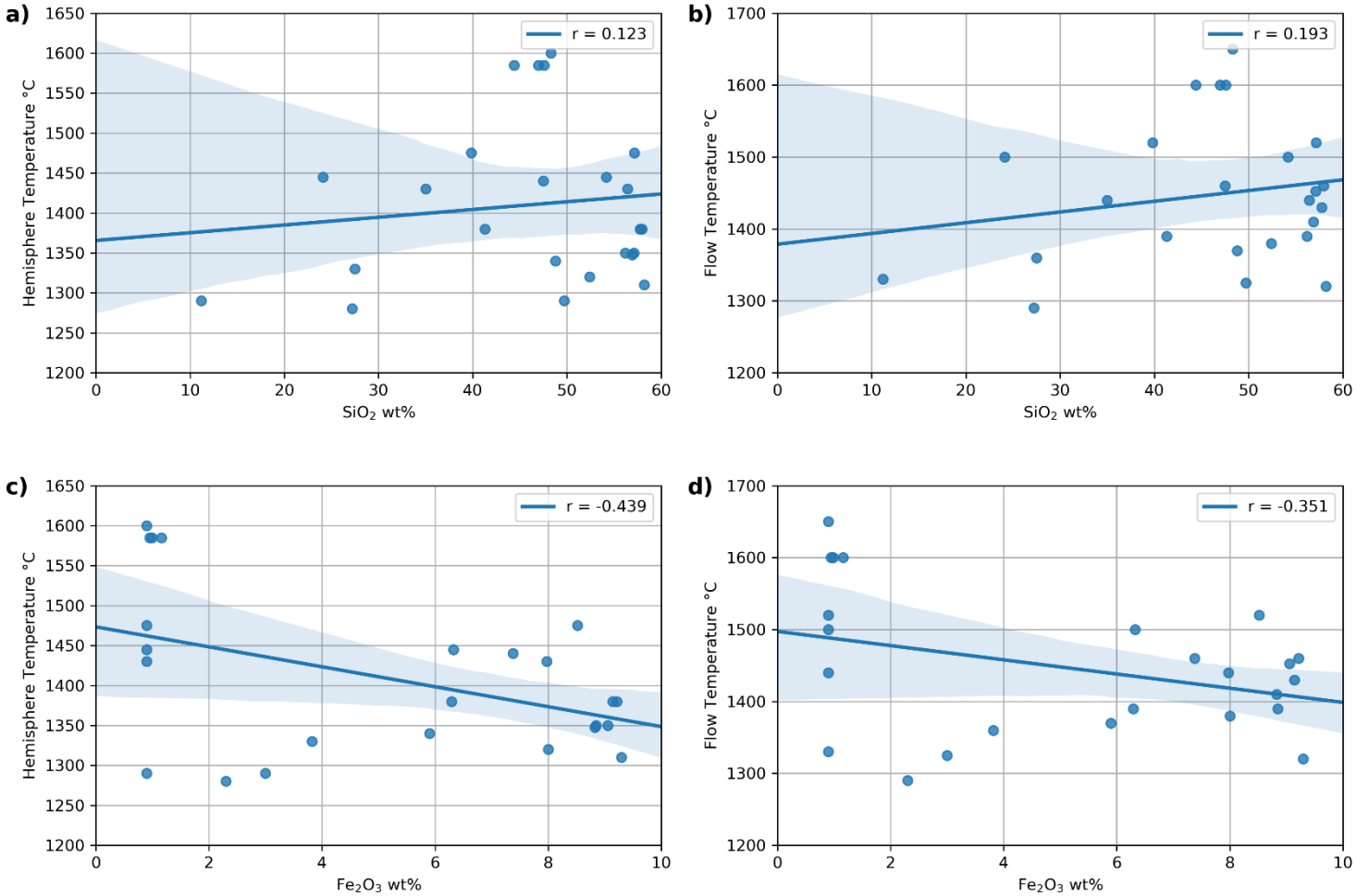

Figure 6.11 – Linear regression for SiO2 with a) hemisphere temperature; and b) flow temperature; and Fe2O3 with c) hemisphere temperature; and d) flow temperature

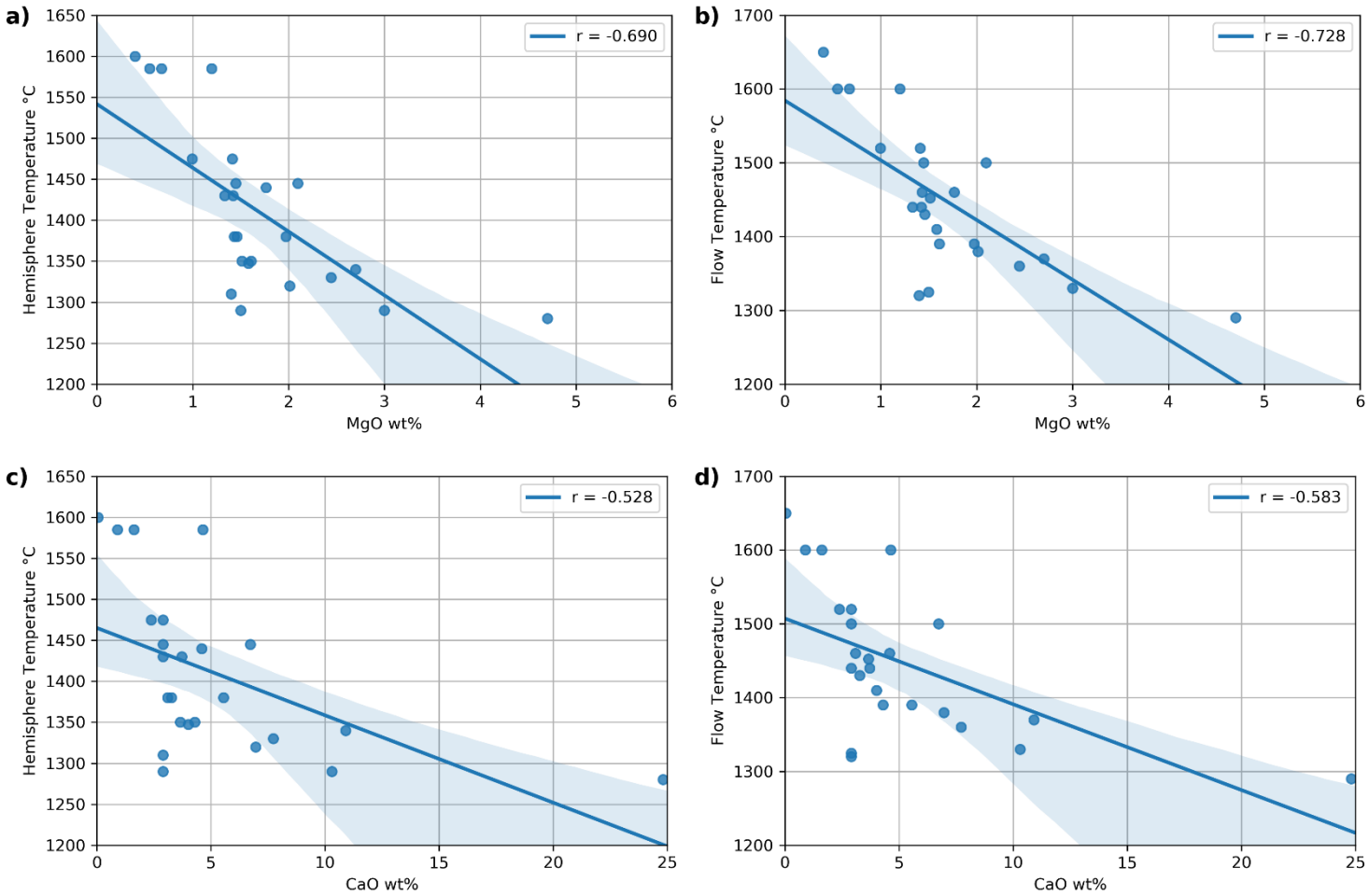

Figure 6.12 – Linear regression of MgO with a) hemisphere temperature; and b) flow temperature; and CaO with c) hemisphere temperature; and d) flow temperature

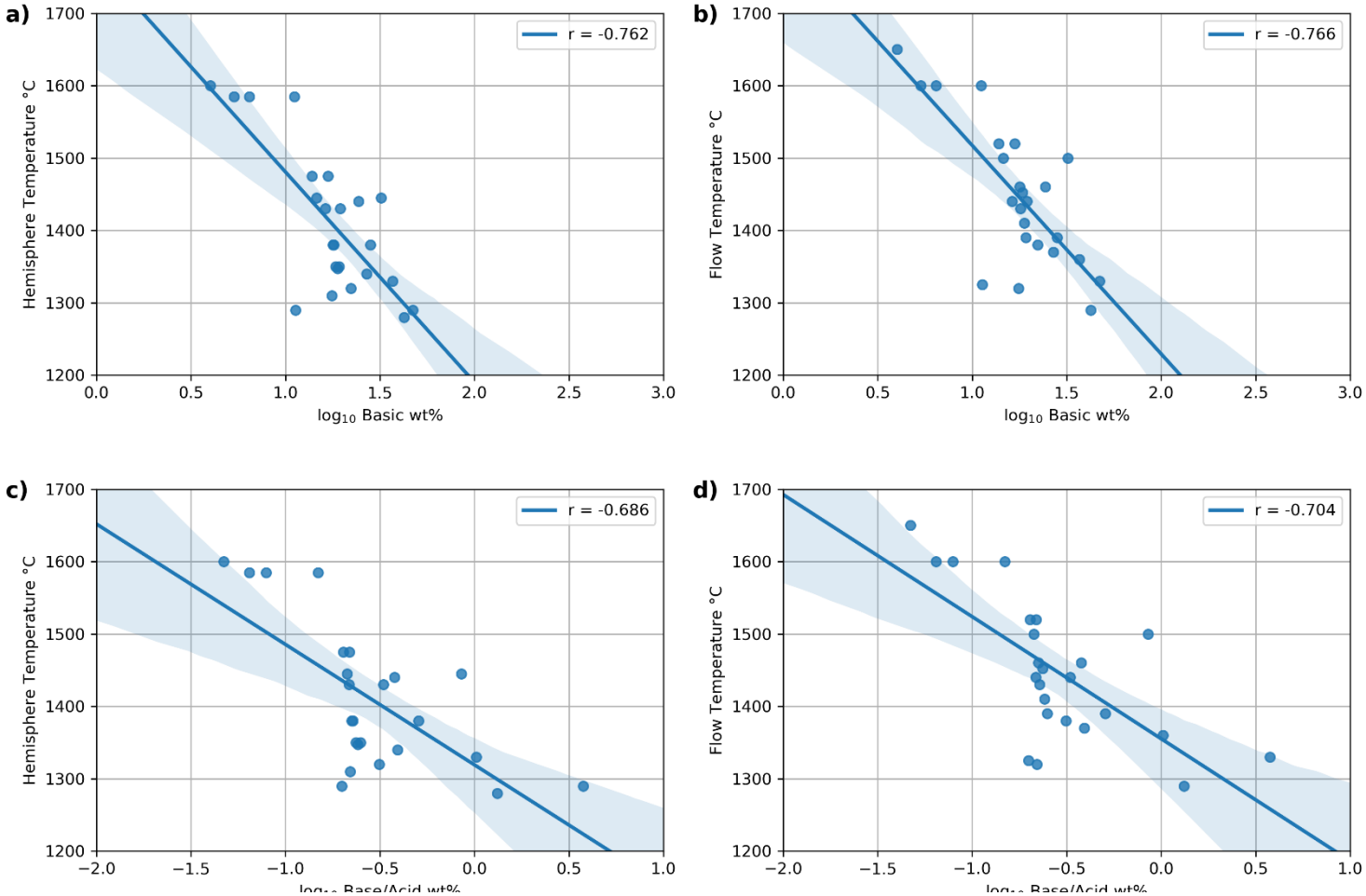

Figure 6.13 – Non-linear regression of basic wt% with a) hemisphere temperature; and b) flow temperature; and base/acid ratio with c) hemisphere temperature; and d) flow temperature

6.5 - Summary

Ash fusion testing is a well-established standard method for investigating the melting behaviour of ashes and hence the slagging and fouling potential of solid fuels. However, a review of literature shows that the standard test suffers from inconsistent results, due to the qualitative nature of the test. As such, new methods have been established in an attempt to improve the ash fusion test.

Ash fusion testing has been conducted upon the biomass ashes and biomass/additive blends used in this study, with the pellet height recorded at temperature intervals of 5°C in order to remove subjectivity as recommended in the literature. Results showed that BA, with its high silica content, had the highest flow temperatures, while OCA experienced significant deformation at lower temperatures when compared to the other samples. The addition of PFA to the samples resulted in higher flow temperatures, indicating that slagging would be lessened within boilers, with the exception of BA where flow temperatures were substantially decreased, indicating that slagging deposition would be severely increased with PFA addition to high silica biomass. OCA5%PFA was observed to increase deformation temperatures by ~100°C, indicating that fouling issues may be reduced with similar additive rates; however higher additive concentrations had a negative effect upon deformation temperatures.

Kaolin was shown to be significantly more effective at increasing flow temperatures when compared to PFA at the same rates, with flow temperatures increased for OCA5%KAO by ~200°C compared to a ~25°C increase for OCA5%PFA, when compared to OCA. In addition, deformation temperatures were also increased, indicating that OCA-KAO ash compositions may offer substantially improved slagging and fouling deposition in comparison to OCA ashes. A comparison of ash fusion profiles with viscosity results showed that the temperature of critical viscosity for OCA corresponded with the point of pellet collapse during ash fusion testing, indicating that this method of ash fusion testing may potentially be used to determine T_{cv}. The addition of 5% kaolin was expected to increase viscosities substantially, and the increase in flow temperatures to typical combustion temperatures reflected this. This will prevent shedding events and produce a flowing viscous slag desirable in large scale PF combustion.

These results indicate that kaolin addition to high K, high Cl biomass such as OCA shows promise in making such compositions viable for pulverised fuel combustion.

Flow temperatures for WWA-KAO blends were increased to beyond the upper temperature limit of the furnace (1585°C), indicating that such compositions would result in non-flowing slagging deposits. Deposits displaying this behavior will experience shedding events, potentially damaging refractory material and boiler tubes. As such, the use of KAO with WWA at blend rates of 5% and above is not recommended. The use of KAO with OCA however results in FTs that are comparable with combustion temperatures.

Ash fusion temperatures were compared to results found in literature. Deformation temperatures were notably lower than those provided in the literature, which was postulated to be due to the Fe_2O_3 and Al_2O_3 concentration and the presence of basic components. Hemisphere temperatures were shown to be slightly lower than in the literature, although ash compositions falling within certain type classifications varied significantly. It was difficult to determine why this was the case, due to the inherent discrepancies of ash fusion temperatures, and since the results here considered both biomass and biomass-additive blends in the context of classifications designed for biomass ash compositions.

Finally, correlations were considered for ash fusion temperatures, ash compositions and slagging indices. Strong correlations were found between HT and FT, while no correlation was observed between ST and both HT and FT. Additionally, ST was found to have no correlation with any ash component or slagging index. Only Al_2O_3 and MgO concentration was found to have any reasonable correlation with both HT and FT. Although SiO_2 and Fe_2O_3 concentrations were shown to correlate strongly with Al_2O_3 concentration in Chapter 4, no correlation was observed here with either HT or FT, indicating that Al_2O_3 concentration is the most crucial component of the ash in determining slagging behavior. Slagging indices showed no linear correlation with HT and FT; however, non-linear semi-logarithmic correlations were established for basic percentage and base to acid ratio.

Chapter 7 - Sinter Strength Testing

7.1 - Introduction

Ash fusion testing and viscometry are useful indicators of the slagging potential of ash compositions. However, viscometry is restricted to above ash flow temperatures, and although ash fusion testing is conducted over a wide range of temperatures, the test is unreliable for hemisphere temperatures and below for the reasons outlined in Chapter 6. As a result, neither test gives a good indication of the fouling potential of an ash composition.

Sinter strength testing was developed in the 1950s to recreate typical fouling deposition behaviour over a range of temperatures, with measurements indicating the strength of the resulting deposit and the subsequent soot blowing force required to remove such deposits.

This chapter begins with a review of sinter strength testing and issues related to deposition strength and soot blowing in boilers, including previous experimental experience in this field. The method used for sinter strength testing is described, with additional information provided with regards to the different behaviours observed. Sinter strength measurements are provided and discussed, with SEM-EDX imaging and XRD spectra of the samples used to supplement the results and to give insight into the mechanisms involved. Finally, sinter strength results were compared to the ash composition of the samples through linear regression, in order to determine whether any particular ash components were having an effect upon sintering behaviour.

7.2 - Deposition Strength

Deposits with less porosity, and therefore a higher degree of sintering, typically exhibit high mechanical strength. This is of importance for soot blowing, since a deposit will only be removed via soot blowing when the PIP exceeds the strength of the material, either by shearing or compression. Senior et al [130] determined that a 25% deposit porosity is a critical rate for deposit removal when soot blowing, using the model developed by Mackenzie and Shuttleworth [199]

(Chapter 6, Equation 6.2) for predicting the change in porosity as a function of time, or the rate of sintering. Liquid phase or viscous flow sintering (as discussed in Chapter 2.4.2) is much faster than solid-state sintering [104], and so samples that contain some liquid at sintering temperature are typically more sintered and hence stronger than those that remain in the solid-state.

A study by Barnes et al [128] found that coal slagging deposits at zero porosity had compressive forces ranging from 96.5 MPa to over 2,740 MPa. As porosity increased to 25%, compressive strength reduced to 68.5 MPa. Although compressive forces are the main method of removal, soot blowing will additionally induce a temperature gradient, creating further thermal stresses in the deposit and aiding removal [114].

Equation 2.13 highlights the importance of ash viscosity in determining the sinter rate, and in turn, it would be expected that porosity would reduce as a result of increasing temperatures leading to decreased viscosity. Senior et al [130] state a viscosity of 10^7-10^9 Pa s is important for sintering of convective deposits, which previous Urbain model predictions for OCA suggest should occur at approximately 700°C. It would be expected that this critical viscosity will be observed as a steep increase in sinter strength with an increase in temperature.

Studies show that the hardest deposits result from strongly sintered components within the ash composition, and that ashes containing significant amounts of alkali salts with low initial melting temperatures (particularly potassium compounds), that remain sticky throughout a larger region of the boiler, are the main cause [98, 113, 133, 135, 142]. This in turn suggests that deposition resulting from biomass containing significant amounts of potassium, such as olive cake, may be particularly problematic in terms of removal via soot blowing. However, the addition of aluminium silicate based additives, such as coal pfa, have been observed to have a significant effect upon the sintering behaviour of biomass ash [89, 134, 140], by promoting the formation of potassium aluminium silicates over lower melting potassium silicate compounds. Barisic et al [134] in particular showed that coal pfa can be used to reduce sintering and fouling via the agglomeration mechanism in olive waste.

7.2.1 - Sinter Strength Compression Testing

Sinter strength compression testing is used to determine the strength of the bonds between ash particles after heating, and in turn the strength of the resulting deposit. Typically, ash pellets are made using a standard method, heat treated at a set temperature for an extended period, allowed to cool and the compressed. The peak compressive strength is recorded. The method differs in significant ways to how full-scale and pilot-scale deposition would form: the effect of any condensed volatile species is likely minimal in such a method. In addition, while deposits are formed from particles cooling and/or condensing from combustion and settling on substrates, the test pieces in this case are only heated once particles are already in close proximity, and never to combustion temperatures. In the case of fluid bed combustion, bed material and ash reactions with this material will also play a role in agglomeration. Finally, if tests are conducted under atmospheric conditions, the role of sulphur and chlorine in sintering, which can play a significant role, may not factor to the same extent.

Barnhart and Williams [202] determined the sintered strength of pellets after heat treatment, made from fly ash taken from an operating boiler, providing a basis upon which a range of studies have been developed for both coal [109, 111, 203-209] and biomass [195, 210-213] sintering, some of which will be discussed below.

Various figures for how compression strength translates to deposit removal are provided in the literature. Pohl and Juniper [114] state that the original Barnhart sinter strength test found that compressive strengths of greater than 34.47 MPa (5,000 psi) were difficult to remove in a furnace. Gibb [203] gives a much lower limit of 5 MPa. Bryers [76] gives the compressive strength of fly ash at ~930°C (1700°F) as an important fouling indicator. Pellet strengths of below 6.89 MPa (1000 psi) are considered to produce low fouling deposits, between 6.89 and 34.47 MPa (1000-5000 psi) are considered to produce medium fouling, between 34.47 and 110.32 MPa (5000-16000 psi) are considered high fouling deposits, and greater than 110.32 MPa produces severe deposition. However, lignitic coal was shown to not correlate with this fouling criteria, despite sinter strength and temperature correlations agreeing reasonably well with other data.

7.2.1.1 - Coal Ash Experiments

The Gibb [203] method differs from the Barnhart and Williams method in that it uses relatively low temperature laboratory prepared ashes. Lab prepared ashes were used in order to increase the consistency of the method, avoid the difficulties of sampling fly ash on site, and the ability to use coal blends that had not been studied. As such, Gibb is often cited as the method upon which sinter strength compression studies are based. Ash pellets were prepared from ash samples created from coals heated to 500°C and held for 2 hours, before being moulded into cylindrical pellets of a set weight and diameter using a 1.37 MPa lever press. The pellets were then preheated for 5-10 minutes at 500°C, before being pushed into the furnace at the desired temperature (typically in 50-degree increments between 900-1050°C) and left for one hour. No mention is made of controlled atmosphere. Strength measurements were made using a tensometer.

Gibb [203] used a temperature index, T_s5, or the temperature at which the sample was estimated to reach a strength of 5 MPa. A consistent trend between experimental points is assumed to do so, since a maximum of four experimental temperatures are used for any single coal. The study showed a strong correlation between Na_2O content and T_s5, one that was not improved when incorporating factors such as Fe_2O_3 and CaO and MgO. A link between chlorine and alkali content was also not observed, contrary to literature at the time. Sulphur content was not provided for the coals, nor were the effects of an atmosphere containing SO_2 considered.

Conn [204] utilised the Gibb method as part of a suite of experiments, including simultaneous ash shrinkage and electrical resistance, in order to determine the sinter points of coal ashes. Good correlations were observed between pilot scale fouling tendency, shrinkage and compressive strength. Further work was conducted using petroleum coke in a circulating fluidised bed (CFB) combustor [207], which is a waste product typically containing high levels of sulphur. In this case, a compressive test was conducted upon a “compacted ash sample”: no information about the dimensions, weight or consistency of the samples involved is given.

Although extremely high levels of V_2O_5 (57%) were observed by Conn [204] after laboratory ashing, the boiler loop seal ash contained high levels of CaO and SO_3

(47.1% and 48% respectively). Only this loop seal ash was used by Conn in sintering compression tests, where no sintering was observed below 1100°C, despite shrinkage of the pellets by as much as 11% being observed. Conn attributes the shrinkage to agglomeration of low melting point phases, created by the interaction of vanadium with other ash components. A liquid layer was observed on samples above 1100°C. Samples sintered in an SO_2/air atmosphere were found to sinter more strongly due to sulphation of unreacted CaO, when compared to a CO/N_2 atmosphere.

Conn [204] additionally studied the effect of commercial boiler additives (containing 88.5% MgO) and calcined dolomite (40% MgO) to reduce deposition from vanadium fuel sources. 1% of the boiler additive was found to have a significant effect upon the compressive strength of the ash, due to the conversion of V_2O_5 to $Mg_3V_2O_8$, while calcined dolomite was observed to perform to a lower standard. In addition, the strength of a several inch-thick boiler deposit was tested, recording a compressive strength of 24 MPa, much greater than that measured during laboratory experiments and almost 5 times the limit suggested by Gibb. The deposit was found to be enriched in vanadium due to the high calcium present, and the extended exposure to high temperatures were given as reasons for the greater strength.

Nowok et al [205] studied the compressive strengths of six coal ashes, ashed under ASTM conditions. Cylindrical pellets of 1.52 cm diameter and 1.90 cm in length were made using a hand press, in contrast to using a consistent sample weight measurement as in the Gibb method. Sinter strengths were found to increase above 5 MPa at 1000°C or higher, apart from Beulah coal which contained the lowest silica content of those studied (27.5 wt.%), alongside the significantly highest Na_2O content (10.8%), the highest CaO content (27.4%) and a high iron content (~10%). The lowest recorded sinter strength for this composition was 10MPa, at 900°C. Sinter strength profiles for the remaining coal ashes are comparable with those found by Gibb [203].

Nowok et al [205] also tested the compressive strength of Beulah coal in an amorphous state, this time at temperatures of 900°C and 1100°C in air, for different residence times. A significant peak strength of 50 MPa at 20 minutes was observed at 1100°C, reducing to 20 MPa after 30 minutes and maintaining

similar strengths beyond this up to 120 minutes. Despite sintering at a lower temperature of 900°C, a much higher compression peak was observed in the same sample, of 70 MPa after 60 minutes, reducing to 50 MPa after 180 minutes. Strengths were consistently higher for amorphous Beulah sintered at 900°C than at 1100°C, at residence times of greater than 20 minutes. This difference is attributed to the stability of crystalline structures: a phase transformation of nepheline to gehlenite was found to occur in the presence of high CaO liquid phase, introducing fractures in the crystalline structure: likely the result of a volume change associated with the phase transformation. Other causes of sinter strength reduction have been noted in other work [209] such as porosity increase caused by the decomposition of carbonates and sulphates.

Further studies on other amorphous coal ash compositions [206] found greater sinter strengths at 1100°C, with no drop in strength with increasing time over a 16 hour period. A strong correlation was found between surface tension/viscosity ratio and sinter strength, indicating that surface tension and viscosity were important factors in agglomeration, and the authors found that sinter strength could be indirectly linked to B/A ratio as a result. Once again, sinter strengths were significantly greater than the 5 MPa index introduced by Gibb.

Skrifvars et al [111] studied the compressive strength of five coal ashes; three brown coals, one anthracite and one bituminous, with an extremely wide range of compositions. Ashes were created using standards under laboratory conditions. A standard pressure of 1 MPa was chosen as the lowest possible pressure under which pellets could be created and handled. No mention is made of standard sample weight or pellet dimensions. The ashes were sintered over a much wider range of temperatures than previous studies, from 200-1000°C, for a period of 4 hours. Skrifvars et al [111] recorded sinter strengths that were all below 4 MPa, up to 1000°C, although measurements stopped for brown coal 1 at 700°C due to observed gas formation. Sintering was observed between 500-600°C for brown coal 1, which contained ~30% Na_2O and Cl, and~25% SO_3, all of which are known to heavily influence sintering and cause problems with deposition. This is below the softening point observed in AFT for the same ash (640°C). Skrifvars et al [111] found a difference between laboratory results and boiler experience: ash 4 was found to have a lower sintering temperature than

ash 3, in opposition to full-scale testing experience, indicating some limitations to the method.

Skrifvars et al [111] additionally investigated the use of additives. Limestone for SO_2 capture and an Al-Si based clay mineral were added separately at rates of 15, 30 and 100 wt. % to the dry fuel. In both cases, a one-to-one ratio with the fuel resulted in the elimination of compressive strength within sintered pellets from brown coal 1 ash at 600°C in dry air for 4 hours. The clay mineral outperformed the limestone at lower addition rates. Increasing the temperature to 700°C resulted in sinter strengths increasing by a factor of two when both additives were used at a 15% addition, with further addition decreasing sinter strengths. Once again, a one-to-one ratio resulted in insignificant compressive strengths. At low rates, the high chlorine and sodium within the ash was postulated to create a liquid phase, resulting in what the authors describe as a "glue" that engulfed the solid additive particles. In insufficient quantities, these particles would only cause the substance to densify, increasing sinter strength.

The same coals were used in a further study [109], shedding light on the sintering mechanisms involved for each coal. Reactive liquid sintering was determined to be the main cause of increased sinter strengths at low temperatures for brown coal 1 containing high sodium, chlorine and sulphur, as a pure $NaCl$-Na_2SO_4 system was shown to form liquid phase at 628°C, which correlated well with sintering and AFT temperatures. Viscous flow sintering was observed in coal ashes with silica as a major constituent, with a K_2O-SiO_2-Al_2O_3 system (with a composition in wt. % of K_2O, 4.8%; SiO_2, 68.6%; Al_2O_3, 26.6%) showing 50% molten phase appearing at 985°C. This molten phase would then create a viscous glassy phase. Full scale FBC firing of such coals showed no agglomeration problems, matching laboratory results where sintering did not start until 1000°C. Finally, chemical reaction sintering was found in coals containing CaO in SO_2 or CO_2 rich environments, forming carbonates and sulphates within any present necks between particles and solidifying.

Dohrn and Müller [209] summarise coal deposition as follows. Fouling deposits occur at below 900°C, and tend to consist of sulphates and carbonates, with the calcium content of the coal responsible for the former. Sodium hydroxide diffusion through the deposit reacts with calcium sulphate to form calcium sodium

sulphate, causing sintering and hardening of the deposit. Slagging occurs with the interaction of silicates through liquid phase sintering.

Dohrn and Müller [209] conducted experiments upon laboratory prepared ashes from five hard coals, producing four alimunosiliceous ashes and one silicoaluminous ash. Cylindrical pellets were prepared with a diameter of 8 mm and under two different pressures, of 8kN and 12kN held for 1 minute each. 8kN over the area of an 8mm pellet corresponds to 0.159kN/mm^2, or approximately 150 MPa: over 100 times the pressure recommended by Gibb [203] and used by Nowok et al [205] to produce a “deposit-like” strength, and 150 times the pressure used by Skrifvars [111]. Additionally, the previous studies did not use a hold time. Both the pressure and hold time have been shown [202, 203] to have a significant effect on the final sintering compression strengths, since a more dense pellet will inherently have a lower porosity and greater contact area between particles leading to increased sintering rates. As such, although the sintering trends in the Dohrn and Müller results [209] have some use, they cannot be compared to previous studies, nor do they give a useful indication of sinter strengths in real boilers.

Ashes were sintered at four temperatures: 600°C, 700°C, 850°C and 950°C. A slight increase in sinter strength was found at 600°C compared to samples sintered at 700°C, which Dohrn and Müller reasoned was due to sulphation [209]. Reactive ashes increased slightly in sintering strength at 850°C, and significantly at 950°C, indicating the onset of network forming. High alkali content was found to result in significant sulphation, which decomposed at higher temperatures leading to a highly porous sample with lower sinter strengths. Conversely, low alkali and iron content with high silicate and metakaolinite content resulted in high sinter strengths.

7.2.1.2 - Biomass Ash Experiments

Skrifvars et al [210] were the first to subject biomass ashes to compression tests, building upon the previous work with coal ashes [109, 111]. Ten biomasses were studied, from grass, wood, straw and other sources. Ashes were made at 550°C: otherwise, the compression testing method was based upon the methods detailed in Section 7.2.1.1 [109, 111]. A wood ash was found to decompose at temperatures of above 800°C, leading to zero readings for compression strength.

The calcium rich ash was found to form calcium carbonates during ashing, which decomposed during sintering leading to porous pellets. As a result, the ashing procedure was altered for high calcium-low silicon biomass to include a 10-minute temperature increase to 850°C directly after ashing, unless high levels of chlorine were also present. Pellets were then made to set dimensions of 11mm in height and 10 mm in diameter. No mention is made of pressure, but previous studies by the same authors used 1 MPa. Pellets were heat treated for 4 hours, using five different temperatures and under both oxidising and reducing conditions.

Skrifvars et al [210] sintered pellets between 600 and 1000°C. Ashes showing a significant onset of sintering between 625-700°C were found to contain high alkali salt concentrations. The authors attempted to estimate the temperature at which a 15% melt occurs for these ashes, and found such predictions to be fairly accurate when compared to sintering onset temperatures. These estimates failed to produce good correlations with other ashes however, even though a similar/high level of alkali salts was also present. In these cases, high calcium was present in both oxide and carbonate forms. Ashes containing high levels of carbonates failed to sinter: this was indicated by comparing ashes with and without the extended 850°C ashing step. Those that had been subjected to the 850°C step sintered more strongly, while the carbonate content of those ashed at 550°C meant that the gas atmosphere had no effect on sintering. Finally, ashes with high silicon content and significant amounts of potassium with few salts, showed evidence of sintering at temperatures of between 800-950°C, leading the authors to conclude that early stage viscous flow sintering was the cause.

Skrifvars et al [210] then compared compression results against operational experience in boilers in the same study. A good correlation was found between sinter strength onset temperatures and agglomeration in full scale and lab scale FBC boilers. High calcium biomass was determined to be more prone to agglomeration when calcium forms $CaCO_3$ from CaO. In operational boilers under atmospheric conditions, the case where calcium carbonates are present in the ash from lab scale tests is not relevant, as CaO would always form under such conditions. Skrifvars et al noted that, despite good correlations, full scale operation will involve other factors such as mineral matter release, particle size distribution, bed material and ash reactions with other material streams in the furnace and should only be used qualitatively.

A further study by Skrifvars et al [211] investigated three methods for predicting agglomeration tendencies for 10 biomasses, including ash fusion testing and sinter strength testing. Sintering temperatures in this case covered a wider range than the previous study, from 500-1100°C; otherwise, the method remained the same. Results were compared against controlled FBC agglomeration temperatures, where the samples were used in a 5kW lab-scale FBC reactor. For this, the reactor is operated normally, until 6 wt. % ash was accumulated in the bed. Once this occurred, combustion was stopped, and the bed temperature was controlled by external heating, increasing at a rate of 3°C until bed agglomeration was observed, giving a value T_{aggl}.

The sinter strength testing results of Skrifvars et al [211] performed significantly better than AFT results in terms of indicating the onset of problematic agglomeration, particularly for wheat straw, grass and olive flesh biomasses. For forest residues and tree bark, sintering temperatures overestimated compared to T_{aggl}. The authors indicated that this may be the result of interactions of the ash with the silica bed material, which the sinter strength test would be unable to account for. Both contained high CaO (25% and 33%, respectively), some silica (25% and 12% respectively) and ~7% K_2O. Although the grass biomass contained similar quantities of CaO, the main differences were that it contained much less silica (3.3%), significantly greater K_2O (28%), and contained chlorine (4.4%).

Although Skrifvars et al [211] did not attempt to explain this difference, it is possible that the grass (with its greater potassium and chlorine content) contained significant amounts of KCl salts, whereas the bark and forest residue did not. This KCl and chlorine content would induce fluxing at much lower temperatures, leading to the low T_{sint} (650°C) and T_{aggl} (670°C) that were observed in experiments. As a result, the dominant sintering mechanisms would be vapour phase and reactive liquid sintering, neither of which are dependent upon SiO_2 content (and as such would not be significantly affected by the bed material), rather than viscous flow sintering. Small differences (<5%) between the sintering temperature and T_{aggl} were found for the remaining five biomasses. T_{aggl} is typically higher than sintering temperatures: the authors noted that, if a strength value of 3 MPa is taken as T_{sint}, a better correlation is found with T_{aggl}, indicating that the Gibb estimate [203] of 5 MPa is fairly accurate. Although results showed

good correlations, only comparisons to lab-scale FBC were used, and there would be uncertainties when applying the results to full-scale units.

Hansen et al [214] compared results from co-fired coal with straw at rates of 0%, 10% and 20% biomass, through the use of sinter strength testing with ash fusion quantification using STA, providing melting curves. Tests were conducted using the same method as Skrifvars et al [210]. Sinter strengths were found to develop at a fast rate over the first hour of heat treatment, to between 64 and 100% of the final strength: heating rates of longer than 4 hours yielded only minor differences. Two ashes showed a lower strength between 950°C and 1000°C, but a general trend was observed with increasing temperatures leading to increased sinter strengths. Sintering temperatures, or the highest temperature at which no sintering is recorded, were found to be between 900°C and 1000°C for all samples. Hansen et al [214] state that keeping deposit surface temperatures below these sintering temperatures would mean that no strength buildup will occur in deposits: however, no mention is made of an attempt to change the atmospheric environment, such as increased CO_2 or sulphur content, which would cause sintering in high calcium biomass.

Hansen et al [214] then compared sinter strength results with pellet density, showing a strong correlation between pellet densities and increasing sinter strength. A density decrease was observed for the two pellets where reduced sinter strengths at 1000°C were recorded, indicating the evaporation of material and increased porosity as a result. A clear correlation between pellet strength and melt fraction was also observed. However, significant strength buildup and agglomeration was observed below the melting onset temperature indicated by STA analysis, which the authors state would indicate the onset of viscous flow sintering: however, vapour phase sintering has also been observed to cause strength increase without densification. The cause of agglomeration was determined to be potassium and calcium binding the particles together.

Malmgren et al [212] studied 9 different biomass samples, alongside 4 coal PFA samples, three coal/biomass blends and a pulverised coal, looking specifically at coal/biomass blends. The ashes were prepared under laboratory conditions at 550°C for 24 hours: although the authors note that the ashing process was used on well mixed samples of coal and biomass, the authors fail to state the actual

blend percentages used in these test within the text; ash analysis is given later that uses 90% coal, 10% biomass blends, and so it is assumed that this is the blend rate used for sinter strengths. Only the percentage contribution of ash by biomass in the blends is given. The pelletisation method chosen was identical to that used by Gibb [203], including the pellet force of 1.37 MPa. In some cases, deionised water was required to handle the pellets, of over 30% concentration. The pellets were air dried and then sintered at temperatures of 100°C steps between 800°C and 1100°C for a period of 8 hours, in dry air.

The results of Malmgren et al [212] showed that, for each sample, a straight line fit was best for sinter strength against temperature. This trend is different to every other study of sinter strength that has been discussed in Sections 7.2.1.1 and 7.2.1.2, where either an exponential trend or a sudden increase/decrease at a higher temperature is observed. Sinter strengths increased above Gibb [203] T_s5 for every sample at less than 900°C. Cereal-co product, Swedish wood and RWE sawdust produced strong pellets beyond this temperature, with a minimum of 8 MPa at 900°C. The sawdust and wood pellet contribute little to the overall ash content when blended, at 1.38% and 2.27% respectively, however an increased iron content (from 6.12% to 7.42% and 6.85%, respectively) is found. The olive waste blend produced weaker pellets than the pure coal blend: however, it was noted that the pellets produced were of a lower density than other blends, and noticeably deformed under sintering. This was despite the olive waste blend having the highest B/A ratio of any of the samples tested.

Despite minor differences in ash contents after blending, Malmgren et al [212] make no attempt to explain the differences in sinter strengths between blends: a fouling factor [215] was compared to sintering data, but no correlation was found. One significant omission from the data is that only components of the B/A ratio calculation are considered in the results: the chlorine and sulphur content of the coal and biomass is unknown. Coal is known to contain significant amounts of sulphur when compared to biomass, while some sources of biomass can contain significant levels of chlorine, both of which are important factors in sintering.

Pang et al [195] ashed 9 biomass samples at 650°C, a higher ashing temperature than in other studies which may affect carbonate and sulphate content compared to ashes in other studies. Pellets were created using a standard weight of 1 ± 0.1

g and a diameter of 10mm, compressed to 34.5 MPa with a hold time of 10 seconds. This pressure is over 25 times the pelletisation compression used by Malmgren and Skrifvars, making a direct comparison of results difficult, especially since Hansen et al. [216] showed the importance of pellet density. Sintering was carried out at two temperatures of 800°C and 1100°C, with a heating rate of 15°C/min and a hold time of 30 minutes at every 150°C, to prevent thermal shock. Temperatures were held at the maximum temperature for five hours.

In contrast to other studies, the biomass samples of Pang et al [195] in general show a decreasing sinter strength with increasing temperature. While biomass such as forest residue and bark were noted to decrease in sinter strength in previous studies [211], grassy biomass has been shown to increase during sintering, contrary to Pang et al [195] where miscanthus sinter strength was recorded to decrease by almost a factor of 10 over a 300°C temperature range.

A major flaw with the Pang et al [195] publication is that the ash compositions are not provided, giving no insight into the mechanisms of sintering that may be present. The authors attempt to explain this sinter strength through ash fusion testing where expansion of pellets is observed, corresponding to an increasing void percentage within the pellet: however, in the case of some pellets a decrease in sinter strength is present even though no expansion is observed. Densification and shrinkage would be expected to increase sinter strengths, while ash fusion testing has been shown to be unreliable both as a predictive tool and when comparing results to sinter strength testing [210, 211]. In addition, sinter strengths were attempted on dome-shaped pellets. The authors tried to account for this by using Vernier callipers before compression testing, however it is difficult to measure the true contact area of the pellet due to its deformity, and sinter strengths may be even more unreliable for such pellets both due to inaccuracies in measured surface area and an increased likelihood of shearing.

7.3 - Experimental Methodology

7.3.1 - Samples

For this study, experiments were conducted upon the full range of biomass-additive blends used in this thesis as outlined in Table 7.1, with ashes prepared according to the methods described in Chapter 3.

7.3.2 - Sample Preparation

Sinter strength testing is typically conducted according to the methodology originally conducted by Barnhart [217]: the methodology used within this study was based upon the methods used by Gibb [203] and Malmgren et al [212], discussed in Section 7.2.1.

Table 7.1 - Test matrix of samples used in sinter strength experiments

Wt% Adtv to dry fuel	0%	5% (PFA)	15% (PFA)	25% (PFA)	5% (Kao)	15% (Kao)	25% (Kao)
OCA	X	X	X	X	X	X	X
WWA	X	X	X	X	X	X	X
BA	X	X	X	X	X	X	X
FA	X	X	X	X	X	X	X
PFA	X						
Kaolin	X						

1.0 g (+/- 0.1g) of sample material was accurately weighted out and then pressed to produce a cylindrical pellet using a 10mm diameter die. Three pellets were produced for each ash studied, at each sintering temperature. Samples were subjected to 1.73 MPa of pressure, as recommended by Gibb [203] and Malmgren et al [212] as the required pressure to produce pellets that, when sintered, simulate similar strengths to those found in boiler deposits. This pressure was applied gradually in order to produce a uniform pellet and prevent additional pressure from being used.

To produce pellets that were strong enough to handle, an amount of deionised water was required, of between 10 and 30% depending upon the ash. The reason for the range in deionised water use was that samples such as the FA and PFA appeared soluble within the water, producing a slush at water concentrations of more than 10%, while the BA sample required significantly more water (30%) before any cohesion was achieved under the required pressure. Pellet height varied depending upon the density of the ash: the PFA samples produced the smallest pellets, at 7mm in height, while the BA samples produced pellets at 11mm height.

7.3.3 - Sintering Process

The pellets were sintered in large batches of multiple samples in triplicate using a muffle furnace. The pellets were placed on ceramic tiles within the oven and heated at a rate of 5°C/min, in order to remain consistent with ash fusion testing and to avoid thermal shock and structural damage within the pellet. Hold temperatures of 800, 850, 900 and 950°C were used, with a holding time of 3 hours, at which point the furnace is switched off and allowed to cool slowly via convection, again to avoid thermal shock. Longer hold times of up to 8 hours were investigated during initial tests but were found to have a negligible impact upon the resulting sinter strength and behaviour of the pellets.

7.3.4 - Compression of Pellets

Once sintered and cooled to room temperature, each pellet was subjected to compression testing, with the point of failure being determined as the sinter strength of the pellet. A H10KS Tinius Olsen tensile strength machine with a modified compression cage (Figure 7.1) was used, with a moving load speed of 5mm/min used during testing. Compression strength in MPa was recorded every 0.001 mm, producing a compressive strength profile for each pellet from which the peak pressure is taken. Measurements were programmed to stop recording once the pellet reached 50% of the highest recorded compression strength.

Figure 7.1 - H10KS Tinius Olsen tensile strength machine with modified compression cage

7.4 - Experimental Results

7.4.1 - Compression Profiles

Four distinct types of compression peaks were observed during experiments:

Clean Fracture - A clean fracture was observed in pellets that had experienced significant sintering throughout, resulting in a fairly uniform, dense structure. The compression curve is non-linear as compression proceeds, followed by a clear instantaneous breaking point during compression. The fracture itself is irregular, reflecting differences in the extent of sintering from region to region in the pellet.

Fragmentation Fracture - Evidence of fragmentation could be observed in sintered pellets where the compression profile during fracture did not show an instantaneous breaking point: instead, the stress would either reduce slightly or not reach a well-defined peak before full fracture occurred. Such a profile would produce an underestimate of pellet strength (as shown in Figure 7.2b) because the main body of the pellet remained intact and instead a region spalled off. Thus, the tests for these samples were repeated.

Two-phase Behaviour - Pohl and Juniper [114] call these “plastic deposits” (although this term may be misleading as ceramics are not normally able to plastically deform), which form when part of the material has a low viscosity. This material flows into the pores of the pellet, creating a two-phase fluid of particulates in a viscous fluid. In the case of OCA samples, sintering and phase changes were clearly observed: however, a clean fracture was not produced. The pellet would compress under pressure, undergoing internal fracture that did not propagate through the pellet such that a clear point of failure was not observed. Instead a series of internal fractures were created, none of which propagated fully, leading to a jagged compression curve consisting of a series of crack-collapse events. This indicates that similar deposits would pose severe problems for soot blower removal. Note how the pellet in Figure 7.2c increase in strength with further compression.

Friable Samples - For some samples, little to no sintering was observed. As a result, the compression curve shows the application of pressure to the sample, but as the arm of the compression rig extends further, no increase in pressure is observed and the sample would powder.

Examples of each type of compression curve are shown in Figures 7.2 a-d.

7.4.1.1 - Behaviour of Pellets under Compression

The behaviour of each sample under compression is crucial in determining how troublesome a deposit from such a sample will be in full-scale boilers, should the pellet accurately simulate the deposition. Ideal deposition will consist of either powdery, loosely adhered deposits that are easily removed or sintered deposits that fracture under soot blowing pressure. The peak impact pressure (PIP) of the soot blower is the important factor in deposition removal. If the deposit is sintered, but the strength remains less than the peak impact pressure, then the deposit will fracture at the point of peak impact pressure, introducing a weakness. Further soot blowing will then blow the deposit apart through the fracture. However, if the deposit withstands the PIP of the soot blower, then removal by other means is required, which may result in boiler shutdown.

In the case of two-phase deposits, a true sinter strength is impossible to determine. Pohl and Juniper [114] explain that the deposit yields under mechanical force and thermal shock before it freezes, likely describing viscous flow sintering [104]. The authors state that once the deposit has partially relaxed, it will no longer develop high stress under pressure, preventing fracture from occurring. As a result, rather than critical weaknesses being introduced under PIP, the deposit may compress and densify. This can give the impression that deposition is being reduced by soot blowing since the deposit may appear to shrink, when in reality it is increasing in mass, creating significant problems later on. Fewster et al [218] indicate that 10-15% liquid phase in a deposit may be sufficient to create compressive or two-phase deposits

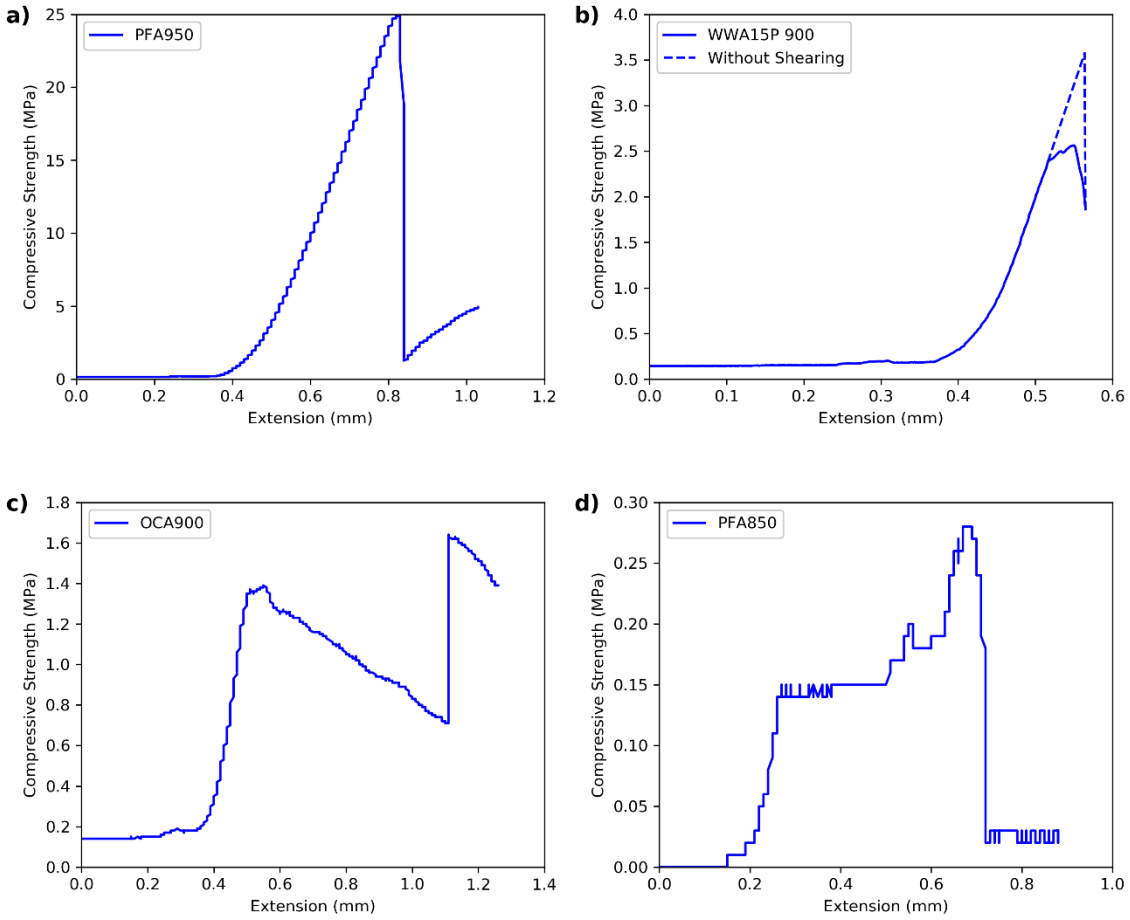

Figure 7.2 - Example compression profiles showing: a) clean fracture, b) shearing fracture, with possible true sinter strength indicated by dotted line, c) compressive sample and d) friable sample

7.4.2 - Peak Compressive Strengths

Table 7.2 shows the average peak compression strengths for all samples across the four temperatures studied, with a description of the pellet behaviour included. In addition to the peak recorded strengths, the type of compression profile seen has been included. Sinter strength results are shown graphically in Figures 7.3 a-d.

Of all samples tested, only OCA samples showed compressive behaviour, indicating difficulties for removal via soot blowing. 100% OCA was the only sample to show a significant increase in sinter strength at 850°C, increasing over 10 times compared to the same sample sintered at 800°C. Sinter strengths reduced in the same sample at 900°C, showing signs of devolatilisation: however, compressive behaviour of the pellet indicated that the peak sinter strength may not be entirely reliable. The addition of 5% KAO resulted in the best performing deposits, with little to no sintering occurring as indicated by a highest recorded sinter strength of 0.08 MPa at 950°C.

Most samples showed a trend of increasing sinter strength with increasing temperature. However, OCA 5% KAO and WWA showed little to no signs of sintering at the temperatures measured. In the case of WWA, previous studies [108, 109, 209] have shown the importance of sulphur in sintering of high calcium fuels. In addition, the presence of carbonates has been shown to induce sintering at 700°C [210], above which they decompose. As sintering was only conducted under atmospheric conditions, the effects of increased SO_2/CO/CO_2 concentrations in the combustion atmosphere have not been taken into account, which may result in a discrepancy between lab-scale results and full-scale experience.

Table 7.2 -Average peak compression strengths (left number, in MPa) and behaviour (right, description) of samples at each sintering temperature.

Samples	Temperature °C							
	800°C		850°C		900°C		950°C	
FA	0.13	Powder	0.22	Powder	2.15	Sintered	3.78	Sintered
FA 5% PFA	0.02	Powder	0.05	Powder	2.28	Sintered	19.20	Sintered
FA 15% PFA	0.02	Powder	0.10	Powder	1.73	Sintered	12.29	Sintered
FA 25% PFA	0.02	Powder	0.03	Powder	1.34	Sintered	7.81	Sintered
WWA	0.25	Powder	0.19	Powder	0.24	Powder	0.15	Powder
WWA 5% PFA	0.14	Powder	0.88	Sintered	2.73	Sintered	3.44	Sintered
WWA 15% PFA	0.05	Powder	0.16	Powder	2.17	Sintered	13.31	Sintered
WWA 25% PFA	0.04	Powder	0.13	Powder	1.28	Sintered	13.92	Sintered
OCA	0.93	Compress	11.09	Sintered	2.60	Compress	1.37	Sintered
OCA 5% PFA	0.47	Sintered	0.81	Sintered	2.65	Compress	2.09	Sintered
OCA 15% PFA	2.08	Sintered	2.34	Sintered	4.49	Sintered	2.98	Sintered
OCA 25% PFA	1.56	Sintered	2.59	Sintered	4.42	Sintered	6.52	Sintered
BA	0.15	Powder	0.28	Powder	0.64	Sintered	1.35	Sintered
BA 5% PFA	0.28	Powder	0.66	Sintered	1.52	Sintered	3.56	Sintered
BA 15% PFA	0.19	Powder	0.38	Sintered	1.22	Sintered	5.92	Sintered
BA 25% PFA	0.14	Powder	0.32	Sintered	1.24	Sintered	6.74	Sintered
PFA	0.14	Powder	0.17	Powder	3.36	Sintered	19.31	Sintered
WWA 5% KAO	0.70	Sintered	0.79	Sintered	1.06	Sintered	2.53	Sintered
WWA 15% KAO	0.85	Sintered	0.96	Sintered	1.32	Sintered	2.12	Sintered
WWA 25% KAO	1.19	Sintered	1.17	Sintered	1.13	Sintered	1.95	Sintered
OCA 5% KAO	0.06	Powder	0.05	Powder	0.06	Powder	0.08	Powder
OCA 15% KAO	0.20	Powder	0.27	Powder	0.99	Sintered	1.59	Sintered
OCA 25% KAO	0.53	Sintered	0.58	Sintered	0.98	Sintered	2.34	Sintered
KAO	1.76	Sintered	1.48	Sintered	1.98	Sintered	2.63	Sintered

Key: powder = no appreciable increase in sinter strength beyond initial contact; sintered = clear increase in compressive strength followed by clean fracture; compress = initial increase in compressive strength followed by deformation and retention of compressive strength under further compression

.

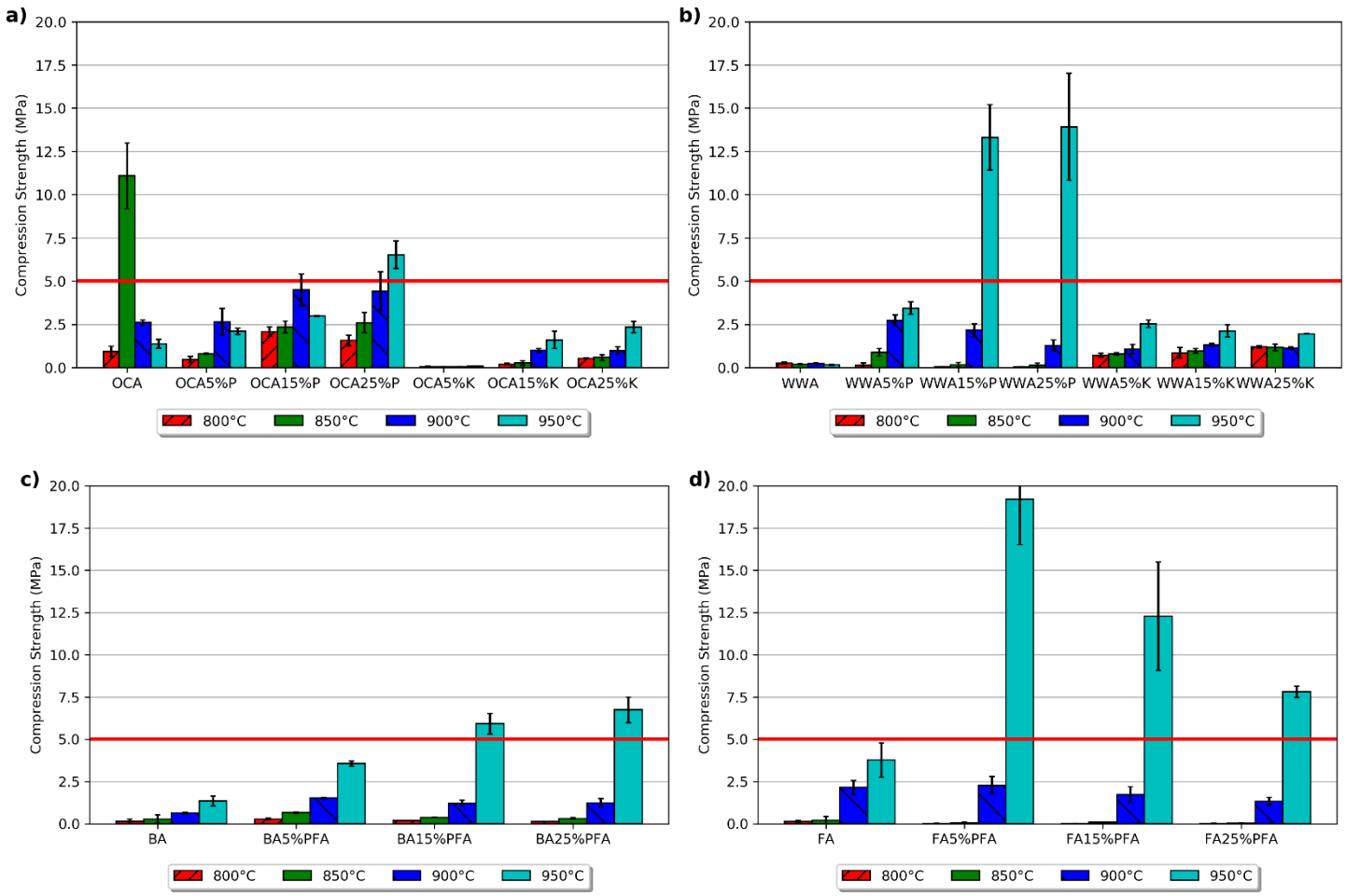

Figure 7.3 - Compression Strengths of pellets sintered between 800-950°C for a) OCA and OCA with PFA/KAO, b) WWA and WWA with PFA/KAO, c) BA and BA with PFA, and d) FA and FA with PFA

7.4.2.1 - OCA/Additive Samples

The addition of PFA to OCA had a significant effect upon pellet behaviour at 850°C; 5% addition of PFA reduced sinter strengths to less than OCA at 800°C. Further, the OCA pellet was observed to experience significant shrinkage and melting at 850°C and above, as well as changing colour to a shade of green, indicating that phase changes had occured. The addition of PFA eliminated both shrinkage and colour from the pellet, indicating that the difference in composition was inhibiting both sintering and the devolatilisation of some species. The difference in behaviour is shown in Figure 7.4.

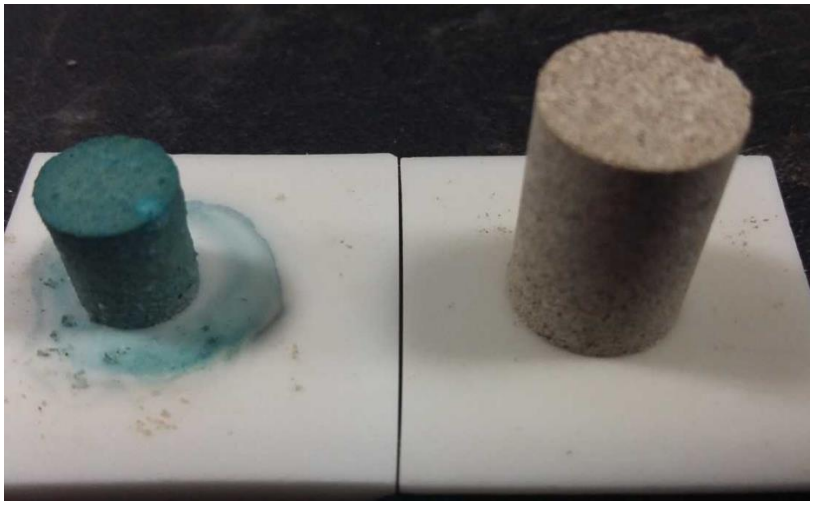

Figure 7.4 - Comparison of OCA pellet (L) and OCA 5% PFA pellet (R) after sintering at 950°C for 4 hours

The OCA sample was the only sample that experienced shrinkage to this extent. SEM-EDX images of the pellet debris after compression further clear evidence of sintering at temperatures of 850°C and above, as shown in Figure 7.5. Little visible porosity was present. EDX imaging showed that potassium and silicon were found to permeate evenly throughout the pellet, with dense regions of chlorine present in the form of crystals, as annotated. In addition, calcium, magnesium and phosphorus were also present throughout the pellet, showing similar trends to the XRF results for OCA shown in Table 5.4 and further indicating that viscosity testing representative. Despite the low Al_2O_3 concentration of OCA, fairly dense regions of aluminium were observed.

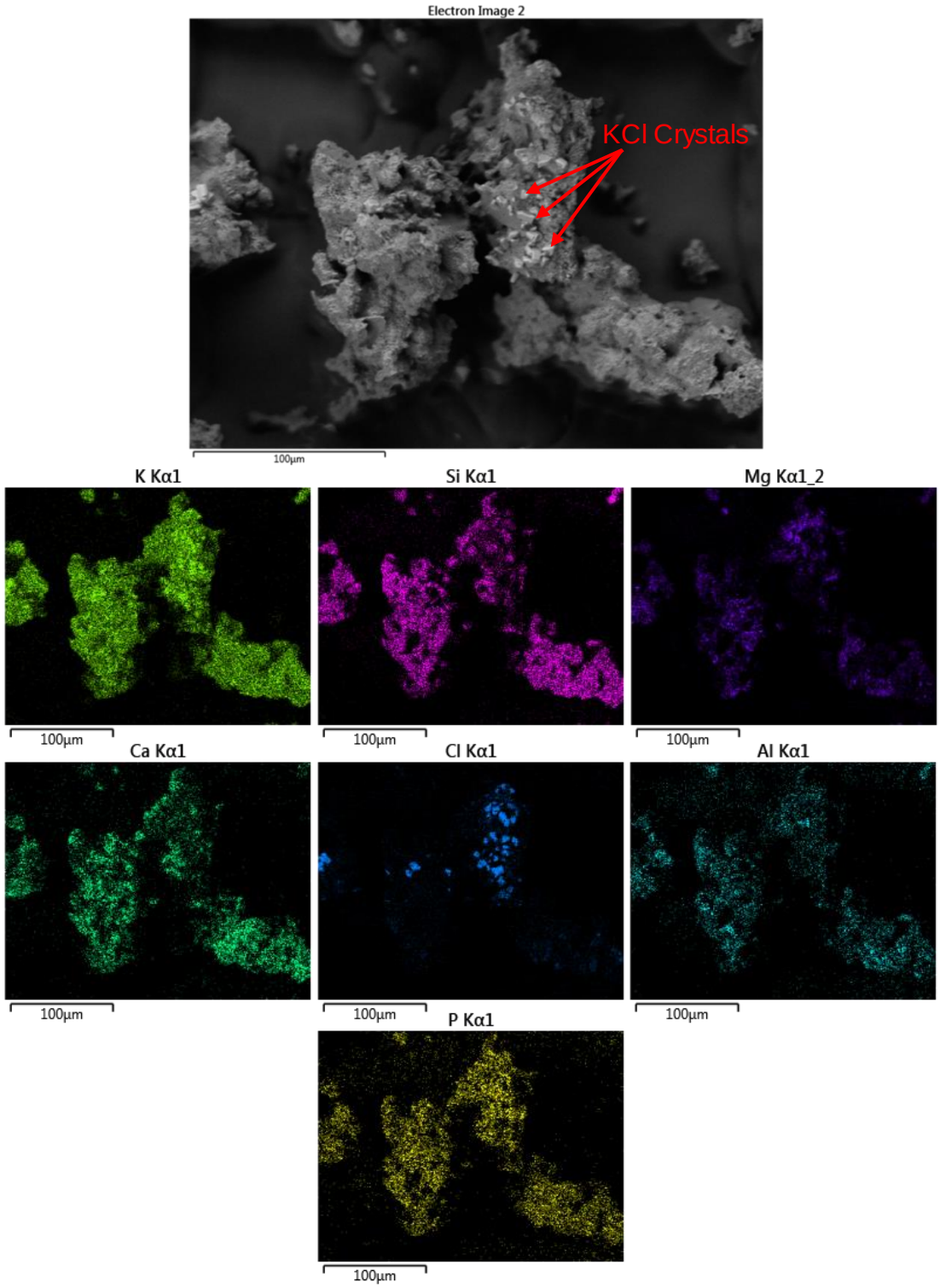

Figure 7.5 - SEM-EDX imaging of debris from OCA 850°C samples after compression testing

OCA5%PFA compositions resulted in more friable pellets with reduced sinter strengths up to 900°C. SEM imaging of the pellet after sintering at 850°C (Figure 7.6) displayed much greater porosity throughout the sample compared to OCA, with fewer large sintered particles present. Aluminium was observed to be present throughout the sample, while magnesium and calcium appeared to be

more evenly dispersed. This indicated that the increased aluminium concentration was leading to the more widespread formation of aluminosilicates.

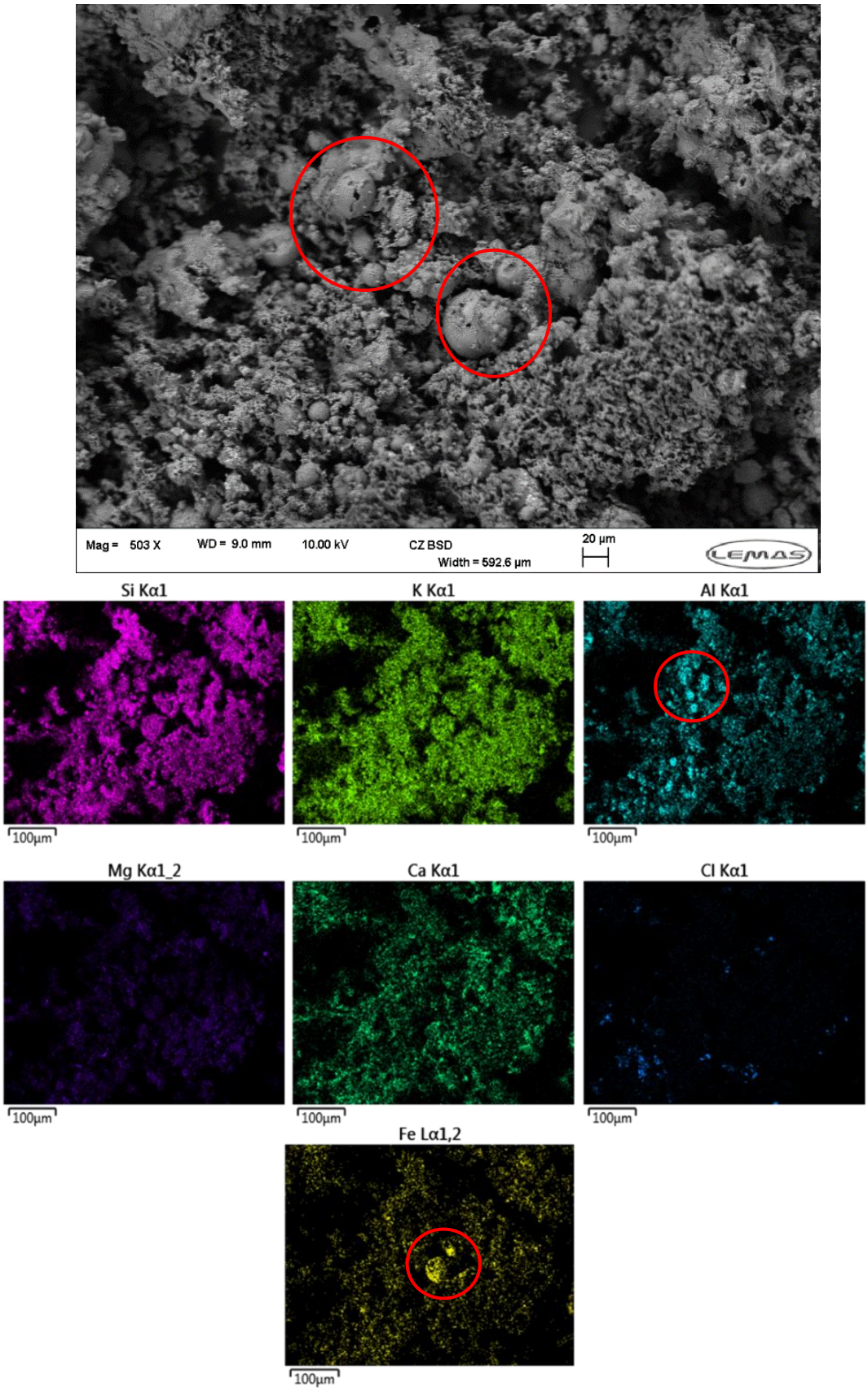

Figure 7.6 - SEM-EDX imaging of debris from OCA5%PFA 850°C samples after compression testing

Although concentrated regions of chlorine remain visible in Figure 7.6, the crystalline features observed in Figure 7.5 are no longer present. However, evidence of partial melting was visible throughout the sample: these regions correspond to regions of high aluminium and iron concentration.

XRD analysis of the OCA and OCA5%PFA samples after sintering at 850°C was conducted. The olive cake biomass contained chlorine (0.26 wt. % d.b.) before ashing, and this was postulated as the most likely cause of sintering, along with its high K_2O content of 32.3%. Initially, hot stage XRD was attempted to try and determine at which temperature the phase changes/fluxing began. A heating rate of 10°C per minute was used up to 640°C, after which temperatures were increased in 20°C intervals up to 700°C. The temperature was then decreased at the same rate, with scans at the same intervals, to 640°C, before cooling to ambient temperature where a final scan was conducted. Hot stage XRD results were compromised by the presence of a salt layer that developed over the sample during heating, obscuring the remainder of the sample. This layer was determined by signal analysis to be KCl salts in the form of sylvine that had been drawn to the surface. This salt layer was recovered for SEM imaging, as shown in Figure 7.7.

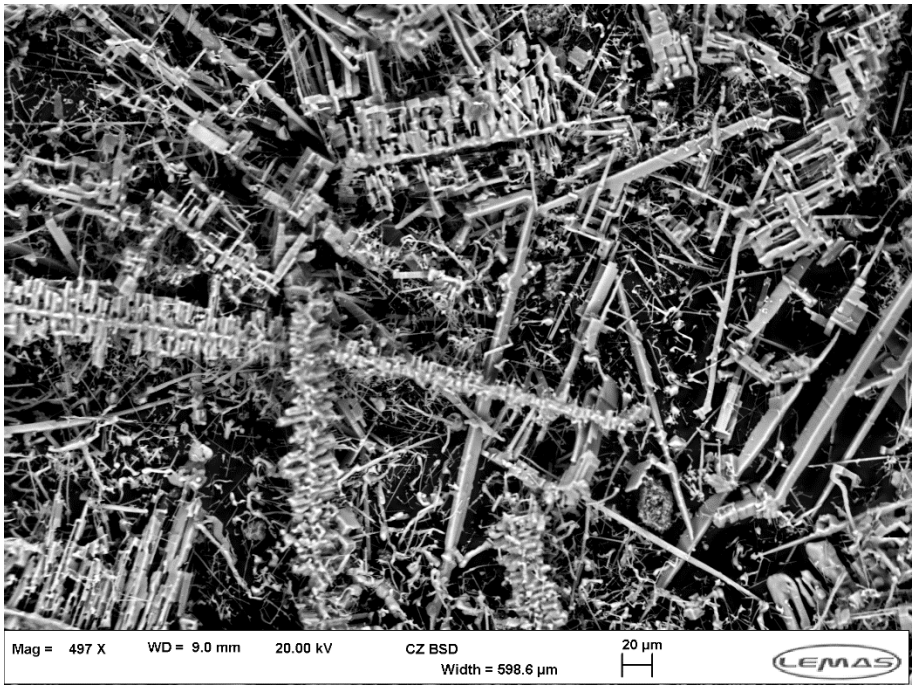

Figure 7.7 - SEM imaging of sylvine salt formation occurring during hot-stage XRD

A comparison of XRD spectra from OCA and OCA5%PFA samples after sintering at 850°C showed a significant difference in peaks attributed to KCl by High Score, as shown in Figure 7.8. Also, of note is the appearance of a large KAlSi peak forming in the sample with additive. It is this sublimation of KCl that is thought to be acting as a sintering transport mechanism and fluxing surrounding silicate minerals within the ash, which has been observed in other studies [219] at similar temperatures. The addition of Al-Si additives has been shown [89, 98, 139] to inhibit alkali vapour release through the conversion of KCl to potassium silicates and potassium aluminium silicates, which explains the observations in Figure 7.4. This formation of aluminosilicates prevents sintering by forming higher melting point compounds, preventing material transport from occuring.

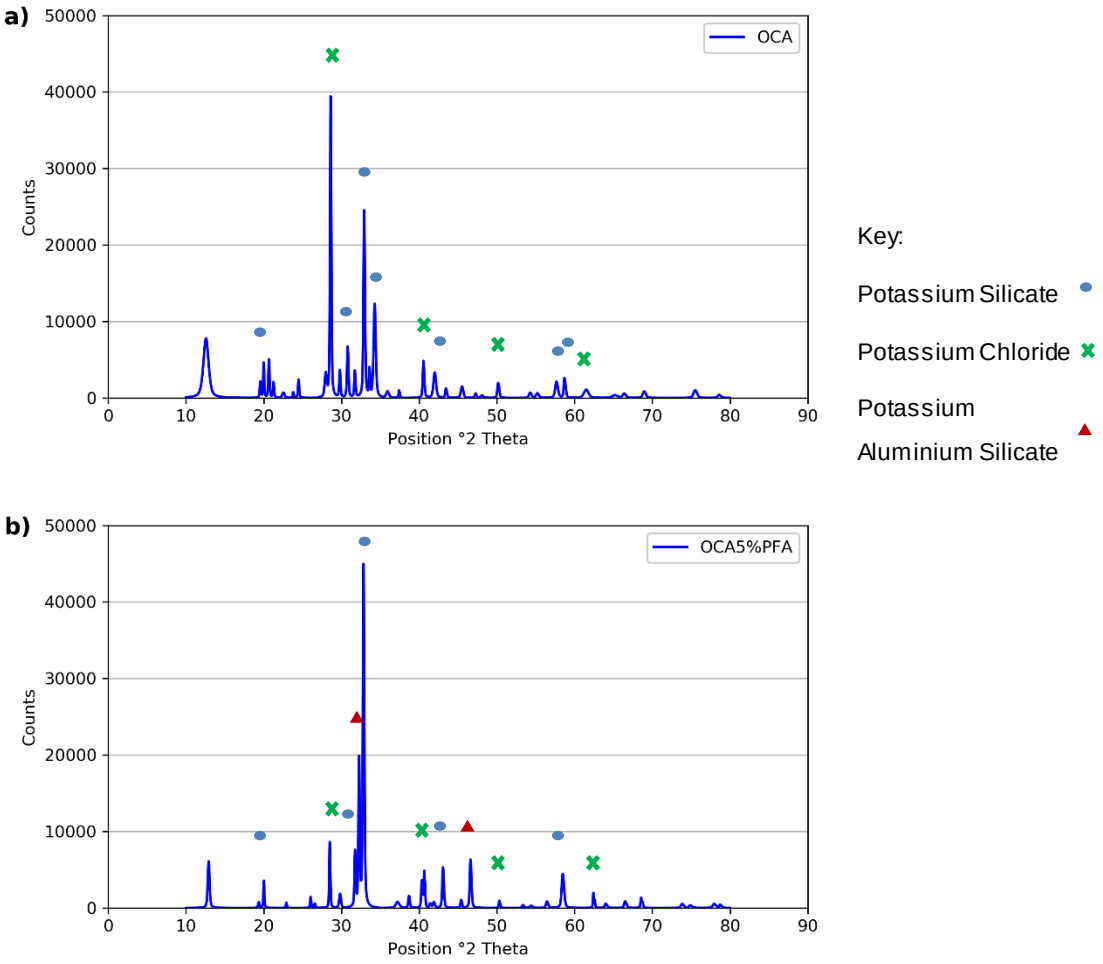

Figure 7.8 - Comparison of XRD spectra for a) OCA and b) OCA 5% PFA after sintering at 850°C

OCA5%KAO performed significantly better than the PFA, eliminating sintering at all temperatures investigated. SEM imaging (Figure 7.9) showed that the sintered consisted of a more granular structure, with visibly increased porosity. Magnesium appeared to have become more concentrated in certain regions with the addition of kaolin. Chlorine, in contrast to the OCA and OCA5%PFA samples, was dispersed evenly throughout the pellet alongside silicon, aluminium, potassium and calcium. Only traces of iron were present, due to the low iron concentration of the kaolin.

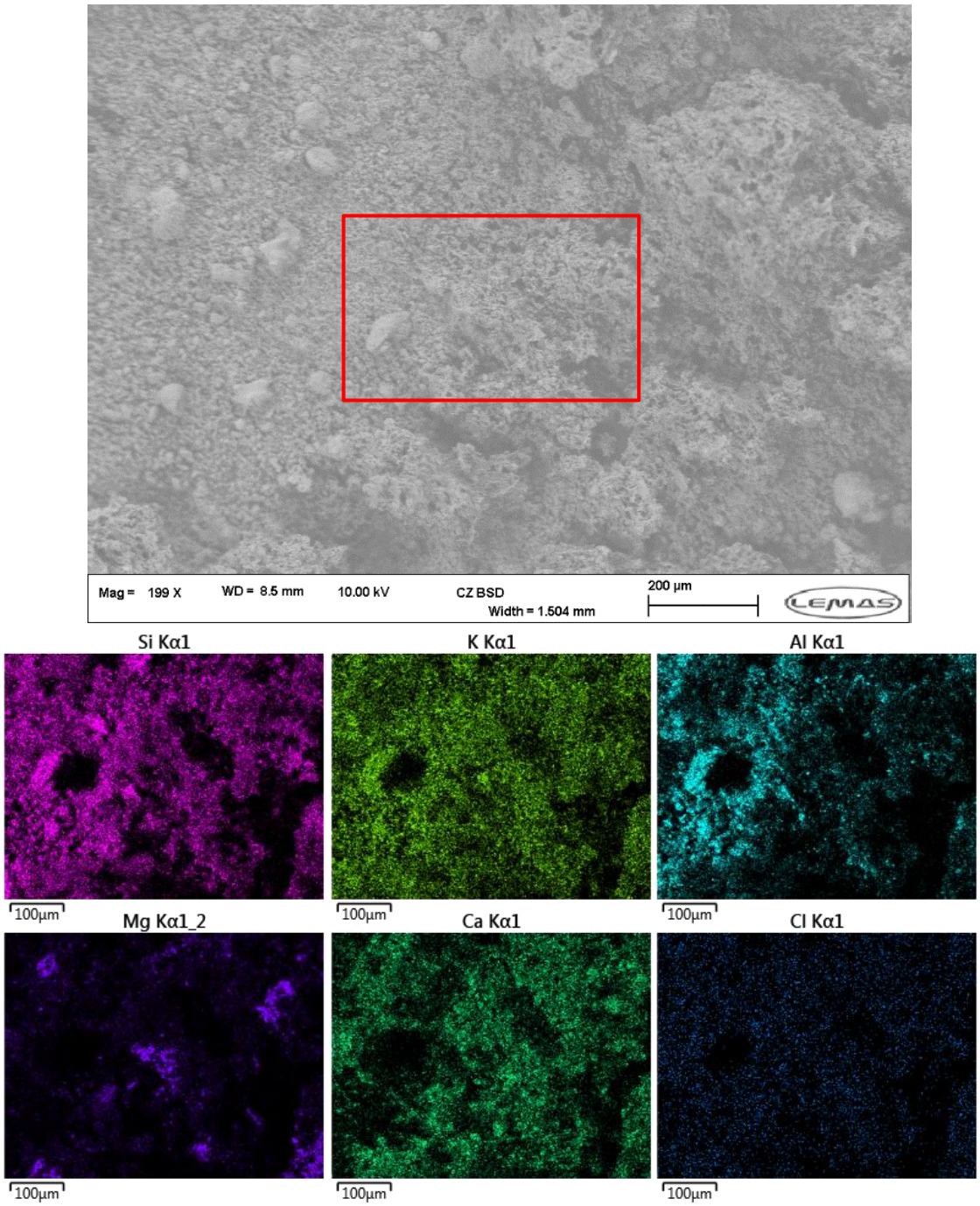

Figure 7.9 - SEM-EDX imaging of debris from OCA5%KAO 850°C samples after compression testing, with mapped region highlighted

Although larger particles existed, closer inspection (Figure 7.10) indicated that these particles were likely minerals that were either formed during heating or were already present in the sample before heating, as no signs of extensive sintering or formation due to agglomeration of particles are observed. XRD analysis using HighScore corroborated these observations, and showed good matches with potassium aluminium silicate, potassium silicate and silicon oxide (Figure 7.11).

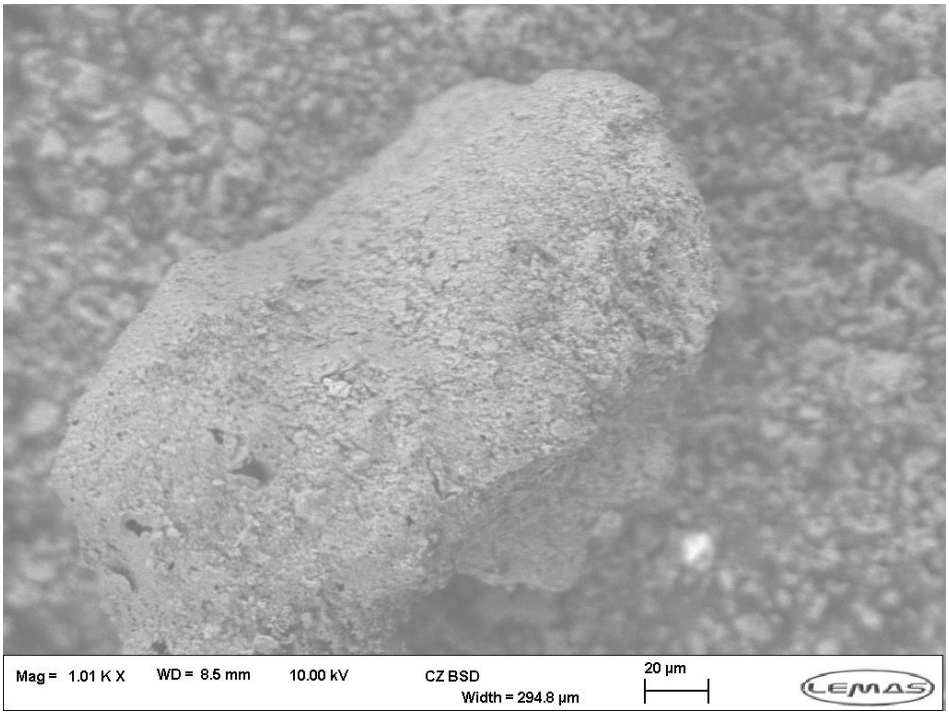

Figure 7.10 - SEM imaging of intact particle from OCA5%KAO sinter strength testing at 850°C

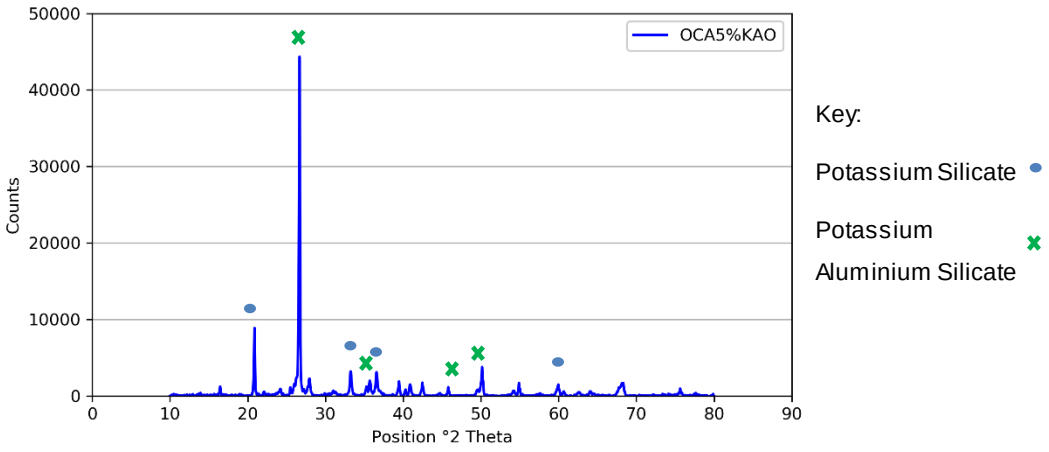

Figure 7.11 - XRD spectrum of OCA5%KAO

7.4.2.2 - WWA/Additive Samples

WWA results indicated that different sintering mechanisms were occurring to those observed in the OCA samples, particularly when PFA was added. Most of the sample was observed to consist of small, unsintered particles (Figure 7.12) as the sinter strength results indicated would be the case. Calcium, potassium, sodium and aluminium were observed to be evenly distributed throughout the sample, with accumulations of silicon and magnesium (Figure 7.12, highlighted) found to occur in large particles. In addition, much greater concentrations of phosphorus were observed than would be expected from the WWA composition. However, although little sinter strength was recorded during experiments, clear evidence of localised viscous sintering was observed in some of the images for WWA at sintering temperatures of 900°C and above, such as in Figure 7.13. These sintered particles corresponded to regions of high silicon and potassium concentration, indicating that they are the result of potassium silicate formation and melting. Closer inspection of these particles (Figure 7.14) showed evidence that these particles were comprised primarily of calcium and magnesium, as indicated by the rough, granular regions highlighted, with potassium silicate acting as the sintering material as indicated by the smooth regions which indicate the presence of liquid phase.

XRD spectra of WWA sintered at 900°C Figure (7.15) was complex, indicating the presence of calcium silicate, magnesium oxide, both calcium and potassium aluminosilicates, and calcium carbonate: the latter is unexpected however, as calcium carbonate is expected to decompose at temperatures of above 850°C [210]. The complex composition of the spectra was due to the presence of little to no sintering, meaning that the minerals within the ash remained exposed: as such, the HighScore peak identification should be taken with caution due to overlapping peaks.

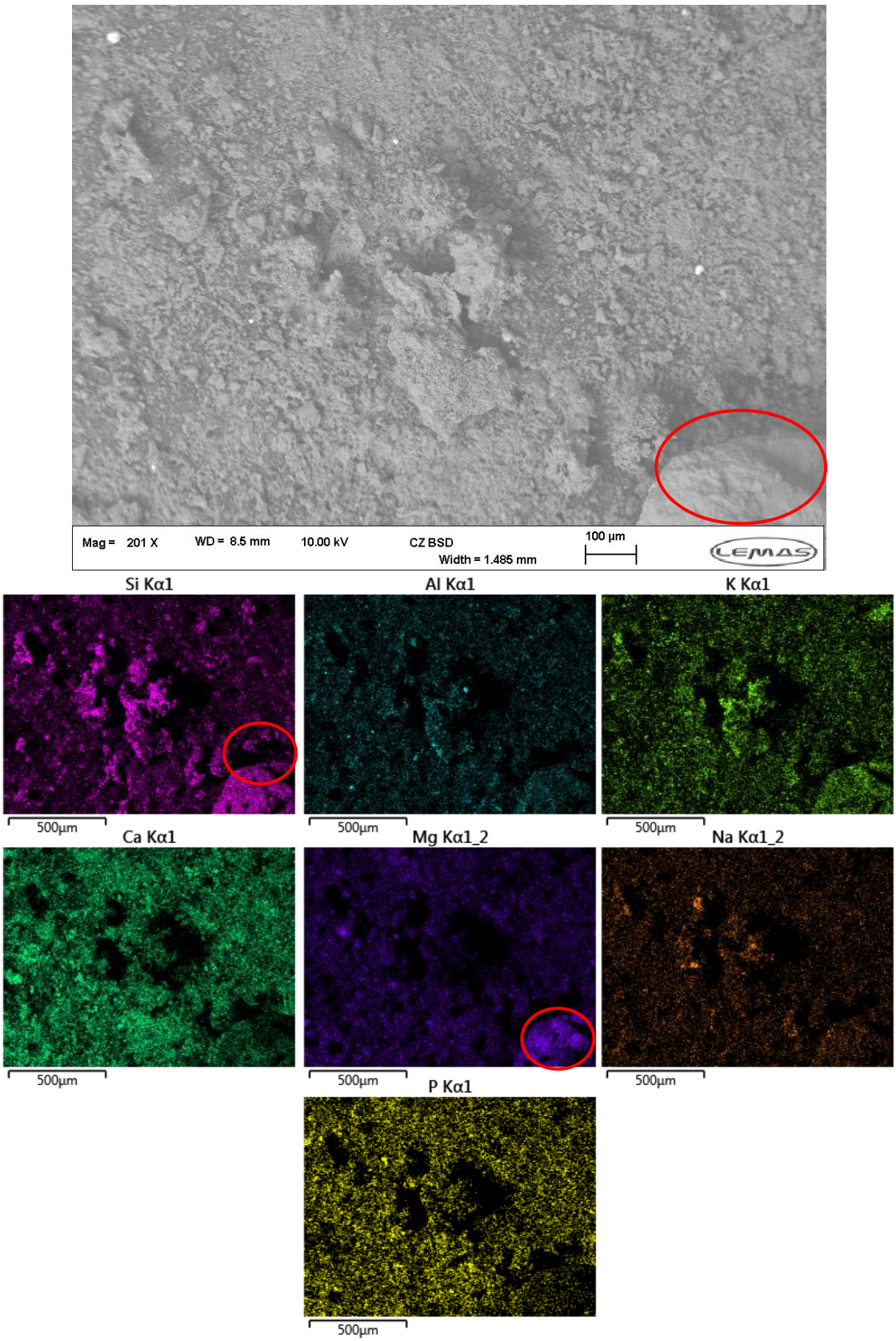

Figure 7.12 – SEM-EDX imaging for WWA sintered at 900°C

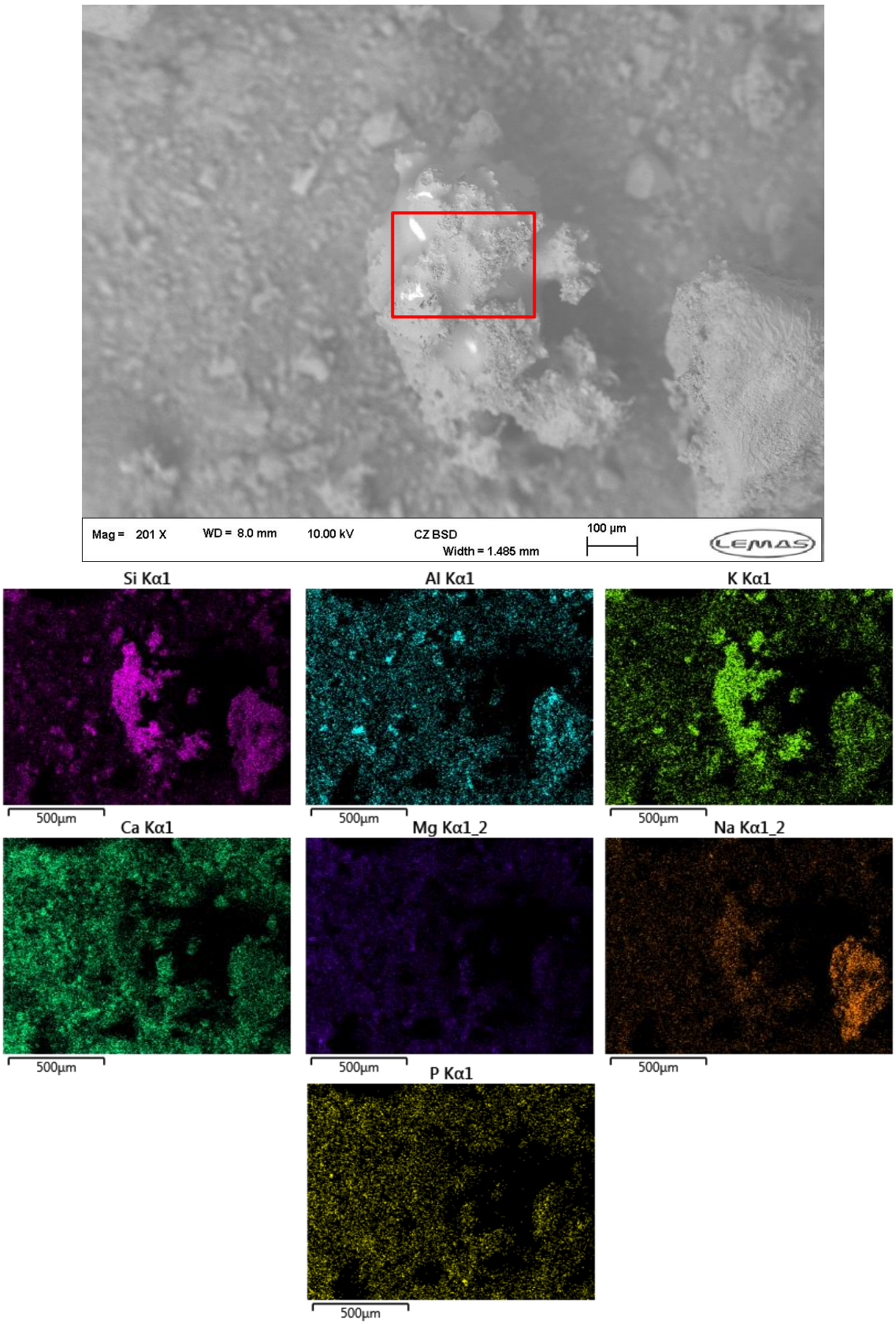

Figure 7.13 – SEM-EDX imaging of particle displaying signs of viscous sintering in WWA sintered at 900°C, corresponding to highlighted region in Figure 7.12

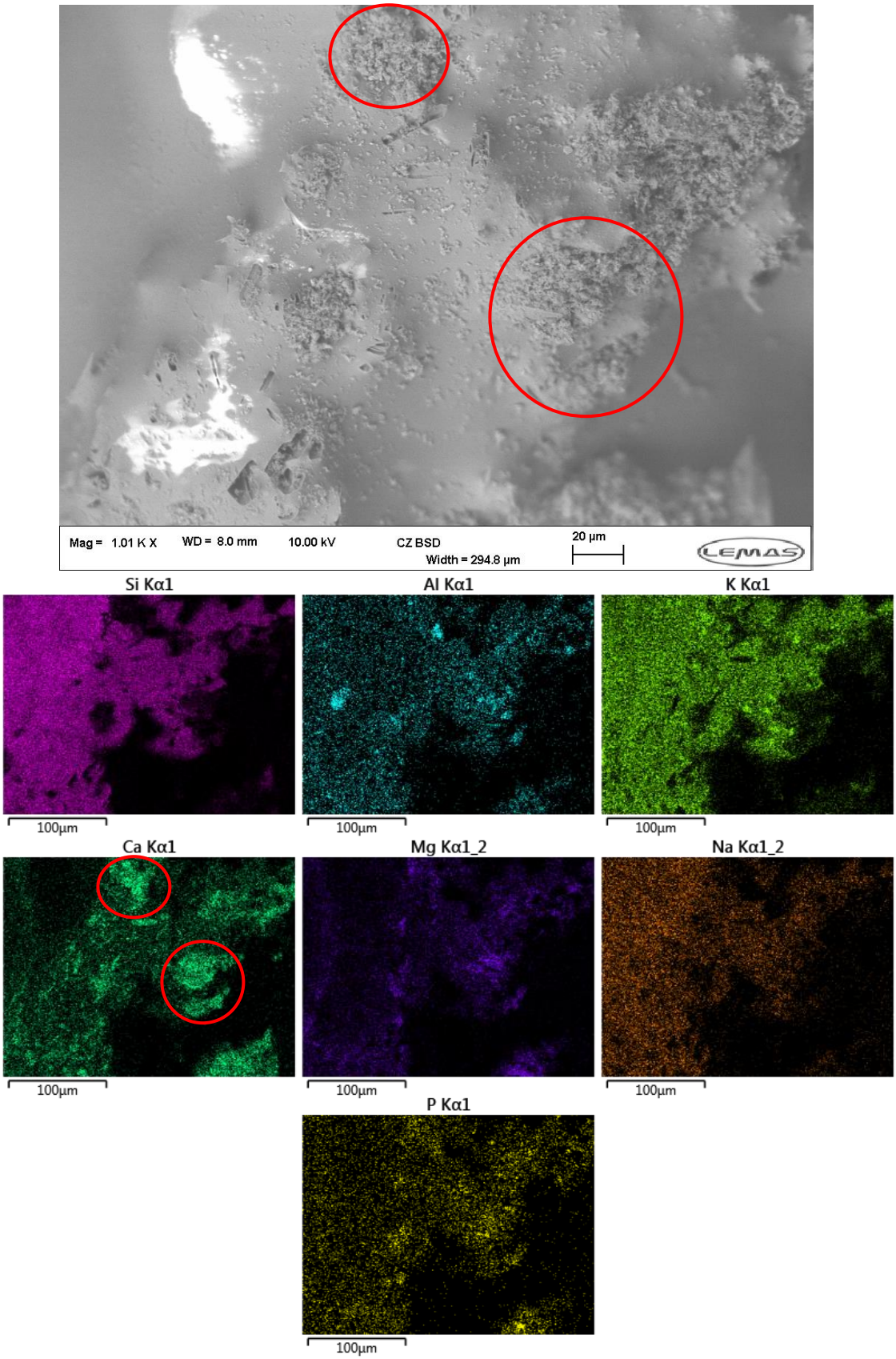

Figure 7.14 - SEM-EDX imaging of the region highlighted in Figure 7.13, showing sintering within WWA at 900°C

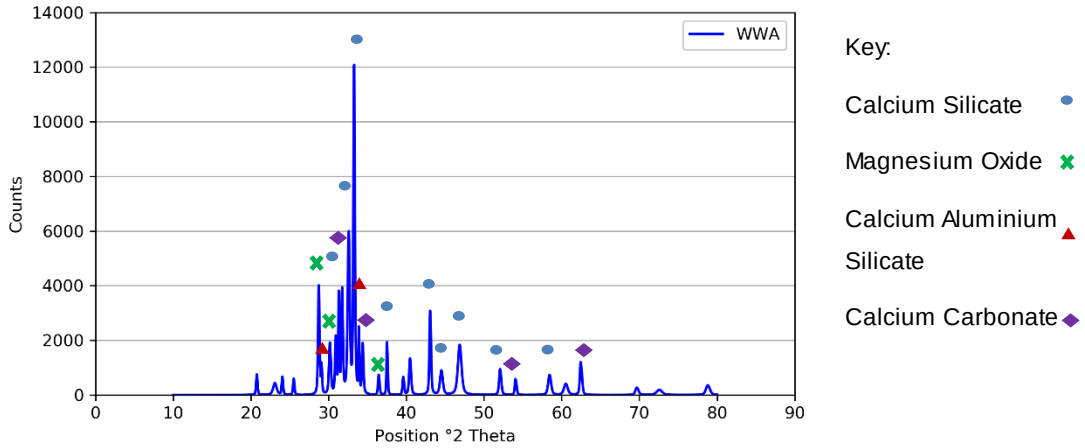

Figure 7.15 - XRD spectra of WWA sintered at 900°C

WWA mixed with 5% PFA and above showed consistently increased sinter strengths at temperatures of 900°C and above when compared to without additive. SEM analysis showed that initial particle agglomeration was clearly occurring during sintering (Figure 7.16, annotated). Mapping of the highlighted region (Figure 7.17) showed that much of the debris surface consisted of aluminium and silicon, with aluminium concentrating within all the agglomerated particles present.

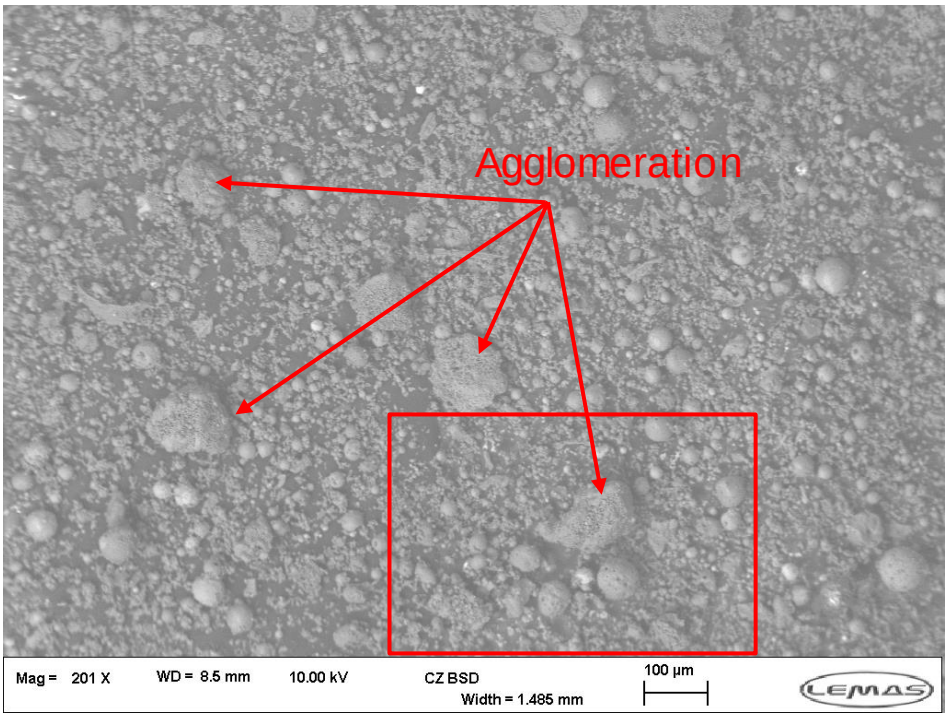

Figure 7.16 - SEM image of WWA5%PFA after sintering at 900°C

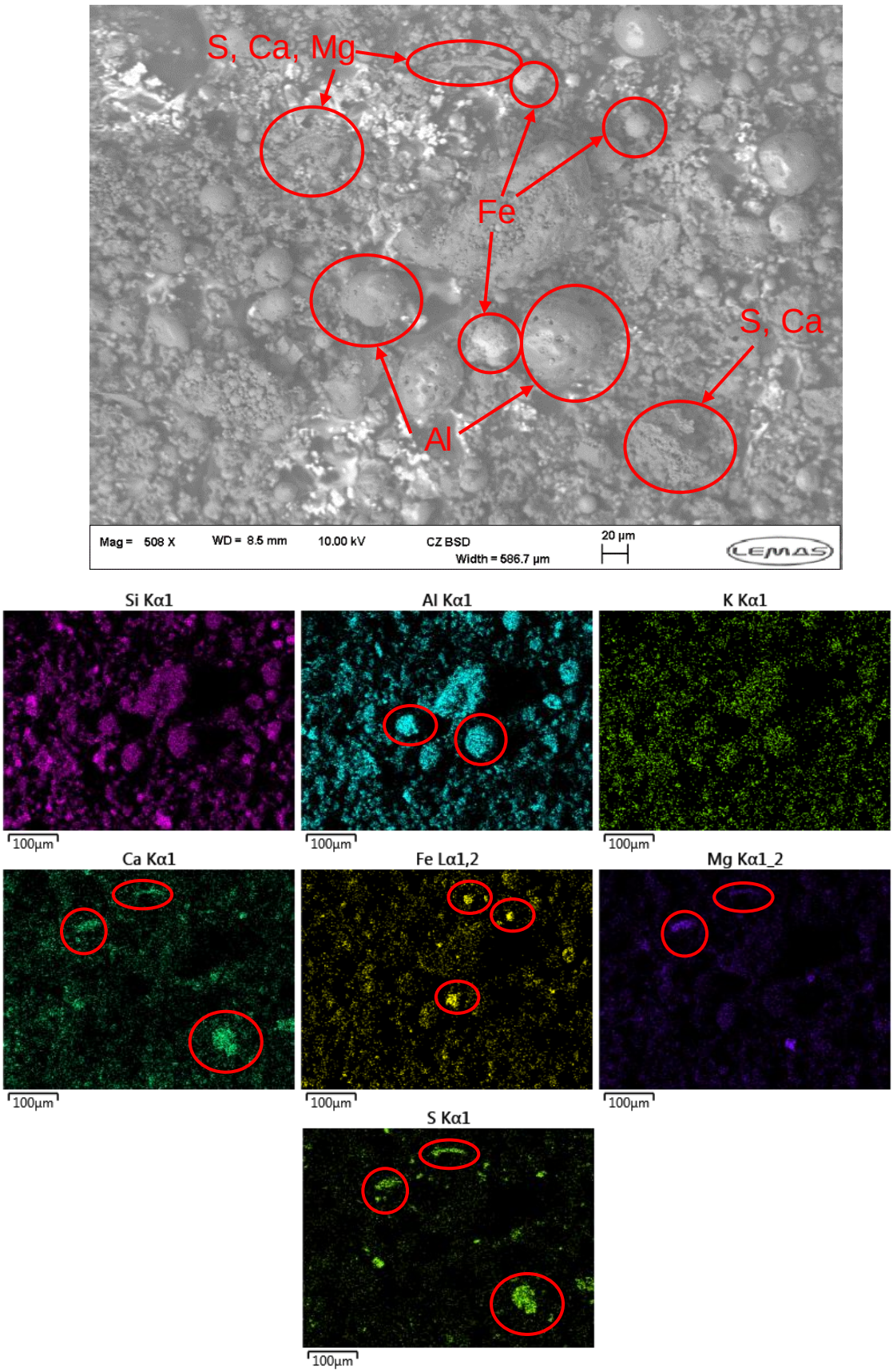

Figure 7.17 – SEM-EDX imaging of WWA5%PFA after sintering at 900°C, with different agglomerate features highlighted

Agglomerates with different features were found to have different elemental composition. Sulphur was observed to have accumulated in regions with high calcium and magnesium concentrations. This is a well-known phenomenon, with the sulphur retaining properties of coal ashes shown to be heavily dependent upon the calcium content of laboratory-prepared coal ashes at similar temperatures in a study by Sheng et al [220], as both calcite ($CaCO_3$) and lime (CaO) have extremely active sulphur retention mechanisms. This same study shows that magnesium present in the form of dolomite ($CaMg((CO_3)_2$ has a similar effect to calcite, due to the following decompositions which occur at temperatures of over 600-700°C:

$$CaCO_3 \rightarrow CaO + CO_2 \qquad \text{(Eqn. 7.1)}$$

$$CaMg(CO_3)_2 \rightarrow CaO + MgO + 2CO_2 \qquad \text{(Eqn. 7.2)}$$

The lime produced by these decompositions is subsequently converted to calcium sulphate ($CaSO_4$), resulting in sulphur retention. Additionally, Sheng et al found that alkali metals play a larger role in sulphur retention within pulverised fuel combustion than under laboratory conditions due to Equation 2.3 (repeated below for convenience).

$$2MCl + SO_2 + \frac{1}{2} O_2 + 2H_2O \leftrightarrow M_2SO_4 + 2HCl \qquad \text{(Eqn. 2.3)}$$

While WWA has an extremely low sulphur content (~0.02 wt.%), the PFA has a dry sulphur concentration of approximately 0.88 wt.%, which will have been dependent upon both the Ca/S and alkali/S molar ratios within the original coal for the reasons discussed above (the composition of which was not available for this study). Bryers [76] reports that calcium sulphate has been shown to form a melt at 830°C in calcium sulphate/calcium sulphide systems, and can cause troublesome deposits due to forming low temperature eutectics in the presence of alkali metals. These results indicate that the use of coal ashes as Al-Si additives may have adverse effects in biomass containing high calcium and magnesium concentrations, as they are likely to introduce additional sulphur into the system that may flux with any alkali metals present. Furthermore, Equation

2.3 results in a competing route for MCl conversion, reducing the effectiveness of aluminosilicate conversion and creating troublesome calcium sulphate deposition.

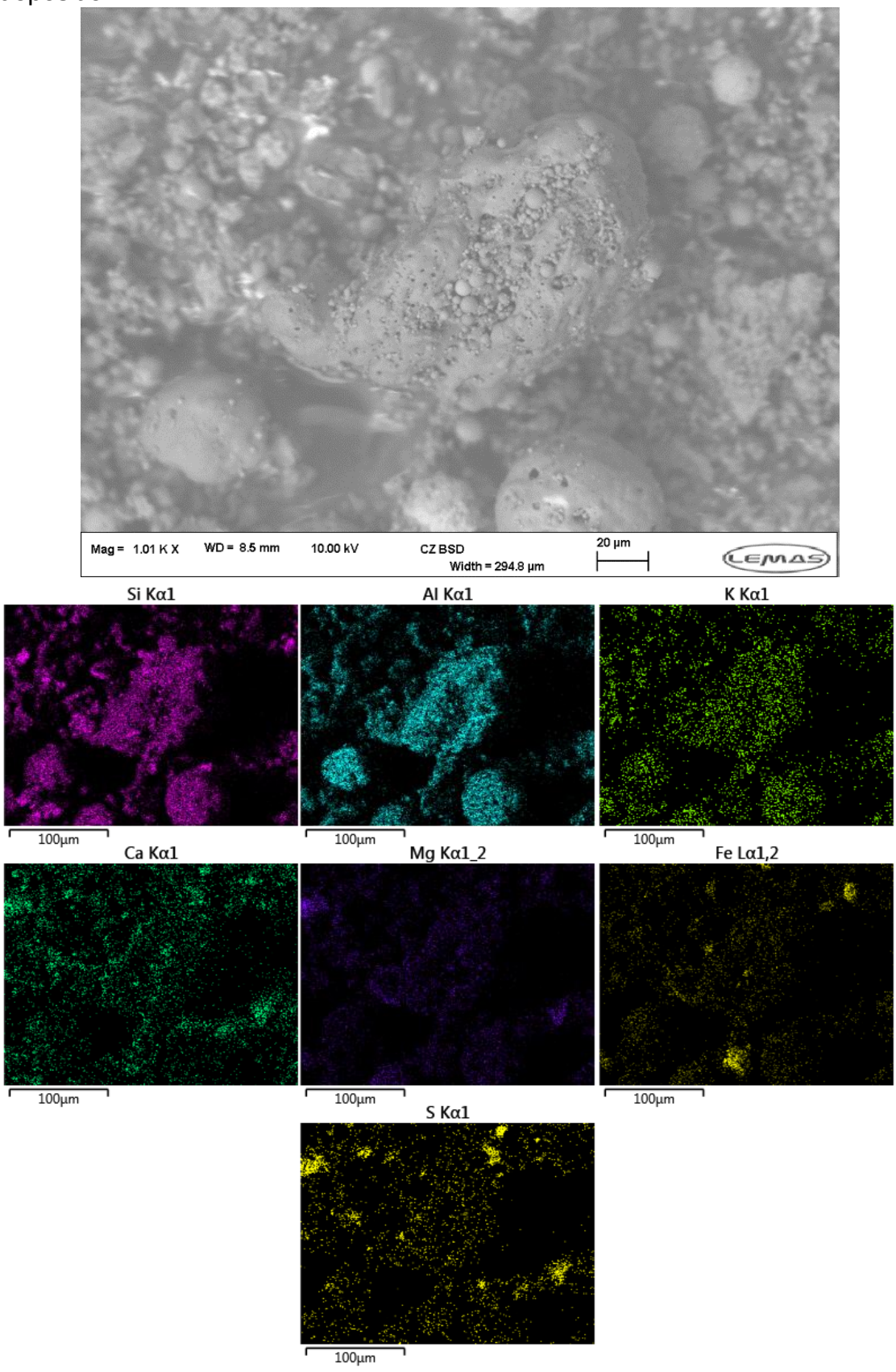

Figure 7.18 – Magnified SEM-EDX images of agglomerated particles from Figure 8.17

In addition, significant agglomeration was observed to have occurred in regions of high aluminium and iron concentration. Closer inspection of the largest agglomerates in Figure 7.17 (Figure 7.18) showed that these agglomerates consisted of many smaller particles encased within sintered aluminium-silicon rich material. Additionally, large, smooth spherical iron particles were observed, indicating sintering of iron. The network theory of silicate melts (as discussed in Chapter 5.2.2) states that Al_2O_3 and particularly Fe_2O_3 will behave as network modifiers in the presence of network formers such as silica, when low concentrations of network modifiers (such as Na_2O and K_2O) are present. The composition of WWA5%PFA results in five times the amphoteric concentration when compared to alkali concentration on a wt. % basis, along with a high SiO_2 concentration of 55.16%. As a result, rather than having a positive effect upon the sintering properties of the ash, the amphoteric concentration is adversely affecting the melting behaviour, behaving as a network modifier and fluxing the SiO_2 within the sample, producing the features shown in Figure 7.17 and 7.18. By contrast, OCA5%KAO had an amphoteric/alkali ratio of 0.64, which resulted in the elimination of sintering. These results suggest that it may be possible to determine the ideal rate of addition of Al-Si additives by the amphoteric/alkali ratio of a sample and should be a focus of further study.

WWA5%KAO showed increased sinter strength when compared to the WWA samples: however, the significant onset of sintering observed for WWA5%PFA and above did not occur for WWA-KAO blends. SEM-EDX imaging showed that, despite the higher sinter strengths compared to WWA at 900°C, WWA5%KAO after sintering at 900°C (Figure 7.19) retained a granular structure with few of the particles exhibiting severe sintering on the surface. Silicon and aluminium make up much of the sample as expected, indicating that the aluminium was behaving as a network former alongside the silica and forming high melting temperature aluminosilicates, while the potassium within the sample was dispersed evenly throughout. Once again, accumulations of magnesium and calcium were observed, similar to the WWA5%PFA sample. Although the iron content was greatly reduced in kaolin (0.9%) compared to PFA (9.3%), iron particles were also visible within the sample (highlighted, Figure 7.19).

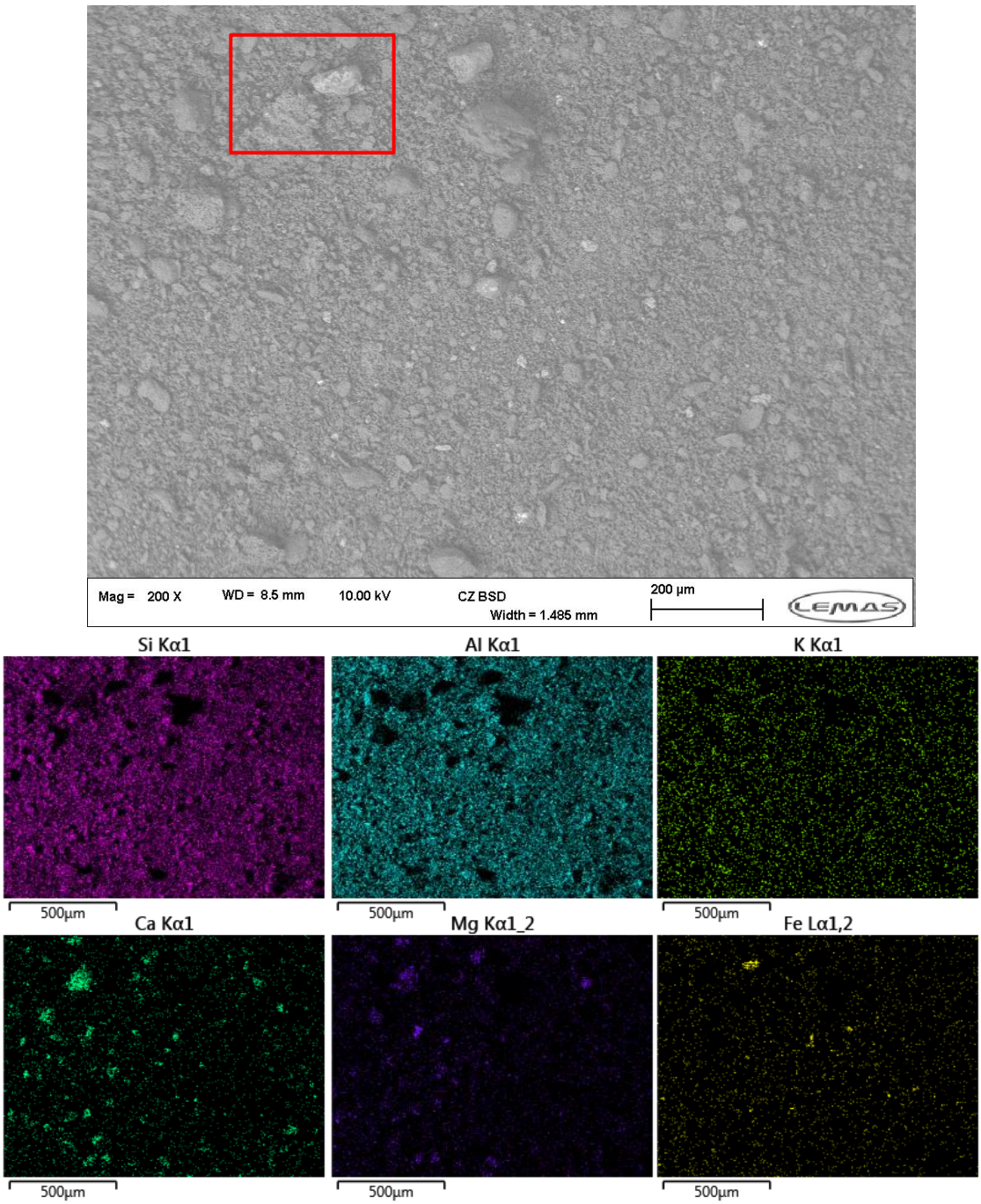

Figure 7.19 – SEM-EDX imaging for WWA5%KAO sintered at 900°C

A closer look at the highlighted region in Figure 7.19 (Figure 7.20) showed that the iron particles were not spherical as in Figure 7.17 for WWA5%PFA, indicating that less sintering due to iron fluxing had occurred, likely due to the lower concentration in the sample resulting in network forming behaviour. However, like WWA5%PFA, the regions of significant calcium and magnesium concentration were shown to coincide with a concentration of sulphur, while a significant phosphorus and sodium presence was observed that was not present in other samples.

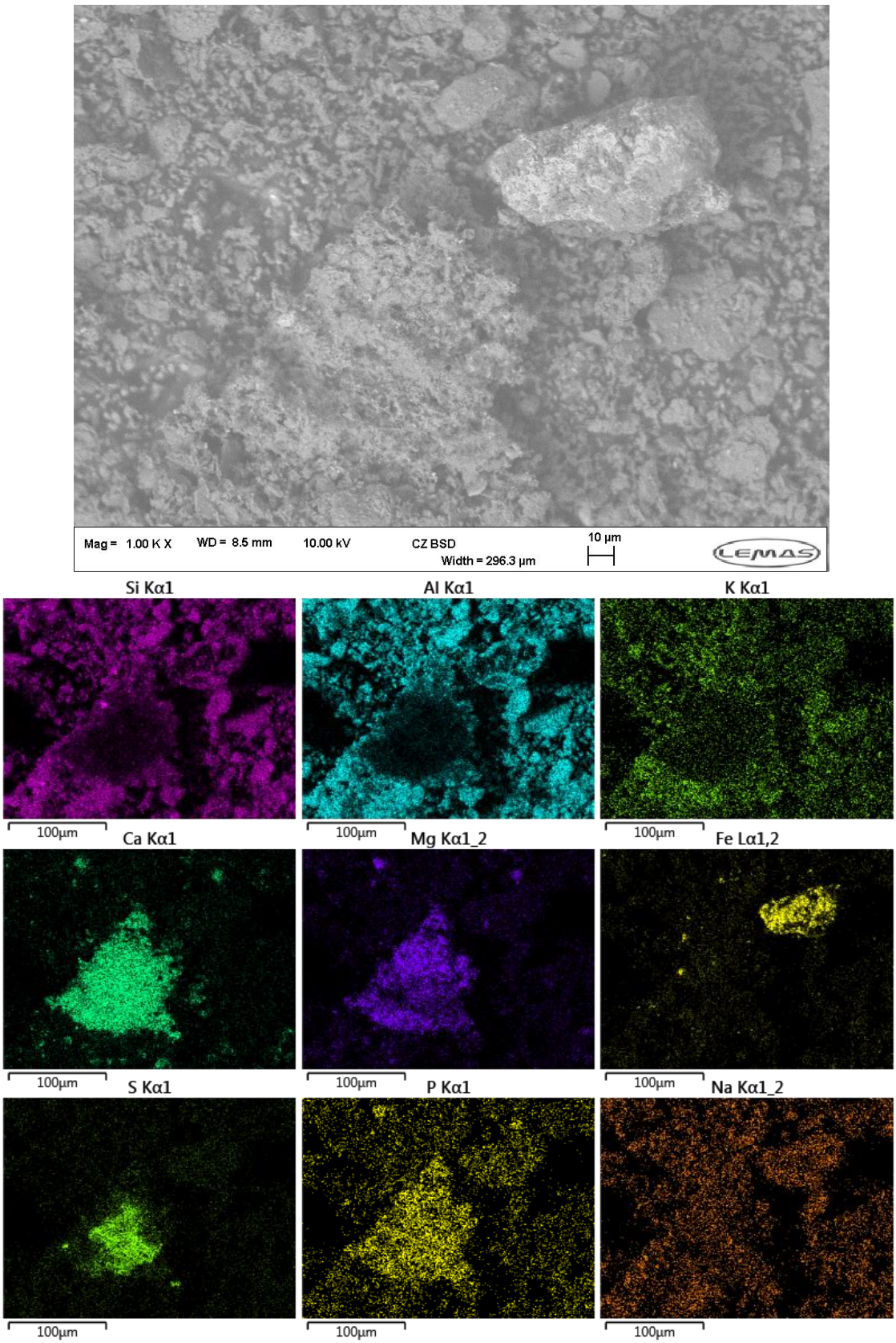

Figure 7.20 - SEM-EDX imaging of highlighted region in 7.17 for WWA5%KAO sintered at 900°C

Sodium is present both in the WWA and as potash mica ($KAl_2(AlSi_3O_{10})(F,OH)_2$) in the kaolin; in contrast, only trace amounts of sulphur are expected from the

composition analysis. However, these features were rare: most of the larger particles in the sample were rich in aluminium and silicon, with accumulations of magnesium and calcium, such as the example in Figure 7.21. As a result, the increase in sintering in WWA5%KAO when compared to WWA is thought to be due to the magnesium and calcium content of the WWA, and their interaction with the minerals in the kaolin powder, while the reduced iron content is the reason that reduced sintering is observed when compared to the WWA5%PFA samples.

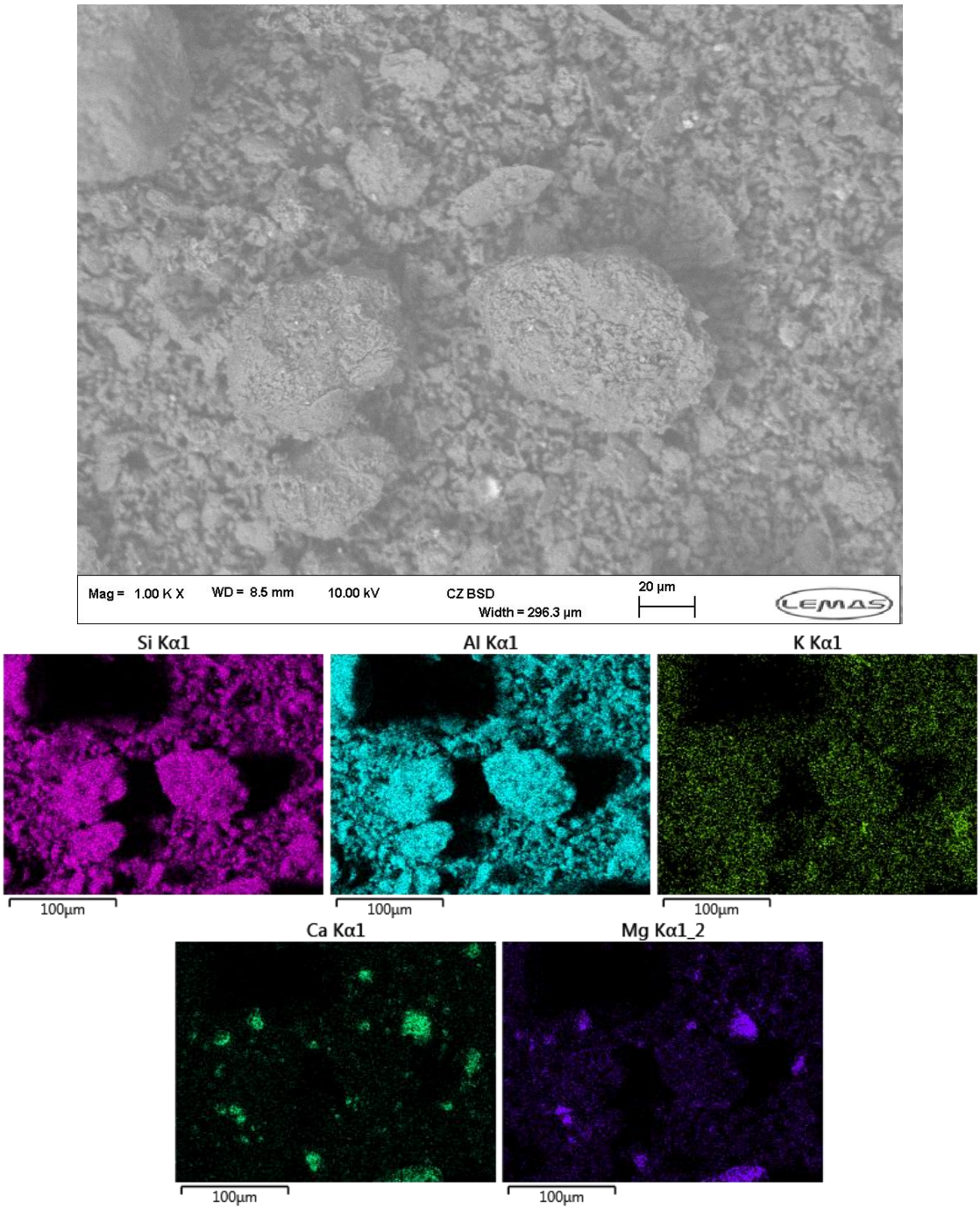

Figure 7.21 - SEM-EDX imaging for WWA5%KAO sintered at 900°C

XRD spectra (Figure 7.22a) showed highly significant silicon dioxide peaks occurring in the WWA5%PFA sample, while a strong match with Fe_2O_3 was also present, further indicating that the iron content of the PFA was having a fluxing effect on the silica through the sample, producing liquid phase on the surface of particles and reducing porosity. WWA5%KAO spectra (Figure 7.22b) also showed silicon dioxide, but aluminium silicon oxide and potassium aluminosilicate peaks were also present, indicating that liquid phase silica had not coated the particles as significantly as in the PFA sample. This behaviour indicates that the iron content within the PFA is crucial in determining its efficacy as an additive at temperature regions of 900°C and above and explains why samples with high PFA concentrations (such as WWA and FA at 15% and above) experience greater sinter strengths.

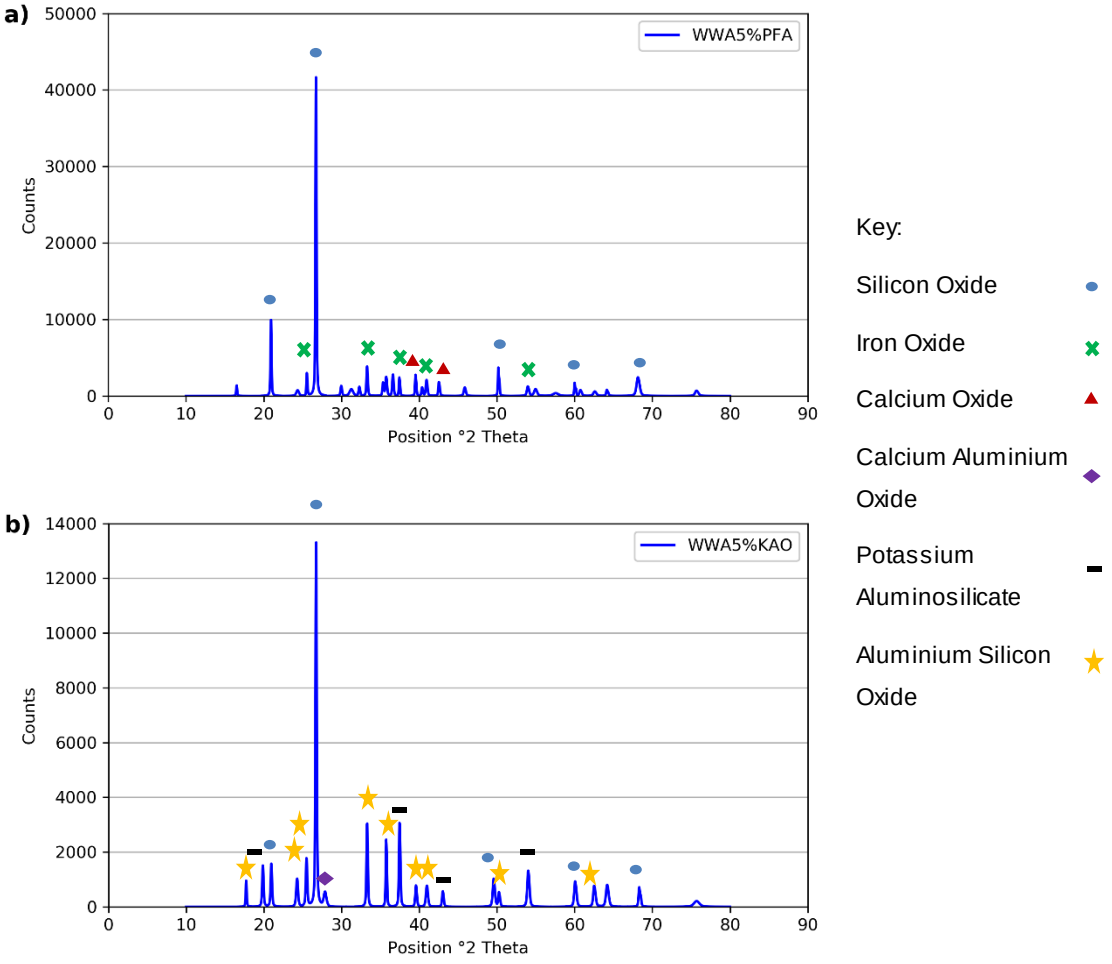

Figure 7.22 - XRD spectra for a) WWA5%PFA; and b) WWA5%KAO. Note different count scales

7.4.2.3 - BA/PFA Samples

The sinter strength results of BA and FA with PFA addition give further weight to the findings from WWA sinter strength testing, with the addition of PFA resulting in an marked increase in sinter strength at temperatures of above 900°C. BA showed little sintering up to 950°C, likely due to its high silica content with melting temperatures of up to 1700°C [80]. SEM imaging showed that BA consisted of two main types of particle. The remnants of the cellulosic structure of the plant cells remained visible after ashing, as shown in Figure 7.23, while silicon-rich particles dominated the sample.

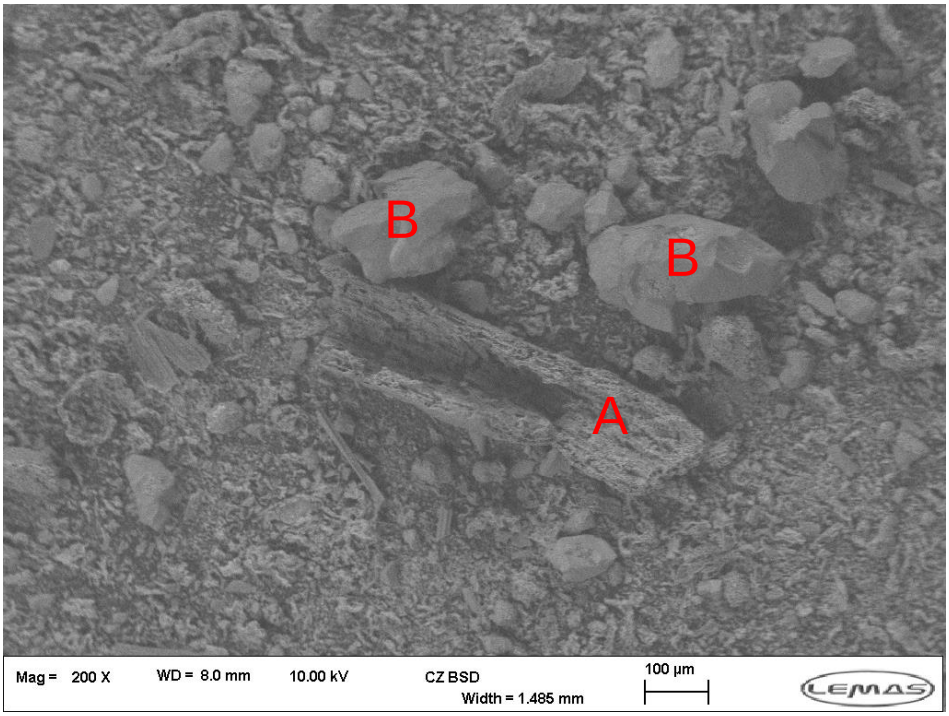

Figure 7.23 - SEM image of BA sample before sintering, showing lignocellulosic structure (A) and silica particles (B)

The gradient of the sinter strength-temperature relationship was observed to increase at above 900°C: as Figure 7.24 shows, the cellulosic structure was completely broken down while the silica particles remained intact. Silicon was observed to dominate the sample, with concentrated regions corresponding to silica particles, with a fairly even dispersion of aluminium, potassium, calcium, iron and magnesium. Particles showing signs of agglomeration onset were also visible. A closer inspection of the silica particles (Figure 7.25) showed that the silica had developed microstructures of iron on the surface of the particle,

extremely similar to those observed by Liu et al in synthetic coal ashes with low iron concentration (an example of which is shown in Figure 5.2). Agglomerated particles (Figure 7.26) were shown to consist of dense silicon, phosphorus and calcium-rich particles connected by a complex network comprised of potassium, magnesium, aluminium and iron, which can be inferred to be the cause of the increased sinter strengths at higher temperatures. This agglomeration appears to be localised however, resulting in sinter strengths below the 5 MPa limit recommended by Gibb [203] for soot blower removal.

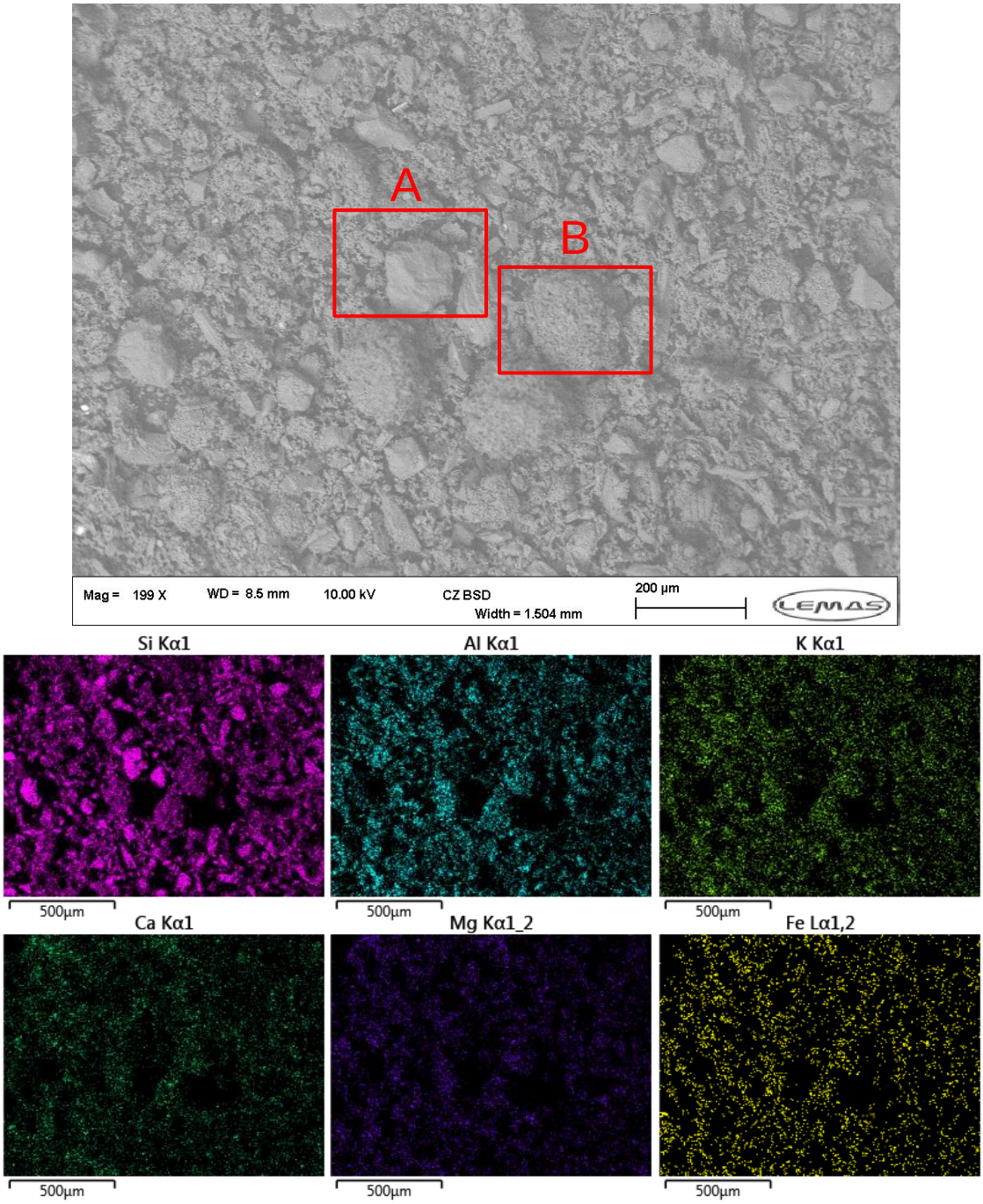

Figure 7.24 - SEM-EDX image of BA sintered at 950°C

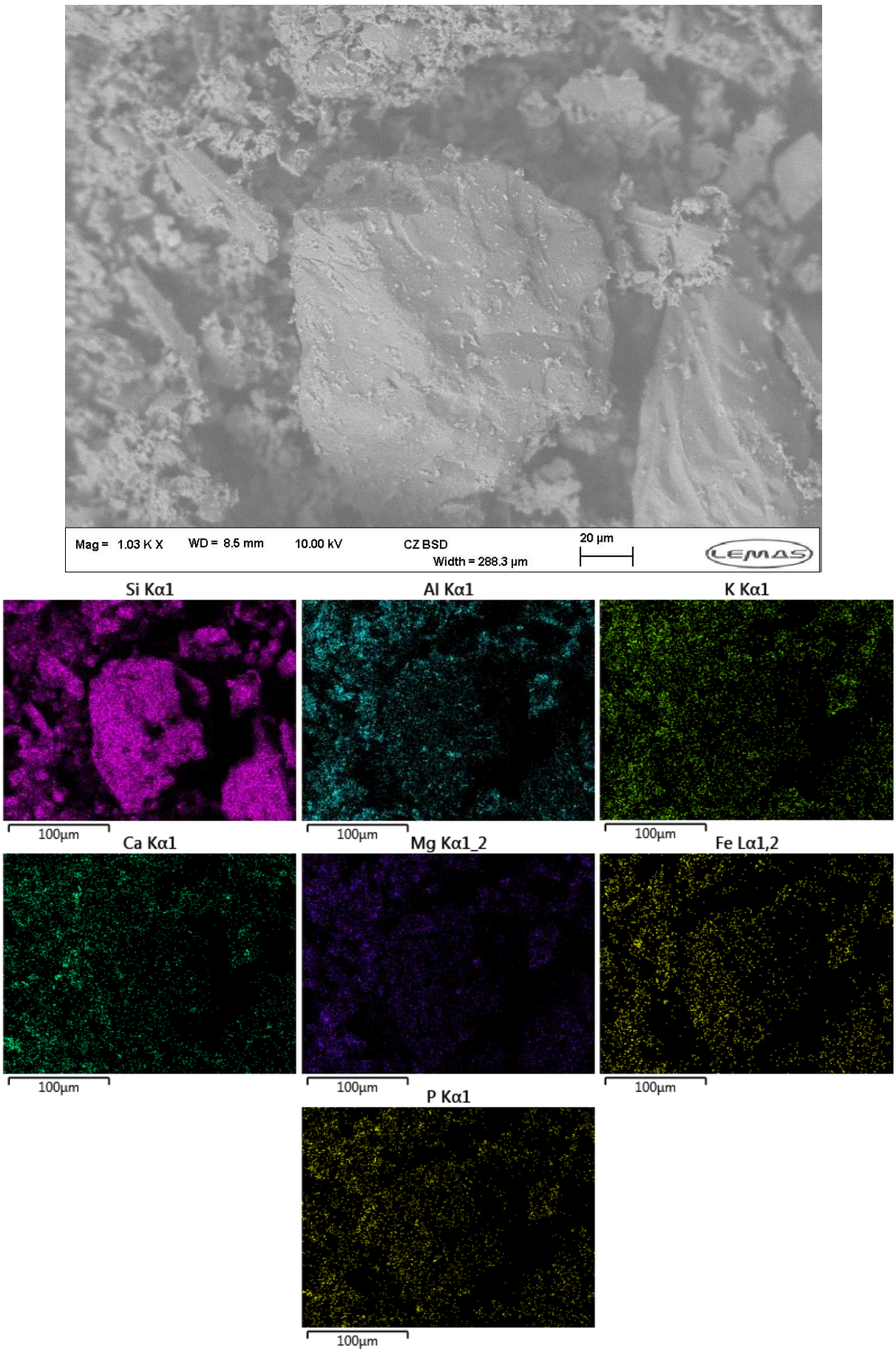

Figure 7.25 - SEM-EDX images of silica particle in BA sintered at 950°C (A, Figure 7.24)

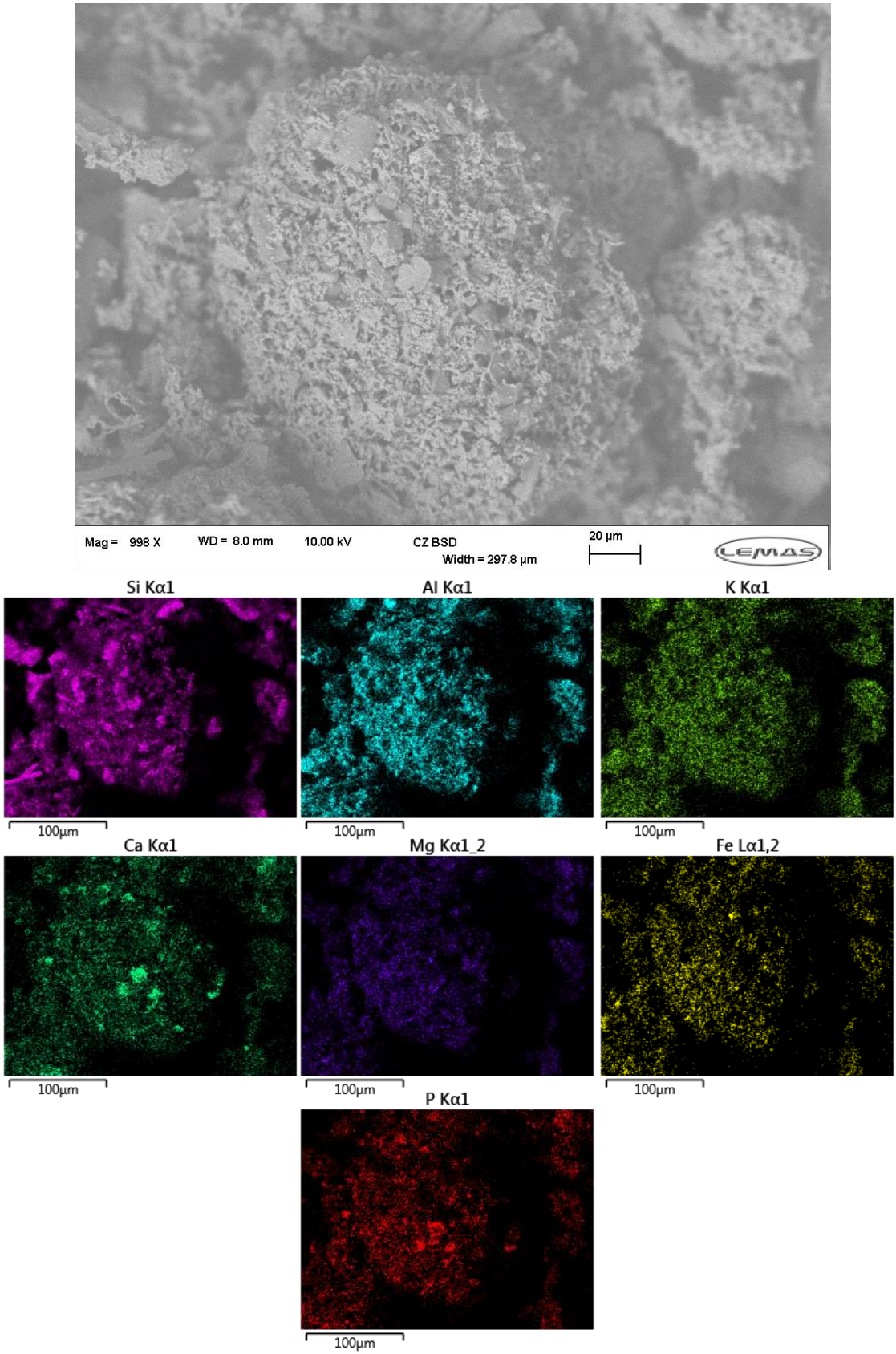

Figure 7.26 - SEM-EDX of agglomerated particle from BA sintered at 950°C (B, Figure 7.24)

The addition of PFA to BA resulted in significantly increased sinter strengths at 950°C, with greater PFA concentrations leading to higher sinter strengths. At BA15%PFA and above, sinter strengths were beyond the Gibb 5 MPa sootblowing recommendation, and as such would be expected to cause deposition that would pose significant removal problems. SEM imaging of BA25%PFA sintered at 950°C (Figure 7.27) showed that the samples had begun to produce much larger agglomerates than observed in BA sintered at the same temperature. Concentrated particles of iron were observed, similar to the WWA-PFA blends (Figure 7.16): however, the large, smooth aluminium-rich particles that encased and agglomerated groups of smaller particles in Figure 7.16 were not present in BA-PFA sample. The greater ash concentration of BA compared to WWA means that the same blends resulted in low iron concentrations, reducing the impact of iron fluxing upon the sample but not eliminating the issue.

Increasing the SEM magnification (Figure 7.28) however showed that similar smooth aluminium-rich particles were present on much smaller scales, indicating that some aluminium-based melting was occurring to some degree. The sintering material EDX imaging showed the sintering material to have a complex composition, with no single element appearing to be responsible for material transport, although this network did correspond to regions of lower silicon and aluminium concentrations. Potassium and sodium additionally appeared to have a high concentration within the agglomerated particles, with some calcium and iron appearing throughout in addition to concentrating within larger particles that had agglomerated within the sintering material. The low basicity of BA likely means that the iron and aluminium oxides will behave as network modifiers, similar to the mechanisms observed in WWA-PFA blends and resulting in greater sintering in fouling deposits at the measured temperatures.

SiO_2 accordingly dominates the XRD spectra for BA (Figure 7.29a). Remaining peaks were small, showing matches corresponding to iron oxide and potassium aluminium silicate. The addition of PFA was found to initiate sintering at temperatures of 900° and above: XRD of PFA at 25% addition to bagasse once again showed strong silica peaks (Figure 7.29b), however a stronger match with Fe_2O_3 was observed, once again indicating the presence of a fluxing mechanism inducing the observed sintering.

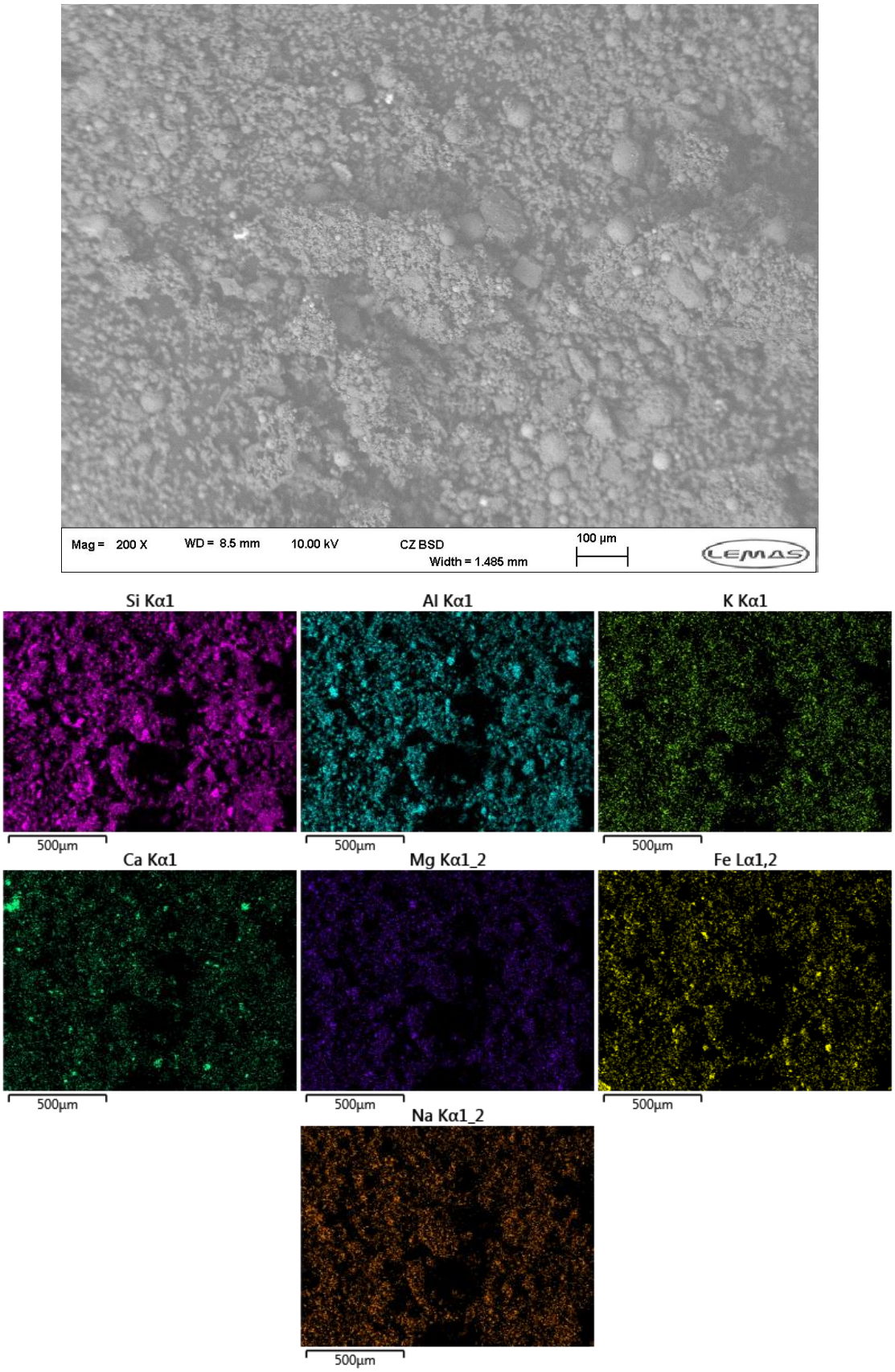

Figure 7.27- SEM-EDX images of BA25%PFA sintered at 950°C

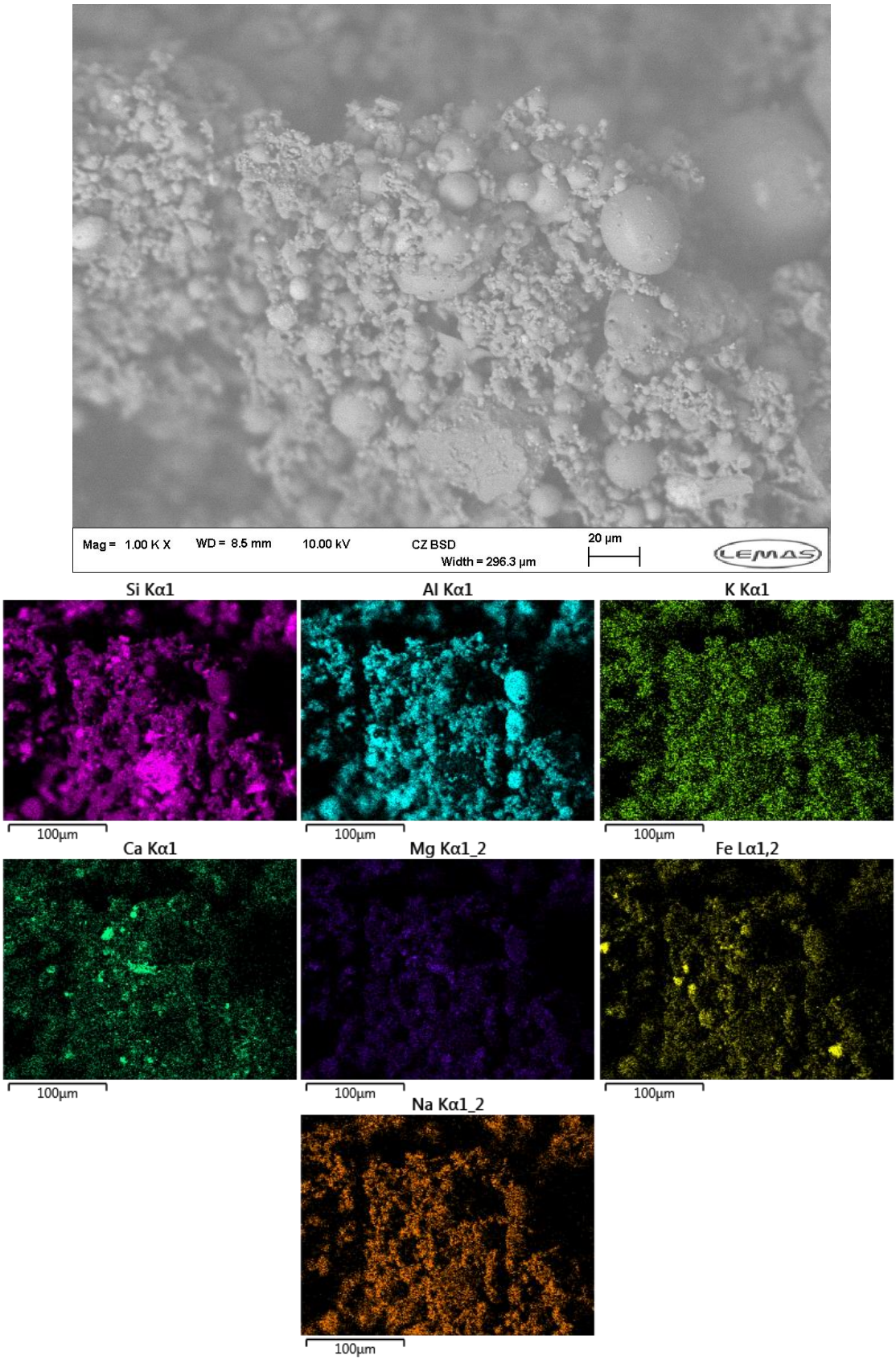

Figure 7.28 - SEM-EDX images of BA25%PFA sintered at 950°C

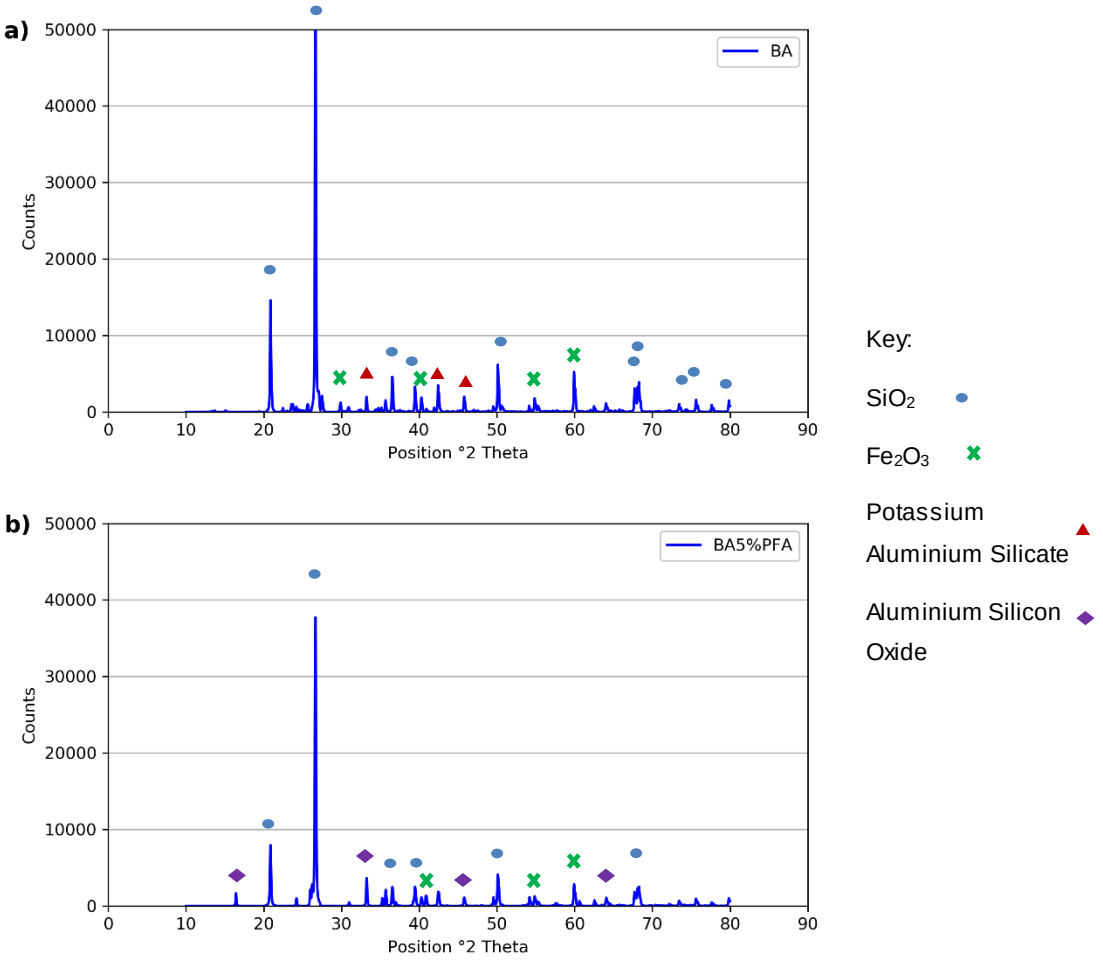

Figure 7.29 - XRD Spectra for a) BA sintered at 950°C and b) BA25%PFA sintered at 950°C

7.4.2.4 - FA/Additive Samples

Sinter strength results for FA samples showed the onset of sintering at approximately 900°C. SEM imaging of FA after sintering at 950°C (Figure 7.30) showed that agglomeration of particles had occurred, with features similar to those observed in WWA-PFA blends, including large spherical aluminium/iron rich particles and calcium-sulphur rich agglomerates, indicating that the sintering mechanisms involved were similar between the FA and WWA-PFA samples. FA had the highest Fe_2O_3 (5.9 wt.%) and Al_2O_3 (19.1 wt.%) concentration of the non-additive samples tested, giving further weight to the hypothesis that a high amphoteric-alkali ratio is the cause of sintering in samples at temperatures of 900°C and above. Magnifying the image in Figure 7.30 (Figure 7.31) showed that

once again, silicon-aluminium rich material was the cause of sintering, with evidence of liquid phase present at 950°C (highlighted).

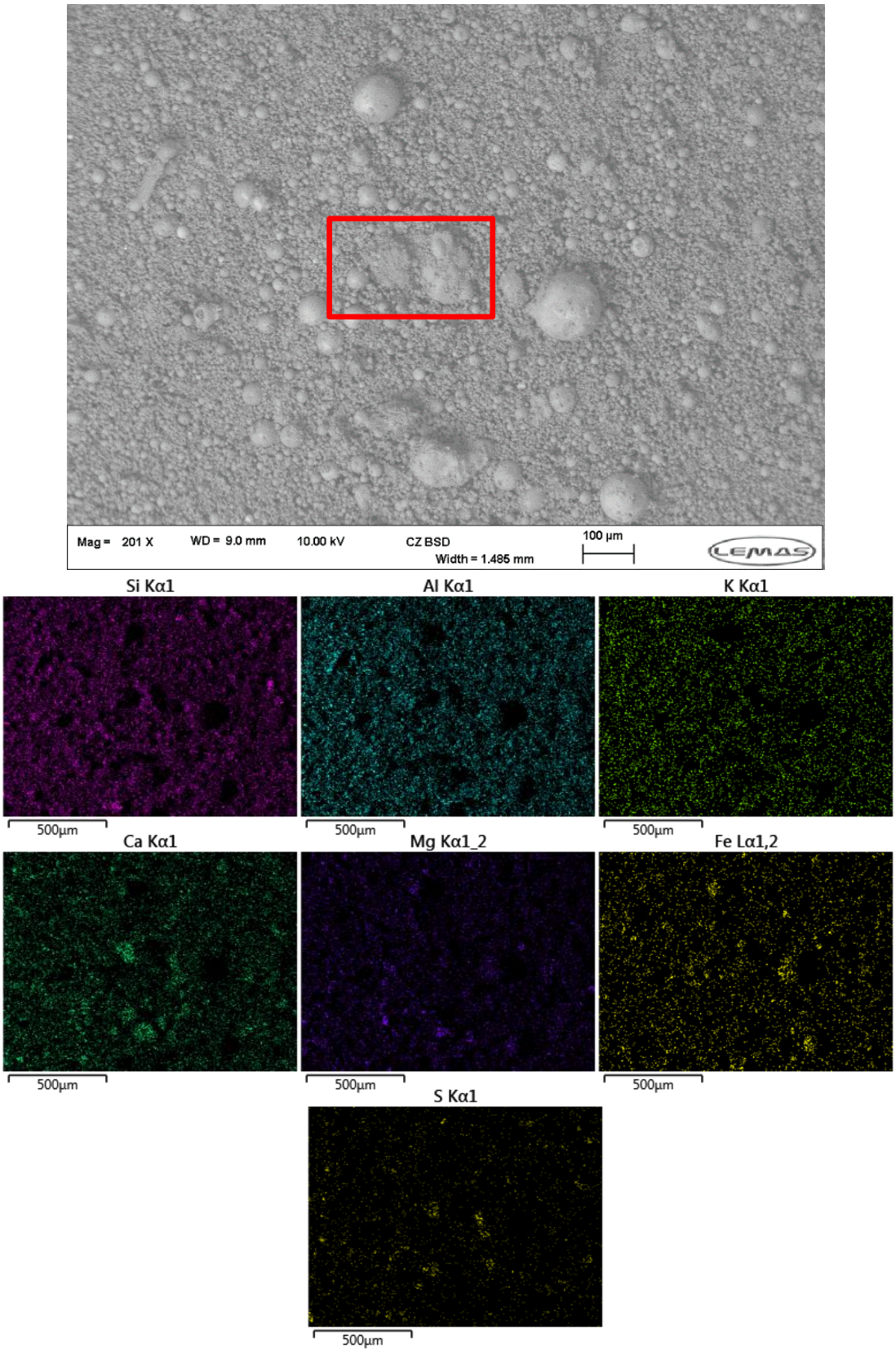

Figure 7.30 - SEM-EDX imaging of FA sintered at 950°C

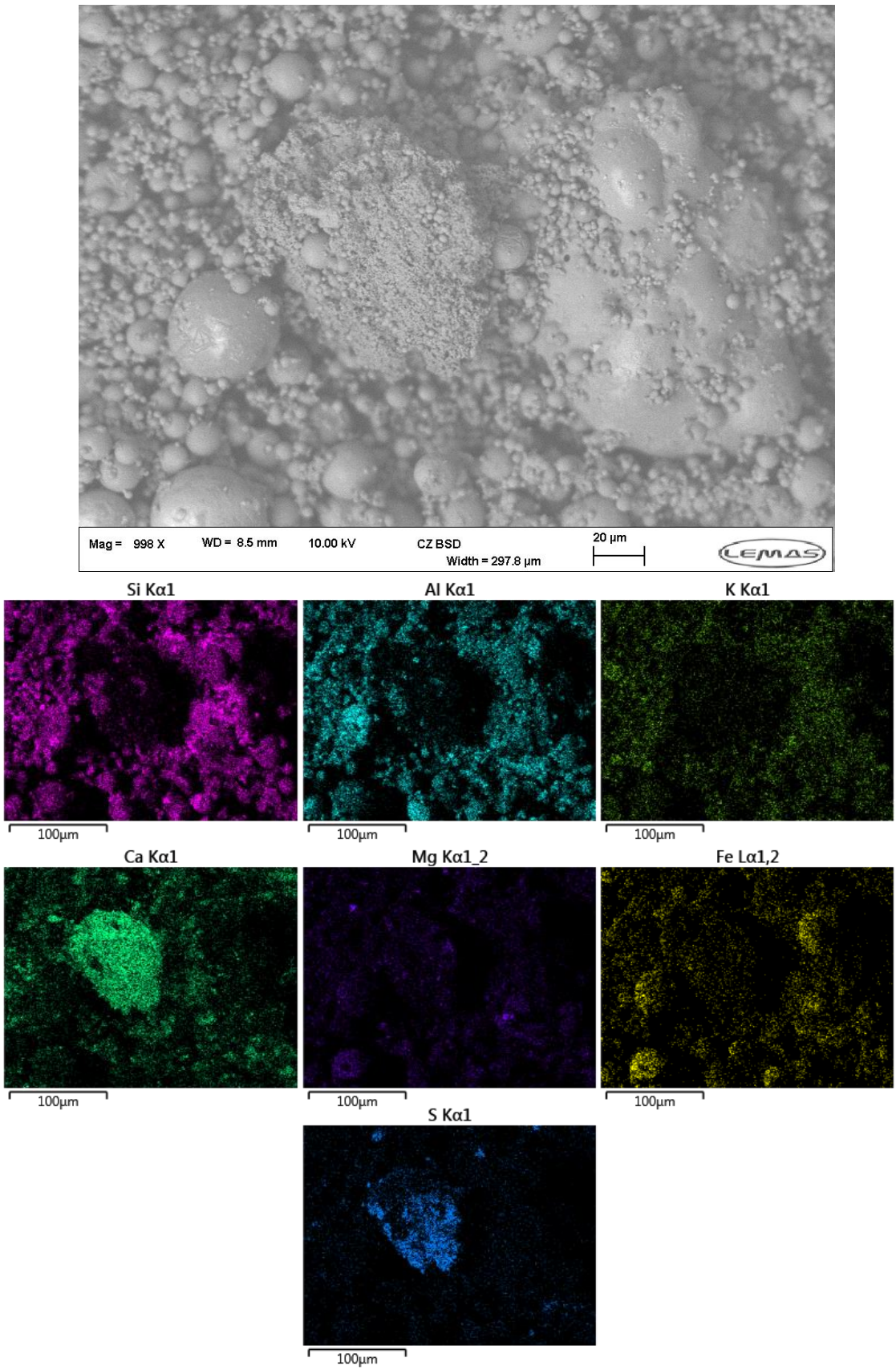

Figure 7.31 - SEM-EDX image of the region highlighted in Figure 7.30

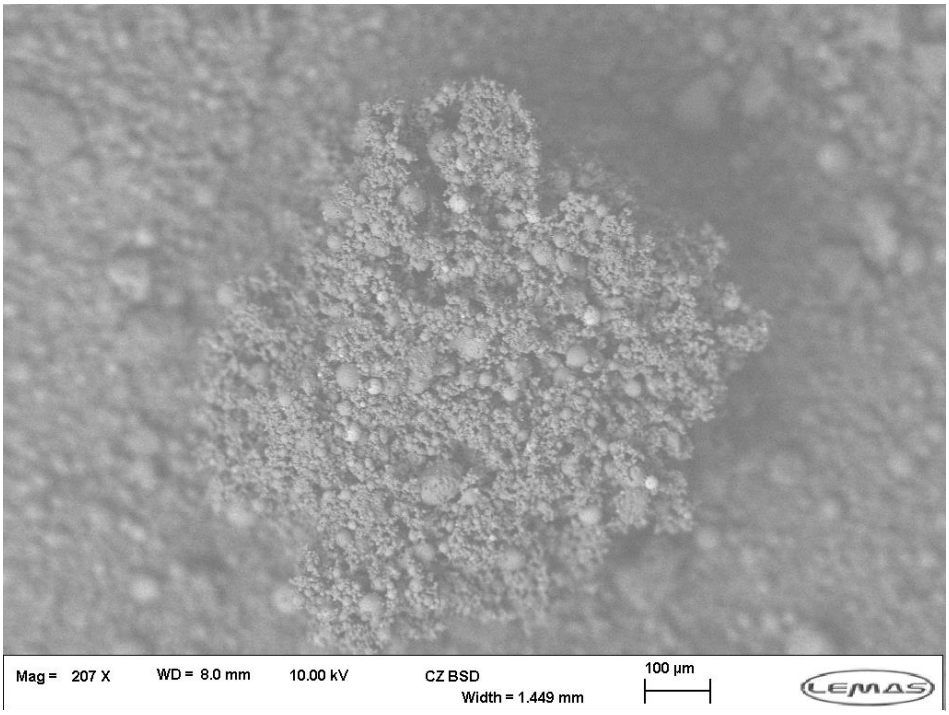

Figure 7.32 - Example of agglomeration observed in FA25%PFA after sintering at 950°C

The scale of agglomeration within the FA samples is most visible in Figure 7.32, which shows an agglomerate many times larger than those observed in other samples. Closer inspection (Figure 7.33) shows clearly that this agglomerate consists of multiple small, smooth particles, and once again reveals the presence of concentrated regions of iron and calcium, in addition to high silicon and aluminium levels.

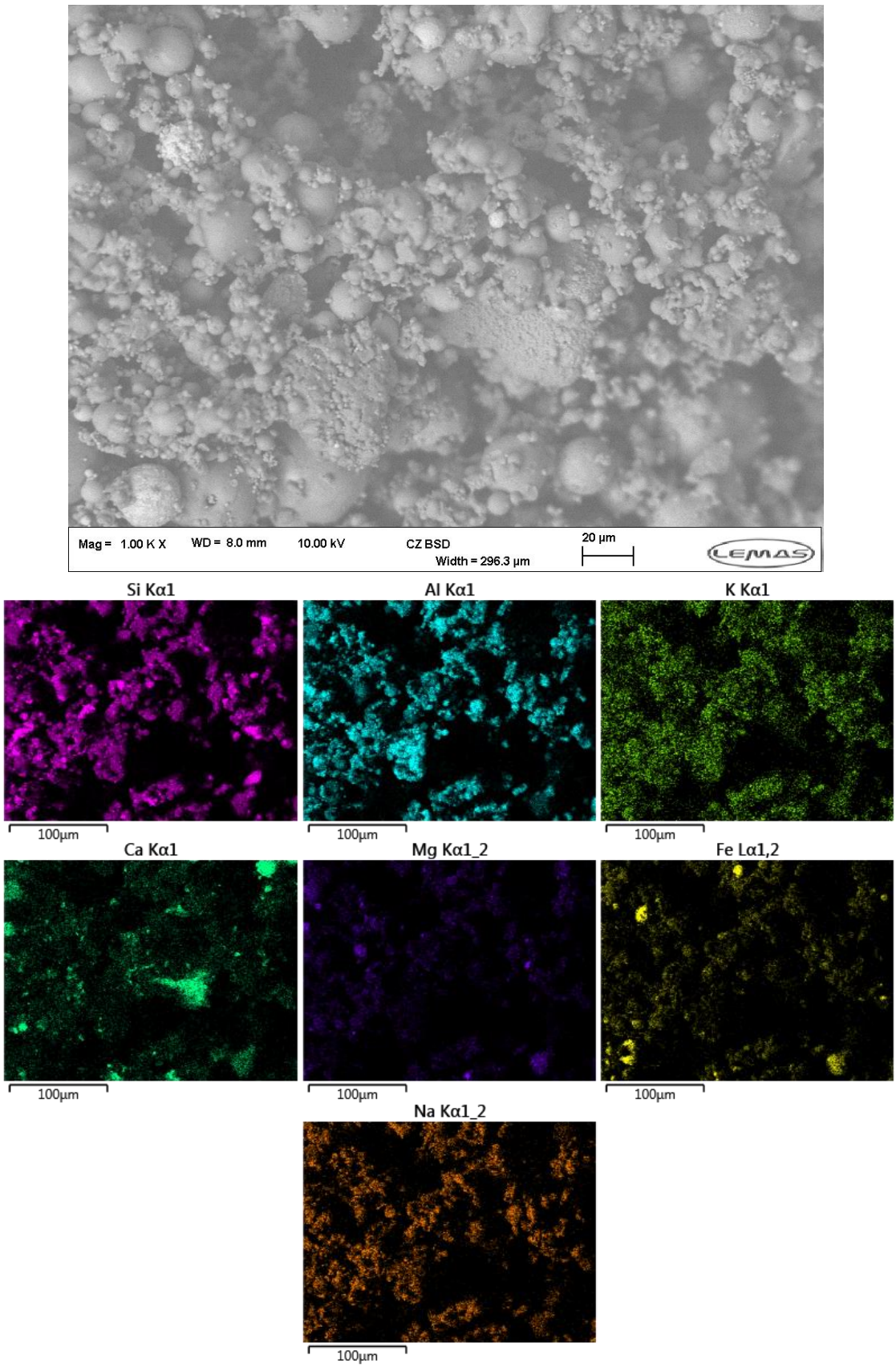

Figure 7.33 - SEM-EDX imaging of FA25%PFA after sintering at 950°C

The FA sample showed a dominant silica peak present in the XRD spectra (Figure 7.34a). Compared to the BA sample, ICP ash analysis showed that FA contains twice as much K_2O, MgO and Fe_2O_3, which are all known silicate fluxes. The addition of PFA (Figure 7.34b), while decreasing K_2O and MgO concentration, will also increase iron content, leading to iron fluxing within the sample due to the lack of network modifiers present in the sample. Therefore, sinter strength testing shows that although BA and FA contain concentrations of potassium that are not insignificant, the use of Al-Si additives will not improve behaviour and should be restricted to use on high K, low silica biomass.

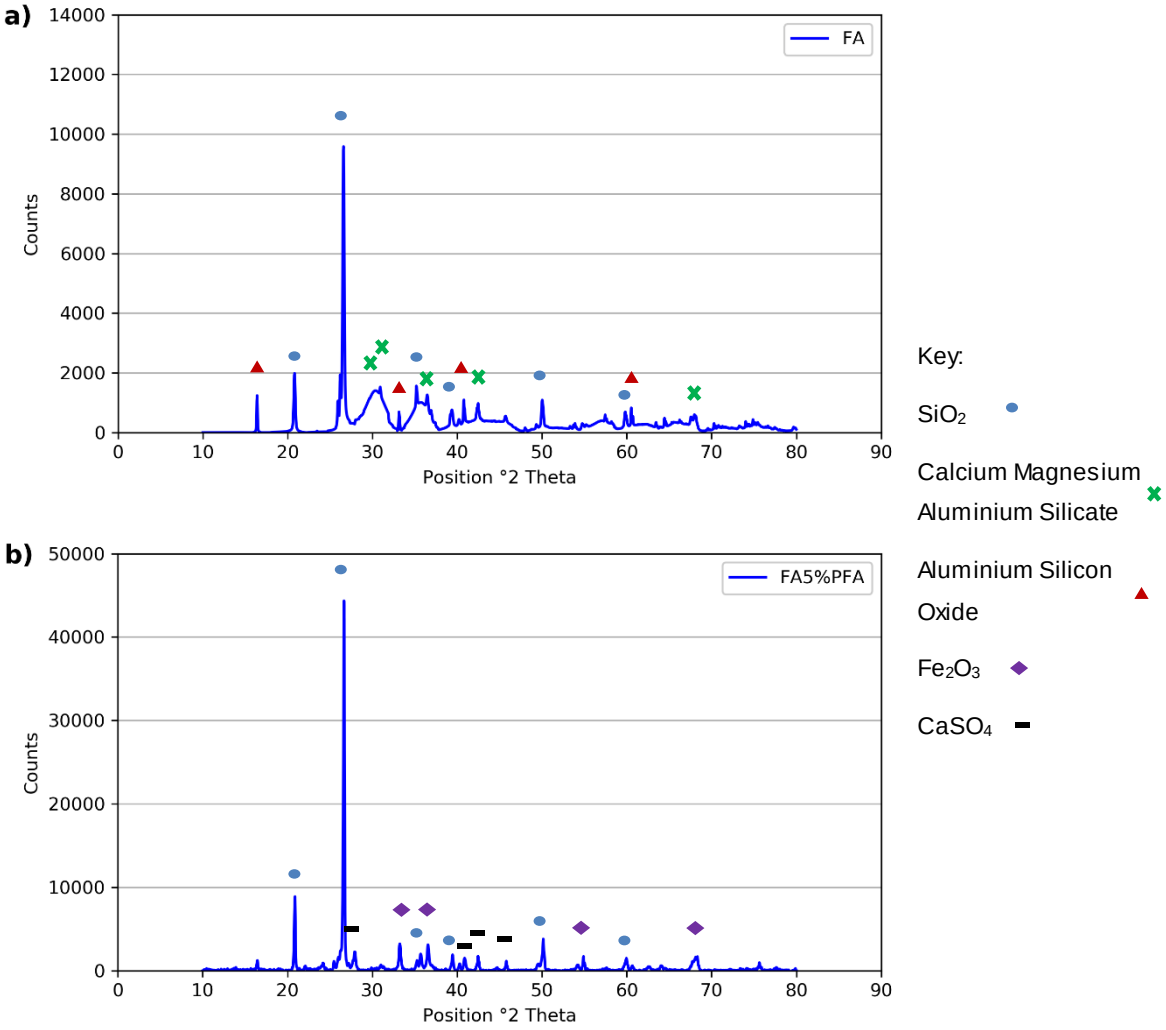

Figure 7.34 – XRD spectra for a) FA and b) FA5%PFA sintered at 950°C

7.4.3 - Correlations

Linear Pearson correlations for sinter strength results at each sintering temperature were calculated, to establish basic trends and to determine whether certain components of ash were responsible for the onset of sintering at certain

temperatures. Of the ash oxide components, very few linear correlations with sinter strengths at the temperatures measured were observed. At 850°C, a slight positive correlation with K_2O concentration was observed, while at 950°C stronger positive correlations were found for Na_2O and Fe_2O_3 concentration, as shown in Figures 7.35 a-c.

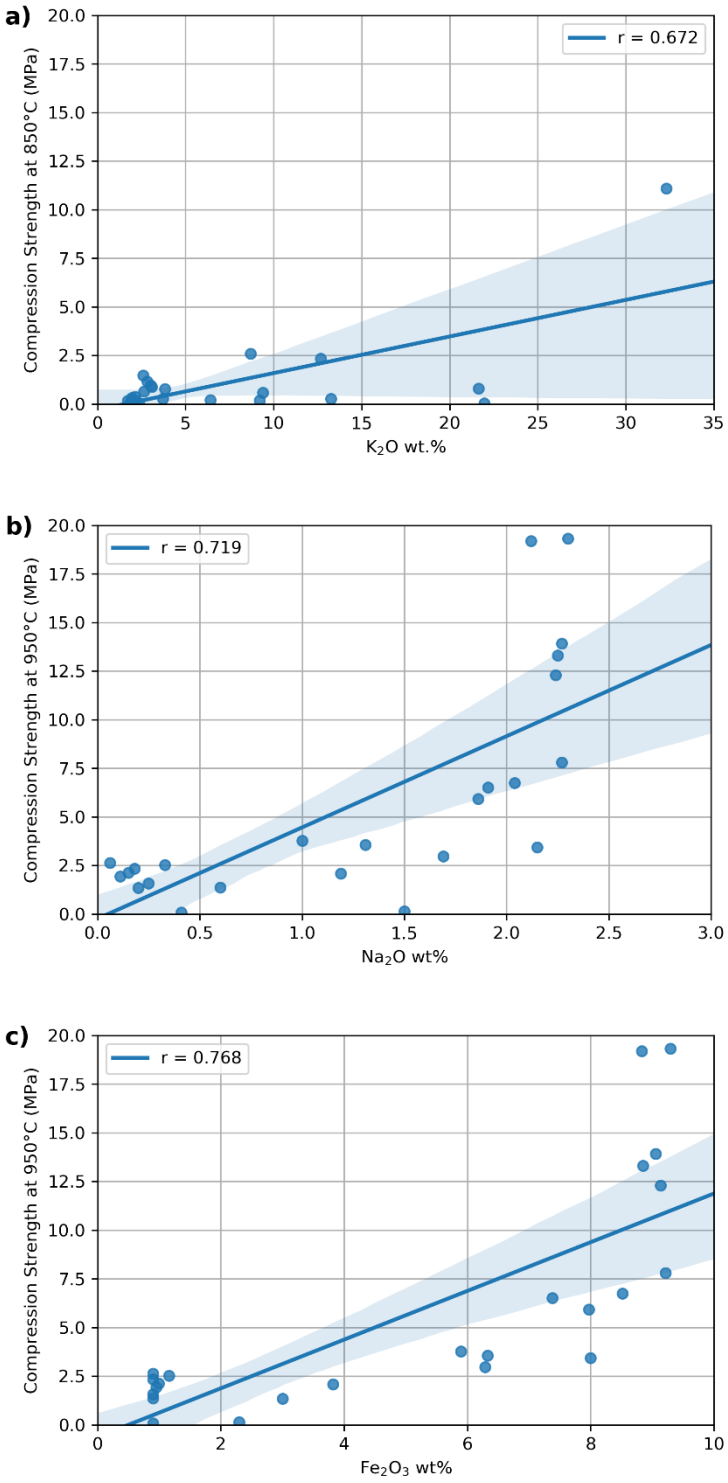

Figure 7.35 - Linear correlations for a) K_2O with sinter strength at 850°C, and b) Na_2O and c) Fe_2O_3 concentrations at 950°C

However, upon splitting the data into separate groups corresponding to PFA and KAO blends, correlations showed much different behaviour. Strong positive correlations were found at all temperatures for Al_2O_3 concentration in samples containing KAO: however, samples containing PFA behaved differently, with negative correlations observed for sinter strengths at temperatures of 800, 850 and 900°C. At 950°C, a strong positive correlation is also observed for PFA blended samples. These results are shown in Figures 7.36 a-d.

The most interesting results were for PFA and KAO correlations comparing K_2O concentrations against sinter strengths, which can be found in Figures 7.37 a-d. Surprisingly, sinter strengths were found to consistently decrease with increasing K_2O concentration for KAO samples. This is somewhat unexpected since, as explained in Section 2.5.1 (see Figure 2.7), increasing K_2O content in a SiO_2-Al_2O_3-K_2O ternary system is expected to significantly decrease the eutectic temperatures of the system. Increasing KAO content leads to systems with extremely high SiO_2-Al_2O_3 concentration in the ash.

This can be explained by looking at the behaviour of kaolinite, of which the KAO sample contains greater than 70%. Kaolinite undergoes four phase changes with increasing temperature [76]. At temperatures of approximately 500°C, kaolinite dehydrates to form amorphous kaolinite (Eqn. 7.3). At 925°C, silicon spinels start to form, releasing silica (Eqn. 7.4). Beyond 1100°C, mullite begins to form (Eqn.7.5), and at 1400°C other mullite phases are observed (Eqn. 7.6).

$$Al_2O_3.2SiO_2 + H_2O \rightarrow 2H_2O + Al_2O_3.2SiO_2 \ (500\text{-}925°C) \qquad \text{(Eqn. 7.3)}$$

$$2(Al_2O_3.2SiO_2) \rightarrow SiO_2 + 2Al_2O_3.3SiO_2 \ (925\text{-}1100°C) \qquad \text{(Eqn. 7.4)}$$

$$2Al_2O_3.3SiO_2 \rightarrow SiO_2 + 2(Al_2O_3.SiO_2) \ (>1100°C) \qquad \text{(Eqn. 7.5)}$$

$$3(Al_2O_3.SiO_2) \rightarrow SiO_2 + 3Al_2O_3.2SiO_2 \ (>1400°C) \qquad \text{(Eqn. 7.6)}$$

Therefore, some minor sintering would be expected in kaolin samples at lower temperatures: dehydration releases water vapour, which can initiate material transport and result in some sintering, while the release of silica at 925°C may drive further reactive liquid sintering by interacting with fluxing impurities in the KAO, such as Mg and K.

However, kaolinite is known to react with KCl, effectively absorbing potassium as potassium aluminosilicates and releasing the chlorine in the form as HCl, as described in Chapter 2 and by Equations 2.4-6, repeated below:

$$Al_2O_3.2SiO_2 + 2KCl + H_2O \leftrightarrow K_2O.Al_2O_3.2SiO_2 + 2HCl \quad \text{(Eqn. 2.4)}$$

$$(Al_2O_3 + 4SiO_2) + 2KCl + H_2O \leftrightarrow 2KAlSi_2O_6 + 2HCl \quad \text{(Eqn. 2.5)}$$

$$(Al_2O_3 + 6SiO_2) + 2KCl + H_2O \leftrightarrow KAlSi_3O_8 + 2HCl \quad \text{(Eqn. 2.6)}$$

Heating OCA5%KAO to 800°C was observed to significantly increase bound potassium within the sample during viscosity experiments (Chapter 5), since KCl was observed precipitating through an OCA sample when heated to 700° for a prolonged period during hot stage XRD analysis. These observations indicate that potassium binding within OCA-KAO blends begins at as low as 800°C, forming potassium aluminosilicates within the ash before the phase transformations in Equations 7.4-6 can take place. This prevents the release of silica at 925°C, inhibiting sintering within the sample.

In contrast, XRD analysis of PFA has shown that much of the aluminosilicates within the sample are already in the form of mullite with some free quartz present, likely due to the high temperatures of combustion used. Mullite has been shown to interact slowly with KCl, on a scale of hours [221]; therefore the potassium within KCl is more likely to interact with the silica, forming potassium silicates. This explains the lower melting temperature behaviour observed by the PFA blends samples compared to the KAO blends.

Finally, sinter strength results were correlated against various indices commonly used to predict deposition issues (Table 6.1). Although no good linear correlations were observed, once again splitting the correlations into groups of PFA blends and KAO blends showed significant differences in behaviour. KAO blends showed strong correlations between sinter strength and base-to-acid ratio, basic percentage, NBO/BO ratio, silica value and R250, while PFA showed no good correlations. Dolomite ratio was the only index that failed to produce a strong correlation. Correlations for sinter strengths and indices are provided in Appendix D.

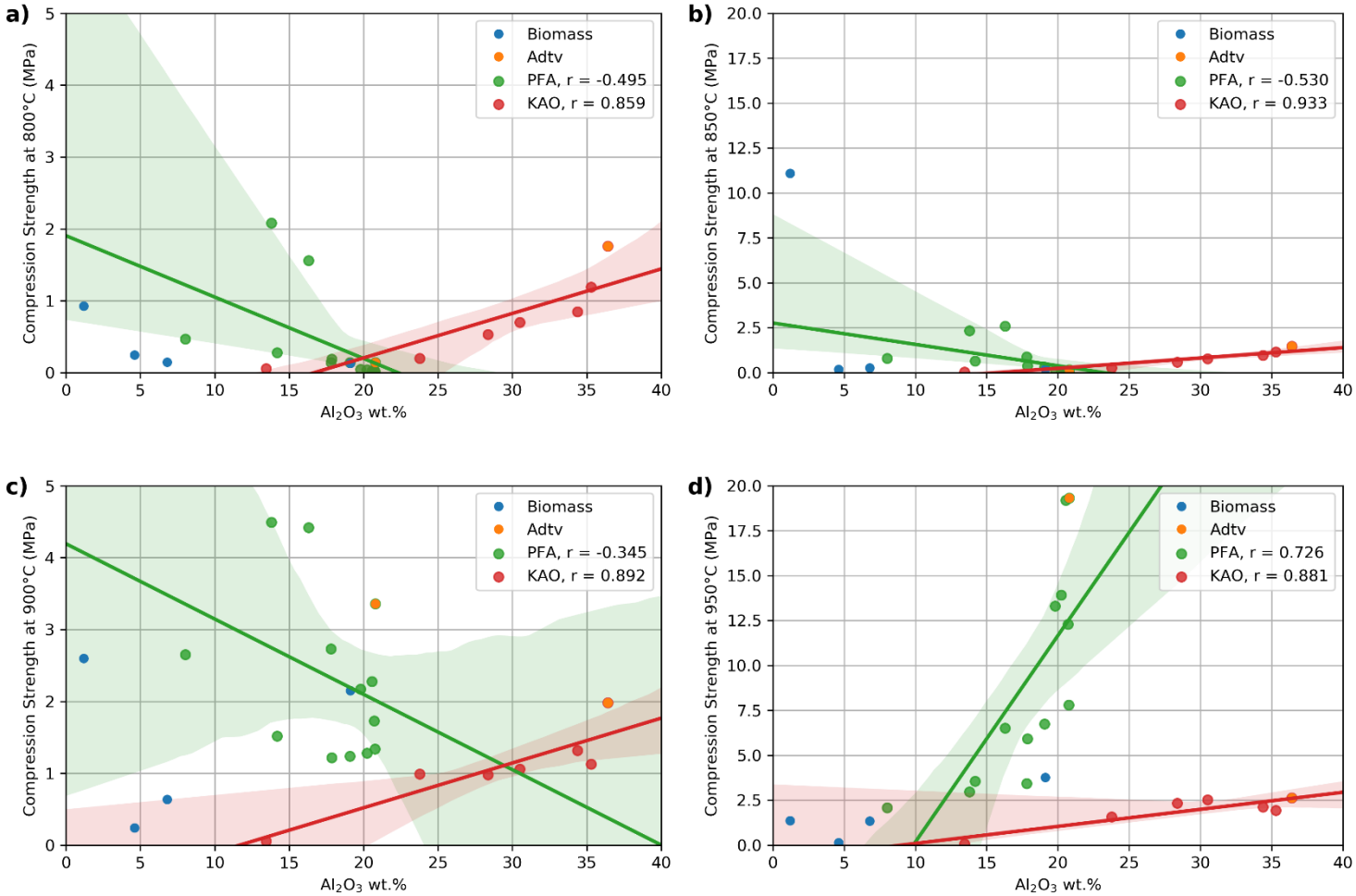

Figure 7.36 – Comparison of Al_2O_3 concentration with sinter strength at a) 800°C, b) 850°C, c) 900°C and d) 950°C for PFA and KAO blend compositions

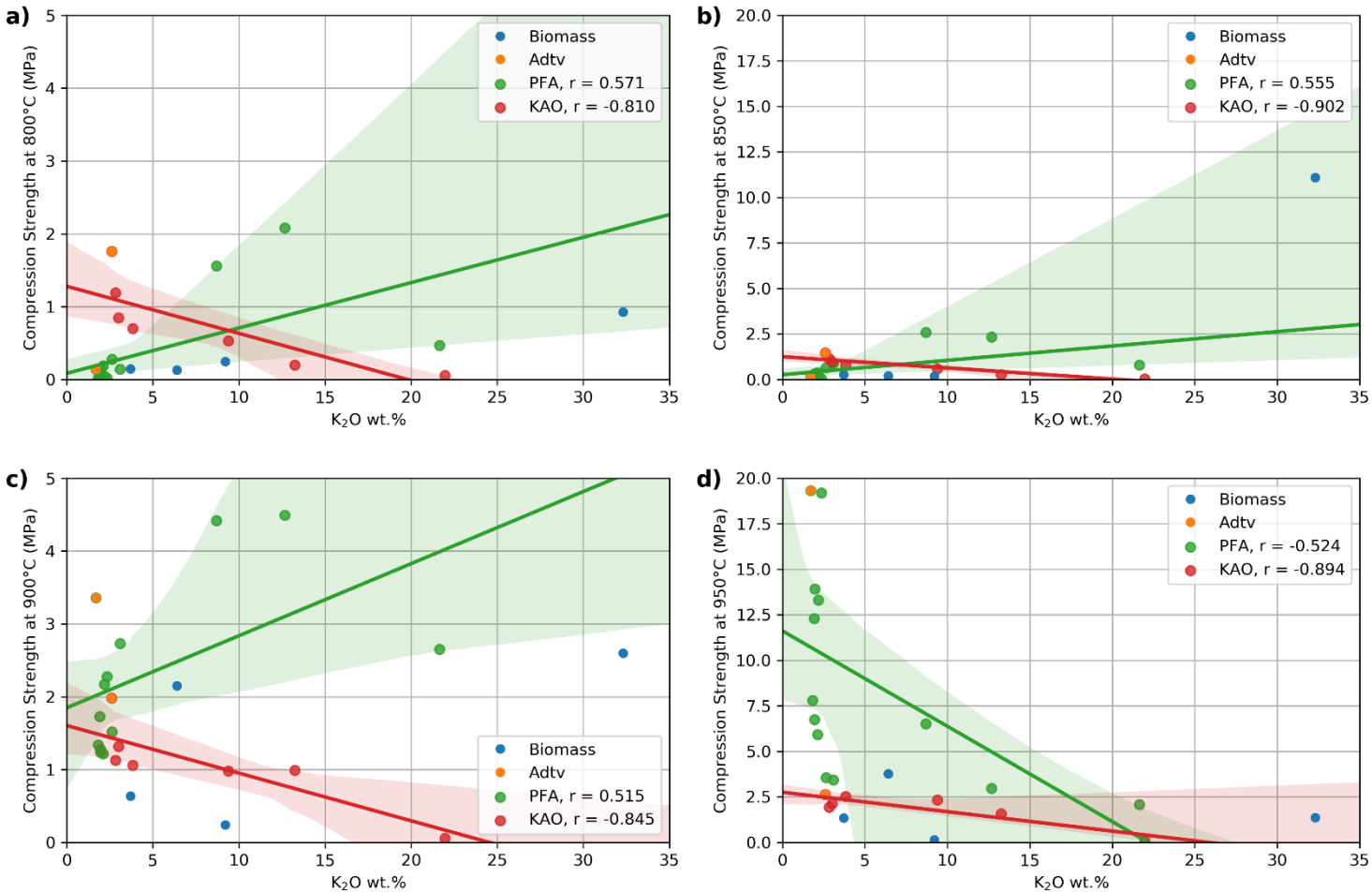

Figure 7.37 - Comparison of K_2O concentration with sinter strength at a) 800°C, b) 850°C, c) 900°C and d) 950°C for PFA and KAO blend compositions

7.5 - Summary

The sinter strength of biomass ashes and biomass/additive blends has been investigated through the use of sinter strength compression testing, a method that has been used to predict the deposition characteristics at fouling temperatures of both coal and biomass with some success. Pellets of the samples were made to a set standard and sintered at a target temperature for 3 hours and allowed to cool, before the peak compressive strength of the pellet was measured.

The different samples showed different sintering behaviour. WWA and BA showed little evidence of significant sintering between 800-950°C, indicating that these ash compositions would not produce troublesome fouling over this temperature range. FA began to sinter at temperatures of 900°C, although compressive strengths remained at an acceptable level for soot blowing up to 950°C. OCA displayed signs of two-phase behaviour due to viscous flow sintering, with severe sintering recorded at 850°C, above which the pellet would simply compress under pressure, undergoing internal fracture that did not propagate through the pellet such that a clear point of failure was not observed. This gave false compressive strengths and indicated that OCA would produce deposition that would be worsened with soot blowing, creating major problems in boilers. This behaviour was postulated to be due to the presence of KCl, which was observed in previous experiments to sublimate at temperatures of as low as 700°C and is known to flux at approximately 770°C in the presence of silica.

The use of additives was shown to have mixed results. PFA addition was shown to increase sinter strengths for WWA, BA and FA, resulting in unacceptable sinter strengths at 950°C and above for all samples at blends of 15% or higher. KAO produced increased sintering in WWA compared to without additive, however the sinter strengths were acceptable across all temperatures at all additives rates.

In contrast, OCA5%KAO eliminated sintering across the range of temperatures measured, indicating that KAO is capable of drastically improving the deposition behaviour of OCA and similar compositions. High rated resulted in slightly greater sinter strengths, although these remained at acceptable levels. PFA addition significantly reduced the severe sintering observed at 850°C, as well as the

subsequent compressive behaviour, indicating that PFA is effective as an additive in reducing fouling issues for OCA and similar compositions. However, sinter strengths were greater than those measured with KAO addition, and high PFA rates resulted in unacceptable compressive strengths. As a result, KAO was determined to be a significantly better additive than PFA.

SEM images highlighted that PFA use resulted in more agglomerated particles, with compositions rich in iron and aluminium appearing to act as the sintering material, creating a fluxing effect in the silica within the samples. In addition, greater agglomerates rich in calcium and sulphur were found in PFA samples, indicating that PFA use as an additive may introduce additional unwanted components that are typical in coal ashes. XRD analysis of PFA sample debris typically showed large peaks corresponding to SiO_2 and Fe_2O_3, further indicating that the silica and iron were coating the particle surfaces and acting as sintering material. SEM-EDX of KAO showed concentrations of calcium and magnesium, with little evidence of liquid phase found on larger particle present. XRD analysis was subsequently noisy and more complex, with peaks corresponding to both aluminosilicates and SiO_2 present along with other components such as Al_2O_3 in OCA, and CaO and $CaSO_4$ in WWA blends, indicating the silicate fluxing had not occurred, leaving the mineral components of the ash exposed. In the case of OCA, chlorine crystals were observed on the surface of sintered particles, which were not present in OCA/additive blends, indicating that both additives were effectively converting KCl to potassium aluminosilicates as reported in literature.

Very few linear correlations were observed between sinter strength at each temperature and the oxide components of the ash. A positive correlation was found for K_2O with sinter strength at 850°C, corresponding to the severe sintering observed in OCA samples, while Fe_2O_3 concentration was found to correlate with sinter strengths at 950°C. PFA and KAO were found to display different behaviour, with Al_2O_3 and Fe_2O_3 concentration found to increase sinter strengths in KAO blends at lower temperatures, while decreasing sinter strengths at lower temperature in PFA blends. Most significantly, increasing K_2O concentration was observed to decrease sinter strengths in KAO blends, indicating that low blends of KAO may be most effective.

Chapter 8 - Discussion of Ash Melting Behaviour Experiments and Conclusions

8.1 - Introduction

This chapter will compare the findings of Chapters 5-7 for the different samples investigated within this study. For each sample type, ash fusion testing results are summarised briefly, before being compared to sinter strength and viscosity results respectively. The ash fusion test is known as a useful indication of slagging and fouling potential, however its flaws, particularly at deformation or fouling temperatures, are well known and discussed in detail in Chapter 6. Sinter strength testing was therefore used to better determine the melting behaviour of the ashes at these temperatures, and a comparison against ash fusion profiles is useful to show both the effectiveness of the ash fusion test in showing the behaviour of the sample and the features that are occurring in both tests. In the case of OCA, viscosity testing was additionally utilised due to the promising AFT and sinter strength testing results. The OCA viscosity results and predictions are therefore compared to AFT height profiles across the appropriate temperature ranges. Finally, a recommendation for Al-Si additive use is made for each sample type based on these results.

8.2 - Effect of Al-Si Additives upon Olive Cake Ash Melting Behaviour

Ash fusion testing of OCA/additive blends showed that KAO and low levels of PFA addition resulted in higher deformation/shrinking temperatures and flow temperatures, indicating that the additives could potentially improve the nature of both fouling and slagging deposits respectively. However, deformation temperatures increased with increasing PFA concentration.

A comparison of ash fusion height profiles and sinter strength results (Figure 8.1) shows that the temperature of severe sintering observed for OCA corresponds closely to the onset of pellet shrinkage during ash fusion testing: the 50°C difference between the two results is likely due to the differences in the experimental methods, with AFT being a continuous process with increasing

temperatures while sinter strength testing occurs at a fixed temperature. As such, it is likely that some melting is occurring within the pellet at lower temperatures that is not visible externally. These results, including SEM-EDX images provided in Chapter 7.4.2.1, strongly indicate that OCA experienced significant sintering at these temperatures due to the fluxing caused by KCl sublimation.

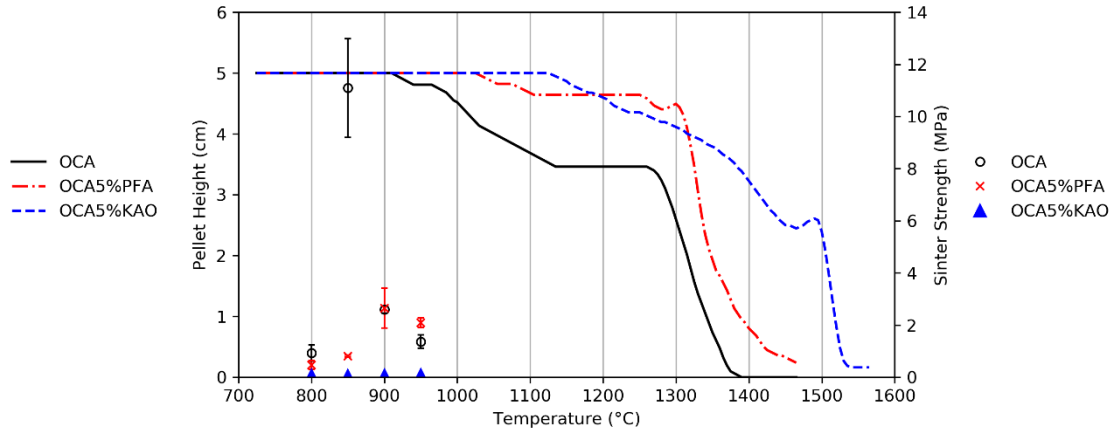

Figure 8.1 – Comparison of AFT results (left axis) and sinter strength results (right axis) for OCA and OCA-5%additive compositions

Both additives clearly had a positive impact on the melting behaviour of OCA at fouling temperatures, and were by significantly more effective in reducing sinter strengths and melting than in the other samples investigated. Severe sintering was prevented at 850°C, while pellet shrinkage was delayed by up to 100°C with PFA addition and 200°C with KAO addition, as observed both during ash fusion testing and during sinter strength testing (Figure 7.4). SEM-EDX imaging (Figures 7.5, 7.6, 7.9 and 7.10) showed that additive use prevented the formation of chlorine-rich crystals on particle surfaces, in addition to reducing sintering and agglomeration at fouling temperatures.

This behaviour is consistent with the mechanisms described for Al-Si additives in the literature; the aluminosilicates in the additives produce an alkali absorption mechanism, while additional silica, alumina and aluminium silicates increase overall sintering temperatures [98]. Akali metals and alkali metal chlorides are converted into potassium aluminosilicates and hydrochloric acid through the mechanisms outlined in Equations 2.4-2.6. Alkali metal chlorides are known fluxes in silicate mixtures [38], and a reduction of alkali metals in the flue gas prevents their formation, in turn reducing deposition issues and preventing corrosion via active oxidation from occurring (as described in Chapter 2.4.5). A study by Ohman and Nordin [89] at similar temperatures utilising kaolin as an

additive in fluidised bed combustion of wheat straw (similarly high in K and Cl) with silica bed material also produced similar results under pilot scale conditions, with agglomeration temperatures increased by approximately 150°C.

In light of these results, it was decided that OCA samples would be most appropriate for viscosity testing. Only KAO was suitable for such tests: the iron content of the PFA is such that the OCA5%PFA sample would contain too much iron and bubble over at high temperatures. OCA experiments produced extremely low viscosities at low temperatures when compared to ideal combustion conditions, with a T_{cv} of 1245°C due to the expected formation of $(Mg^{2+},Fe^{2+})_2SiO_4$ and $\alpha CaSiO_2$, minerals with lower than desired melting temperatures. Although direct viscometry was not possible for OCA5%KAO, predictive modelling results were promising, with viscosities at combustion temperatures expected to increase significantly due to the formation of aluminosilicate minerals (particularly $Na_3K(Al_4Si_4O_{16})$) and aluminium spinel.

Viscosity results and ash fusion testing results can be directly compared, in order to give an indication of T_{cv} for OCA5%KAO and hence slagging behaviour. Examples of studies that combine or compare the two include Luan et al [144], Xing et al [197] and Hsieh et al [194]. Hsieh et al in particular investigated correlations between ash fusion testing and viscosity, finding a reasonable correlation (R^2=0.77) between the temperature of critical viscosity (T_{cv}) and flow temperature for multiple samples. In contrast to previous studies, there was an extremely poor correlation with measured critical viscosity temperatures and previously developed predictive indices that utilise hemisphere temperatures to predict critical viscosity.

In this study, it was not possible to determine correlations of T_{cv} with AFT temperatures since only one sample was subjected to viscosity testing. However, HT and FT are strongly related to the viscosity of the sample, and a comparison may be useful. Figure 8.2 compares the ash fusion testing height profiles for OCA and OCA5%KAO with the results of viscosity testing for OCA and FactSage predictions for OCA5%KAO that were discussed in Chapter 5.

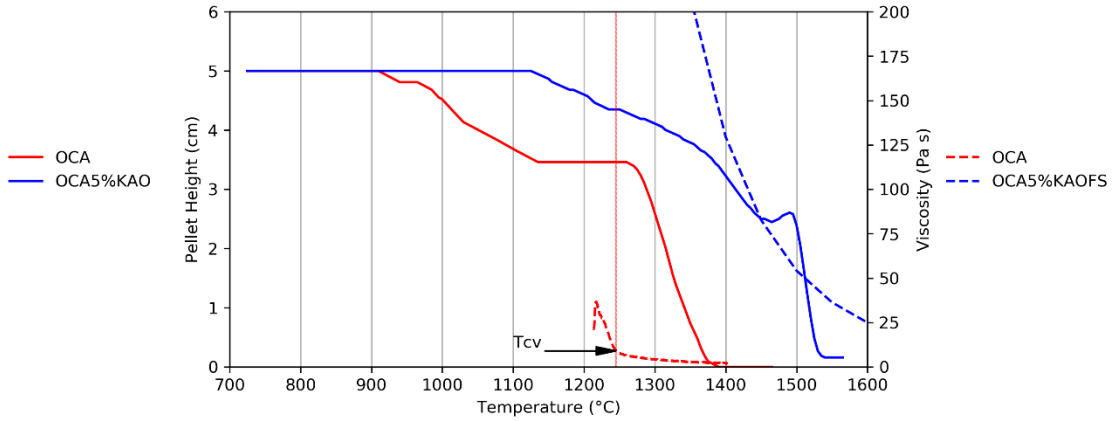

Figure 8.2 - A comparison of AFT height profiles with OCA viscosity measurement and OCA5%KAO viscosity prediction from FactSage

T_{cv} of OCA is labelled, corresponding closely with the point of collapse of the OCA pellet during ash fusion testing. This point of pellet collapse does not correspond to any traditional AFT temperature, with flow temperature occurring after collapse and hemisphere temperature varying between samples as occurring either before or after the full collapse of the pellet. As this is a single result, it is not possible to draw definitive conclusions: however, this tentatively shows that T_{cv} may be accurately determined from ash fusion testing using the improved techniques introduced by Pang et al [195], further improving the usefulness of ash fusion testing. Should this postulation hold true for OCA5%KAO, T_{cv} would be expected to occur at approximately 1500°C based upon AFT results, reducing the extent of slagging occurrence throughout the boiler.

Overall, these experimental results reinforce the previously available literature that aluminosilicate additives have the potential to significantly improve the deposition properties of biomass fuels containing high quantities of potassium and chlorine in the ash. In particular, kaolin powder was noted to be the most effective, with sinter strength results indicating highly desirable melting behaviour at fouling temperatures for OCA5%KAO compositions, while melting behaviour at slagging temperatures was also significantly improved during ash fusion and viscosity testing. Although OCA5%PFA was observed to improve the properties of OCA during heating, sinter strengths were observed to increase at 900°C, indicating that initial melting and sintering was occurring at lower temperatures than the KAO compositions. In addition, flow temperatures were only slightly improved, while viscosity testing was not possible due to issues introduced by

compositions with similar iron concentrations, indicating that such a composition would not result in desirable behaviour at slagging temperatures.

Based upon these results, kaolin use is recommended when utilising OCA-like compositions for large scale combustion, and further study should be undertaken on larger scales. The PFA composition in this study showed some promise, however the iron content was determined to cause issues as temperatures increased. It is possible that coal PFA compositions containing lower concentrations of iron may be more effective in improving the behaviour of OCA and similar ash compositions, and this should be the focus of further study. However, the use of the PFA composition investigated in this study is not recommended.

8.3 - Effect of Al-Si Additives upon White Wood Ash Melting Behaviour

WWA showed similar behaviour to OCA during ash fusion testing, with flow temperatures occurring at approximately 1300°C, indicating that similar compositions may cause slagging issues in biomass boilers. However, initial deformation and shrinking temperatures were greater for WWA compared to OCA. Once again, flow temperatures were increased with additive usage: however, WWA5%KAO reduced initial shrinking temperatures, while WWA5%KAO increased flow temperatures to beyond the limit of the furnace, indicating that flow temperatures and viscosities would be much greater than is desired for biomass-fired boilers.

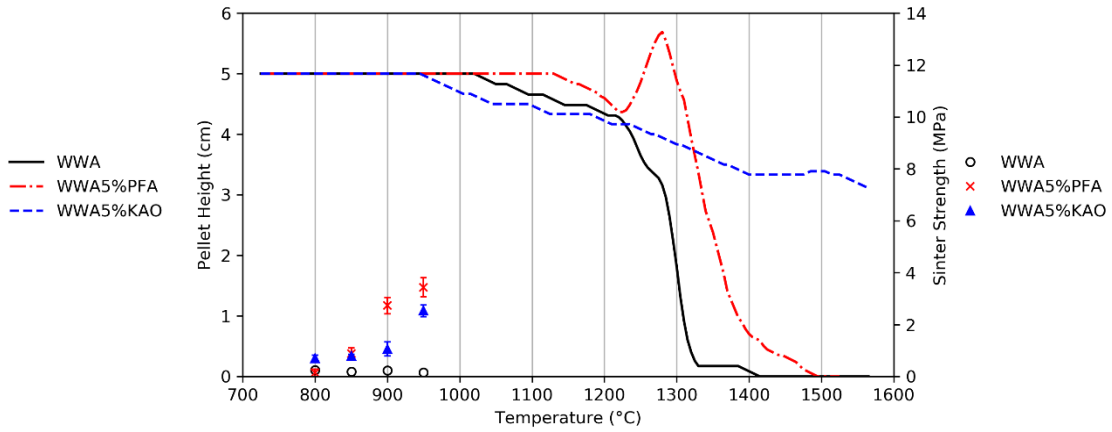

Figure 8.3 - Comparison of AFT results (left axis) and sinter strength results (right axis) for WWA and WWA-5%additive compositions

8.3 - Effect of Al-Si Additives upon White Wood Ash Melting Behaviour

A comparison of AFT and sinter strength results (Figure 8.3) highlighted some of the issues with ash fusion testing, and why the traditional test can produce flawed results. Sinter strength testing showed that compressive strengths were actually greater for WWA5%PFA when compared to WWA5%KAO, in contrast to the indications of ash fusion testing where PFA was observed to increase shrinking temperatures to up to 200°C greater than KAO samples. Sinter strengths were noticeably increased for WWA when 5% additive was used, and although these sinter strengths were below the 5MPa value given by Gibb for effective soot blower removal, it can be inferred that sinter strengths of above this value will be encountered at temperatures of 1000°C. As no such sintering was observed for WWA samples across the sample temperature range, the additives were determined to have a negative impact on the behaviour of WWA at fouling temperatures, which could lead to increased fouling in large-scale boilers.

PFA in particular had an extremely negative effect upon sinter strengths, producing significant sintering at temperatures of 900°C and above. SEM-EDX imaging (Figures 7.16 and 7.17) showed clear evidence of agglomeration in regions containing high aluminium and iron concentrations. The low ash content of white wood means that the components of PFA outweigh the components in WWA at a ratio of 5:1 in a WWA5%PFA composition, strongly diluting the alkali concentration within the ash. This has an adverse effect on amphoteric components found within the ash, such as Al_2O_3 and Fe_2O_3, which can behave as network modifiers in the presence of SiO_2 when network modifying alkali metals are not present or are present in low concentrations, reducing the melting temperatures and viscosity of the silicate melt. In addition, regions corresponding to high calcium and sulphur concentrations were observed in the SEM images. The sulphur retaining properties of coal ashes, particularly in coals containing higher calcium and magnesium concentrations, is a known phenomenon which means that sulphur is impossible to avoid in coal PFA compositions. As a result, coal PFAs are highly likely to introduce additional sulphur into the boiler system, which can have an adverse effect in the presence of biomass such as white wood. The calcium and alkali metal chlorides within the biomass will react with sulphur, creating troublesome calcium sulphate within the deposits (Equations 2.1-2.3) rather than aluminosilicates.

Overall, additive use with WWA was shown to be much less effective than with OCA. PFA is unsuitable for use as an additive with white wood compositions at the rates examined in this study. Lower rates may produce more favourable behaviour than observed here, and additive use at 1:1 ratios with the ash concentration of white wood should be explored. However, the PFA was once again clearly shown to be less effective than the kaolin, due to the greater impurities within the ash (namely higher amphoteric and sulphur concentrations), and it may be possible that the unavoidable sulphur within coal ashes renders PFA an unsuitable additive for high calcium biomass in general.

Kaolin use shows promise, in that it increases flow temperatures significantly. However, flow temperatures were increased too much at the rates investigated, and further study is required using lower additive rates that may reduce both ash flow temperatures and sinter strengths. These results are in contrast to literature on entrained-flow gasification of clean wood, where kaolinite and silica have been advocated as significant fluxing materials in order to reduce viscosities to acceptable levels, at lower rates than where used in this study [222, 223]. An important difference is that the beech in the Coda et al study [223] contains significantly less SiO_2 (1.7%) than the white wood in this study (34.38 wt. %): the low silica content of beech results in a calcium-dominated ash composition that leads to extremely high flow temperatures, and so the introduction of silica from the kaolin interacts much differently. This correlates with the findings of Ohman et al [136], who observed that kaolin addition resulted in improved behaviour for wood pellet containing silica, while slagging was made significantly worse for wood pellet with little silica due to the formation of Ca-Al-K silicates rather than higher melting temperature Ca-Mg oxides.

Therefore, the findings of this study are only applicable to white wood compositions with higher quantities of silica, and Al-Si additive use would be strongly discouraged for wood compositions with extremely low silica concentrations such as beech.

8.4 - Effect of coal PFA upon Bagasse Ash Melting Behaviour

The main differences between the BA and WWA samples were the K_2O (3.7% and 9.2%, respectively), SiO2 (49.7% and 27.1% respectively) and CaO (2.9%

and 24.8%, respectively) concentrations, resulting in a much lower base-to-acid ratio for the BA samples. Despite this, greater sinter strengths were measured for BA (Figure 8.4) compared to WWA without additive, in contradiction to common practice where a lower base-to-acid ratio is expected to improve deposition properties. However, BA recorded significantly higher flow temperatures indicating that slagging deposition issues would be reduced in comparison to WWA as expected and indicating that base-to-acid ratio may be less important in determining fouling issues.

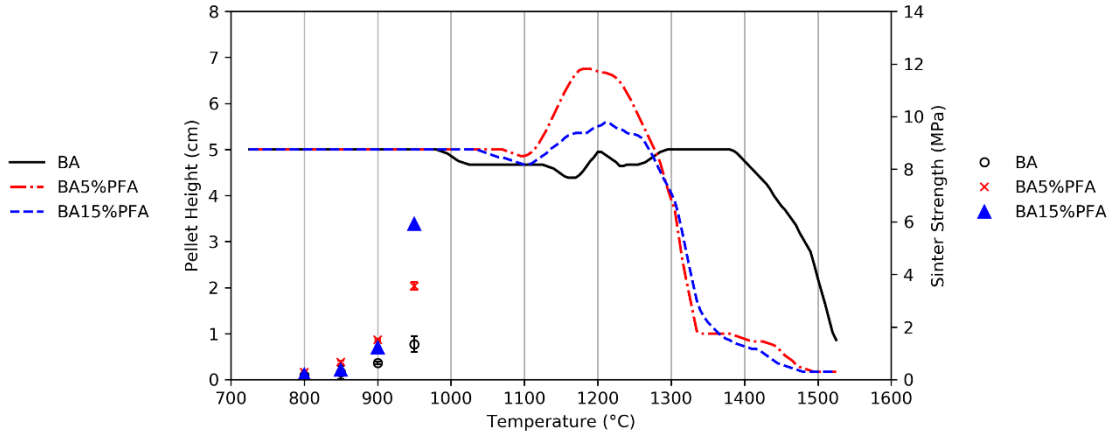

Figure 8.4 - Comparison of AFT results (left axis) and sinter strength results (right axis) for BA, BA-5% and BA15% additive compositions

The use of PFA was shown to have a significant detrimental effect upon flow temperatures of BA, with flow temperatures reduced by approximately 200°C for each additive rate investigated. This resulted in flow temperatures comparable to OCA and WWA without additive, and would cause low viscosity running slags at combustion temperatures, leading to severe slagging deposition. In addition, the sinter strength of BA was increased with increasing PFA addition, with significant agglomeration observed (Figure 7.28) indicating that fouling would be worsened with additive use. BA had the lowest potassium concentration (5.25 wt.%) of the samples in this study, with high SiO2 concentration (70.5 wt.%). The use of PFA resulted in extremely low alkali metal (and hence network modifier) concentrations within the ash, resulting in amphoteric fluxing as observed in WWA-additive compositions. These results show that PFA use is unsuitable for use with bagasse. Whether kaolin produces better results should be a focus of further study: however, the low potassium concentration of BA may mean that Al-

Si additives in general will have no positive impact on BA and similar compositions.

8.5 - Effect of coal PFA upon Fly Ash Melting Behaviour

As FA already has a high aluminium concentration (19.59 wt.%), it is unlikely to be a candidate for Al-Si additive use. This was reflected in the experimental results, with PFA addition leading to significantly worse sintering and deformation behaviour during heating (Figure 8.5). The already high Al_2O_3 and Fe_2O_3 (6.05 wt.%) concentrations were only exacerbated with the addition of PFA, leading to fluxing at lower temperatures resulting in significant sinter strengths at temperatures of 900°C and above. Although flow temperatures were improved for FA-PFA compositions during ash fusion testing when compared to FA, substantial deformation was observed to begin at below 1000°C, corresponding to the sharp increase in sinter strengths. This would result in a much larger region of fouling within the boiler, with extremely strong deposition that would be difficult to remove through soot blowing. Although tests only confirmed that FA compositions are inappropriate for additive use, the results were useful in testing the postulations of previous results, namely that extreme Al_2O_3 and Fe_2O_3 concentrations within ash compositions can have adverse effects upon melting behaviour.

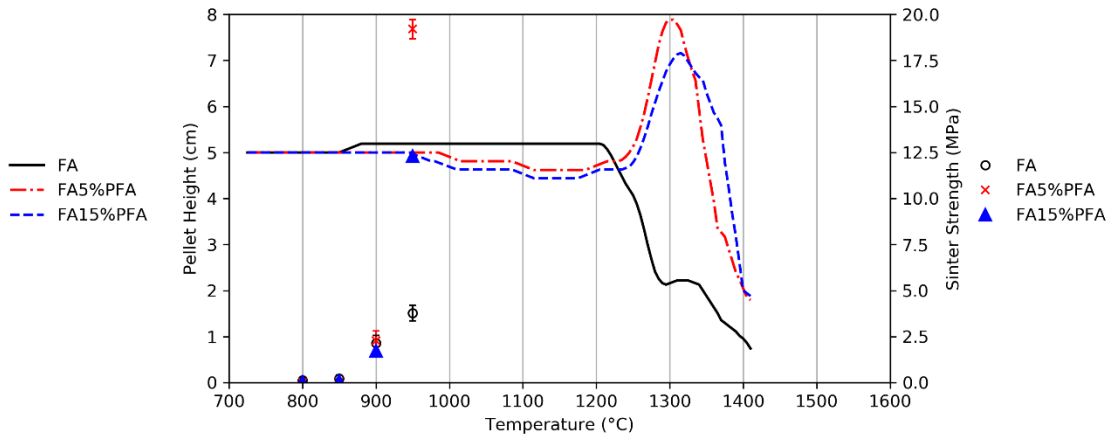

Figure 8.5 - Comparison of AFT results (left axis) and sinter strength results (right axis) for FA, FA-5% and FA-15% additive compositions

8.6 - Additive Recommendations

8.6.1 - Kaolin

Throughout all experiments, kaolin was shown to perform consistently better as an additive than the coal PFA, resulting in lower sinter strengths and higher flow temperatures at identical additive rates. In particular, kaolin showed exceptional promise in reducing OCA deposition issues through OCA5%KAO compositions. However, KAO was shown to have negative effects on other compositions, despite biomass ashes such as WWA containing significant concentrations of K_2O (11.63 wt.%).

The mineral kaolinite accounts for much of the KAO sample (~70%), which undergoes a series of phase transformations under increasing temperatures. Above 500°C, kaolinite dehydrates, resulting in amorphous metakaolinite. Above 925°C, silicon spinel begins to form. Mullite formation occurs at temperatures of 1100°C alongside spinel formation, up to 1400°C where mullite remains the only stable phase [224]. These transformations were summarised in Equations 7.3-7.6.

$$Al_2O_3.2SiO_2 + H_2O \rightarrow 2H_2O + Al_2O_3.2SiO_2 \ (500\text{-}925°C) \quad \text{(Eqn. 7.3)}$$

$$2(Al_2O_3.2SiO_2) \rightarrow SiO_2 + 2Al_2O_3.3SiO_2 \ (925\text{-}1100°C) \quad \text{(Eqn. 7.4)}$$

$$2Al_2O_3.3SiO_2 \rightarrow SiO_2 + 2(Al_2O_3.SiO_2) \ (>1100°C) \quad \text{(Eqn. 7.5)}$$

$$3(Al_2O_3.SiO_2) \rightarrow SiO_2 + 3Al_2O_3.2SiO_2 \ (>1400°C) \quad \text{(Eqn. 7.6)}$$

Kaolin was observed to have an effect on OCA behaviour at temperatures of 700°C and above, with extensive sintering of OCA eliminated at 850°C. At these temperatures the kaolin exists as metakaolinite, which has been extensively shown to be effective in absorbing alkali metals such as potassium [76, 89, 136, 138, 140]. The reaction of KCl with metakaolinite is expected to result in potassium aluminosilicates and minerals such as muscovite [137], in line with the XRD observations for OCA5%KAO in Figure 7.11. With increasing temperatures up to 950°C, KCl capture rates have been observed to decrease by both Tran et al [138] and Steenari and Linqvist [137]. Tran et al [138] propose a number of reasons for this, such as surface area changes and reversible adsorption. At

higher temperatures mullite begins to form, which reacts slowly with KCl [221]. During sinter strength testing especially, the sample is held at these temperatures, allowing time for these reactions to take place on a significant scale and before the remaining kaolin transformations (Equations 7.4-7.6) can take place. Therefore, kaolin may be less effective at the high combustion temperatures of pulverised fuel combustion than these lab-scale results suggest.

Due to the lack of chlorine in the WWA, BA and FA samples, the same reactions do not occur with KAO addition. Instead, the high SiO_2 content of the samples promotes the formation of lower melting temperature potassium silicates. In addition, the dehydration (Equation 7.3) and amorphous transformation (Equation 7.4) of much of the kaolinite can take place without additional reactions with alkali metals occurring, which would be expected to increase sintering of KAO samples relative to the non-additive samples. This is most prominent during ash fusion testing, where WWA-KAO samples experience significant deformation at approximately 950°C (Figure 8.3), corresponding to Equation 7.2, while OCA-KAO blends (Figure 8.1) do not. As such, kaolin effectiveness as an additive is governed strongly by both the alkali metal and silica content of the biomass.

8.6.2 - Coal PFA

Coal PFA was shown to perform worse than kaolin in terms of reducing sintering and ash fusion temperatures. In particular, severe sinter strengths were observed to occur in PFA blends at temperature of 900°C and above. Flow temperatures were increased (although to a lesser extent than equivalent KAO compositions) for all samples with increasing PFA concentration, apart from BA, where flow temperatures were significantly reduced. This behaviour was determined to be due to the high silica concentration within the samples, exacerbated by the behaviour of amphoterics when low concentrations of network modifying alkali metals were present. This resulted in a fluxing effect by the Fe_2O_3 and Al_2O_3 within the PFA, corresponding to the features observed in all samples during SEM-EDX and XRD analysis.

Although PFA showed an improvement in the behaviour of OCA under heating, this was reduced compared to the impact of kaolin. As the PFA is derived from coal and produced at typical pf combustion temperatures of >1400°C, much of the aluminosilicates in the additive are in the form of mullite which only reacts

with KCl after a prolonged period of time. Rather, the KCl reacts with the remaining silica within the PFA, forming potassium silicates and resulting in lower flow temperatures during ash fusion testing when compared to equivalent KAO compositions (Figure 8.1), that are too low for large scale pulverised fuel combustion.

Although a different PFA composition containing less Fe_2O_3 may improve sintering results, the inherent nature of the coal ash after combustion at high temperatures means that its effectiveness as an additive is compromised. As a result, it is unlikely that PFA will be viable as an Al-Si additive, although further testing is required to confirm this.

The conclusions for both PFA and kaolin are summarised below in Table 8.1.

Table 8.1 -Summary of recommendations for the use of additives to mitigate slagging and fouling in biomass combustion

Biomass	PFA		KAO	
	Viable as an additive?	Reasoning	Viable as an additive?	Reasoning
OCA	Unlikely, but possible	High mullite concentration resulting in low K-Al-Si production, low flow temperatures as a result Further testing of other PFA compositions required, as KCl absorption observed	Yes	Effective KCl capture, significantly improved sinter strength and fusion temperatures, viscosity at combustion temperatures may be ideal with correct blend ratio
WWA	Maybe	Current composition too high in iron - further testing required	Maybe	Flow temperatures too high at rates tested: lower rates possible
BA	No	Flow temperatures drastically reduced due to iron content	N/A	
FA	No	Inappropriate composition for additive use	N/A	

Chapter 9 - Conclusions

The world's energy supply must transition away from the use of fossil fuels, in order to limit further temperature increases due to greenhouse emissions. Coal has historically played an important role as part of the energy mix, and has continued to do so in recent years despite the very high carbon emissions associated with its use. In 2015, coal accounted for 28% of the world's total primary energy supply, but accounted for 45% of CO_2 emissions. A crucial part of current and future energy strategy involves the replacement of coal with biomass. Bioenergy can be used within the existing infrastructure already in place for coal with comparatively little investment needed providing an economical and practical solution with immediate results, if implemented in a sustainable way. The use of BECCS has the potential for negative carbon emissions, and both bioenergy and BECCS are considered crucial components of the future energy grid for reaching climate targets.

However, the composition of biomass, in particular its ash composition, may pose significant issues in large scale combustion when switching from coal to biomass firing, and increased slagging and fouling deposition has been frequently encountered when doing so. Additives have shown promise in improving the deposition properties of biomass ashes, by altering the composition of the ash and subsequently improving the melting behaviour and deposit properties. However, the effect of these additives upon the performance of large scale combustion boilers is not fully understood.

This is the motivation for this research. Two different aluminosilicate additives, coal PFA and kaolin powder, and their effect upon the ash composition and behaviour of three biomass samples (olive cake (OCA), white wood (WWA) and bagasse (BA)) and a power station fly ash (FA), have been investigated, and the resulting impact upon boiler performance has been inferred.

9.1 - Summary of Findings

9.1.1 - Impact of Al-Si Additives upon Ash Resistivity

The first topic of research was to determine the impact of additive use upon the electrical behaviour of the ashes over a range of temperatures, and the effect that this would have upon electrostatic precipitator performance. Although biomass ash resistivity has been looked at in the literature, this research is highly limited, and much of the existing information is based upon experience with coal ash compositions. Resistivity testing showed that biomass ash resistivity is typically lower than that of coal ash (using coal PFA as a baseline) by an order of magnitude or more. In the case of OCA and WWA, resistivities at ESP working temperatures were found to be close to the lower effective operating limits of ESPs under test conditions: with additional moisture and sulphur that would be present during large scale combustion, this would likely be even lower, posing operational problems and potentially resulting in increased emissions.

The use of coal PFA resulted in increased resistivities for all biomass ashes investigated, in turn reducing the risk of operational issues with ESPs. At ESP working temperatures, the addition of PFA to WWA increased resistivity by a factor of 26 at the lowest blends tested, due to the low ash content of white wood. BA-PFA blends showed a small increase with increasing PFA concentration, while the FA-PFA blends experienced no significant change in resistivity with increasing PFA concentration. OCA-PFA blends displayed increased resistivity compared to OCA, although this effect was negligible at lower blend rates.

Previous experience with coal ash compositions indicated that potassium is not a key component in coal ash conductivity and hence ESP performance. However, analysis of the results in this work indicated that potassium has an important influence upon ash resistivity when present at higher concentrations than found in coal ashes. As a result, existing ash resistivity models are unsuitable for use with biomass and biomass-additive blend compositions. A modification to one such model (the Bickelhaupt model) was attempted using experimental data and, although additional data is required before such a model can be properly validated, the model showed some promise in resistivity predictions for both coal and biomass results available in the literature.

The use of additives will increase ESP loading by (i) increasing the amount of non-combustible material within the boiler and (ii) decreasing deposition on boiler walls. Nevertheless, low rates of additive addition would result in ash percentages comparable with some coals, and improve capture efficiency in the ESP. It was therefore determined that Al-Si additive use will not negatively impact emissions, although for some biomass minor operational changes may be required to maintain high ESP collection efficiencies.

9.1.2 - Impact of Al-Si Additives upon Deposition Behaviour

The impact of the additives upon ash deposition behaviour was determined by utilising a number of complimentary experiments, in order to observe melting behaviour across a wide range of temperatures. High temperature viscosity was used to determine ash flow behaviour at temperatures encountered in and around the combustion zone of large scale boilers. Ash fusion testing qualitatively shows ash melting behaviour across a wide range of temperatures, covering both combustion temperatures and cooler temperatures encountered in fouling regions of the boiler. Finally, sinter strength testing was conducted, focusing on ash behaviour across a range of temperatures corresponding to those encountered in fouling regions, to determine the strength of such deposits and the implications for soot blower removal.

OCA and OCA5%KAO blends were subjected to high temperature viscometry and thermodynamic predictive modelling. OCA-PFA blends resulted in iron concentrations that would prove problematic to the instruments used in the experiments. The addition of kaolin increased the amount of potassium bound within the ash after being prepared at 700°C, indicating that the binding of potassium to aluminosilicates occurs at such temperatures. Viscosity testing indicated that, despite the increased potassium concentration, OCA-KAO compositions have significantly increased viscosities when compared to OCA compositions. MTData indicated that this was due to the decreased concentrations of magnesium and phosphorus and increased alumina concentrations within the ash, resulting in the formation of high melting temperature minerals and compounds. The viscosities recorded at combustion temperatures were close to those required for favourable slagging conditions,

indicating that KAO use in large scale combustion would significantly improve problems from slagging deposition.

Ash fusion testing revealed that BA had the highest flow temperatures of the biomass ashes, while OCA showed significant deformation at lower temperatures. PFA addition resulted in increased flow temperatures for OCA, WWA and FA, while PFA addition to BA significantly decreased flow temperatures, indicating that slagging may in fact be worsened with PFA addition to BA compositions. 5%PFA addition to OCA resulted in increased deformation temperatures when compared to OCA alone, although higher PFA concentrations had an adverse effect. KAO was significantly more effective at improving flow temperatures, with a ~200°C increase measured for OCA5%KAO (1500°C) compared to a 35°C increase for OCA5%PFA (1325°C), when compared to OCA alone (1290°C); deformation temperatures were also increased. This indicated that OCA-KAO ash compositions may highly beneficial for mitigating slagging and fouling deposition problems in comparison to OCA ashes. However, KAO addition to WWA resulted in extremely high flow temperatures, indicating that slagging deposition of such compositions may have undesirable behaviour that may lead to increased shedding event frequency and damaged boiler components.

Finally, the sinter strength of the ashes and additive-ash blends was investigated across a temperature range of 800-950°C. WWA and BA showed little evidence of significant sintering between 800-950°C, indicating that these ash compositions would not produce troublesome fouling over this temperature range. FA began to sinter at temperatures of 900°C, although compressive strengths remained at an acceptable level for soot blowing up to 950°C. However, OCA showed severe sintering occurring at 850°C due to KCl sublimation and the subsequent fluxing of silicates, resulting in significantly increased sinter strengths and two-phase behaviour. This two-phase behaviour indicated that OCA, when used in large scale combustion, would produce deposition that would in fact be worsened with soot blowing, creating major deposition problems. The use of additives was shown to have mixed results. PFA addition was shown to increase sinter strengths for WWA, BA and FA, resulting in unacceptable sinter strengths at 950°C and above for all samples at blends of 15% or higher. However, PFA significantly improved OCA sinter strengths, eliminating the severe sintering and

two-phase behaviour at 850°C and above. Although KAO produced increased sintering in WWA compared to without additive, the sinter strengths were acceptable across all temperatures at all additives rates, while OCA5%KAO completely eliminated sintering across all temperatures measured. As a result, KAO was determined to be a significantly better additive than PFA, in that it would significantly improve fouling deposition behaviour and soot blower effectiveness.

Overall, it was determined that kaolin has the greatest potential to reduce deposition issues in biomass combustion, as it consists mostly of kaolinite. Kaolinite has been shown to effectively convert KCl to potassium aluminosilicates (thereby increasing melting and flow temperatures), and prevent potassium release, therefore preventing the formation of troublesome KCl in cooler regions of the boiler. Coal PFA was determined to be less effective as an additive due to its high mullite concentration, which reacts slowly with KCl, and high iron content, which had a fluxing effect at higher temperatures. However, both additives were found to be less effective for WWA and BA compositions, indicating that their use should be reserved for biomass with high KCl concentration and low SiO_2.

9.2 - Future Research

9.2.1 - Pilot Scale Testing

The most significant area of continued research, based upon the results of this study, would be to determine whether the findings of these lab scale tests hold true on larger scales, or whether additional factors contribute to different deposition behaviour. As a result, extended pilot scale testing of biomass and biomass additive blends would be useful, with deposition rates and behaviour monitored during testing. Sampling of bottom and fly ash would allow for a direct comparison by repeating the experiments in this study. Bottom ash could be subjected to both viscosity and ash fusion testing, while fly ash would be subjected to sinter strength testing and resistivity testing, and compared against the results of this study for the same initial biomass/biomass-additive blends. Ideally such pilot scale testing would be conducted upon olive cake and olive cake-additive mixtures, given the severe deposition that would be expected from OCA compositions and the significant improvement in behaviour that has been observed with the use of Al-Si based additives.

9.2.2 - Ash Resistivity

This work has shed new light upon the electrical behaviour of biomass ash, and in particular the importance of potassium concentration in the ash with regards to the ash resistivity. A predictive empirical model, a modification of the Bickelhaupt model [163], has shown promising results in predicting the resistivity-temperature relationships for both coal and biomass ashes found in the literature based upon the potassium concentration of the ash. However, the current dataset is too small to sufficiently validate the model. This is a promising area of research, and a predictive model would be of use to biomass power station operators, in order to easily determine whether a biomass-additive ash composition may reduce the collection efficiency of the ESPs. As such, future work should be focused upon repeating these experiments for a wider range of biomass ash compositions and additive blends, with the aim of producing an effective empirical model that can be applied to a wide range of ash compositions. Such a model would be the first resistivity model applicable to biomass ash compositions.

Under ideal conditions, the resistivity tests would be repeated using an experimental method that is capable of controlling the test environment to include the effects of water vapour and sulphur. This would result in a more flexible and effective model that would be capable of predicting resistivities under real conditions experienced in large scale power stations.

9.2.3 - Ash Melting Behaviour

A useful extension of the work on ash melting behaviour would be to extend the data set and investigate the impact of the additives upon other biomass ash compositions, at additive rates of approximately a 1:1 ratio of additive to ash content, based upon the results of this study. Further, a crucial area of future research should be the effect of different additive rates upon different blends of biomass. Many power stations use a mixture of different biomass as fuel, which would result in more complex interactions than the single-fuel compositions investigated during this study. This may have a significant impact upon the performance of additives in large scale combustion, and is an area of research that may have significant importance in improving issues of fuel flexibility.

References

1. Stearns, P.N., *The Industrial Revolution in World History*. 1998: Westview Press.
2. Schaffartzik, A., et al., *The global metabolic transition: Regional patterns and trends of global material flows, 1950–2010.* Global Environmental Change, 2014. **26**: p. 87-97.
3. Smil, V., *Energy Transitions: Global and National Perspectives*. 2017: ABC-CLIO, LLC.
4. Zou, C., et al., *Energy revolution: From a fossil energy era to a new energy era.* Natural Gas Industry B, 2016. **3**(1): p. 1-11.
5. Eichengreen, B., *Institutions and economic growth: Europe after World War II.* Economic growth in Europe since, 1945: p. 38-72.
6. Inc. IBP, *UK Energy Policy, Laws and Regulations Handbook Volume 1 Strategic Information and Basic Laws*. 2015: Lulu.com.
7. Pfister, C., *The "1950s syndrome" and the transition from a slow-going to a rapid loss of global sustainability*. 2010.
8. Fleming, J.R., *Joseph Fourier, the 'greenhouse effect', and the quest for a universal theory of terrestrial temperatures.* Endeavour, 1999. **23**(2): p. 72-75.
9. Tyndall, J., *Contributions to Molecular Physics in the Domain of Radiant Heat*. 2014: Cambridge University Press.
10. Rohde, R.A., *Global warming art project*, 2005.
11. Solomon, S., et al., *Climate change 2007-the physical science basis: Working group I contribution to the fourth assessment report of the IPCC*. Vol. 4. 2007: Cambridge university press.
12. Karl, T.R., et al., *Global climate change impacts in the United States*. 2009: Cambridge University Press.
13. Kyoto Protocol, *United Nations framework convention on climate change.* Kyoto Protocol, Kyoto, 1997. **19**.
14. UNFCCC, C. *Report of the Conference of the Parties on its sixteenth session, held in Cancun from 29 November to 10 December 2010*. in *Part Two: Action taken by the Conference of the Parties at its sixteenth session*. 2011.
15. European Parliament and of the Council, *Directive 2009/28/EC*, 2009, European Union: Official Journal of the European Union.
16. Latvian Presidency of the Council of the European Union. *Intended Nationally Determined Contribution of the EU and its Member States*. 2015 [cited 2018 20th August]; Available from: http://www4.unfccc.int/Submissions/INDC/Submission%20Pages/submissions.aspx.

17. Farstad, F., N. Carter, and C. Burns, *What does Brexit Mean for the UK's Climate Change Act?* The Political Quarterly, 2018. **89**(2): p. 291-297.

18. Lockwood, M., *The political sustainability of climate policy: The case of the UK Climate Change Act.* Global Environmental Change, 2013. **23**(5): p. 1339-1348.

19. Committee on Climate Change, *UK climate action following the paris agreement*, 2016: London.

20. Hepburn, C. and A. Teytelboym, *Climate change policy after Brexit.* Oxford Review of Economic Policy, 2017. **33**(suppl_1): p. S144-S154.

21. Barnard, C., *Law and Brexit.* Oxford Review of Economic Policy, 2017. **33**(suppl_1): p. S4-S11.

22. Nunez-Ferrer, J. and D. Rinaldi, *The Impact of Brexit on the EU Budget: A non-catastrophic event.* 2016.

23. Davies, T.H., et al., *Meeting Carbon Budgets - Implications of Brexit for UK climate policy.* 2016.

24. United Nations, *Energy Statistics Yearbook 2015*. 2018.

25. International Energy Agency, *Global Energy and CO2 Status Report 2017*, 2017.

26. *International Energy Outlook*, U.S. Energy Information Administration, Editor 2017.

27. *BP Statistical Review of World Energy June 2017.* 2017.

28. Enerdata. *Global Energy Statistical Yearbook 2018*. 2018 [cited 2018 22nd August]; Available from: https://yearbook.enerdata.net/total-energy/world-consumption-statistics.html.

29. Birol, F., *CO2 Emissions from Fuel Combustion 2017-Highlights.* Int. Energy Agency, 2017. **1**: p. 1-162.

30. Birol, F., *Energy and Climate Change.* World Energy Outlook Special Report - International Energy Agency, 2015.

31. Department for Business, Energy & Industrial Strategy; , *UK Energy Statistics, 2017 & Q4 2017*, 2017.

32. Department for Business, E.I.S., *Energy Trends December 2017.* 2017.

33. Department for Business, Energy & Industrial Strategy;, *IMPLEMENTING THE END OF UNABATED COAL BY 2025*, 2018.

34. European Parliament and of the Council, *Directive 2001/80/EC*, 2001, European Union: Official Journal of the European Union.

35. Vanlint, K. and A. Judd, *Running hours during winter 2013/14 for plants opted-out of the Large Combustion Plant Directive (LCPD)* DECC, Editor 2014.

36. Drax Group PLC. *Fourth biomass unit conversion*. 2018 [cited 2018 24th August]; Available from: https://www.drax.com/investors/fourth-biomass-unit-conversion/.

37. European Commission, *Intergrated Pollution Prevention and Control: Reference document on best available techniques for large combustion plants*, 2006.

38. Van Loo, S. and J. Koppejan, *The Handbook of Biomass Combustion and Co-firing*. 2012: Taylor & Francis Group.

39. Beér, J.M., *Combustion technology developments in power generation in response to environmental challenges.* Progress in Energy and Combustion Science, 2000. **26**(4–6): p. 301-327.

40. Williams, A., M. Pourkashanian, and J.M. Jones, *Combustion of pulverised coal and biomass.* Progress in Energy and Combustion Science, 2001. **27**(6): p. 587-610.

41. Buhre, B.J.P., et al., *Oxy-fuel combustion technology for coal-fired power generation.* Progress in Energy and Combustion Science, 2005. **31**(4): p. 283-307.

42. Daood, S.S., et al., *Fuel additive technology – NOx reduction, combustion efficiency and fly ash improvement for coal fired power stations.* Fuel, 2014. **134**: p. 293-306.

43. Laursen, K. and J.R. Grace, *Some implications of co-combustion of biomass and coal in a fluidized bed boiler.* Fuel Processing Technology, 2002. **76**(2): p. 77-89.

44. Bartels, M., et al., *Agglomeration in fluidized beds at high temperatures: Mechanisms, detection and prevention.* Progress in Energy and Combustion Science, 2008. **34**(5): p. 633-666.

45. Arvelakis, S., et al., *Effect of leaching on the ash behavior of wheat straw and olive residue during fluidized bed combustion.* Biomass and Bioenergy, 2001. **20**(6): p. 459-470.

46. Miller, B.G. and S.F. Miller, *Chapter 8 - Fluidized-Bed Firing Systems*, in *Combustion Engineering Issues for Solid Fuel Systems*, B.G. Miller and D.A. Tillman, Editors. 2008, Academic Press: Burlington. p. 275-340.

47. Lin, W., K. Dam-Johansen, and F. Frandsen, *Agglomeration in bio-fuel fired fluidized bed combustors.* Chemical Engineering Journal, 2003. **96**(1–3): p. 171-185.

48. Bend, S.L., *The origin, formation and petrographic composition of coal.* Fuel, 1992. **71**(8): p. 851-870.

49. O'Keefe, J.M.K., et al., *On the fundamental difference between coal rank and coal type.* International Journal of Coal Geology, 2013. **118**: p. 58-87.

50. Pierce, B.S. and K.O. Dennen, *The national coal resource assessment overview*, 2009, US Geological Survey.

51. Livingston, W.R., et al., *The status of large scale biomass firing*, 2016, IEA Bioenergy.

52. World Bioenergy Association, *WBA Global Energy Statistics 2017*, 2018.

53. Vassilev, S.V., et al., *An overview of the chemical composition of biomass.* Fuel, 2010. **89**(5): p. 913-933.

54. Vassilev, S.V., et al., *An overview of the organic and inorganic phase composition of biomass.* Fuel, 2012. **94**: p. 1-33.

55. Arundale, R.A., et al., *Environment Has Little Effect on Biomass Biochemical Composition of Miscanthus × giganteus Across Soil Types, Nitrogen Fertilization, and Times of Harvest.* BioEnergy Research, 2015. **8**(4): p. 1636-1646.

56. Jaya, S.T., et al., *REVIEW: A review on biomass torrefaction process and product properties for energy applications.* Industrial Biotechnology, 2011. **7**(5): p. 384-401.

57. Isikgor, F.H. and C.R. Becer, *Lignocellulosic biomass: a sustainable platform for the production of bio-based chemicals and polymers.* Polymer Chemistry, 2015. **6**(25): p. 4497-4559.

58. Yang, H., et al., *Characteristics of hemicellulose, cellulose and lignin pyrolysis.* Fuel, 2007. **86**(12): p. 1781-1788.

59. Bauen, A., et al., *Bioenergy: a sustainable and reliable energy source. A review of status and prospects*, 2009, IEA Bioenergy: Paris. p. 108 pp.

60. Chmielniak, T. and M. Sciazko, *Co-gasification of biomass and coal for methanol synthesis.* Applied energy, 2003. **74**(3-4): p. 393-403.

61. McKone, T., et al., *Grand challenges for life-cycle assessment of biofuels*, 2011, ACS Publications.

62. Pa, A., et al., *Environmental footprints of British Columbia wood pellets from a simplified life cycle analysis.* The International Journal of Life Cycle Assessment, 2012. **17**(2): p. 220-231.

63. Curran, M.A., *Environmental life-cycle assessment.* The International Journal of Life Cycle Assessment, 1996. **1**(3): p. 179-179.

64. Azar, C., et al., *The feasibility of low CO2 concentration targets and the role of bio-energy with carbon capture and storage (BECCS).* Climatic Change, 2010. **100**(1): p. 195-202.

65. McKendry, P., *Energy production from biomass (part 1): overview of biomass.* Bioresource Technology, 2002. **83**(1): p. 37-46.

66. Spliethoff, H., *Power generation from solid fuels*. 2010: Springer Science & Business Media.

67. Williams, O., et al., *Influence of mill type on densified biomass comminution.* Applied Energy, 2016. **182**: p. 219-231.

68. Williams, O., et al., *Investigation into the applicability of Bond Work Index (BWI) and Hardgrove Grindability Index (HGI) tests for several biomasses compared to Colombian La Loma coal.* Fuel, 2015. **158**: p. 379-387.

69. Khalsa, J.H.A., et al., *Torrefied Biomass Pellets—Comparing Grindability in Different Laboratory Mills.* Energies, 2016. **9**(10): p. 794.

70. Mani, S., et al., *Economics of producing fuel pellets from biomass.* Applied Engineering in agriculture, 2006. **22**(3): p. 421-426.

71. Demirbaş, A., *Calculation of higher heating values of biomass fuels.* Fuel, 1997. **76**(5): p. 431-434.

72. De Jong, W. and J.R. van Ommen, *Biomass as a sustainable energy source for the future: fundamentals of conversion processes*. 2014: John Wiley & Sons.

73. Oakey, J.E., *Power plant life management and performance improvement*. 2011: Elsevier.

74. Smethurst, P., *TREE PHYSIOLOGY | Nutritional Physiology of Trees*, in *Encyclopedia of Forest Sciences*, J. Burley, Editor. 2004, Elsevier: Oxford. p. 1616-1622.

75. Boström, D., et al., *Ash Transformation Chemistry during Combustion of Biomass.* Energy & Fuels, 2012. **26**(1): p. 85-93.

76. Bryers, R.W., *Fireside slagging, fouling, and high-temperature corrosion of heat-transfer surface due to impurities in steam-raising fuels.* Progress in Energy and Combustion Science, 1996. **22**(1): p. 29-120.

77. Doshi, V., et al., *Development of a modeling approach to predict ash formation during co-firing of coal and biomass.* Fuel Processing Technology, 2009. **90**(9): p. 1148-1156.

78. Vassilev, S.V., et al., *An overview of the composition and application of biomass ash. Part 1. Phase–mineral and chemical composition and classification.* Fuel, 2013. **105**: p. 40-76.

79. Vassilev, S.V., C.G. Vassileva, and V.S. Vassilev, *Advantages and disadvantages of composition and properties of biomass in comparison with coal: An overview.* Fuel, 2015. **158**: p. 330-350.

80. Vassilev, S.V., D. Baxter, and C.G. Vassileva, *An overview of the behaviour of biomass during combustion: Part I. Phase-mineral transformations of organic and inorganic matter.* Fuel, 2013. **112**: p. 391-449.

81. Vassilev, S.V., D. Baxter, and C.G. Vassileva, *An overview of the behaviour of biomass during combustion: Part II. Ash fusion and ash formation mechanisms of biomass types.* Fuel, 2014. **117, Part A**: p. 152-183.

82. Vassilev, S.V., et al., *Ash contents and ash-forming elements of biomass and their significance for solid biofuel combustion.* Fuel, 2017. **208**: p. 377-409.

83. Zhou, C., et al., *Combustion characteristics and arsenic retention during co-combustion of agricultural biomass and bituminous coal.* Bioresource Technology, 2016. **214**: p. 218-224.

84. Izquierdo, M., et al., *Influence of the co-firing on the leaching of trace pollutants from coal fly ash.* Fuel, 2008. **87**(10): p. 1958-1966.

85. Wu, H., et al., *Trace elements in co-combustion of solid recovered fuel and coal.* Fuel Processing Technology, 2013. **105**: p. 212-221.

86. Gogebakan, Z. and N. Selçuk, *Trace elements partitioning during co-firing biomass with lignite in a pilot-scale fluidized bed combustor.* Journal of Hazardous Materials, 2009. **162**(2): p. 1129-1134.

87. Saqib, N. and M. Bäckström, *Trace element partitioning in ashes from boilers firing pure wood or mixtures of solid waste with respect to fuel composition, chlorine content and temperature.* Waste Management, 2014. **34**(12): p. 2505-2519.

88. Arvelakis, S., et al., *Effect of leaching on the ash behavior of olive residue during fluidized bed gasification.* Biomass and Bioenergy, 2002. **22**(1): p. 55-69.

89. Öhman, M. and A. Nordin, *The Role of Kaolin in Prevention of Bed Agglomeration during Fluidized Bed Combustion of Biomass Fuels.* Energy & Fuels, 2000. **14**(3): p. 618-624.

90. Vassileva, C.G. and S.V. Vassilev, *Behaviour of inorganic matter during heating of Bulgarian coals: 2. Subbituminous and bituminous coals.* Fuel Processing Technology, 2006. **87**(12): p. 1095-1116.

91. Beyers, L.J., et al., *Effects of Structure on the Thermodynamic and Transport Properties of Na2O-CaO-SiO2-FeO-Fe2O3 Melts*, in *Advances in Molten Slags, Fluxes, and Salts: Proceedings of the 10th International Conference on Molten Slags, Fluxes and Salts 2016*, R.G. Reddy, et al., Editors. 2016, Springer International Publishing: Cham. p. 511-518.

92. Vargas, S., F.J. Frandsen, and K. Dam-Johansen, *Rheological properties of high-temperature melts of coal ashes and other silicates.* Progress in Energy and Combustion Science, 2001. **27**(3): p. 237-429.

93. Niu, Y., H. Tan, and S.e. Hui, *Ash-related issues during biomass combustion: Alkali-induced slagging, silicate melt-induced slagging (ash fusion), agglomeration, corrosion, ash utilization, and related countermeasures.* Progress in Energy and Combustion Science, 2016. **52**: p. 1-61.

94. Riedl, R., et al. *Corrosion in fire tube boilers of biomass combustion plants*. in *China International Corrosion Control Conference*. 1999. Beijing, China.

95. Nutalapati, D., et al., *Assessing slagging and fouling during biomass combustion: A thermodynamic approach allowing for alkali/ash reactions.* Fuel Processing Technology, 2007. **88**(11): p. 1044-1052.

96. Aho, M. and J. Silvennoinen, *Preventing chlorine deposition on heat transfer surfaces with aluminium–silicon rich biomass residue and additive.* Fuel, 2004. **83**(10): p. 1299-1305.

97. Theis, M., et al., *Fouling tendency of ash resulting from burning mixtures of biofuels. Part 2: Deposit chemistry.* Fuel, 2006. **85**(14): p. 1992-2001.

98. Shao, Y., et al., *Ash Deposition in Biomass Combustion or Co-Firing for Power/Heat Generation.* Energies, 2012. **5**(12): p. 5171.

99. Kaufmann, H., et al., *Deposit formation on a single cylinder during combustion of herbaceous biomass.* Fuel, 2000. **79**(2): p. 141-151.

100. Nielsen, H., et al., *Deposition of potassium salts on heat transfer surfaces in straw-fired boilers: a pilot-scale study.* Fuel, 2000. **79**(2): p. 131-139.

101. Masia, A.A.T., *Characterisation and prediction of deposits in biomass co-combustion*, 2010, Universidad de Sevilla.

102. Plaza, P.P., *The Development of a Slagging and Fouling predictive methodology for large scale pulverised boilers fired with coal/biomass blends*, in *Institute of Energy*2013, Cardiff University: Cardiff.

103. Vargas, S., *Straw and Coal Ash Rheology*, in *Chemical Engineering*2001, Technical University of Denmark: Lyngby.

104. Richerson, D., D.W. Richerson, and W.E. Lee, *Modern Ceramic Engineering: Properties, Processing, and Use in Design, Third Edition*. 2005: Taylor & Francis.

105. Öhman, M., et al., *Bed Agglomeration Characteristics during Fluidized Bed Combustion of Biomass Fuels.* Energy & Fuels, 2000. **14**(1): p. 169-178.

106. Ergudenler, A. and A. Ghaly, *Agglomeration of silica sand in a fluidized bed gasifier operating on wheat straw.* Biomass and Bioenergy, 1993. **4**(2): p. 135-147.

107. Salour, D., et al., *Control of in-bed agglomeration by fuel blending in a pilot scale straw and wood fueled AFBC.* Biomass and Bioenergy, 1993. **4**(2): p. 117-133.

108. Materazzi, M., *Clean Energy from Waste: Fundamental Investigations on Ashes and Tar Behaviours in a Two Stage Fluid Bed-Plasma Process for Waste Gasification*. 2016: Springer International Publishing.

109. Skrifvars, B.-J., et al., *Sintering mechanisms of FBC ashes.* Fuel, 1994. **73**(2): p. 171-176.

110. Kingery, W.D., *Introduction to ceramics*. 1960: Wiley.

111. Skrifvars, B.J., M. Hupa, and M. Hiltunen, *Sintering of ash during fluidized bed combustion.* Industrial & Engineering Chemistry Research, 1992. **31**(4): p. 1026-1030.

112. Cooke, S.J., *A characterisation of combustion and gasification residues from biomass and other fuels*, in *Department of Materials*1998, University of London: Imperial College of Science, Technology and Medicine.

113. Baxter, L.L., et al., *The behavior of inorganic material in biomass-fired power boilers: field and laboratory experiences.* Fuel Processing Technology, 1998. **54**(1–3): p. 47-78.

114. Pohl, J.H. and L.A. Juniper, *Slagging: Problem Definition*, in *Applications of Advanced Technology to Ash-Related Problems in Boilers*, L. Baxter and R. DeSollar, Editors. 1996, Springer US: Boston, MA. p. 567-577.

115. Wang, L., et al., *Investigation of Biomass Ash Sintering Characteristics and the Effect of Additives.* Energy & Fuels, 2014. **28**(1): p. 208-218.

116. Niu, Y., et al., *Investigations on biomass slagging in utility boiler: Criterion numbers and slagging growth mechanisms.* Fuel Processing Technology, 2014. **128**: p. 499-508.

117. Wang, X., et al., *Mechanism Research on the Development of Ash Deposits on the Heating Surface of Biomass Furnaces.* Industrial & Engineering Chemistry Research, 2012. **51**(39): p. 12984-12992.

118. Öhman, M., et al. *Slag formation during combustion of biomass fuels*. in *International Conference on Solid Biofuels: 12/08/2009-14/08/2009*. 2009.

119. Jenkins, B.M., et al., *Combustion properties of biomass.* Fuel Processing Technology, 1998. **54**(1–3): p. 17-46.

120. Theis, M., et al., *Fouling tendency of ash resulting from burning mixtures of biofuels. Part 1: Deposition rates.* Fuel, 2006. **85**(7-8): p. 1125-1130.

121. Pettersson, J., et al., *KCl Induced Corrosion of a 304-type Austenitic Stainless Steel at 600°C; The Role of Potassium.* Oxidation of Metals, 2005. **64**(1-2): p. 23-41.

122. Nielsen, H.P., et al., *The implications of chlorine-associated corrosion on the operation of biomass-fired boilers.* Progress in Energy and Combustion Science, 2000. **26**(3): p. 283-298.

123. Uusitalo, M.A., P.M.J. Vuoristo, and T.A. Mäntylä, *High temperature corrosion of coatings and boiler steels below chlorine-containing salt deposits.* Corrosion Science, 2004. **46**(6): p. 1311-1331.

124. Wang, B.-Q., *Erosion-corrosion of coatings by biomass-fired boiler fly ash.* Wear, 1995. **188**(1-2): p. 40-48.

125. Rayaprolu, K., *Boilers for Power and Process*. 2009, Florida: CRC Press.

126. van Loo, S. and J. Koppejan, *Biomass Ash Characteristics and Behaviour in Combustion Systems*, 2009, International Energy Agency: Task 32: Biomass Combustion and Co-Firing.

127. Rahimi, M., I. Owen, and J. Mistry, *Thermal stresses in boiler tubes arising from high-speed cleaning jets.* International Journal of Mechanical Sciences, 2003. **45**(6–7): p. 995-1009.

128. Barnes, D.I., M.W. Lewit, and M. Smith. *The slagging behaviour of three UK power station coals in an ash deposition rig*. in *The Impact of Ash Deposition on Coal Fired Plants: Proceedings of the Engineering Foundation Conference*. 1993. Solihull, England: Taylor & Francis.

129. Sandberg, J., U. Sand, and R.B. Fdhila, *Long time investigation of the effect of fouling on the super-heaters in a circulating fluidized biomass boiler.* International Journal of Energy Research, 2006. **30**(13): p. 1037-1053.

130. Senior, C.L., *Predicting Removal of Coal Ash Deposits in Convective Heat Exchangers.* Energy & Fuels, 1997. **11**(2): p. 416-420.

131. Kalisz, S. and M. Pronobis, *Investigations on fouling rate in convective bundles of coal-fired boilers in relation to optimization of sootblower operation.* Fuel, 2005. **84**(7–8): p. 927-937.

132. Armesto, L., et al., *Combustion behaviour of rice husk in a bubbling fluidised bed.* Biomass and Bioenergy, 2002. **23**(3): p. 171-179.

133. Siedlecki, M., W. De Jong, and A.H.M. Verkooijen, *Fluidized Bed Gasification as a Mature And Reliable Technology for the Production of Bio-Syngas and Applied in the Production of Liquid Transportation Fuels—A Review.* Energies, 2011. **4**(3): p. 389.

134. Barišić, V., K. Peltola, and E. Coda Zabetta, *Role of Pulverized Coal Ash against Agglomeration, Fouling, and Corrosion in Circulating Fluidized-*

Bed Boilers Firing Challenging Biomass. Energy & Fuels, 2013. **27**(10): p. 5706-5713.

135. Wang, L., et al., *A Critical Review on Additives to Reduce Ash Related Operation Problems in Biomass Combustion Applications.* Energy Procedia, 2012. **20**: p. 20-29.

136. Öhman, M., et al., *Effect of Kaolin and Limestone Addition on Slag Formation during Combustion of Wood Fuels.* Energy & Fuels, 2004. **18**(5): p. 1370-1376.

137. Steenari, B.M. and O. Lindqvist, *High-temperature reactions of straw ash and the anti-sintering additives kaolin and dolomite.* Biomass and Bioenergy, 1998. **14**(1): p. 67-76.

138. Tran, K.-Q., et al., *A kinetic study of gaseous alkali capture by kaolin in the fixed bed reactor equipped with an alkali detector.* Fuel, 2005. **84**(2): p. 169-175.

139. Wu, H., et al., *Dust-Firing of Straw and Additives: Ash Chemistry and Deposition Behavior.* Energy & Fuels, 2011. **25**(7): p. 2862-2873.

140. Steenari, B.-M., et al., *Investigation of Ash Sintering during Combustion of Agricultural Residues and the Effect of Additives.* Energy & Fuels, 2009. **23**(11): p. 5655-5662.

141. Wu, H., et al., *Impact of coal fly ash addition on ash transformation and deposition in a full-scale wood suspension-firing boiler.* Fuel, 2013. **113**: p. 632-643.

142. Wigley, F., et al., *Ash deposition at higher levels of coal replacement by biomass.* Fuel Processing Technology, 2007. **88**(11–12): p. 1148-1154.

143. British Standards Institute, *Solid Biofuels - Determination of moisture content - oven dry method*, 2009.

144. Luan, C., C. You, and D. Zhang, *An experimental investigation into the characteristics and deposition mechanism of high-viscosity coal ash.* Fuel, 2014. **119**: p. 14-20.

145. British Standards Institute, *Solid Biofuels - Determination of ash content*, 2009.

146. Halford, M., *Prince*, 2017. p. Factor analysis for in Python.

147. White, H.J., *Electrostatic Precipitation Of Fly Ash.* Journal of the Air Pollution Control Association, 1977. **27**(1): p. 15-22.

148. Parker, K., *Electrical operation of electrostatic precipitators*. Power and Energy Series. Vol. 41. 2003, London: Institution of Electrical Engineers.

149. Environmental Quality Management, Inc, *Ohio EPA's Operation and Maintenance Guidelines for Air Pollution Control Equipment*, 1993, Ohio Environmental Protection Agency.

150. Jędrusik, M. and A. Świerczok, *The influence of fly ash physical and chemical properties on electrostatic precipitation process.* Journal of Electrostatics, 2009. **67**(2–3): p. 105-109.

151. Navarrete, B., et al., *Influence of plate spacing and ash resistivity on the efficiency of electrostatic precipitators.* Journal of Electrostatics, 1997. **39**: p. 65-81.

152. Jaworek, A., A. Krupa, and T. Czech, *Modern electrostatic devices and methods for exhaust gas cleaning: A brief review.* Journal of Electrostatics, 2007. **65**(3): p. 133-155.

153. Bäck, A., *Enhancing ESP Efficiency for High Resistivity Fly Ash by Reducing the Flue Gas Temperature*, in *Electrostatic Precipitation: 11th International Conference on Electrostatic Precipitation, Hangzhou, 2008*, K. Yan, Editor. 2009, Springer Berlin Heidelberg: Berlin, Heidelberg. p. 406-411.

154. Bickelhaupt, R.E., *Surface Resistivity and the Chemical Composition of Fly Ash.* Journal of the Air Pollution Control Association, 1975. **25**(2): p. 148-152.

155. Nussbaumer, T. *Characterisation of particles from wood combustion with respect to health relevance and electrostatic precipitation*. in *3rd Mid-European Biomass Conference*. 2011. Graz: Austrian Biomass Association.

156. Mizuno, A., *Electrostatic precipitation.* IEEE Transactions on Dielectrics and Electrical Insulation, 2000. **7**(5): p. 615-624.

157. Jaworek, A., et al., *Properties of biomass vs. coal fly ashes deposited in electrostatic precipitator.* Journal of Electrostatics, 2013. **71**(2): p. 165-175.

158. Dalmon, J. and D. Tidy, *A comparison of chemical additives as aids to the electrostatic precipitation of fly-ash.* Atmospheric Environment (1967), 1972. **6**(10): p. 721-722,IN1-IN2,723-734.

159. Shanthakumar, S., D.N. Singh, and R.C. Phadke, *Flue gas conditioning for reducing suspended particulate matter from thermal power stations.* Progress in Energy and Combustion Science, 2008. **34**(6): p. 685-695.

160. Morrell, R., *Handbook of properties of technical and engineering ceramics. Part 1 An Introduction for the Engineer and Designer*. 1985, London: H.M.S.O.

161. Bickelhaupt, R.E., *Influence of fly ash compositional factors on electrical volume resistivity*, 1974, Southern Research Inst., Birmingham, Ala.;Environmental Protection Agency, Washington, D.C. Office of Research and Development.

162. Bickelhaupt, R., *Effect of Chemical Composition on Surface Resistivity of Fly Ash*, 1975, Environmental Protection Agency: National Service Center for Environmental Publications (NSCEP). p. 51.

163. Bickelhaupt, R., *A Technique for Predicting Fly Ash Resistivity*, U.S. Environmental Protection Agency, Editor 1979: Research Triangle Park, North Carolina.

164. Noda, N. and H. Makino, *Influence of operating temperature on performance of electrostatic precipitator for pulverized coal combustion boiler.* Advanced Powder Technology, 2010. **21**(4): p. 495-499.

165. Nussbaumer, T., *Combustion and Co-combustion of Biomass: Fundamentals, Technologies, and Primary Measures for Emission Reduction.* Energy & Fuels, 2003. **17**(6): p. 1510-1521.

166. Lu, J., et al., *Capture efficiency of coal/biomass co-combustion ash in an electrostatic field.* Particuology, 2018.

167. Sanz, D., et al., *Review of critical parameters in biomass combustion emissions control by means of hybrid filter.* IOP Conference Series: Earth and Environmental Science, 2015. **28**(1): p. 012012.

168. Obernberger, I., et al., *Concentrations of inorganic elements in biomass fuels and recovery in the different ash fractions.* Biomass Quality for Power Production, 1997. **12**(3): p. 211-224.

169. Lind, T., et al., *Volatilization of the Heavy Metals during Circulating Fluidized Bed Combustion of Forest Residue.* Environmental Science & Technology, 1999. **33**(3): p. 496-502.

170. Vainio, E., et al., *The fate of chlorine, sulfur, and potassium during co-combustion of bark, sludge, and solid recovered fuel in an industrial scale BFB boiler.* Fuel Processing Technology, 2013. **105**: p. 59-68.

171. Lillieblad, L., M.R. Strand, and K. Porle. *Conditions for Electrostatic Precipitators after Biomass Fired Boilers*. in *International Society for Electrostatic Precitators (ICESP) IX Conference*. 2004. Mpumalanga (South African Republic)

172. Chesner, W.H., R.J. Collins, and M.H. MacKay, *User Guidelines for Waste and By-product Materials in Pavement Construction*, 1997, U.S. Department of Transportation.

173. Chandra, A., *Some Investigations on Fly Ash Resistivity Generated in Indian Power Plants*, in *Electrostatic Precipitation: 11th International Conference on Electrostatic Precipitation, Hangzhou, 2008*, K. Yan, Editor. 2009, Springer Berlin Heidelberg: Berlin, Heidelberg. p. 399-405.

174. Li, X., et al., *Sensitivity analysis on the maximum ash resistivity in terms of its compositions and gaseous water concentration.* Journal of Electrostatics, 2012. **70**(1): p. 83-90.

175. IEEE, *IEEE Standard criteria and guidelines for the laboratory measurement and reporting of fly ash resistivity*, 1984, Institute of Electrical and Electronics Engineers.

176. Dryden, I.G.C., *The Efficient Use of Energy*. 1975: IPC Science and Technology Press.

177. Mysen, B., *Physics and chemistry of silicate glasses and melts.* European Journal of Mineralogy, 2003. **15**(5): p. 781-802.

178. Arvelakis, S. and F.J. Frandsen, *Rheology of fly ashes from coal and biomass co-combustion.* Fuel, 2010. **89**(10): p. 3132-3140.

179. Park, J.H., D.J. Min, and H.S. Song, *Amphoteric behavior of alumina in viscous flow and structure of CaO-SiO2 (-MgO)-Al2O3 slags.* Metallurgical and Materials Transactions B, 2004. **35**(2): p. 269-275.

180. Herath Banda, R.M. and F.P. Glasser, *Role of iron and aluminum oxides as fluxes during the burning of Portlamd cement.* Cement and Concrete Research, 1978. **8**(3): p. 319-324.

181. Bowker, J.C., C.H.P. Lupis, and P.A. Flinn, *Structural Studies of Slags by Mössbauer Spectroscopy.* Canadian Metallurgical Quarterly, 1981. **20**(1): p. 69-78.

182. Liu, B., et al., *Relationship between coal ash composition and ash fusion temperatures.* Fuel, 2013. **105**: p. 293-300.

183. Bool, L.E. and J.J. Helble, *Iron oxidation state and its effect on ash particle stickiness.* Applications of Advanced Technology to Ash-Related Problems in Boilers, 1996: p. 281-292.

184. Seki, K. and F. Oeters, *Viscosity measurements on liquid slags in the system CaO-FeO-Fe2O3-SiO2.* ISIJ International, 1984. **24**(6): p. 445-454.

185. Arvelakis, S., et al., *Studying the melting behaviour of fly ash from the incineration of MSW using viscosity and heated stage XRD data.* Fuel, 2008. **87**(10): p. 2269-2280.

186. BCURA, *Annual Report*, 1963: Leatherhead.

187. Streeter, R.C., E.K. Diehl, and H.H. Schobert, *Measurement and Prediction of Low-Rank Coal Slag Viscosity*, in *The Chemistry of Low-Rank Coals*. 1984, American Chemical Society. p. 195-209.

188. Bottinga, Y. and D.F. Weill, *The viscosity of magmatic silicate liquids; a model calculation.* American Journal of Science, 1972. **272**(5): p. 438-475.

189. Urbain, G., Y. Bottinga, and P. Richet, *Viscosity of liquid silica, silicates and alumino-silicates.* Geochimica et Cosmochimica Acta, 1982. **46**(6): p. 1061-1072.

190. Shaw, H.R., *Viscosities of magmatic silicate liquids; an empirical method of prediction.* American Journal of Science, 1972. **272**(9): p. 870-893.

191. Riboud, P., et al., *Improvement of continuous casting powders.* Fachberichte Huttenpraxis Metallweiterverarbeitung, 1981. **19**: p. 859 - 869.

192. Li, F., et al., *Influencing Mechanism of Additives on Ash Fusion Behaviors of Straw.* Energy & Fuels, 2018. **32**(3): p. 3272-3280.

193. Arvelakis, S., et al., *Studying the Melting Behavior of Coal, Biomass, and Coal/Biomass Ash Using Viscosity and Heated Stage XRD Data.* Energy & Fuels, 2006. **20**(3): p. 1329-1340.

194. Hsieh, P.Y., K.-S. Kwong, and J. Bennett, *Correlation between the critical viscosity and ash fusion temperatures of coal gasifier ashes.* Fuel Processing Technology, 2016. **142**: p. 13-26.

195. Pang, C.H., et al., *An automated ash fusion test for characterisation of the behaviour of ashes from biomass and coal at elevated temperatures.* Fuel, 2013. **103**: p. 454-466.

196. Baxter, X.C., et al., *Study of Miscanthus x giganteus ash composition – Variation with agronomy and assessment method.* Fuel, 2012. **95**: p. 50-62.

197. Xing, P., et al., *Experimental and theoretical methods for evaluating ash properties of pine and El Cerrejon coal used in co-firing.* Fuel, 2016. **183**: p. 39-54.

198. Wieland, C., et al., *Evaluation, comparison and validation of deposition criteria for numerical simulation of slagging.* Applied Energy, 2012. **93**: p. 184-192.

199. Mackenzie, J.K. and R. Shuttleworth, *A Phenomenological Theory of Sintering.* Proceedings of the Physical Society. Section B, 1949. **62**(12): p. 833.

200. Bryers, R.W., *Factors Critically Affecting Fireside Deposits in Steam Generators*, in *Impact of Mineral Impurities in Solid Fuel Combustion*, R.P. Gupta, T.F. Wall, and L. Baxter, Editors. 1999, Springer US: Boston, MA. p. 105-131.

201. Seggiani, M., *Empirical correlations of the ash fusion temperatures and temperature of critical viscosity for coal and biomass ashes.* Fuel, 1999. **78**(9): p. 1121-1125.

202. Barnhart, D. and P. Williams, *The sintering test—an index to ash fouling tendency.* Trans. ASME, 1956. **78**(5-6): p. 1229-1236.

203. Gibb, W., *The Slagging and Fouling Characteristics of Coals-II. Sintering Test for the Determination of Fouling Propensity.* Powder Industry Research, 1981. **1**(269): p. 198l.

204. Conn, R.E. and M.L. Jones. *Comparison of low-rank coal ash sintering characteristics with pilot plant ash fouling tendencies*. in *Conference: 3. conference on slagging and fouling due to impurities in combustion gases*. 1984. Copper Mountain, CO, USA: North Dakota Univ., Grand Forks (USA). Energy Research Center.

205. Nowok, J.W., et al., *Sintering behaviour and strength development in various coal ashes.* Fuel, 1990. **69**(8): p. 1020-1028.

206. Nowok, J.W., et al., *The effect of surface tension/viscosity ratio of melts on the sintering propensity of amorphous coal ash slags.* Fuel, 1993. **72**(7): p. 1055-1061.

207. Conn, R.E., *Laboratory techniques for evaluating ash agglomeration potential in petroleum coke fired circulating fluidized bed combustors.* Fuel Processing Technology, 1995. **44**(1): p. 95-103.

208. Anthony, E.J., L. Jia, and K. Laursen, *Strength development due to long term sulfation and carbonation/sulfation phenomena.* The Canadian Journal of Chemical Engineering, 2001. **79**(3): p. 356-366.

209. Dohrn, M. and M. Müller, *Influence of Load Changes on the Deposit Behavior during Combustion of Five Different Hard Coals.* Energy & Fuels, 2018. **32**(3): p. 3985-3994.

210. Skrifvars, B.-J., A. Moilanen, and R. Lundqvist, *Characterization of biomass ashes.* Applications of Advanced Technology to Ash-Related Problems in Boilers, 1996: p. 383-407.

211. Skrifvars, B.J., et al., *Predicting Bed Agglomeration Tendencies for Biomass Fuels Fired in FBC Boilers: A Comparison of Three Different Prediction Methods.* Energy & Fuels, 1999. **13**(2): p. 359-363.

212. Malmgren, A., E. Lester, and C. Snape, *The effect of biomass on PF combustion efficiency and ash properties during coal/biomass co-combustion*, in *Project B77 Final Report*, BCURA, Editor 2007, University of Nottingham.

213. Melissari, B., *Ash related problems with high alkali biomass and its mitigation experimental evaluation.* Memoria Investigaciones en Ingeniería, 2014. **12**: p. 31-44.

214. Hansen, L.A., et al., *Characterization of Ashes and Deposits from High-Temperature Coal−Straw Co-Firing.* Energy & Fuels, 1999. **13**(4): p. 803-816.

215. Skorupska, N. and G. Couch. *Coal characterization for predicting ash deposition: An international perspective*. in *Fuel and Energy Abstracts*. 1995.

216. Hansen, L.A., et al., *Ash Fusion and Deposit Formation at Straw Fired Boilers*, in *Impact of Mineral Impurities in Solid Fuel Combustion*, R.P. Gupta, T.F. Wall, and L. Baxter, Editors. 1999, Springer US: Boston, MA. p. 341-356.

217. Raask, E., *Mineral Impurities in Coal Combustion: Behavior, Problems, and Remedial Measures*. 1985: Hemisphere Publishing Corporation.

218. Fewster, M. and Q.E. Commission. *Plant investigation of slagging at Callide Power Station*. in *Practical workshop on impact of coal quality on power plant performance. Australia Combustion Technology Centre, ACIRL Ltd., Brisbane QLD*. 1994.

219. Johansen, J.M., et al., *Release of K, Cl, and S during Pyrolysis and Combustion of High-Chlorine Biomass.* Energy & Fuels, 2011. **25**(11): p. 4961-4971.

220. Sheng, C., et al., *Comparison of sulphur retention by coal ash in different types of combustors.* Fuel Processing Technology, 2000. **64**(1): p. 1-11.

221. Wang, G., et al., *Potassium Capture by Kaolin, Part 2: K2CO3, KCl, and K2SO4.* Energy & Fuels, 2018. **32**(3): p. 3566-3578.

222. Van der Drift, A., et al., *Entrained flow gasification of biomass*, 2004, ECN.

223. Coda, B., et al., *Slagging Behavior of Wood Ash under Entrained-Flow Gasification Conditions.* Energy & Fuels, 2007. **21**(6): p. 3644-3652.

224. Tomeczek, J. and H. Palugniok, *Kinetics of mineral matter transformation during coal combustion.* Fuel, 2002. **81**(10): p. 1251-1258.

Appendix A - Complete Sample Ash Compositions

Table A.1 - Ash compositions for samples and additive blends in wt. %, based upon ICP ash analysis

Ash Component (wt. %)	PFA	OCA	OCA 5% PFA	OCA 15% PFA	OCA 25% PFA	WWA	WWA 5% PFA	WWA 15% PFA	WWA 25% PFA
SiO_2	58.20	11.20	27.55	41.34	47.47	27.20	52.44	56.23	57.12
Al_2O_3	20.80	1.20	8.02	13.77	16.32	4.60	17.79	19.77	20.24
Fe_2O_3	9.30	0.90	3.82	6.29	7.38	2.30	8.00	8.85	9.06
CaO	2.90	10.30	7.73	5.55	4.59	24.80	6.97	4.29	3.66
TiO_2	0.90	0.10	0.38	0.61	0.72	0.30	0.79	0.86	0.88
MnO	0.00	0.00	0.00	0.00	0.00	0.00	0.00	0.00	0.00
MgO	1.40	3.00	2.44	1.97	1.77	4.70	2.01	1.61	1.51
Na_2O	2.30	0.60	1.19	1.69	1.91	1.50	2.15	2.25	2.27
K_2O	1.70	32.30	21.65	12.67	8.69	9.20	3.09	2.18	1.96
Mn_3O_4	0.10	0.10	0.10	0.10	0.10	1.50	0.36	0.19	0.15
P_2O_5	0.20	5.00	3.33	1.92	1.30	2.00	0.53	0.31	0.26
Cl	0.01	2.89	1.89	1.04	0.67	1.00	0.19	0.07	0.04
SO_3	0.90	2.40	1.88	1.44	1.24	0.02	0.74	0.84	0.87

Ash Component (wt. %)	FA	FA 5% PFA	FA 15% PFA	FA 25% PFA	BA	BA 5% PFA	BA 15% PFA	BA 25% PFA
SiO_2	48.80	56.89	57.77	57.97	49.70	54.19	56.41	57.15
Al_2O_3	19.10	20.56	20.72	20.76	6.80	14.20	17.86	19.07
Fe_2O_3	5.90	8.83	9.14	9.22	3.00	6.33	7.97	8.52
CaO	10.90	4.01	3.27	3.10	2.90	2.90	2.90	2.90
TiO_2	0.80	0.89	0.90	0.90	0.40	0.66	0.79	0.84
MnO	0.00	0.00	0.00	0.00	0.00	0.00	0.00	0.00
MgO	2.70	1.58	1.46	1.43	1.50	1.45	1.42	1.41
Na_2O	1.00	2.12	2.24	2.27	0.20	1.31	1.86	2.04
K_2O	6.40	2.35	1.92	1.82	3.70	2.64	2.12	1.95
Mn_3O_4	0.40	0.14	0.11	0.11	0.10	0.10	0.10	0.10
P_2O_5	0.90	0.30	0.23	0.22	1.40	0.77	0.45	0.35
Cl	0.00	0.01	0.01	0.01	0.20	0.10	0.05	0.03
SO_3	0.60	0.86	0.89	0.89	0.80	0.85	0.88	0.89

Ash Component (wt. %)	Kaolin	OCA 5%KAO	OCA 15%KAO	OCA 25%KAO	WWA 5%KAO	WWA 15%KAO	WWA 25%KAO
SiO_2	48.30	24.11	34.99	39.83	44.38	46.96	47.57
Al_2O_3	36.40	13.44	23.78	28.36	30.50	34.38	35.29
Fe_2O_3	0.90	0.90	0.90	0.90	1.16	0.99	0.95
CaO	0.04	6.73	3.72	2.38	4.64	1.62	0.90
TiO_2	0.06	0.09	0.07	0.07	0.10	0.08	0.07
MnO	0.00	0.00	0.00	0.00	0.00	0.00	0.00
MgO	0.40	2.10	1.33	0.99	1.20	0.67	0.55
Na_2O	0.06	0.41	0.25	0.18	0.33	0.15	0.11
K_2O	2.60	21.97	13.25	9.38	3.83	3.02	2.83
Mn_3O_4	0.00	0.07	0.04	0.02	0.28	0.10	0.05
P_2O_5	0.00	3.26	1.79	1.14	0.37	0.13	0.07
Cl	0.00	1.88	1.04	0.66	0.19	0.06	0.03
SO_3	0.00	1.57	0.86	0.55	0.00	0.00	0.00

Table A.2 - Ash compositions for samples and additive blends, in mol. %

Ash Component (mol. %)	PFA	OCA	OCA 5% PFA	OCA 15% PFA	OCA 25% PFA	WWA	WWA 5% PFA	WWA 15% PFA	WWA 25% PFA
SiO_2	69.35	21.15	37.91	43.23	61.76	37.18	64.01	67.55	68.37
Al_2O_3	14.60	1.34	5.95	7.41	12.52	3.71	12.80	13.99	14.27
Fe_2O_3	4.17	0.64	1.87	2.26	3.61	1.18	3.67	4.00	4.08
CaO	3.70	20.84	14.88	12.99	6.40	36.32	9.11	5.53	4.69
TiO_2	0.81	0.14	0.37	0.45	0.70	0.31	0.72	0.78	0.79
MnO	0.00	0.00	0.00	0.00	0.00	0.00	0.00	0.00	0.00
MgO	2.49	8.45	6.37	5.72	3.42	9.58	3.66	2.88	2.70
Na_2O	2.66	1.10	1.64	1.81	2.41	1.99	2.55	2.62	2.64
K_2O	1.29	38.90	25.82	21.67	7.21	8.02	2.41	1.67	1.50
Mn_3O_4	0.03	0.05	0.04	0.04	0.03	0.54	0.12	0.06	0.05
P_2O_5	0.10	4.00	2.64	2.21	0.71	1.16	0.28	0.16	0.13
SO_3	0.80	3.40	2.50	2.21	1.21	0.02	0.67	0.76	0.78

Ash Component (mol. %)	FA	FA 5% PFA	FA 15% PFA	FA 25% PFA	BA	BA 5% PFA	BA 15% PFA	BA 25% PFA
SiO_2	57.70	67.72	68.81	69.05	77.35	72.60	70.70	70.12
Al_2O_3	13.31	14.42	14.54	14.57	6.24	11.21	13.19	13.79
Fe_2O_3	2.62	3.95	4.10	4.13	1.76	3.19	3.76	3.93
CaO	13.81	5.12	4.17	3.96	4.84	4.16	3.89	3.81
TiO_2	0.71	0.79	0.80	0.80	0.47	0.67	0.75	0.77
MnO	0.00	0.00	0.00	0.00	0.00	0.00	0.00	0.00
MgO	4.76	2.80	2.59	2.54	3.48	2.89	2.65	2.58
Na_2O	1.15	2.45	2.59	2.62	0.30	1.70	2.26	2.43
K_2O	4.83	1.79	1.46	1.38	3.67	2.26	1.70	1.52
Mn_3O_4	0.12	0.04	0.04	0.03	0.04	0.04	0.03	0.03
P_2O_5	0.45	0.15	0.12	0.11	0.92	0.43	0.24	0.18
SO_3	0.53	0.77	0.79	0.80	0.93	0.86	0.83	0.82

Ash Component (mol. %)	Kaolin	OCA 5%KAO	OCA 15%KAO	OCA 25%KAO	WWA 5%KAO	WWA 15%KAO	WWA 25%KAO
SiO_2	66.63	40.34	53.44	58.54	61.12	64.74	65.60
Al_2O_3	29.59	13.26	21.40	24.57	24.75	27.93	28.68
Fe_2O_3	0.47	0.57	0.52	0.50	0.60	0.51	0.49
CaO	0.06	12.07	6.09	3.75	6.84	2.39	1.33
TiO_2	0.06	0.11	0.09	0.08	0.11	0.08	0.07
MnO	0.00	0.00	0.00	0.00	0.00	0.00	0.00
MgO	0.82	5.23	3.03	2.18	2.46	1.38	1.13
Na_2O	0.08	0.67	0.38	0.26	0.44	0.20	0.15
K_2O	2.29	23.45	12.91	8.80	3.36	2.66	2.49
Mn_3O_4	0.00	0.03	0.01	0.01	0.10	0.03	0.02
P_2O_5	0.00	2.31	1.16	0.71	0.22	0.07	0.04
SO_3	0.00	1.97	0.99	0.60	0.00	0.00	0.00

Table A.3 - Ash compositions for samples and additive blends, in atomic concentration. %

Ash Component (At. conc. %)	PFA	OCA	OCA 5%PFA	OCA 15%PFA	OCA 25%PFA	WWA	WWA 5%PFA	WWA 15%PFA	WWA 25%PFA
Si	22.88	6.98	14.27	18.74	20.38	12.27	21.12	22.29	22.56
Al	5.84	0.53	2.97	4.46	5.01	1.48	5.12	5.60	5.71
Fe	1.67	0.26	0.90	1.30	1.45	0.47	1.47	1.60	1.63
Ca	1.85	10.42	6.49	4.09	3.20	18.16	4.56	2.76	2.35
Ti	0.27	0.05	0.15	0.21	0.23	0.10	0.24	0.26	0.26
Mn	0.00	0.00	0.00	0.00	0.00	0.00	0.00	0.00	0.00
Mg	1.24	4.22	2.86	2.02	1.71	4.79	1.83	1.44	1.35
Na	1.78	0.74	1.21	1.51	1.62	1.33	1.71	1.75	1.77
K	0.87	26.07	14.52	7.44	4.83	5.37	1.61	1.12	1.00
Mn	0.02	0.04	0.03	0.03	0.03	0.40	0.09	0.04	0.04
P	0.03	1.16	0.64	0.32	0.21	0.34	0.08	0.05	0.04

Ash Component (At. conc. %)	FA	FA 5% PFA	FA 15% PFA	FA 25% PFA	BA	BA 5% PFA	BA 15% PFA	BA 25% PFA
Si	19.04	22.35	22.71	22.79	25.53	23.96	23.33	23.14
Al	5.32	5.77	5.82	5.83	2.49	4.48	5.27	5.52
Fe	1.05	1.58	1.64	1.65	0.70	1.28	1.50	1.57
Ca	6.90	2.56	2.09	1.98	2.42	2.08	1.95	1.91
Ti	0.23	0.26	0.26	0.27	0.15	0.22	0.25	0.26
Mn	0.00	0.00	0.00	0.00	0.00	0.00	0.00	0.00
Mg	2.38	1.40	1.30	1.27	1.74	1.45	1.33	1.29
Na	0.77	1.64	1.73	1.75	0.20	1.14	1.51	1.63
K	3.23	1.20	0.98	0.92	2.46	1.51	1.14	1.02
Mn	0.09	0.03	0.03	0.03	0.03	0.03	0.02	0.02
P	0.13	0.04	0.03	0.03	0.27	0.13	0.07	0.05

Ash Component (At. conc. %)	Kaolin	OCA 5%KAO	OCA 15%KAO	OCA 25%KAO	WWA 5%KAO	WWA 15%KAO	WWA 25%KAO
Si	21.99	13.31	17.64	19.32	20.17	21.36	21.65
Al	11.84	5.30	8.56	9.83	9.90	11.17	11.47
Fe	0.19	0.23	0.21	0.20	0.24	0.21	0.20
Ca	0.03	6.03	3.04	1.88	3.42	1.19	0.67
Ti	0.02	0.04	0.03	0.03	0.04	0.03	0.02
Mn	0.00	0.00	0.00	0.00	0.00	0.00	0.00
Mg	0.41	2.61	1.52	1.09	1.23	0.69	0.56
Na	0.05	0.45	0.25	0.18	0.29	0.14	0.10
K	1.53	15.71	8.65	5.89	2.25	1.78	1.67
Mn	0.00	0.02	0.01	0.01	0.08	0.03	0.01
P	0.00	0.67	0.34	0.21	0.06	0.02	0.01

Appendix B - Bottinga-Weill Viscosity Modelling Constants

Table B.1 – Table of constants used in the Bottinga-Weill Model

For 0.75 < xSiO2 < 0.81

T (K)	1473	1523	1573	1623	1673	1723	1773	1823	1873	1923	1973	2023	2073
SiO_2	5.92	5.56	5.19	4.87	4.56	4.26	4.00	3.72	3.49	3.26	3.03	2.83	2.62
TiO_2	0.00	0.00	0.00	0.00	0.00	0.00	0.00	0.00	0.00	0.00	0.00	0.00	0.00
FeO	0.00	1.91	2.21	2.48	2.97	2.97	3.21	3.39	0.00	0.00	0.00	0.00	0.00
MnO	0.00	0.00	-1.99	-2.05	-2.78	-1.91	0.00	0.00	0.00	0.00	0.00	0.00	0.00
MgO	-0.26	1.66	-0.52	-0.59	-0.97	-0.89	-1.14	-1.17	-1.30	-1.30	-1.48	-1.56	-1.65
CaO	-1.09	-1.38	-1.47	-0.81	-1.57	-1.51	-2.25	-1.95	0.00	0.00	0.00	0.00	0.00
SrO	0.00	0.00	0.00	0.00	0.00	0.00	0.00	0.00	0.00	0.00	-2.55	-2.48	-2.28
BaO	0.00	0.00	0.00	0.00	0.00	-2.43	-2.33	-2.25	-2.24	-2.24	-2.07	-2.06	-1.95
Li_2O	0.00	-7.17	-6.94	-6.46	-6.30	-6.02	-5.80	-5.42	-5.28	-5.28	-4.91	-4.65	0.00
Na_2O	-8.21	-8.10	-7.66	-7.07	-6.69	-5.98	-5.70	-5.34	0.00	0.00	0.00	0.00	0.00
K_2O	-6.60	-6.39	-6.08	-5.87	-5.63	-5.39	0.00	0.00	0.00	0.00	0.00	0.00	0.00
$NaAlO_2$	-6.60	7.99	7.51	6.99	6.56	6.18	5.75	5.42	5.02	5.02	4.38	4.03	3.78
$BaAl_2O_4$	8.47	0.00	0.00	0.00	0.00	0.00	0.00	0.00	0.00	0.00	0.00	0.00	0.00
$CaAl_2O_4$	0.00	0.34	0.13	-0.54	-0.76	-1.23	-1.78	-2.10	-2.29	-2.29	-2.51	-2.69	-2.74
$MgAl_2O_4$	0.91	-0.09	-0.69	-1.51	-2.09	-2.62	-2.88	-3.44	-3.52	-3.52	-3.59	-3.66	-3.67
$MnAl_2O_4$	0.65	0.00	-5.02	-5.12	-4.99	-4.49	0.00	0.00	0.00	0.00	0.00	0.00	0.00

For 0.65 < xSiO2 < 0.75

T (K)	1473	1523	1573	1623	1673	1723	1773	1823	1873	1923	1973	2023	2073
SiO_2	5.74	5.39	5.02	4.69	4.36	4.08	3.81	3.53	3.30	3.06	2.82	2.62	2.41
TiO_2	-2.82	-2.87	-2.21	-1.98	-1.91	-1.78	-1.52	0.00	0.00	0.00	0.00	0.00	0.00
FeO	-1.69	-1.85	-1.05	-0.81	-0.90	-0.95	-0.52	0.00	0.00	0.00	0.00	0.00	0.00
MnO	0.00	0.00	0.00	0.00	0.00	0.00	0.00	0.00	0.00	0.00	0.00	0.00	0.00
MgO	-1.87	-1.71	-1.19	-1.49	-1.68	-1.55	-1.35	-1.18	-1.17	-1.39	-1.21	-0.96	-0.55
CaO	-1.24	-3.01	-2.84	-2.74	-2.71	-2.63	-2.78	-2.61	-1.87	-2.57	-2.59	-2.53	-2.44
SrO	0.00	0.00	0.00	0.00	0.00	0.00	-2.04	-3.54	-1.99	-2.01	-2.04	-2.01	-2
BaO	0.00	0.00	0.00	0.00	0.00	-3.65	-3.43	-3.37	-3.36	-3.17	-3.07	-2.95	-2.83
Li_2O	-6.05	-5.83	-5.61	-5.35	-5.09	-4.89	-4.75	-4.76	-4.58	-4.39	0.00	0.00	0.00
Na_2O	-5.63	-5.30	-5.05	-4.94	-4.69	-4.89	-4.31	-4.80	-5.39	-4.47	-3.94	-3.52	-2.67
K_2O	-4.43	-4.43	-4.21	-4.06	-3.98	-3.91	0.00	0.00	0.00	0.00	0.00	0.00	0.00
$NaAlO_2$	1.45	1.36	1.05	2.14	2.13	2.14	2.12	2.64	2.84	2.75	2.67	1.82	2.73
$BaAl_2O_4$	0.00	0.00	0.00	0.00	0.00	0.00	0.00	0.00	0.00	-0.61	-0.74	-0.88	-0.99
$CaAl_2O_4$	2.08	1.30	0.63	-0.14	-0.53	-1.11	-1.47	-2.27	-2.26	-2.28	-2.33	-2.40	-2.44
$MgAl_2O_4$	1.56	0.81	-0.45	-1.04	-1.54	-2.48	-2.79	-2.92	-2.98	-2.29	-3.01	-3.06	-3.09
$MnAl_2O_4$	0.00	0.00	0.00	0.00	0.00	0.00	0.00	0.00	0.00	0.00	0.00	0.00	0.00

For 0.55 < xSiO2 < 0.65

T (K)	1473	1523	1573	1623	1673	1723	1773	1823	1873	1923	1973	2023	2073
SiO_2	5.35	5.00	4.66	4.33	4.02	3.73	3.46	3.19	2.95	2.72	2.48	2.29	2.07
TiO_2	0.00	-1.82	-1.88	-1.92	-1.85	-1.81	-1.78	0.00	0.00	0.00	0.00	0.00	0.00
FeO	-1.34	-2.34	-2.59	-2.69	-2.88	-2.83	-1.99	-3.13	0.00	0.00	0.00	0.00	0.00
MnO	0.00	0.00	0.00	0.00	-2.35	0.00	0.00	0.00	0.00	0.00	0.00	0.00	0.00
MgO	-1.35	-1.39	-1.59	-1.82	-1.85	-1.64	-1.71	-2.03	-1.75	-1.69	-1.61	-1.55	-1.4
CaO	-1.12	-1.86	-1.99	-2.29	-2.41	-2.40	-2.40	-2.46	-2.35	-2.33	-2.25	-2.24	-2.12
SrO	0.00	0.00	0.00	0.00	0.00	0.00	-2.17	-2.14	-2.13	-2.11	-2.03	-2.05	-1.95
BaO	0.00	0.00	0.00	0.00	0.00	-2.17	-2.08	-2.17	-2.17	-2.14	-2.03	-1.98	-1.83
Li_2O	-4.63	-4.45	-4.26	-4.07	-3.91	-3.66	-3.51	-3.56	0.00	0.00	0.00	0.00	0.00
Na_2O	-3.77	-3.68	-3.61	-3.48	-3.47	-3.41	-3.38	-3.74	-3.53	-2.36	-1.61	0.00	0.00
K_2O	0.00	0.00	0.00	0.00	0.00	0.00	0.00	0.00	0.00	0.00	0.00	0.00	0.00
$NaAlO_2$	2.45	2.31	2.68	2.57	3.25	3.04	2.84	2.82	2.58	2.34	2.14	1.64	1.61
$BaAl_2O_4$	0.00	0.00	0.00	0.00	0.00	0.00	0.00	0.00	0.00	0.00	0.00	0.00	0.00
$CaAl_2O_4$	0.80	1.08	0.32	0.31	-0.10	-0.61	-0.71	-1.26	-1.32	-1.37	-1.39	-1.52	-1.56
$MgAl_2O_4$	-0.17	-1.52	-0.79	-0.97	-0.74	-1.52	-1.65	-1.57	-1.95	-2.05	-2.08	-2.16	-2.12
$MnAl_2O_4$	0.00	0.00	0.00	0.00	0.00	0.00	0.00	0.00	0.00	0.00	0.00	0.00	0.00

For 0.45 < xSiO2 < 0.55

T (K)	1473	1523	1573	1623	1673	1723	1773	1823	1873	1923	1973	2023	2073
SiO_2	4.49	4.13	3.78	3.46	3.15	2.87	2.61	2.34	2.12	1.87	1.64	1.45	1.24
TiO_2	0.00	0.00	-0.50	-1.63	-1.76	-1.06	0.00	0.00	0.00	0.00	0.00	0.00	0.00
FeO	-1.78	-1.82	-2.09	-2.35	-2.08	-2.81	-2.34	-2.87	0.00	0.00	0.00	0.00	0.00
MnO	0.00	0.00	-1.78	-0.98	-1.98	0.00	0.00	0.00	0.00	0.00	0.00	0.00	0.00
MgO	-1.22	-1.18	-1.33	-1.27	-1.25	-1.17	-1.01	-0.76	-0.97	-1.06	-0.93	-0.95	-0.9
CaO	-0.61	-0.62	-0.77	-0.96	-1.12	-1.18	-1.25	-1.33	-1.35	-1.47	-1.38	-1.38	-1.3
SrO	0.00	0.00	0.00	0.00	0.00	0.00	-1.17	-1.13	-1.12	-1.09	-1.07	-1.08	-1.04
BaO	0.00	0.00	0.00	0.00	0.00	0.00	-1.22	-1.22	-1.23	-1.20	-1.15	-1.12	-1.04
Li_2O	-3.37	-3.30	-3.17	-3.04	-2.92	-2.80	-2.58	-2.61	0.00	0.00	0.00	0.00	0.00
Na_2O	-3.20	-3.13	-2.98	-2.97	-2.88	-2.75	-2.65	-1.68	-1.52	0.00	0.00	0.00	0.00
K_2O	0.00	0.00	0.00	0.00	0.00	0.00	0.00	0.00	0.00	0.00	0.00	0.00	0.00
$NaAlO_2$	4.84	4.60	4.33	4.16	3.97	3.54	3.29	2.91	2.67	2.36	2.16	1.94	1.77
$BaAl_2O_4$	0.00	0.00	0.00	0.00	0.00	0.00	0.00	0.00	0.00	0.00	0.00	0.00	0.00
$CaAl_2O_4$	3.08	2.64	2.11	1.52	1.19	0.76	0.32	-0.11	-0.22	-0.46	-0.50	-0.56	-0.56
$MgAl_2O_4$	0.00	1.52	1.12	1.19	1.50	2.75	1.05	-0.52	-0.28	-0.03	-0.07	0.20	0.4
$MnAl_2O_4$	0.00	0.00	0.00	0.00	0.00	0.00	0.00	0.00	0.00	0.00	0.00	0.00	0.00

For 0.45 < xSiO2 < 0.55

T (K)	1473	1523	1573	1623	1673	1723	1773	1823	1873	1923	1973	2023	2073
SiO_2	2.32	2.18	2.05	1.92	1.81	1.69	1.59	1.48	1.39	1.30	1.22	1.14	1.05
TiO_2	-0.96	-0.48	-0.35	-0.57	0.38	0.86	0.83	0.00	0.00	0.00	0.00	0.00	0.00
FeO	-0.79	-1.09	-1.22	-1.25	-1.39	-1.30	-1.75	-1.74	0.00	0.00	0.00	0.00	0.00
MnO	-1.56	-1.35	-1.31	-1.38	-1.08	-0.93	-0.96	0.00	0.00	0.00	0.00	0.00	0.00
MgO	0.87	0.66	1.05	0.23	-0.15	-0.33	-0.53	0.64	0.49	0.46	-0.32	-0.45	-0.49
CaO	0.32	0.32	0.31	0.17	-0.07	0.31	-0.51	-1.51	1.44	-1.02	-1.12	-1.22	-1.27
SrO	0.00	0.00	0.00	0.00	0.00	0.00	0.00	0.00	0.00	0.00	0.00	0.00	0.00
BaO	0.00	0.00	0.00	0.00	0.00	0.00	0.00	0.00	0.00	0.00	0.00	0.00	0.00
Li_2O	-1.87	-1.85	-1.90	-1.94	-1.98	-2.02	-2.04	0.00	0.00	0.00	0.00	0.00	0.00
Na_2O	-1.93	-2.04	-2.09	-2.14	-2.17	-2.18	-2.22	-2.26	0.00	0.00	0.00	0.00	0.00
K_2O	0.00	0.00	0.00	0.00	0.00	0.00	0.00	0.00	0.00	0.00	0.00	0.00	0.00
$NaAlO_2$	0.00	0.00	0.00	0.00	0.00	0.00	0.00	0.00	0.00	0.00	0.00	0.00	0.00
$BaAl_2O_4$	0.00	0.00	0.00	0.00	0.00	0.00	0.00	0.00	0.00	0.00	0.00	0.00	0.00
$CaAl_2O_4$	3.73	3.34	2.91	2.36	2.34	1.87	1.74	2.54	2.82	3.07	2.76	2.76	2.42
$MgAl_2O_4$	0.00	0.00	0.00	0.00	0.00	0.00	0.00	1.51	0.55	-0.99	0.11	0.11	0.06
$MnAl_2O_4$	0.00	0.00	0.00	0.00	0.00	0.00	0.00	0.00	0.00	0.00	0.00	0.00	0.00

Appendix C - Range of Experimental Data used in Empirical Models

Table C.1 - Table of empirical modelling constraints, based upon the range of experimental data used

Composition Range	SiO_2 (wt.%)	Al_2O_3 (wt.%)	Equiv. Fe_2O_3 (wt.%)	CaO (wt.%)	MgO (wt.%)	CaF_2 (wt.%)	Na_2O + K_2O (wt.%)	Silica Ratio ς	SiO_2 /Al_2O_3
S-squared (S^2)	31 - 59	19 - 37	0-38	1-37	1 - 12	-	1 - 6	45 - 75	1.2 - 2.3
Watt-Fereday	30 - 60	15 - 35	3 - 30	2 - 30	1 - 10	-	-	40 - 80	1.4 - 2.4
Bottinga-Weill**	35 - 81	>5	>5	>5	>5	-	>5	-	-
Shaw	35 - 81	>5	>5	>5	>5	-	>5	-	-
Urbain	-	-	-	-	-	-	-	-	-
Riboud	27 - 56	0 - 12	-	8 - 46	-	-	0 - 22	-	-
Lakatos	0.61 - 0.77*	0 - 0.05*	-	0.09 - 0.14*	0 - 0.10*	0 - 18	0.10 - 0.21*	-	-

* Values in molar fractions rather than wt. %.

** Using the Bottinga-Weill, and hence also the Shaw method, the values given in the table of constants in Appendix B should only be used when the composition contains greater than 5% of the compound. Therefore, the model is only valid for values greater than 5%.

Appendix D - Correlations of Indices with Sinter Strength Results

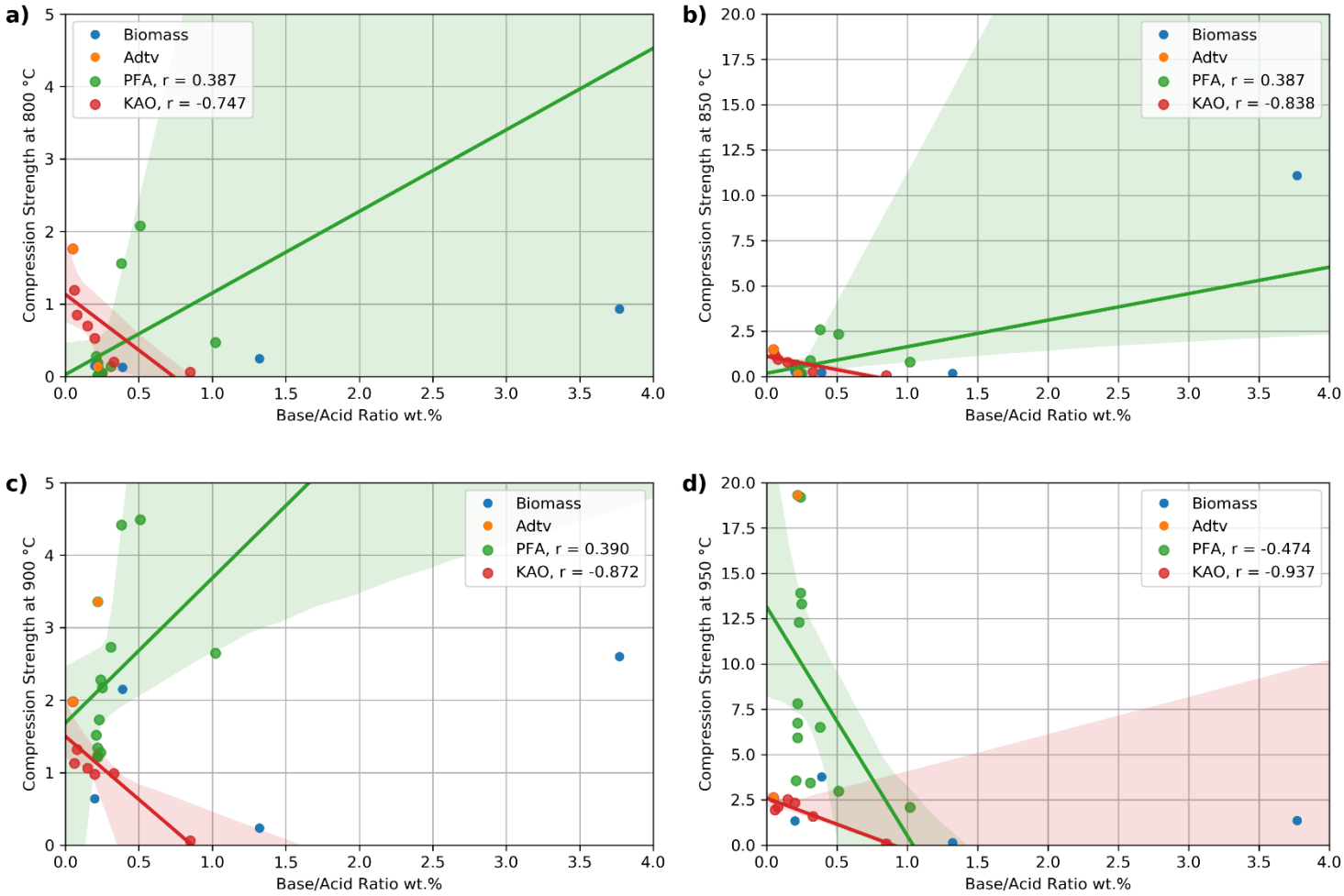

Figure D.1 - Comparison of Base/Acid Ratio with sinter strength at a) 800°C, b) 850°C, c) 900°C and d) 950°C for PFA and KAO blend compositions

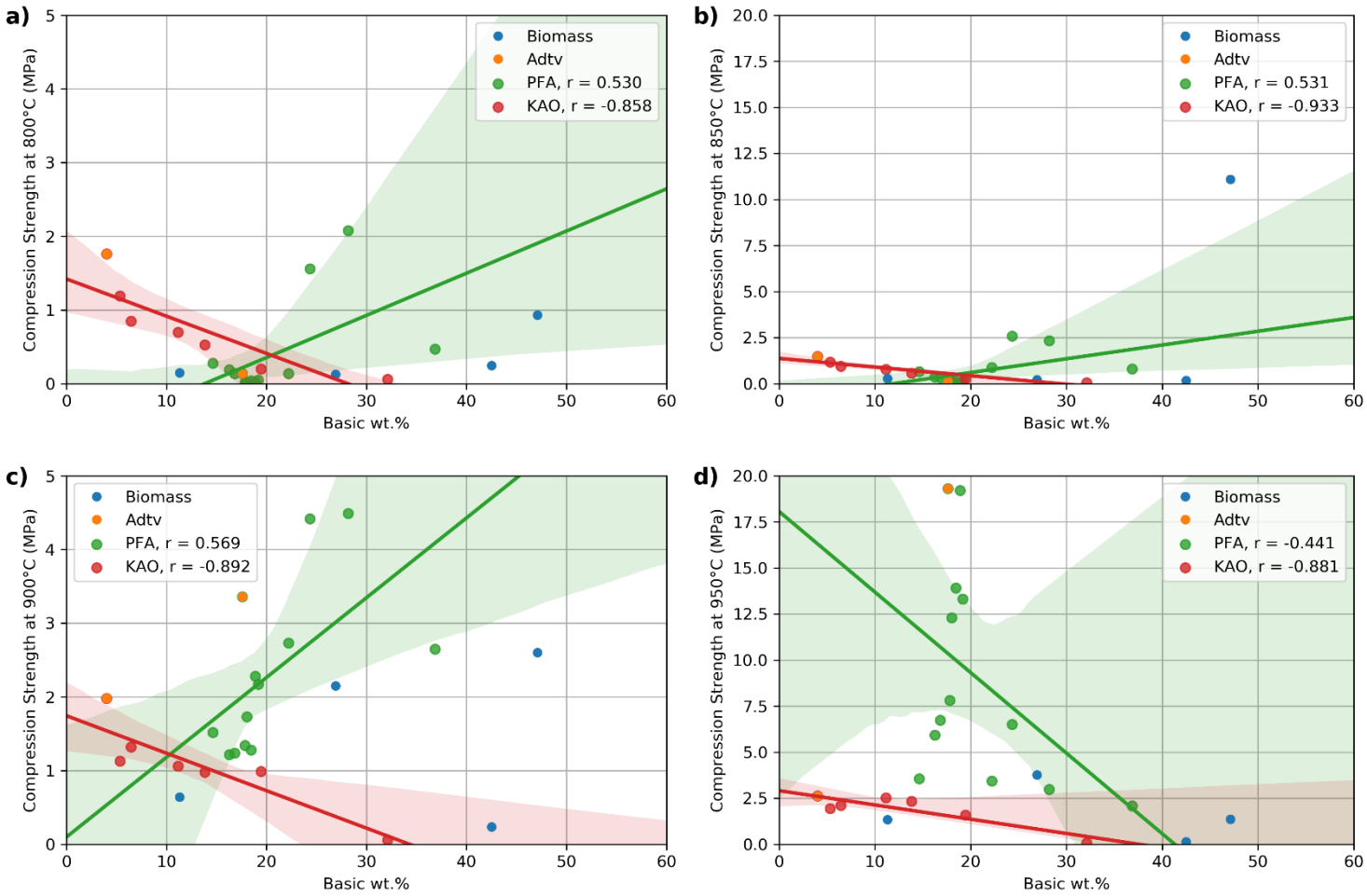

Figure D.2 - Comparison of Basic Concentration with sinter strength at a) 800°C, b) 850°C, c) 900°C and d) 950°C for PFA and KAO blend compositions

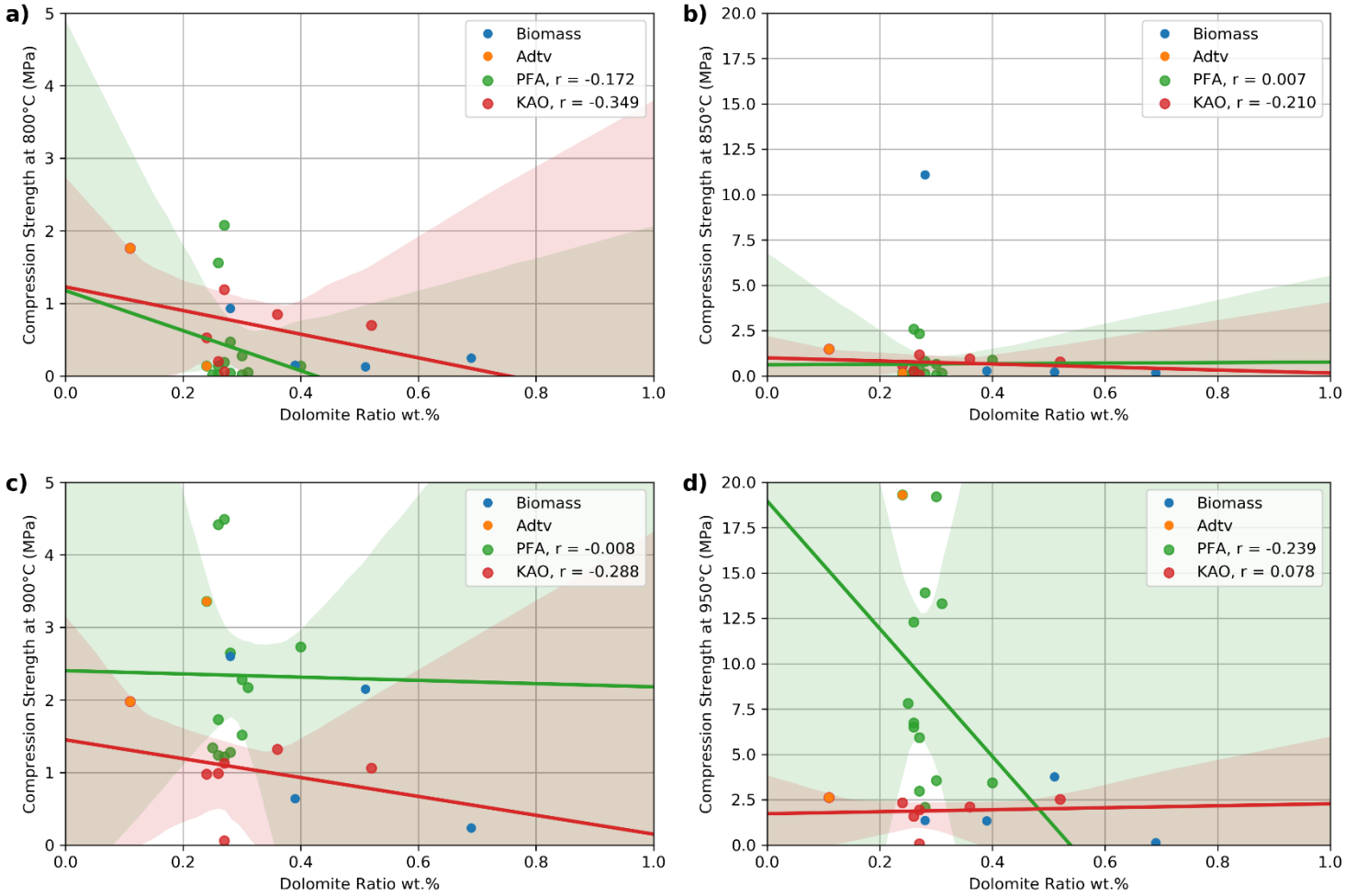

Figure D.3 - Comparison of Dolomite Ratio with sinter strength at a) 800°C, b) 850°C, c) 900°C and d) 950°C for PFA and KAO blend compositions

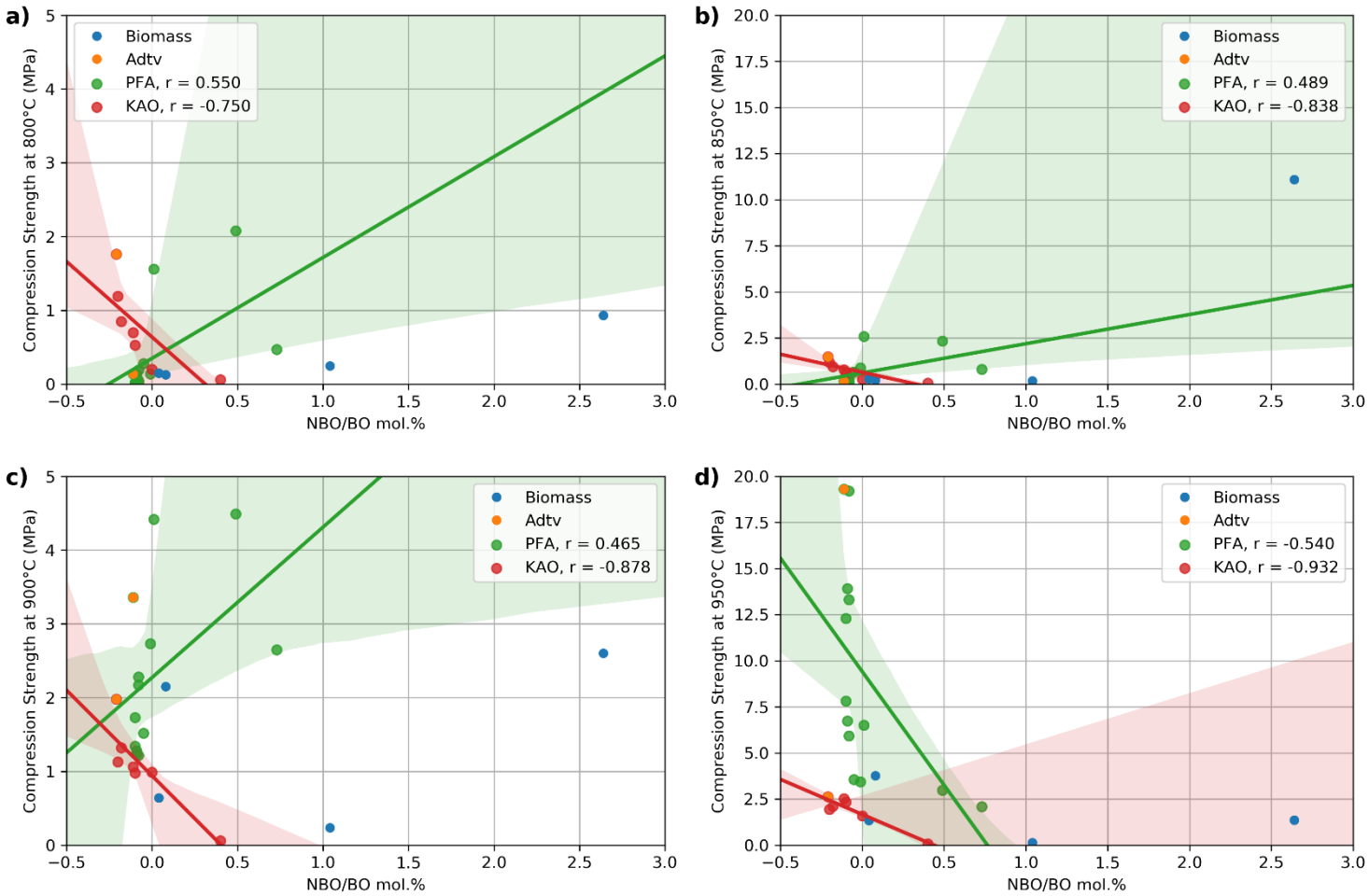

Figure D.4 - Comparison of NBO/BO Ratio with sinter strength at a) 800°C, b) 850°C, c) 900°C and d) 950°C for PFA and KAO blend compositions

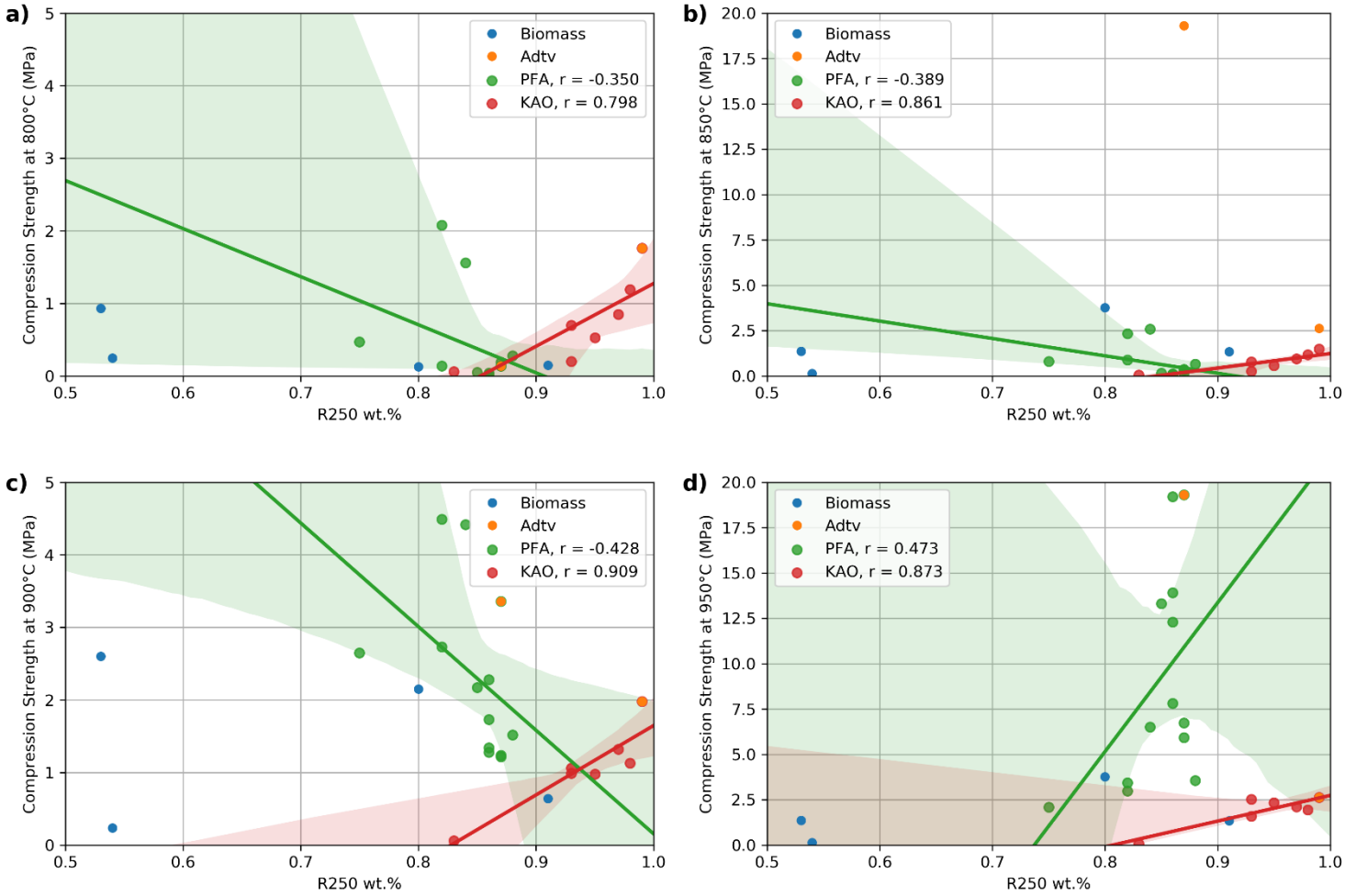

Figure D.5 - Comparison of R250 index with sinter strength at a) 800°C, b) 850°C, c) 900°C and d) 950°C for PFA and KAO blend compositions

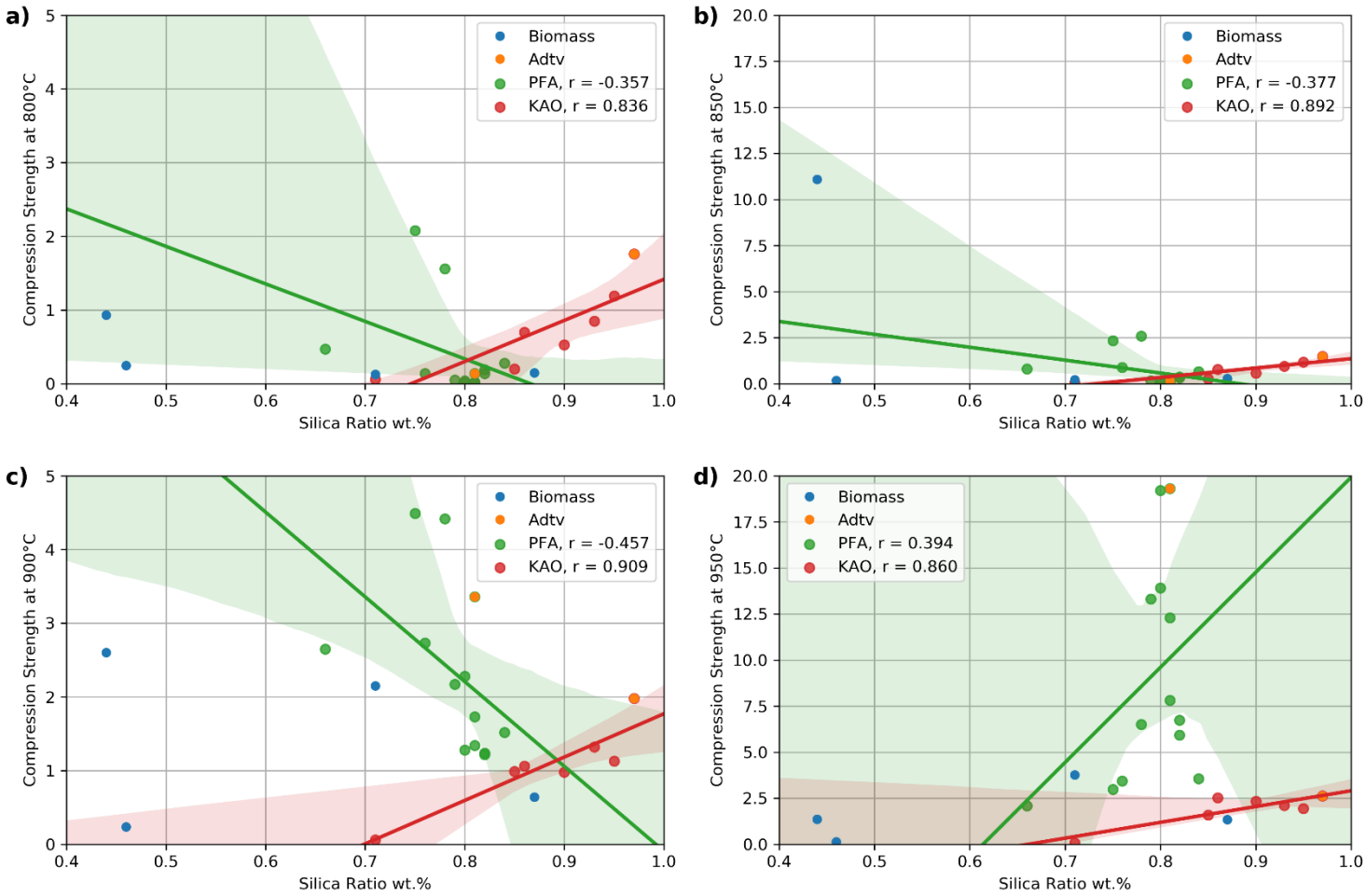

Figure D.6 - Comparison of Silica Ratio with sinter strength at a) 800°C, b) 850°C, c) 900°C and d) 950°C for PFA and KAO blend compositions